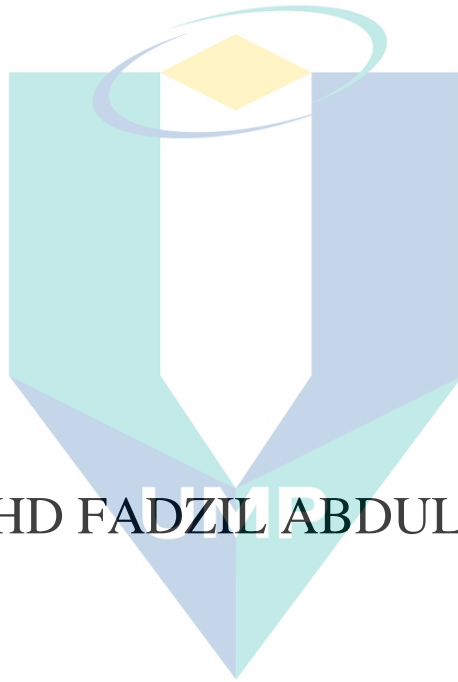


MODELLING AND CALIBRATION OF HIGH-
PRESSURE DIRECT INJECTION
COMPRESSED NATURAL
GAS ENGINE



MOHD FADZIL ABDUL RAHIM

اونيورسيتي ملايسيا قهغ

UNIVERSITI MALAYSIA PAHANG

DOCTOR OF PHILOSOPHY
(AUTOMOTIVE ENGINEERING)

UNIVERSITI MALAYSIA PAHANG

UNIVERSITI MALAYSIA PAHANG

DECLARATION OF THESIS AND COPYRIGHT

Author's Full Name : MOHD FADZIL BIN ABDUL RAHIM

Date of Birth : 19 APRIL 1980

Title : MODELLING AND CALIBRATION OF HIGH-PRESSURE
DIRECT INJECTION COMPRESSED NATURAL GAS
ENGINE

Academic Session : SEMESTER 2 2020/2021

I declare that this thesis is classified as:

- CONFIDENTIAL (Contains confidential information under the Official Secret Act 1997)*
- RESTRICTED (Contains restricted information as specified by the organization where research was done)*
- OPEN ACCESS I agree that my thesis to be published as online open access (Full Text)

I acknowledge that Universiti Malaysia Pahang reserves the following rights:

1. The Thesis is the Property of Universiti Malaysia Pahang
2. The Library of Universiti Malaysia Pahang has the right to make copies of the thesis for the purpose of research only.
3. The Library has the right to make copies of the thesis for academic exchange.

Certified by:



(Student's Signature)

800419-06-5125

New IC/Passport Number

Date: 7 JULY 2021



(Supervisor's Signature)

DR ABDUL AZIZ B. JAAFAR

Name of Supervisor

Date: 7 JULY 2021

NOTE : * If the thesis is CONFIDENTIAL or RESTRICTED, please attach a thesis declaration letter.

SUPERVISOR'S DECLARATION

We hereby declare that we have checked this thesis and in our opinion, this thesis is adequate in terms of scope and quality for the award of the degree of Doctor of Philosophy (Automotive Engineering).



(Supervisor's Signature)

Full Name : DR. ABDUL AZIZ B. JAAFAR

Position : ASSOCIATE PROFESSOR

Date : 7 JULY 2021



(Co-supervisor's Signature)

Full Name : DR. RIZALMAN B. MAMAT

Position : PROFESSOR

Date : 7 JULY 2021

STUDENT'S DECLARATION

I hereby declare that the work in this thesis is based on my original work except for quotations and citations, which have been duly acknowledged. I also declare that it has not been previously or concurrently submitted for any other degree at Universiti Malaysia Pahang or any other institution.



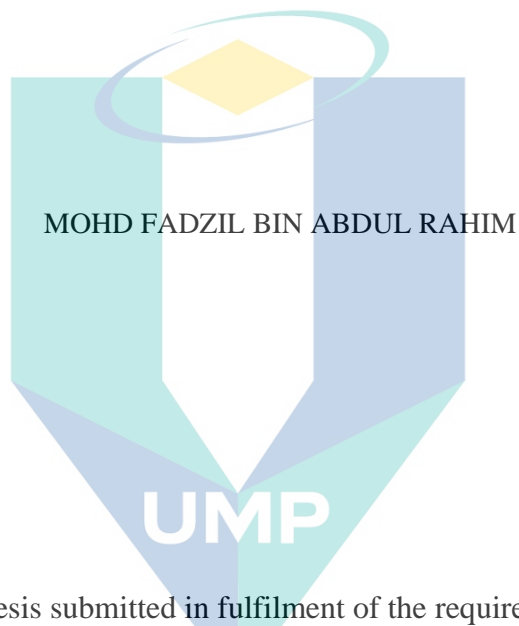
(Student's Signature)

Full Name : MOHD FADZIL B. ABDUL RAHIM
ID Number : PMA12003
Date : 7 JULY 2021

اونيورسيتي ملايسيا قهغ

UNIVERSITI MALAYSIA PAHANG

MODELLING AND CALIBRATION OF HIGH-PRESSURE DIRECT INJECTION
COMPRESSED NATURAL GAS ENGINE



Thesis submitted in fulfilment of the requirements
for the award of the degree of
Doctor of Philosophy
(Automotive Engineering)

اونيورسيتي ملايسيا قهغ

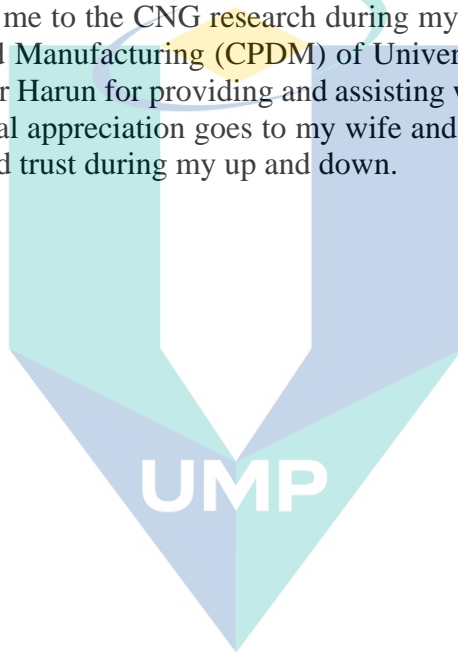
UNIVERSITI MALAYSIA PAHANG

Faculty of Manufacturing and Mechatronics Engineering Technology
UNIVERSITI MALAYSIA PAHANG

JULY 2021

ACKNOWLEDGEMENTS

I would like to express my extreme gratitude to my supervisors, Associate Professor Dr Aziz Jaafar and my co-supervisor, Professor Dr Rizalman Mamat. Also, thanks to my former PhD supervisor, Professor Dr Zahari Taha. I appreciate their guidance and supervision throughout my study at IMAMS Laboratory of FTKMP and Automotive Laboratory, FTKMA. I want to thank all the IMAMS associates for their invaluable help with the electronics and software and not forgetting the Automotive Laboratory FTKMA associates for their helpful assistance on all testing facilities and spaces as well as making my stay during the period of the study an enjoyable one. I would also like to take this chance to thank my former supervisor Professor Ts. Dato Dr Rosli Abu Bakar, Prof Ir Dr Azhar Abd Aziz and Prof Ir Dato Dr Alias Mat Noor of Universiti Teknologi Malaysia, UTM who introduced me to the CNG research during my undergraduate. To the Centre of Product Design and Manufacturing (CPDM) of Universiti Malaya, UM and its staff, especially En. Mokhtar Harun for providing and assisting with the HPDI-CNG prototype vehicle. Finally, special appreciation goes to my wife and kids, parents, and siblings for continuous support and trust during my up and down.



اونيورسيتي مليسيا قهغ

UNIVERSITI MALAYSIA PAHANG

ABSTRAK

Kajian yang dibentangkan berkisar tentang permodelan dan pengoptimuman sistem Suntikan Terus Bertekanan Tinggi Gas Asli Termampat (HPDI-CNG) didalam kenderaan penumpang. Keberkesanan sistem HPDI-CNG perlu dinilai kerana ciri-ciri rekabentuknya yang unik dan berlainan. Model analitik yang komprehensif bagi kenderaan HPDI-CNG diperlukan bagi penyelakuan pengujian dinamik kenderaan. Penyuntik terus gas perlu ditentukur semula setelah pertukaran. Kaedah penentukuran yang lebih ringkas diperlukan bagi mengurangkan beban pengujikajian. Model Rangkaian Neuron Tiruan (ANN) yang optimum diperlukan bagi menjayakan penentukuran berasaskan model (MBC). Penataan yang lengkap diperlukan untuk menjalankan prosedur MBC dengan menggunakan Algoritma Genetik (GA). Objektif kajian adalah untuk 1) menilai kesan konfigurasi sistem HPDI-CNG dan parameter parameter yang mempengaruhi, 2) menilai kadar alir jisim bahan api penyuntik dan kesesuaiannya memenuhi keperluan enjin 3) menilai prestasi keseluruhan kenderaan HPDI-CNG, dan 4) menentukur peta asas unit kawalan elektronik (ECU) kenderaan dengan menggunakan prosedur MBC. Sasaran muktamad kajian ini adalah untuk membuat penilaian lengkap keatas sistem HPDI-CNG. Metodologi kajian melibatkan permodelan analitik kenderaan untuk penyelakuan dinamik kenderaan serta permodelan analitik penyuntik terus beserta pengujikajian penyuntik secara bersendirian. Ini diikuti pengujikajian kenderaan HPDI-CNG dengan menggunakan dinamometer casis dengan parameter penilaian utama adalah daya kilas brek, kuasa brek, kecekapan haba brek (BTE), dan penggunaan bahan api tentu brek (BSFC). Prosedur MBC pula dijalankan dengan menggunakan Kotak Alat MBC, Matlab. Rangka kerja penentukuran melibatkan permodelan berasaskan data menggunakan ANN dan pengoptimuman parameter ECU dengan menggunakan GA. Berdasarkan metodologi yang dicadangkan, berikut adalah keputusan yang direkodkan: Model analisis kenderaan HPDI-CNG menghasilkan jangkaan daya kilas brek maksimum sebanyak 123.11 Nm pada tekanan penyuntik 60 bar. Kadar alir jisim maksimum melalui ujikaji penyuntik adalah sebanyak 1.24 g/s pada tekanan penyuntik 60 bar. Daya kilas dan kuasa brek enjin yang diukur adalah 69.6 Nm dan 19.1 kW. Prosedur MBC keatas peta asas ECU terbukti mampu meningkatkan prestasi keseluruhan enjin kenderaan HPDI-CNG. Peningkatan terbaik yang direkodkan daripada ujian pengesahan pengoptimuman untuk daya kilas brek, kuasa brek, halaju putaran enjin, BSFC, dan BTE adalah 5.76%, 23.46%, 11.93%, 12.10% and 16.04% berdasarkan peratusan ralat purata (MPE). Sebagai kesimpulan, permodelan analisis kenderaan memberi jangkaan prestasi kenderaan secara ideal. Parameter yang paling mempengaruhi prestasi adalah tekanan penyuntik, tempoh suntikan dan pemasaan pencucuhan. Secara ideal, penyuntik terus mampu memenuhi keperluan enjin sehingga 6000 ppm untuk pembakaran stoikiometri. Konfigurasi sistem HPDI-CNG yang sedia ada didapati kurang cekap. Ia mengurangkan pengambilan udara atau kecekapan isipadu enjin. Ia juga melambatkan tindakbalas enjin terutamanya halaju putaran maksimum enjin disebabkan lengah masa dalam penghantaran bahan api. Keputusan pengoptimuman menunjukkan pengujikajian secara halaju sapuan mamadai digunakan semasa penentukuran bagi mengurangkan titik pengujikajian. Impak kajian kepada badan pengetahuan adalah penghasilan penilaian lengkap konfigurasi HPDI-CNG yang berasaskan penyelakuan menggunakan model analitik dan model berasaskan data, dan pengujikajian secara eksperimen. Prosedur MBC dalam kajian ini menghasilkan kaedah terperinci untuk peningkatan prestasi dengan penentukuran peta asas ECU.

ABSTRACT

This study deals with the modelling and optimisation of a High-Pressure Direct Injection Compressed Natural Gas (HPDI-CNG) system in a passenger vehicle. The effectiveness of the HPDI-CNG system needs to be assessed due to its novel and distinctive design. A comprehensive analytical model is required to simulate dynamic vehicle testing. The converted gas direct injector needs to be recalibrated. A simpler calibration method is necessary to reduce the experimentation burden. An optimal Artificial Neural Network (ANN) model is required to facilitate model-based calibration (MBC) procedure. A proper setting for the MBC procedure using the Genetic Algorithm (GA) needs to be identified. The objectives of the study are 1) to analyse the effect of HPDI-CNG system configuration and influential parameters, 2) to evaluate the injector mass flow rate and its suitability to fulfil engine requirement, 3) to assess the HPDI-CNG vehicle performance as a whole, and 4) to calibrate the electronic control unit (ECU) base maps by using MBC procedure. The ultimate goal of the study is a complete evaluation of the HPDI-CNG system. The methodology consisted of analytical vehicle modelling for transient vehicle operation and independent injector analytical modelling and testing. It follows by the HPDI-CNG vehicle testing using chassis dynamometer with the main assessed parameters is the engine brake torque and power, brake thermal efficiency (BTE) and brake specific fuel consumption (BSFC). The MBC procedure was carried out by using the MBC Toolbox of Matlab. The calibration framework consists of the development of the data-driven model by using ANN and ECU parameters optimisation by using GA. Based on stated methodologies, the following findings were recorded; the analytical model of the HPDI-CNG vehicle predicted a maximum of 123.11 Nm of brake torque at 60 bar of injection pressure. The maximum mass flow rate obtained by the injector test is about 1.24 g/s at 60 bar injection pressure. Measured peak brake torque and power is about 69.6 Nm and 19.1 kW, respectively. The MBC procedure on the ECU maps has proven to be able to increase the overall performance of the HPDI-CNG engine. The best improvement recorded from the optimisation verification for the brake torque, brake power, engine rotational speed, BSFC, and BTE is 5.76%, 23.46%, 11.93%, 12.10% and 16.04%, respectively, based on mean percentage error. In conclusion, the analytical vehicle model able to predict the ideal engine performance. The most influential parameters are injection pressure, injection duration, and ignition timing. Ideally, the injector is found to be able to fulfil engine requirements until 6000 rpm for stoichiometric combustion. The configuration of HPDI-CNG is less efficient based on the current geometrical configuration. It reduced air intake or the engine's volumetric efficiency. It also affected the engine response, especially the maximum engine rotational speed, due to the delay in the fuel delivery. The optimization results suggested the use of the speed-sweep test method is sufficient for calibration purposes with reduced test-point. The impact of the study on the body of knowledge is a generation of a comprehensive evaluation of the HPDI-CNG configuration, which is based on analytical and data-driven model simulation and experimental testing. The model-based calibration procedure performed in the study provides a detailed methodology for performance improvement by calibrating the ECU maps.

TABLE OF CONTENT

DECLARATION

TITLE PAGE

ACKNOWLEDGEMENTS **ii**

ABSTRAK **iii**

ABSTRACT **iv**

TABLE OF CONTENT **v**

LIST OF TABLES **x**

LIST OF FIGURES **xi**

LIST OF SYMBOLS **xv**

LIST OF ABBREVIATIONS **xix**

LIST OF APPENDICES **xxii**

CHAPTER 1 INTRODUCTION **1**

1.1 Background of the Study 1

1.2 Problem Statement 3

1.3 The Objective of the Study 3

1.4 Research Questions 4

1.5 Hypotheses of the Study 4

1.6 Scope of the Study 5

1.7 Contribution of the Study 7

1.8 Organisation of the Thesis 8

1.9 Summary of the Chapter 10

CHAPTER 2 LITERATURE REVIEW	11
2.1 Introduction	11
2.2 Properties of Compressed Natural Gas (CNG)	11
2.3 Existing Configuration of CNGDI Engine	14
2.4 Existing CNGDI Engine Performances	21
2.4.1 Effect of Engine Compression Ratio	21
2.4.2 Effect of Injection Timing and Ignition Timing	22
2.4.3 Effect of CNGDI Combustion System Configuration	24
2.4.4 Essential Remarks on CNGDI Engine Performance	25
2.5 Engine Modelling using Analytical Approach	27
2.5.1 Modelling Technique using Analytical Approach	30
2.5.2 Previous Work on Analytical Engine Modelling	42
2.6 Engine Modelling using Artificial Neural Network (ANN)	44
2.6.1 Advantages of Artificial Neural Network (ANN)	48
2.6.2 Challenges for Successful ANN Application	49
2.6.3 Classification of ANN	50
2.6.4 ANN Application in Engine Modelling, Control and Optimization	52
2.7 Electronic Control Unit (ECU) Maps Calibration and Its Requirement	59
2.7.1 Traditional Calibration Versus Model-based Calibration (MBC)	59
2.7.2 Optimisation Based Calibration using Genetic Algorithm (GA)	69
2.7.3 Setting and Tuning of GA Parameters	72
2.7.4 Application of GA for ECU Maps Calibration	73
2.8 Gaps in the Study	77

CHAPTER 3 METHODOLOGY OF THE STUDY	78
3.1 Introduction	78
3.2 Flow Chart of the Study	78
3.3 Analytical Injector Modelling	78
3.3.1 The Electromagnetic Model	80
3.3.2 The Mechanical Model	81
3.3.3 The Flow Model	83
3.3.4 Injector Simulation Setup	85
3.4 Vehicle Analytical Modelling	85
3.4.1 Integration of Simulink and Simscape Model	87
3.4.2 The Gas Flow Dynamics	87
3.4.3 In-Cylinder Thermo-Fluid Process	93
3.4.4 The Crankshaft Dynamics	100
3.4.5 Multi-Cylinder Synchronization	102
3.4.6 The Net Mean Brake Torque Solution	103
3.4.7 The Coupling between Engine and Drivetrain	105
3.4.8 The ECU Look-Up Table	106
3.4.9 Simulation Procedure	106
3.5 Independent Injector Testing	108
3.5.1 Experimental Apparatus	108
3.5.2 Experimental Procedures for Injector Testing	110
3.6 Vehicle Speed-Sweep Test Using Chassis Dynamometer	110
3.6.1 The HPDI-CNG Prototype Vehicle Specification	111
3.6.2 Modification of Cylinder Head for Direct Injection CNG	111
3.6.3 Experimental Setup	115
3.6.4 Data Collection Procedure	119

3.7	Model-based Calibration of ECU Parameters	120
3.7.1	Correlation Study between Engine Torque with Other Engine Parameters	120
3.7.2	Selection of Model Types for ECU Calibration	121
3.7.3	Artificial Neural Network and Optimization of Network Structure	122
3.7.4	Definition of ECU Optimization Maps	124
3.7.5	Objective Function for the Optimization Based Calibration	125
3.7.6	Selection of Optimization Constraint	126
3.7.7	Fixed Variables Setup	127
3.7.8	Genetic Algorithm (GA) Operators Setup	128
3.8	Error Quantities for Results Evaluation	129
3.9	Summary of The Chapter	129

CHAPTER 4 RESULTS AND DISCUSSION OF INJECTOR TESTING AND ANALYTICAL SIMULATION **132**

4.1	Introduction	132
4.2	Independent Injector Testing	132
4.2.1	Injector Control Characteristics	132
4.2.2	Effect of the Injection Pressure on Mass Flow Rate	133
4.2.3	Effect of Injection Duration on Mass Flow Rate	137
4.3	Summary of Results	141

CHAPTER 5 RESULTS AND DISCUSSION ON ANALYTICAL VEHICLE MODELLING AND CHASSIS DYNAMOMETER TESTING **142**

5.1	Introduction	142
5.2	Parametric Analysis of Control Parameters using Vehicle Simulation	142

5.3	Experimental Vehicle Testing using Chassis Dynamometer	157
5.3.1	Measured Engine Input Parameters	157
5.3.2	The Measured Engine Output Parameters	165
5.4	The Operating Envelope and Detail Analysis of Influential Parameters	172
5.5	Summary of Results	184

CHAPTER 6 RESULTS AND DISCUSSION OF MODEL-BASED CALIBRATION OF ECU MAPS **187**

6.1	Introduction	187
6.2	Data-driven Modelling using Artificial Neural Network (ANN)	187
6.2.1	Correlation Study between Brake Torque and Other Parameters	187
6.2.2	Optimization of ANN Structure	189
6.3	Model-based Calibration of ECU Maps	198
6.3.1	Visualisation of Calibration Results	198
6.3.2	Verification by Simulation	204
6.3.3	Verification by Actual Hardware	208
6.4	Summary of Results	227

CHAPTER 7 CONCLUSION AND RECOMMENDATION OF THE STUDY **228**

7.1	Introduction	228
7.2	Conclusion of the Study	228
7.3	Contribution of the Study	232
7.4	Recommendation for Future Works	233

REFERENCES **235**

LIST OF TABLES

Table 2.1	Typical natural gas compositions by volume	12
Table 2.2	Previous work on analytical modelling of vehicle for performance prediction	45
Table 2.3	Previous work on ANN application in automotive engine modelling	55
Table 2.4	Comparison of calibration methods offered by MBC Toolbox	62
Table 2.5	Application of MBC for automotive engine calibration study	66
Table 2.6	The Genetic Algorithm iterative process	71
Table 2.7	Suggested setup for GA application in MBC calibration	76
Table 3.1	Injector simulation model input	86
Table 3.2	Definition of case study for injector testing	86
Table 3.3	The clutch spring-damper model properties	105
Table 3.4	Description of the cases for the parametric study	106
Table 3.5	Specification of the baseline case for vehicle simulation analysis	107
Table 3.6	Vehicle and engine specification use for analytical modelling	107
Table 3.7	General injector specification, model HDEV 5, made of Bosch	108
Table 3.8	Experimental conditions for the injector testing	110
Table 3.9	Specification of the vehicle and engine used for HPDI-CNG conversion	112
Table 3.10	Selected variables for correlation analysis	121
Table 3.11	The default setup of NBI solver for the optimisation study	124
Table 3.12	The optimisation constraint for the free variables	127
Table 3.13	Example of fixed variables setup for 45 bar case	128
Table 3.14	The Genetic Algorithm Operators and Parameters	129
Table 3.15	Quantities calculated for results evaluation	131
Table 4.1	Tabulated results of injection pressure effect on injector mass flow rate	134
Table 4.2	Fuel requirement at different engine speed	135
Table 4.3	Statistical results for the effect of injection duration study	140
Table 5.1	The predicted relationship between parameters based on the simulation	156
Table 5.2	The measured variables and their descriptive statistics	173
Table 6.1	Ranking of the selected variables based on Pearson correlation	188
Table 6.2	The quantitative error evaluations for data-driven modelling	197

LIST OF FIGURES

Figure 2.1	The DI engine mixture preparation strategy a) homogenous charge mode b) stratified charge mode.	15
Figure 2.2	The DING combustion system concept	16
Figure 2.3	The jet ignition concepts	17
Figure 2.4	The spark plug fuel injector (SPFI) concept	19
Figure 2.5	The classification of engine modelling technique	29
Figure 2.6	Components of an analytical engine model and governing equations	31
Figure 2.7	Standard procedures of MBC based on MBC Toolbox of Matlab	60
Figure 3.1	Flowchart of the study based on the task sequences	79
Figure 3.2	Major task based on the study's objective.	80
Figure 3.3	Pintle free body diagram based on a mass-spring-damper system	82
Figure 3.4	Definitions of effective flow area for nozzle flow calculation	84
Figure 3.5	Illustration of the throttle model valve	90
Figure 3.6	Open system boundary of the combustion chamber	95
Figure 3.7	The plot of different torque produced by the analytical model	104
Figure 3.8	Bosch single-hole gasoline direct injector	109
Figure 3.9	Schematic diagram of the experimental setup.	109
Figure 3.10	Schematic of HPDI-CNG system configuration with added fuel path	113
Figure 3.11	The actual configuration of the HPDI- CNG system	114
Figure 3.12	The actual HPDI-CNG vehicle on the chassis dynamometer.	116
Figure 3.13	The schematic of the data acquisition system and the test layout	116
Figure 3.14	The surface plot of the ECU maps when initialised with zero values	125
Figure 3.15	Genetic algorithm process flow chart	130
Figure 4.1	Mean mass flow rate of CNG at increased injection pressures	133
Figure 4.2	The mass flow rate of CNG at an increased injection duration	138
Figure 5.1	The variation of mean brake torque at different throttle opening rates	143
Figure 5.2	Variation of peak torque at different throttle opening rate	144
Figure 5.3	The variation of the mean brake torque due to the varied ignition timing	146
Figure 5.4	Variation of peak torque at increased ignition timing advance	147
Figure 5.5	The variation of mean brake torque at different injection pressures	148

Figure 5.6	(a) The variation of peak torque at an increased CNG mass flow rate (b) The variation of peak torque at an increased injection pressure	149
Figure 5.7	The variation of mean brake torque at different injection duration	152
Figure 5.8	The variation of peak torque at increased injection duration	153
Figure 5.9	Comparison of a different fuel-inlet type boundary on the engine brake torque response	154
Figure 5.10	Manifold absolute pressure for the speed-sweep test at a different injection pressure	158
Figure 5.11	Injection timing for the speed-sweep test at a different injection pressure	160
Figure 5.12	Corrected injection duration of HPDI-CNG vehicle at different injection pressures	161
Figure 5.13	Corrected ignition timing of HPDI-CNG vehicle at different injection pressures	163
Figure 5.14	Air to fuel ratio of HPDI-CNG vehicle at different injection pressures	165
Figure 5.15	Engine speed of HPDI-CNG vehicle at different injection pressures	166
Figure 5.16	Engine brake torque of HPDI-CNG vehicle at different injection pressures	167
Figure 5.17	Engine brake power of HPDI-CNG vehicle at different injection pressures	168
Figure 5.18	Brake thermal efficiency of HPDI-CNG vehicle at different injection pressures	170
Figure 5.19	Brake specific fuel consumption of HPDI-CNG vehicle at different injection pressures	171
Figure 5.20	Variation of averaged engine torque at an increased injection pressure of CNG	175
Figure 5.21	Variation of averaged engine torque at increased averaged AFR of cylinder mixture	176
Figure 5.22	Variation of averaged engine torque at increased injection duration	177
Figure 5.23	Variation of averaged engine torque at ignition timing advance	178
Figure 5.24	The averaged theoretical and measured mass flow rate of air at different injection pressures	180
Figure 5.25	The averaged theoretical and measured mass flow rate of CNG at different injection pressures	181
Figure 5.26	The coefficient of variation (COV) of engine brake torque and control parameters	182

Figure 5.27	Valve timing diagram for HPDI-CNG engine and the location for minimum and maximum EOI	184
Figure 6.1	The contour plot of the RMSE error function modelled in Model Browser	190
Figure 6.2	Comparison of predicted and observed data points for RMSE error function.	190
Figure 6.3	The contour plot of VRMSE error function modelled in Model Browser	191
Figure 6.4	Comparison of predicted and observed data points for VRMSE error function	191
Figure 6.5	(a) Contour plot of the minimized RMSE with the proposed solution as a function of neuron in layer 1 and 2 (b) The Pareto front of the optimization which highlight the proposed solutions in terms of the objective function.	194
Figure 6.6	Comparison of predicted and measured data points of the best ANN structure using training and validation data sets reproduced in Model Browser	195
Figure 6.7	Comparison of simulated and measured engine brake torque by using training data sets for the optimum ANN structure	196
Figure 6.8	Comparison of simulated and measured engine brake torque by using validation data sets for the optimum ANN structure	196
Figure 6.9	Surface plot of BSFC (the objective function) before the optimization-calibration process for the case of 45 bar injection pressure	199
Figure 6.10	Surface plot of BSFC after an optimization-calibration process for the case of 45 bar injection pressure	199
Figure 6.11	Surface plot of ignition timing (the optimise variables) before the optimization-calibration process for the case of 45 bar injection pressure	200
Figure 6.12	Surface plot of ignition timing after the optimization-calibration process for the case of 45 bar injection pressure	201
Figure 6.13	Surface plot of injection duration (the optimise variables) before the optimization-calibration process for the case of 45 bar injection pressure	202
Figure 6.14	Surface plot of injection duration after the optimization-calibration process for the case of 45 bar injection pressure	203
Figure 6.15	Line plot of injection timing (the optimise variables) before and after the optimization-calibration process for the case of 45 bar injection pressure	204
Figure 6.16	Comparison of optimised engine brake torque with the baseline torque for injection pressure of 45 bar.	205
Figure 6.17	Comparison of optimized engine brake torque with the baseline experiment for injection pressure of 50 bar.	206

Figure 6.18	Comparison of optimized engine brake torque with a baseline experiment for injection pressure of 55 bar	207
Figure 6.19	Comparison of optimised engine brake torque with the baseline experiment for injection pressure of 60 bar	208
Figure 6.20	Experimental engine setup for the verification of optimal setup	209
Figure 6.21	The throttle opening recorded during the verification test for the baseline and optimised case	210
Figure 6.22	Comparison of the optimized engine brake torque and the baseline case for 45 bar injection setup	211
Figure 6.23	Error plot for the comparison of the optimised engine brake torque and the baseline case for 45 bar injection setup	212
Figure 6.24	Comparison of the optimised engine brake torque with the baseline case for 50 bar injection setup	213
Figure 6.25	Plot of Mean Percentage (MP) and Mean Absolute Percentage Error (MAPE) for the comparison of the optimised engine brake torque and the baseline case for 50 bar injection setup	213
Figure 6.26	Comparison of the engine rotational speed with the baseline case for 45 bar injection setup	216
Figure 6.27	Comparison of the engine rotational speed with the baseline case for 50 bar injection setup	216
Figure 6.28	Comparison of the engine brake power with the baseline case for 45 bar injection setup	218
Figure 6.29	Comparison of the engine brake power with the baseline case for 50 bar injection setup	218
Figure 6.30	Comparison of the engine brake specific fuel consumption (BSFC) with the baseline case for 45 bar injection setup	219
Figure 6.31	Comparison of the engine brake specific fuel consumption with the baseline case for 50 bar injection setup	220
Figure 6.32	Comparison of the optimized engine brake thermal efficiency (BTE) with the baseline case for 45 bar injection setup	221
Figure 6.33	Comparison of the optimized engine brake thermal efficiency (BTE) with the baseline case for 50 bar injection setup	222

LIST OF SYMBOLS

α	Ratio of inductance to relative permeability of armature material
β	Angle of connecting rod and piston axis
γ	Ratio of coil material resistivity to coil wire cross section area
γ	The specific heat ratio
$\Delta\theta$	The burning duration of fuel
δ	Piston pin offset
θ	The needle tip angle
θ	Crank angle degree
$\dot{\theta}$	Crankshaft angular velocity
θ_{thr}	Throttle angle
$\dot{\theta}_{thr}$	The rate of throttle opening
θ_{seg}	The segment angle
θ_{thc}	the throttle plat angle
θ_o	the start of heat release or ignition timing
$\dot{\theta}_x$	Crankshaft angular velocity
$\ddot{\theta}_x$	Crankshaft angular acceleration
$\lambda(\theta_x)$	Geometrical function, x=1,2,3..
μ_r	Relative magnetic permeability of armature/pintle material
μ_o	Air gaps magnetic permeability
ρ	Density
$\sum T_{fk}$	Sum of friction torque due to internal engine assemblies
$\sum T_s$	Sum of stiffness torque at the coupling
$\sum T_D$	Sum of damping torque at the coupling
$\sum T_L$	Sum of external load implied on the engine
τ	Moment of inertia of the engine and crankshaft assembly
τ	Time factor
ϕ	Connecting rod angle when the piston is at TDC
a	Wiebe model constant
a	Linear acceleration
A	Combustion chamber surface area
A_o	Effective area for the nozzle flow
A_{th}^{max}	Maximum throttle flow area
A_{th}^{plate}	Elliptic throttle flow area

$A(\theta)$	Cylinder surface area as a function of crank angle degree
A_{cur}	Valve curtain area
A_{th}	The effective throttle flow area
A_{pis}	Piston face area
B	Bore
C_d	Flow discharge coefficient
c_v	Constant volume specific heat
C_{heat}	Heating factor for air temperature and pressure
D_{th}	Throttle bore diameter
D_{sh}	Throttle shaft diameter
D_p	The throttle plate diameter
D_{iv}, D_{ev}	Intake or exhaust valve diameter
dQ_{loss}	The rate of heat loss
f	Frequency
F_{mag}	The electromagnetic force
F_{sol}	The solenoid force
F_{spring}	The spring force
$F_{contactfriction}$	The armature contact friction force
$F_{upperwall}$,	The upper and bottom blocking force
$F_{bottomwall}$	
$F_{pressure}$	The force due to gases fuel pressure
F_0	The initial compression force
$G(\theta_x)$	Geometrical function, $x=1,2,3..$
h	Convective heat transfer coefficient
h_p	The plate height
h_{inj}	Enthalpy of injected fuel
HV	Heating value of fuel
I_{VO}	Intake valve opening crank angle
I_{VC}	Intake valve closing crank angle
J_{cran}	Inertia of the crankshaft
k	Specific heat ratio
K_{nv}	The nozzle discharge co-efficient
K_{spring}	The spring constant
l	Connecting rod length
l	Length of coil body

L_{iv}, L_{ev}	Intake or exhaust valve lift function
m	Mass
m	Wiebe model constant
\dot{m}_a	Mass flow rate of air
M	Molecular mass of the gas
\dot{m}_f	Mass flow rate of fuel
\dot{m}_{exh}	Mass flow rate of exhaust gas
M_{pass}	Piston assembly mass
MW	Molecular weight of fuel
N	Engine rotational speed
p	Pressure
P	Power
P_b	Brake power
p_{inj}	Injection pressure
p_{baro}	Barometric pressure
p_c	The critical pressure ratio
p_o	Upstream stagnation pressure
p_{st}	Static downstream pressure
p_r	Pressure ratio of upstream and downstream
p_{im}	Intake manifold pressure
p_{cyl}	Engine cylinder pressure
p_{exh}	Exhaust manifold pressure
p_{ind}	Indicated pressure
p_{atm}	Atmospheric pressure

اونیورسیتی ملیسیا قهق

UNIVERSITI MALAYSIA PAHANG

Q	Total energy
Q_{in}	The total heat input
r	Crank radius
R	Specific gas constant
R	The nozzle hole radius
r_c	Compression ratio
R_u	Universal gas constant
r_o	Inner radius of coil cross section
r_a	Average radius of coil cross section
S	Stroke
T	Temperature
T	Torque
t_{ign}	Ignition timing
t_{inj}	Injection timing
t_{dur}	Injection duration
T_{cool}	Coolant temperature
T_{air}	Air temperature
$T_{b,g}$	Bulk temperature of gases
T_w	Cylinder wall temperature
T_{ind}	Indicated torque
T_r	Reciprocating torque
U	Internal energy
\bar{U}_p	Mean piston speed
V	The signal voltage
V_{veh}	Vehicle speed
V_d	Displacement volume
W_f	Winding factor
x	The needle displacement/ lift
x	Instantaneous position of armature
\ddot{x}	The armature acceleration

LIST OF ABBREVIATIONS

2D	Two dimensional
AFR	Air to fuel ratio
ANN	Artificial neural network
ATDC	After top dead centre
AWG	American wire gauge
BMEP	Brake mean effective pressure
BSFC	Brake specific fuel consumption
BTDC	Before top dead centre
BTE	Brake thermal efficiency
CA	Crank angle
CA50	Crank angle at 50% mass fraction burned
CAGE	Calibration generation
CCEM	Cylinder to cylinder engine model
CNG	Compressed natural gas
CNGBI	Compressed natural gas throttle body injection
CNGDI	Compressed natural gas direct injection
CNGPFI	Compressed natural gas port fuel injection
CNGTBI	Compressed natural gas throttle body injection
CO	Carbon monoxide
COP	Coil on plug
CoV	Coefficient of variation of
CR	Compression ratio
DAQ	Data acquisition sensor
DI	Direct injection
DING	Direct injection natural gas
DISC	Direct injection stratified charge
DOE	Design of experiment
DC	Duty cycle
ECU	Electronic control unit
EFI	Electronic fuel injection
EGR	Exhaust gas recirculation

EOI	End of injection
FIPC	Fuel injection pre-chamber
N	Engine revolution per minute
GA	Genetic algorithm
GDI	Gasoline direct injection
GPI	Gasoline port injection
GOT	Global optimization toolbox
HC	Hydrocarbon
HIL	Hardware in the loop
HPDI-CNG	High pressure direct injection-compressed natural gas
IANGV	The international association of natural gas vehicle
IMEP	Indicated mean effective pressure
IRBF	Interpolating radial basis function
LFE	Laminar flow element
LIF	Laser-Induced Fluorescent
MAP	Manifold absolute pressure
MEP	Mean effective pressure
MBC	Model-based calibration
MBT	Maximum brake torque timing
MC	Main chamber
MISO	Multiple input single output
MLP	Multi-layer perceptron
MOSFET	Metal oxide semiconductor field-effect transistor
mph	Mile per hour
MPI	Multi-point injection
MRT	Mass rapid transit
MSE	Mean square error
MAE	Mean absolute error
MPE	Mean percentage error
MVEM	Mean value engine model
NG	Natural gas
NGV	Natural gas vehicle
NGVP	The natural gas commercial programme

NO _x	Nitrogen oxides
NTP	Normal temperature and pressure
OEM	Original equipment manufacturer
PI	Port injection
PM	Particulate matters
PS	Physical signal
PWM	Pulse width modulation
RBF	Radial basis function
RMSE	Root mean square error
RON	Research octane number
RPM	Revolution per minute
SIL	The software in the loop
SOI	Start of injection
SPFI	Spark plug fuel injection
TDC	Top dead centre
TPS	Throttle position sensor
TWCC	Three-way catalytic converter
WOT	Wide-open throttle
VE	Volumetric efficiency



اونيورسيتي مليسيا قهغ

UNIVERSITI MALAYSIA PAHANG

LIST OF APPENDICES

APPENDIX A	ADDITIONAL EQUATION OF VEHICLE MODEL	254
APPENDIX B	ANALYTICAL VEHICLE MODEL FLOW CHART	260
APPENDIX C	INPUT FOR ANALYTICAL MODEL PER CYLINDER	267
APPENDIX D	EXCITATION FOR PARAMETRIC SIMULATION USING VEHICLE MODEL	268
APPENDIX E	DYNAMOMETER SPECIFICATION	270
APPENDIX F	HALTECH E8 SPECIFICATION	271
APPENDIX G	INNOVATE AFR METER SPECIFICATION	272
APPENDIX H	LIST OF PUBLICATIONS	273



اونيورسيتي مليسيا قهغ

UNIVERSITI MALAYSIA PAHANG

CHAPTER 1

INTRODUCTION

1.1 Background of the Study

A four-cylinder, port-injection, gasoline spark-ignition engine converted to direct-injection CNG engine. The engine is installed in a sedan vehicle. The direct injection configuration possesses a novel but irregular design compared to a standard gasoline direct injection (GDI) engine. Even though a direct injection system is known to be a promising method to increase CNG engine performance (Choi, Lee, & Park, 2015), any irregular concept compared to the standard GDI configuration might yield an inefficient injection process. Therefore, this study has proposed to assess the effect of the designed CNG direct injection system. The major drawback of such a design is the introduction of time delay in the fuel path. Zhao, Lai, & Harrington (1999) stated that the worst scenario due to delay is truncated maximum engine rotational speed since the delay created a lag effect in engine responses. This potential problem needs to be addressed by performing vehicle testing. A cheaper means is to perform modelling and simulation to predict the vehicle performances. The fuel injection system consists of the injector unit, driver, controller and the CNG supply unit. The direct gas injector is converted from a gasoline direct-injector. Hence, recalibration of the injector is needed to redefine the injector's flow specification and its suitability with the engine requirement. The most critical flow specification is the injector mass flow rate (Erfan, Chitsaz, Ziabasharhagh, Hajjalimohammadi, & Fleck, 2015). Other spray properties such as the spray penetration length, the cone spray angle and the droplet size became insignificant as the current study is dealing with gaseous fuel spray. One of the significant changes made to the engine's fuel injection system is the addition of a new electronic control unit (ECU). The main parameters adjusted in the ECU to realise the engine working condition is the ECU base maps. These base maps contain predefined setups for ignition timing, injection duration and injection timing. Since the engine is to be operated with CNG fuel, the engine

performance, especially the brake power and torque, is expected to drop. In order to increase the engine performances, this study has proposed to optimise the ECU base map parameters, which is cheaper than any physical modification on the engine. Traditional ECU tuning or calibration was performed on chassis dynamometer by using trial and error method, by a tuning expert. It is not a viable option for a regular technician, without broad experiences on engine ECU mapping and tuning. A speed sweep test procedure (transient testing) is used to check the overall engine performance. Whereas, constant-speed or constant-load procedure (steady-state tests) is used for detail adjustment at specific engine operating point. The procedure require hundred of operating points to be tested thus increasing the experimentation cost. Hence, this study has proposed the sole use of the speed-sweep test procedure to obtain engine performance data at full-load in order to reduce the burden of experimentation. This test procedure is selected as it will provide a power and torque curve for the whole engine operating range in a single execution. This study also proposed the use of a modern calibration technique called the model-based calibration method. The vital requirement of the calibration is an accurate engine model. The analytical engine model is expected to be inappropriate for the calibration or control-oriented study since its calculation time is expensive by nature. Thus, the study has proposed developing another model based on a data-driven modelling method using a Multi-Layer Perceptron Artificial Neural Network (MLP-ANN). The data-driven modelling required input-output data pairs. The data pairs from the earlier vehicle testing can be used in this modelling stage. The use of speed-sweep test data for the data-driven modelling shall produce a transient engine model, which was previously concluded to be better represent the actual engine driving condition at higher accuracy. The critical steps in MLP-ANN modelling are the selection of the model input parameters and the determination of an optimal neural network structure. The calibration is proposed based on the optimization-based approach using the Genetic Algorithm (GA) technique. It is critical to define the objective function, optimization constraints, as well as tuning of GA parameters. The optimal map obtained from the optimisation may be verified by using the existing model and experimental verification test.

1.2 Problem Statement

The effect of the HPDI-CNG system needs to be assessed due to its irregular design, which may introduce lagged engine response (Lake, Stokes, Whitaker, & Crump, 1998). This study proposed comprehensive analytical vehicle modelling and vehicle testing to evaluate the impact of the HPDI-CNG system on engine brake torque, brake power, brake thermal efficiency and brake specific fuel consumption. Both the simulation and testing shall be performed in a transient, speed-sweep test mode for rapid performance evaluation (Mustang, 2005). The conversion of the GDI injector required recalibration of the injector flow specification (Taha, Rahim, & Mamat, 2017). Independent injector testing and simulation is suggested to evaluate the injector mass flow rates. This is important to assess the suitability of the injector to fulfil engine fuelling requirements. An injector test on a flow bench with a simplified controller and gas flow measurement is expected to be able to provide the injected fuel quantity data (Erfan et al., 2015). The speed-sweep test procedure is proposed to be used in the model-based calibration procedure to reduce the experimentation time and cost. It is a significant step to generate engine performance data pair in a simpler and faster process. This data pair is the critical input for data-driven modelling. However, many data pairs are required (Chiang, Chang, & Chang, 2004), and statistical analysis needs to be carried out to identify influential parameters as the model input. An optimal Artificial Neural Network (ANN) model is needed to facilitate the model-based calibration (Turkson, Yan, Ali, & Hu, 2016). Special optimization study needs to be performed to minimise the ANN modelling error and to obtain the simplest network structure. Optimization-based calibration using the Genetic Algorithm (GA) is proposed to optimize the ECU maps parameter to enhance the HPDI-CNG engine performance. A proper setup for GA optimization needs to be identified, especially the objective function, optimization constraint, and set up of GA parameters.

1.3 The Objective of the Study

Based on the problem statements, the study objectives can be summarized as:

1. To evaluate the injector mass flow rate and injector suitability to fulfil engine fuel requirements using independent injector testing and analytical modelling technique.

2. To analyse the effect of the new direct-injection system configuration on the engine brake torque and identify influential parameters on the engine brake torque by using analytical engine modelling.
3. To evaluate the HPDI-CNG vehicle engine brake torque, brake power, brake thermal efficiency, and brake specific fuel consumption as a whole by using chassis dynamometer testing and identify the influential vehicle parameters by using statistical method.
4. To calibrate the ECU base maps based on optimization-based calibration by using the Genetic Algorithm technique and Artificial Neural Network in the framework of the model-based calibration process.

1.4 Research Questions

The conducted study is expected to answer the following question:

1. Is the direct gas injector able to deliver the mass flow rate of fuel to meet engine requirements for the whole engine operating range?
2. What are the parameters of the HPDI-CNG system which affect the engine brake torque, brake power, brake thermal efficiency and brake specific fuel consumption?
3. Is the use of the HPDI-CNG system able to improve the engine output brake torque compared to the port-injection gasoline engine?
4. Is the optimization of ECU base maps of ignition timing, injection timing and injection duration able to improve the engine brake torque, brake power, brake thermal efficiency and brake specific fuel consumption?
5. Is the use of the speed-sweep test method in model-based calibration is possible to reduce the experimentation time and cost while improving the engine performance?
6. What is the most crucial calibration requirements of ECU base maps using a model-based calibration approach?

1.5 Hypotheses of the Study

The study is executed based on the following hypotheses:

1. The injector mass flow rate is proportional to the CNG injection pressure. Hence, an increment to the injection pressure of the CNG will increase the injector mass flow rate.
2. The CNG mass flow rate is proportional to the engine output brake torque. Therefore, an increment in the CNG mass flow rate will increase the engine output brake torque.
3. Injection duration, ignition timing and injection timing are the main parameters of the newly installed direct injection system. These parameters were set up to enable injector operation. Thus, the optimal set-up of each parameter affects the overall engine performance.
4. The speed sweep test produces a torque curve in a single run of the vehicle on a chassis dynamometer, whereas the stationary test required *point-to-point* tests to fit the torque curve. Hence, the speed-sweep test procedure is a practical method to be used in a model-based calibration to reduce the expensive testing cost and time.

1.6 Scope of the Study

This study evaluates the HPDI-CNG system and calibrates the engine control parameters to improve the baseline HPDI-CNG vehicle performances. The performance parameters of interest in the study are the engine brake torque, brake power, brake specific fuel consumption (BSFC), and brake thermal efficiencies (BTE).

The injector assessment consists of injector testing and analytical injector modelling. The injector testing is performed on a flow bench with a simplified controller and gas flow measurement to measure the injector mass flow rate at different injection pressure and injection duration. The analytical injector model used in the study is developed based on the electromagnetic, mechanical and flow submodels. The injector model is used to estimate the theoretical trend of the mass flow rate at different injection pressure and injection duration on the injector mass flow rate. The parameters measured during the testing include the injection duration, injection count, and CNG storage tanks' mass. Based on this measurement, the injector mass flow rate is calculated.

The analytical vehicle model is used to simulate the operation of the HPDI-CNG vehicle during the transient speed-sweep test procedure and to identify the influential parameters on the engine brake torque. The model consists of submodels of every

significant system from the engine to the tyre. In detail, the model considers the throttle dynamics, intake manifold dynamics, in-cylinder processes, crankshaft dynamics, and driveline dynamics and the vehicle body. The analytical engine model was developed by using Matlab, Simulink and Simscape toolbox.

The speed-sweep test procedure, carried out by using a chassis dynamometer, is the primary method to evaluate the performance of the HPDI-CNG vehicle. Even though the dynamometer can perform various test methods, it is decided to demonstrate that the speed-sweep test method is sufficient and appropriate for the calibration purpose. All the tests were carried out from the lowest idle speed attainable at the test gear ratio until the maximum engine speed. The primary data source during the testing is the dynamometer brake torque, ECU parameters (such as the injection timing, injection duration, and ignition timing), and the air to fuel ratio meter. Based on this basic data, the engine brake specific fuel consumption (BSFC) and brake thermal efficiencies (BTE) are calculated. The engine emission is not measured due to the unavailability of a quick response exhaust gas analyzer.

An Artificial Neural Network (ANN) model has been proposed to compensate for certain drawbacks of the analytical model. The complexity of selecting an optimum ANN structure is treated by the use of the Normal Boundary Intersection (NBI) technique for multi-objective optimisation. This optimisation caters to the objectives to minimise the RMSE, validation RMSE and the total number of neurons in the model structure. A total of 14 inputs variables from the measured engine data is used as the model input. The engine brake torque is set as the model response.

The model-based calibration utilised a standard Genetic Algorithm (GA) solver for the constrained optimization-based calibration of the ECU parameters. Single objective optimisation formulated based on the BSFC is used and expected to minimise fuel consumption and improve engine brake torque. The current study is centred on evaluating maximum engine performances, which corresponds to the WOT condition. The determination of suitable optimisation constraints has become one of the major problems solved during the study.

The free variables of the optimisation are ignition timing, injection duration and injection timing. These are the core variables which formed the ECU lookup tables in the feed-forward control strategies of modern engine control. In order to isolate the effect of the lookup table variables from the impact of other variables and control strategy, all other parameters are set as fixed parameters. The AFR feedback from the exhaust lambda sensor, which enables the correction of injected fuel quantity, has also been shut off during the progression of the test. The model-based calibration performed in the study was fully utilized the Model-Based Calibration (MBC) Toolbox.

The final stage of the study is to verify the optimal map values obtained from the GA optimisation procedure. The chassis dynamometer testing was being used as the primary verification method. The comparison between the effect of baseline and optimal maps setup are presented based on engine brake torque, brake power, brake specific fuel consumption (BSFC), and brake thermal efficiency (BTE).

1.7 Contribution of the Study

The main contributions of the present study are:

1. The study has been executed based on a vehicle platform that utilised a high-pressure direct injection of compressed natural gases (HPDI-CNG) system. The configuration of the direct injection system is a novel but distinctive design to minimise the modification of the cylinder head.
2. A comprehensive dynamic vehicle model is developed based on an analytical approach, which coupled Simulink's engine model and SimScape's driveline model. The model used to replicate a dynamic condition of the vehicle during the speed-sweep test procedure. A co-simulation technique for a complete vehicle such as developed in the study is hardly found in the literature.
3. The injector flow characteristics study produced a new flow specification of the injector when operated with CNG at four sets of injection pressure. The study has revealed the dynamic effects of the solenoid driver setup on the injector mass flow rate.
4. The MBC procedure detailed a method to select a proper range for the free variables based on engine operating speed. This method is proven to produce an optimal setup

that is entirely feasible for implementation in model simulation and actual engine operation.

5. The study also proved that the speed-sweep test method is an applicable method to reduce the calibration test-point since the verification test demonstrated an increased engine performance. This is found to be relevant in a combination used of ANN modelling and GA optimization procedure.
6. The success of data-driven modelling using ANN is significant proof of the ANN superiority over other engine response modelling methods, even for ill-performed engine data. Besides, the study proved that standard MLP-ANN could be used to model a transient process provided that large data pairs are available.
7. The study produced comprehensive HPDI-CNG vehicle evaluations using various methods comprising analytical and data-driven vehicle simulation and experimental vehicle testing using a chassis dynamometer.

1.8 Organisation of the Thesis

The remaining chapters of the thesis are structured as follows:

Chapter two presents a review of the thermochemical and physical properties of CNG. The review is followed by a discussion on the various configuration of the CNGDI system. The following section presents the approaches taken in the analytical engine modelling technique in the past. The next section is dedicated to the review of the data-driven modelling using the ANN technique. The last sections demonstrate the applications of the MBC technique in the framework of the MBC Toolbox of Matlab. A listing of gaps of study finalised the literature review chapter.

Chapter three presents the methodology of the study, which consists of five major sections. The first part of the chapter presents the flow chart of the study. The following section covers the analytical injector submodels and their case studies. It is followed by the description of the analytical vehicle model and modelling approach employed in the study. The next section presents the injector testing method. It follows by the descriptions of vehicle testing using the speed-sweep test method, and finally, the model-based calibration method.

Chapter four presents the injector modelling and testing results to assess the injector performance and its suitability with the engine requirement. The chapter is

subdivided into three sections. The first section presents the injector control characteristics during the testing. The following section presents the effect of the injection pressure case study. And the next section presents the impact of the injection duration case study. The results are also compared with previous studies. Justifications on the discrepancies are highlighted and elaborated. Understanding the actual trend is important to understand its effect on overall engine performances. The results are corresponding to the literature presented in Section 2.3, 2.5.1.5 and the methodology presented in Section 3.3 and 3.5.

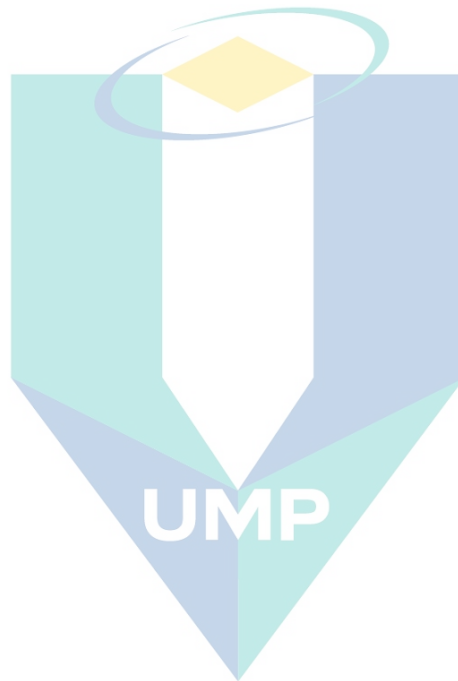
Chapter five presents the results of the parametric analysis of the HPDI-CNG vehicle model and vehicle testing results. The simulated results consist of the effect of throttle position rate, ignition timing advance, injection pressure, and injection duration on the engine's brake torque performance. In the next subtopic, the results of prototype vehicle testing using a chassis dynamometer are presented. The results can be broadly categorised as the engine input and engine output parameters. Justification on the discrepancies is highlighted and elaborated. The results are corresponding to the literature presented in Section 2.3-2.5 and the methodology presented in Section 3.4 and 3.6.

Chapter six presents the results of the MBC procedure performed in the framework of the MBC Toolbox. The essential results under this chapter included the data data-driven modelling and the ECU maps calibration. The main result of the data-driven modelling is the optimisation of the ANN structure and comparison of the ANN model against measured engine data. It is followed by the model-based calibration results, which consists of optimal calibration results, verification by simulation and verification by experimental testing. The results are corresponding to the description of the data-driven theory in Section 2.6 and its methodology in Section 3.7.3. The MBC results are reflected by the theory and methodology presented in Section 2.7 and Section 3.7, respectively.

Chapter seven concludes this thesis by drawing important conclusions and highlighting the contributions of the present work to the body of knowledge. The conclusions are centred upon answering the objective of the study and the suggestions for future work.

1.9 Summary of the Chapter

This chapter presents the main framework of the study. It consists of the background, problem statement, objective, research question, hypothesis, scope, and contributions of the study. Finally, the chapter presents the organisation of the thesis. The next chapter presents the literature review of the study.



اونيورسيتي مليسيا قهغ

UNIVERSITI MALAYSIA PAHANG

CHAPTER 2

LITERATURE REVIEW

2.1 Introduction

This chapter presents the literature review of the topics related to the study. The first review presents the CNG properties as a fuel in Section 2.2, follows by a review of existing CNG direct injection configurations in Section 2.3 and performances in Section 2.4. The review then covers analytical engine modelling in Section 2.5, data-driven modelling using ANN in Section 2.6 and the ECU maps calibration in Section 2.7. The chapter summarised the gaps of the study in the last section.

2.2 Properties of Compressed Natural Gas (CNG)

The characteristics of compressed natural gas (CNG) as fuel for road vehicles are highly affected by the thermo-chemical and physical properties of the fuel. This section is intended to highlight important properties of the fuel, which affect the engine performances based on previous studies.

Natural gas is a non-toxic, odourless and non-corrosive fuel. Natural gas remains in a gaseous state at standard room pressure and temperature. Natural gas has a lower density than air; thus, any leaks will spread skyward (Khan, Yasmin, & Shakoor, 2015; Semin & Abu Bakar, 2008). In the absence of an ignition source, the leaked gases would not produce combustion flames, and it is not easily ignited due to its high ignition temperature. The real threat is an unsafe, non-compliance storage tank and gas piping of the natural gas storage tanks which is usually stored at a pressure exceeded 200 bar (Khan & Yasmin, 2014).

The ventilation system in the area of CNG vehicle maintenance garages, buildings and CNG system bay are compulsory to prevent harmful CNG accumulations. As the CNG pressure is reduced during vehicle operation, the temperature will drop, producing

condensed water vapour outside the CNG piping system. The internally freezing condition may restrict fuel flow (Balat, 2005). The molar mass of gasoline (114.23 g/mol) is much higher than natural gas (16 g/mol).

As lightweight fuel, natural gas can produce a much better homogeneous air-fuel mixture in a faster period (Alagumalai, 2014). It opposes the liquid fuel, which needs a longer time for complete atomization and vaporization (Jahirul et al., 2010). The composition of natural gas might differ depending on the region or continent where it is originated. Based on Table 2.1, it can be seen that natural gas is primarily composed of methane, where the methane percentage may exceed 90% per volume of gas. Hence, natural gas properties are similar to methane properties (Korakianitis, Namasivayam, & Crookes, 2011).

Table 2.1 Typical natural gas compositions by volume

Composition	% Content by volume
Methane	92
Ethane	3
Propane	0.7
Butane	0.02
Pentane	0.1
Carbon dioxide	0.6
Nitrogen	3

Source: Korakianitis et al. (2011)

A significant advantage of CNG is that the fuel-air mixing process is simplified since the atomisation phase is not required. However, the density of CNG, which is about 30% lesser than air, has lowered the engine's volumetric efficiency, especially in a port-injected engine (Cho & He, 2007). The CNG gases burn at a slower burning rate compared to the gasoline fuel, which is indicated by the higher laminar flame speed values. It will affect the combustion duration of CNG fuel inside a standard SI engine configuration (Khan et al., 2015).

Standard practice to overcome the losses due to prolonged combustion duration is to advance the ignition timing of CNG-air mixture compared to the gasoline-air mixture

in the range of 10-20 degree at all engine speed (Liu, Liu, Liu, Zeng, & Huang, 2010). Other useful approaches are to increase the flame speed, including optimising combustion chamber design and intensifying in-cylinder turbulence (Bakar, Sera, & Wong, 2002). Another effective way is to blend the CNG with some amount of hydrogen since it has many desirable characteristics, such as high laminar burning velocity and low ignition energy (Ma et al., 2008).

The wide flammability limits of CNG fuel allow its utilisation in a lean-burn, thus enhancing fuel economy (Boretti & Watson, 2009; Cho & He, 2007). However, the lean-burn process must be controlled as lean combustion in an extreme regime is exposed to high cyclic variations (Ma et al., 2008). Other advantages of lean combustion are combustion efficiency enhancement, reduced combustion temperature for NO_x reduction, and increased thermal efficiency. Moreover, a leaner mixture reduced the likelihood of knock (Ma et al., 2008).

The CNG octane number, which is about 120-130, enables CNG usage at a higher compression ratio engine with an increased thermal efficiency of about 10% compared to the gasoline engine (Poulton, 1994). CNG also has a higher self-ignition temperature at about 540 °C than gasoline fuel, reducing the risk of flammable explosion in leakage (Das, 2000). CNG has a high auto-ignition temperature of 540 °C compared to 258 °C of gasoline and 316 °C of diesel. At concentrations in air below 4.3% and above 15.2%, natural gas will not burn even in the presence of a spark (Khan & Yasmin, 2014).

CNG has a low carbon/hydrogen (C/H) ratio. Thus, it produces less CO₂ per unit of energy released (Ibrahim & Bari, 2008; Liu, Yeom, & Chung, 2013). Baldassarri et al. (2006) showed that CI natural gas engine emissions of HC, NO_x, and PM were significantly lower than that of diesel engines by 67%, 98%, and 96%, respectively. If compared to gasoline engine emission, the CNG-SI engines have the potential to reduce CO, CO₂, NO_x and non-methane hydrocarbon emissions of 90–97%, 25%, 35–60%, and 50–75%, respectively (Ibrahim & Bari, 2010). In a recent study by Park, Kim, Lee, Lee, & Lee (2019), it was found that the variety of natural gas calorific values affect the NGV performances and emissions significantly. The torque and nitrogen oxide emission increase proportionally with a slight increase in the amount of carbon monoxide.

In summary, CNG has excellent traits as vehicle fuel based on its physical and thermochemical properties. Theoretically, it can deliver considerable performance compared to gasoline and diesel, except for the burning speed, which is slower and a lower energy density. The lower energy density requires a sufficient gas injection into the chamber to produce a comparable performance to gasoline or diesel. In contrast, the slow-burning characteristics require special techniques to speed up the combustion process to ensure that the combustion is completed at about the TDC.

2.3 Existing Configuration of CNGDI Engine

This section is dedicated to discussing the CNG direct injection (CNGDI) system configuration developed based on the SI and CI engine platform. The section highlights direct injection (DI) configurations commonly used for both types of engines. The configurations in the focus of this discussion are the direct injection mixing strategies, combustion system design and system parameters set up.

The gasoline direct injection (GDI) engine technologies provide *state of the art* method for optimal DI engine performances. The most popular mixing strategies of GDI are the homogenous and stratified charge methods (Çelik & Ozdalyan, 2010). Compared to the existing port fuel injection (PFI) engines, the GDI fuel is injected directly into the combustion chamber at high pressure. Figure 2.1 presents the basic charge modes of the GDI engine, which are the stratified and homogeneous charge mixture modes.

At partial-load conditions, stratified charge with late injection is used where the fuel is injected late of the compression stroke to form a stratified charge mixture. The engine can operate at a very lean mixture, and fully unthrottled operation is possible. Contrary, a homogeneous charge with early injection is preferred for the higher load conditions. The fuel is injected early of the compression stroke, and the engine is usually operated under stoichiometric or a slightly rich condition at full load (Binder, Ecker, Glaser, & Müller, 2015).

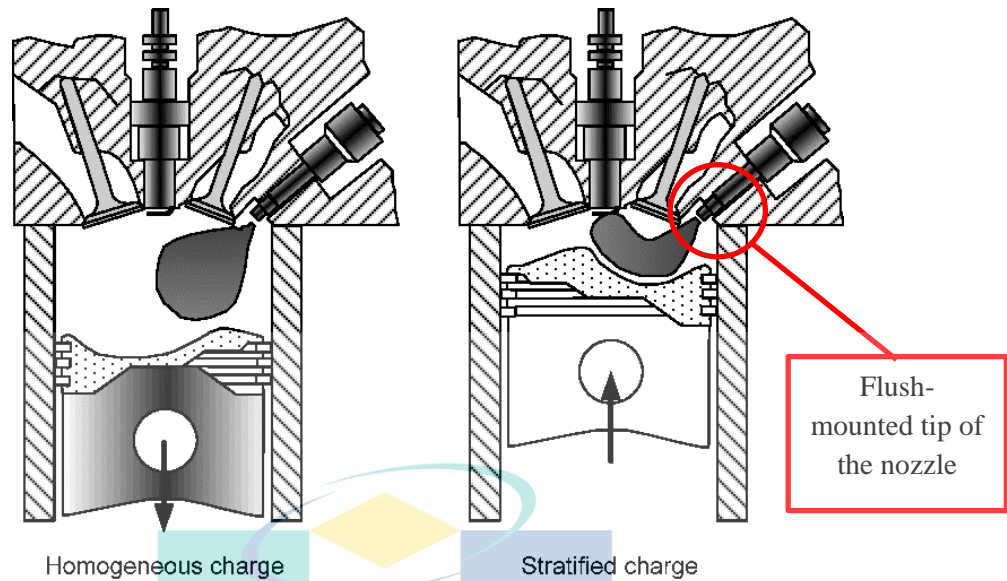


Figure 2.1 The DI engine mixture preparation strategy a) homogenous charge mode b) stratified charge mode.

Source: Çelik & Ozdalyan (2010)

The physical design of the GDI combustion chamber is tailored to deliver the fuel directly into the cylinder at a precise mass within the shortest time possible. In a standard GDI engine, the position of the direct injector's nozzle is flush-mounted with the surface of the combustion chamber. Hence, the gases will instantly mix with the bulk amount of fresh air to form a combustible mixture. Based on Zhao et al. (1999), this is a clear advantage of a gasoline direct injection engine compared to the port injection engine. The mixture preparation time lag is shortened; hence the engine response time shall be improved.

A feasibility study of the GDI technique on the existing engine design was performed by Lake, Stokes, Whitaker, & Crump (1998). They summarised four configurations available to realise the direct injection engine configuration capable of producing adequate combustion. The realisable configuration for direct injection are 1) top-entry ports with side injector, 2) side-entry ports with side injector for swirl flow, 3) side-entry ports with side injector for tumble flow, and finally 4) side-entry ports with central plug and injector. However, the finding is still debatable since the GDI system can be tailored by advanced technologies such as air-assisted, variable spray pattern, injector pulsing strategy, advanced control and ignition system technology.

CNG direct injection engine mostly developed based on the conversion of conventional compression ignition (CI) diesel or spark ignition (SI) gasoline engine. Both the CI and SI engines offer favourable characteristics. In a CI engine, the high compression ratio is a significant attraction for CNG conversion. The high octane number of CNG can tolerate high compression. The required addition is a new gas direct injector and ignition assistance. The ignition assistance is required because CNG has a high self-ignition temperature which makes it difficult to burn.

The hot surface ignition concept (Bartunek & Hilger, 2000) is comparable to the glow plug ignition assistance (Cox et al., 2000), as presented by Figure 2.2. This concept is widely used in diesel engines for a long time. It resulted in low overall emission characteristics and enables stable ignition and combustion behaviour. Lee, Park, Hyun, Lee, & Song (2019) developed a dedicated CNGDI engine based on a CI engine with a strategy to perform truly diesel-like combustion without ignition assistance. As combustion initiation, the intake air temperature was raised to 400 °C to achieve the auto-ignition temperature of methane after compression.

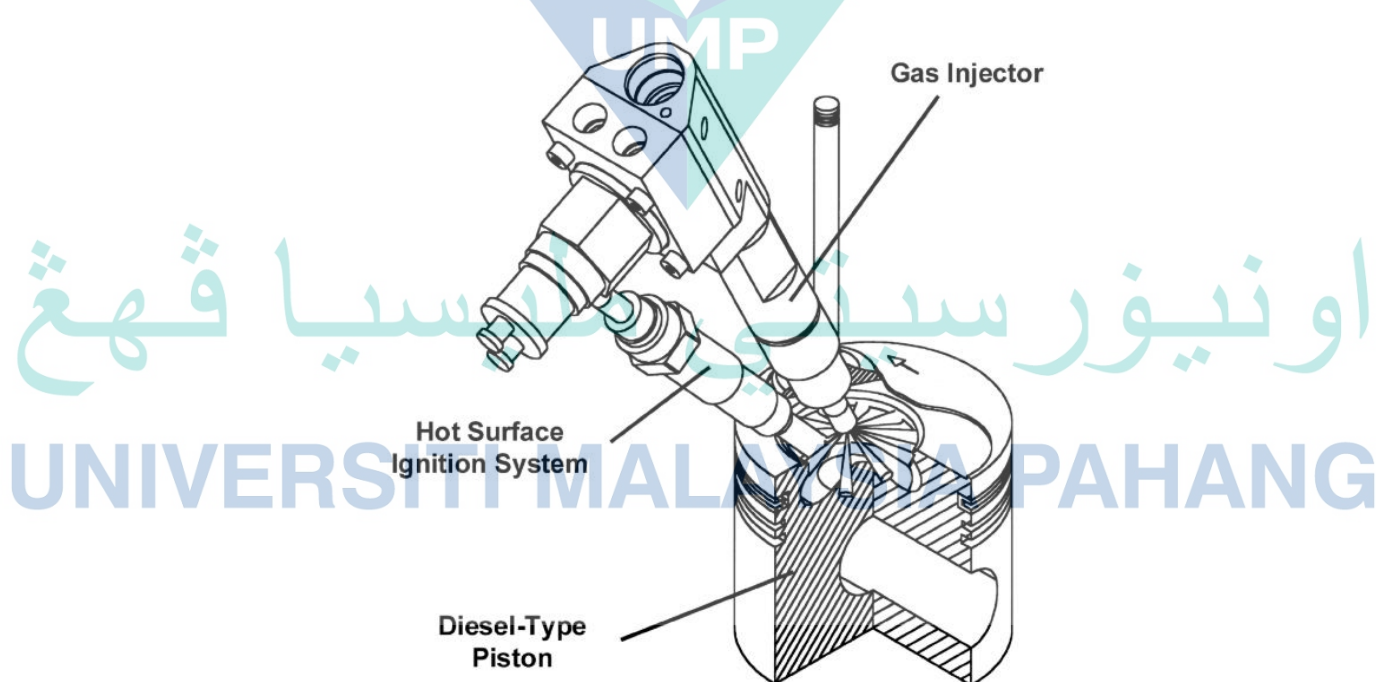


Figure 2.2 The DING combustion system concept

Source: Bartunek & Hilger (2000)

Another method of controlling the mixture stratification instead of injection timing is by using pre-chamber ignition. It is a common technique for an indirect injection diesel engine (Kamel, 2005). Kubesh and Podnar (1998) investigated the mixture stratification methods under part-load conditions: the direct injection stratified charge (DISC) and a fuel-injected pre-chamber (FIPC). They concluded that the pre-combustion system was found to be a more practical solution to enhance the charge stratification.

In the framework of the SI engine, a novel combustion system for the gas engine was proposed by Boretti and Watson (2009). The combustion system is called a jet ignition device. The system consisted of a centrally located direct injection (DI) injector and a jet ignition (JI) device for combustion initiation of the main chamber (MC) mixture. The JI system used a second DI injector to inject a small amount of fuel in a small pre-chamber, as presented in Figure 2.3. It was an expensive stratification method because of the extra injectors used. Besides, the insertion of the JI unit into a cylinder head is almost intolerable due to the limited space in the cylinder head area.

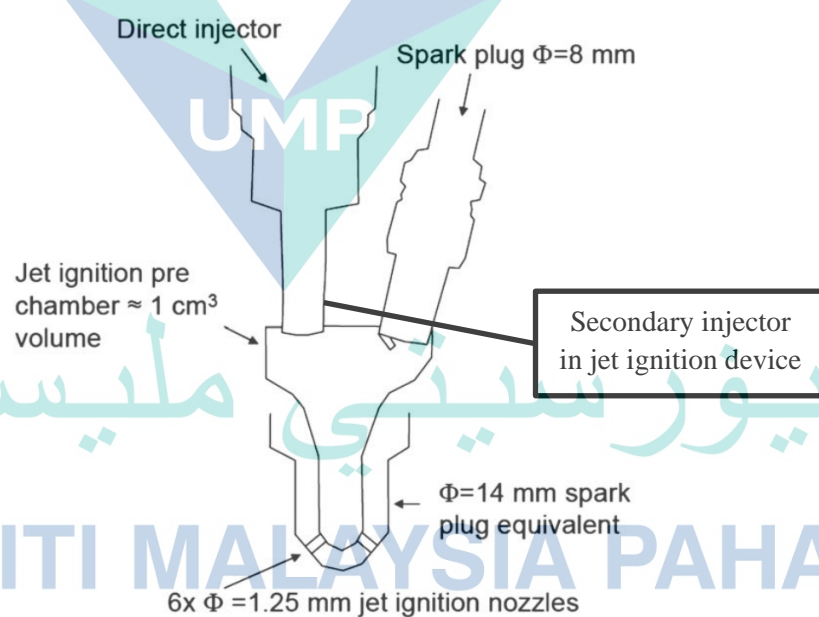


Figure 2.3 The jet ignition concepts

Source: Boretti & Watson (2009)

Based on Kubesh and Podnar (1998) and Boretti and Watson (2009), it was found that the pre-chamber technique produced a better mixture stratification effect for the gas engine compared to the direct injection technique. However, the addition of the pre-chamber added the difficulty to optimally utilise the limited space in the vicinity of the spark plug on the cylinder head. Besides, indirect injection to the pre-chamber is literally meant an indirect injection, which is of a different class than the direct injection.

Hassan, Aris, Mahmud, & Sidek (2009) explored a better mixture stratification method in the CNGDI engine using two modified piston crowns, namely the homogeneous and stratified piston crown. Greater stratification is expected with the assistance of the piston bowl, comparable to the wall-guided injection concept in the GDI engine. Yadollahi and Boroomand (2013) concluded that the narrow bowl configuration showed to be a better choice because of better mixture stratification near the ignition timing angle. They also concluded that the narrow bowl piston head was helpful to achieve a more flammable mixture in the vicinity of the spark plug location.

In dedicated CNGDI and dedicated CNG port injection engines, both are hardly found in the market. Thus, most of the CNGDI engines were developed by using SI or CI engine conversion. Orbital Australia Pvt. Ltd proposed a dedicated direct injector for CNG, as reported by Caley and Cathcart (2006). The proposed prototype targeted high performance and durability characteristics suitable for engine combustion. It was found out that the engine performance was improved by up to 10% through the direct injection of natural gas without other modifications of the engine.

Another novel concept of a direct injection system for a CNGDI engine is the spark plug fuel injector (SPFI) system. It is a combination of a fuel injector and a spark plug (Iskandar, 2010; Mohamad, Harrison, Jermy, & Heoy Geok, 2010; Mohamad & Geok, 2009). The design of SPFI consists of a direct fuel injector which is combined with a spark plug using a specially fabricated bracket. A fuel path running along the periphery of a spark plug body is designed to deliver the injected fuel to the combustion chamber. Figure 2.4 presents the spark plug fuel injector (SPFI) concept.

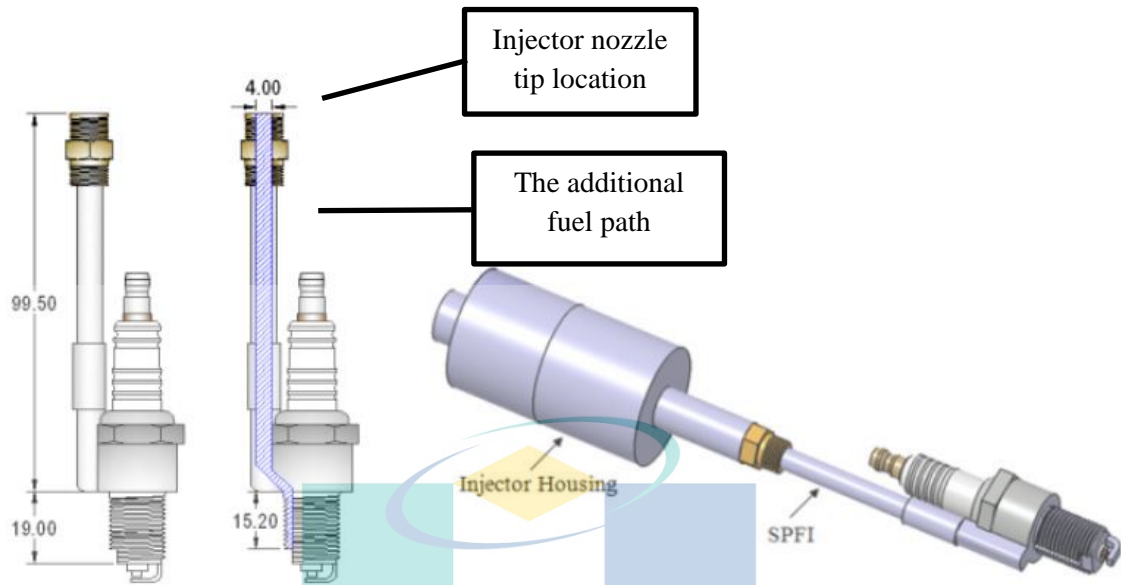


Figure 2.4 The spark plug fuel injector (SPFI) concept
Source: Mohamad (2009)

Monofuel SI engine running on CNG required a high compression ratio to optimise the CNG fuel characteristics. Baratta, Misul, Viglione, & Xu (2019) design a high-performance, mono-fuel, spark-ignition engine running on natural gas. An important conclusion from the study, the value of the compression ratio of 13:1 was selected as the best compromise between combustion variability, engine performance at full load and fuel consumption at partial load. The variable valve actuation can compensate for the slow-burning of CNG by prolonged the valve closing period to extract the maximum work transfer from the gas to the piston.

The previous discussion only considers the combustion system of the CNGDI combustion system as a whole. In particular, the CNG direct injector is another critical requirement for CNGDI engine performance. It is because most of the CNG direct injector was converted from the GDI injector. The flow specification of the injector needs to be recalibrated to meet the baseline engine requirement. The injector must be capable of providing a slightly rich mixture for maximum engine power at WOT conditions. For that purpose, several injector testings have been performed to evaluate the mass flow rate of CNG. The mass flow rate is affected by the pintle movement, which defines the opening and closing of the nozzle flow area. The opening and closing of the nozzle define

the injection duration, injection timing, rate shape, opening delay time and closing delay time (Zhang et al., 2014).

Another parameter which crucial is the CNG injection pressure. Most of the CNG injectors operated at choking conditions; hence the mass flow rate is directly affected by the upstream and downstream pressure of the injector. The gas pressure supply for CNGDI is known to be operated at a higher pressure compared to the gasoline or CNG port-injection system but lower than GDI fuel injection pressure. The GDI pressure might increase up to 200 bar to enhance liquid fuel atomisation, but CNG is already in a gaseous state. Most of the studies based on SI engines utilised an injection pressure of CNG at about 20 bar and lower (Abdullah, Adril, Muchtar, & Ariffin, 2010; Kalam & Masjuki, 2011; Mohamad et al., 2010). It is believed that the CNG injection pressure in the SIDI engine is limited to 20 bar to reduce starting difficulties of the CNG engine.

Characterisation work of direct fuel injectors for CNG is rarely found. However, the work of Chitsaz, Saidi, Mozafari, & Hajjalimohammadi (2013), Erfan, Chitsaz, Ziabasharhagh, Hajjalimohammadi, & Fleck (2015), and Erfan et al. (2015) are among the significant work concentrated on the direct fuel injector characterisation for CNG. Most of the study is based on experimental injector testing. No work dedicated to the analytical modelling of the injector was reported. The injector dynamic-analytical model is vital for detail cause-effect relationship studies and can be coupled with analytical engine models to develop a fully predictive engine model.

Based on the discussion, the challenge for successful CNG utilisation in SI or CI engines, in the context of direct injection applications are 1) to produce an optimum combustion system design and positioning of the direct injector for CNG, 2) to ensure the mixing and combustion process is controllable as various mixture strategies are required, 3) to provide sufficient ignition assistance for the CNG as the fuel is difficult to combust, 4) to increase the compression ratio of the engine (if possible) to increase the thermal efficiency of the engine, 5) to select a suitable direct injector for CNG which matched the engine capacity and its fuel requirement. The standalone injector study is found to be essential to characterise the flow specification of the direct gasoline injector converted to natural gas. The important injector parameter is the mass flow rate of the injector since it must be able to provide a sufficient amount of fuel mass at every engine speed and load.

2.4 Existing CNGDI Engine Performances

This section presents a review of previous works which set the benchmarked performances for the current study. It includes; 1) the effect of compression ratio, 2) the effect of injection timing, injection duration, ignition timing, 3) the effect of CNGDI combustion system design, and 4) essential remarks on the CNGDI engine performances.

2.4.1 Effect of Engine Compression Ratio

The essential parameter which affects the CNGDI engine performance is the engine compression ratio. Increased CR resulted in increased engine output. Fang, Ping, Hou, & Sun (1998) found that by increasing the CR from 6:1 to 8:1, the CNG port-injected engine produced the increment of power and torque by 6.9% and 5.7%, respectively. When the port injection was converted to direct injection, at the CR of 8:1, the power and torque were further increased 11.3% and 10.8%, respectively. Zheng, Wang, Wang, & Huang (2009) studied the effect of compression ratio on combustion and emissions of a natural gas direct-injection spark-ignition engine. They found that the brake thermal efficiency increased with a compression ratio up to a limit of 12:1 at high engine loads. Zheng et al. (2009) also reported that the maximum combustion pressure increased with an increased compression ratio. Experiments showed that a compression ratio of 12 is a reasonable value for a compressed-natural-gas direct-injection engine to obtain a better thermal efficiency without a large penalty of emissions.

Based on the reported work, the output power and torque increment are proportional to the compression ratio. The use of direct injection could further increase the engine torque and power. The results showed that the penetration distance of the natural gas jet decreased when the compression ratio increased. It is because of the strong mixture stratification formed at a higher compression ratio. On the positive side, it also resulted in a fast-burning rate and higher thermal efficiency, especially at low and medium engine loads. The CNG direct injection utilises high-pressure gas injection, thus producing higher in-cylinder turbulence but lowering the tolerable compression ratio. The flame development duration was decreased with an increased compression ratio. It indicates that the compression ratio has a significant influence on the combustion duration at lean combustion. A shorter combustion duration was desirable for a faster burning process.

2.4.2 Effect of Injection Timing and Ignition Timing

Crucial control-related parameters which affect engine performances are injection timing, injection duration, and ignition timing. Hassan et al. (2009) concluded that advanced ignition timing might result in NO_x increment. It was because advancing the ignition timing promoted faster combustion and higher cylinder pressure and temperature. The unburned hydrocarbon (HC) concentration was relatively low at early injection, but a higher concentration occurs when a late injection was applied due to incomplete mixing and combustion. The ignition timing has no significant effect on the HC concentration. Low CO concentration occurred at late injection timing. The most influential factor for CO development was ignition timing. They found that complete combustion occurred at 300° EOI and 25° - 28° of ignition BTDC. The lowest CO emission was equal to 0.011% when the ignition timing equal to 30° BTDC for and the end of injection (EOI) is equal to 360° BTDC.

Hassan, Aris, Zainuddin, & Alina (2009) found that the start of injection (SOI) in between 120° BTDC to 180° BTDC produced constant power and torque. An advanced injection timing angle is required because the CNG has a slower burning speed than gasoline. The results have also shown that the ignition timing has to be advanced from 18° BTDC to 24° BTDC to obtain the best results. A homogenous crown with a nearly flat surface produced better torque than the stratified crown design. The maximum torque is 31.8 Nm at 3000 rpm, compared to 24.65Nm for the stratified crown. For the stratified crown, the torque is drastically decreased after 3000 rpm. The maximum power is 12.29 KW at 4000 rpm for homogeneous but 6.5KW at 2500 rpm for the stratified crown.

Liu, Liu, Liu, Zeng, & Huang (2010) converted a CI engine to run on CNG to analyse the effect of injection timing and ignition timing on the emission. The study showed that the particulate number (PN) increased with advanced fuel injection. The amounts of NO_x and HC emissions increased with advanced fuel injection timing and ignition timing. At the same time, the CO concentration experienced small variations under all operating conditions. Particulate matter is identified as another harmful emission produced by the CNGDI based CNGDI instead of NO_x , HC and CO. The initial combustion duration was increased as the spark timing were advanced, and the fastest rapid combustion duration is obtained at the maximum brake torque spark timing (MBT).

A more recent study was reported by Yang et al. (2014) on the effect of injection timing on the CNGDI engine performances. Yang et al. found that the flame duration can be reduced by retarding the injection timing. Reducing the flame duration is desirable since it promotes fast combustion hence reduces power loss. However, the CoV_{imep} increased with the retarded injection timing. They concluded that the brake thermal efficiency is increased, but the combustion stability slightly deteriorates. By retarding the injection timing, a stratified mixture is formed. A stratified mixture can be operated in ultra-lean conditions. The leanness of the mixture is usually related to combustion instability.

Aljamali, Abdullah, Mahmood, & Ali (2016) investigated the effect of various injection timings on the performance and emissions of a stratified combustion CNGDI engine. The EOI setup was 120° , 180° , 300° , 360° BTDC. The results showed the best power, torque, BSFC and BMEP were obtained at 120° BTDC. The lowest NO and HC were found at 120° BTDC of injection timing. But, the CO_2 emission was high at 120° BTDC on the high engine speeds. The lambda showed that the engine was operated under overall lean conditions. The most retarded timing gave the best performance because mixture stratification is better where combustible mixture formed in the vicinity of spark plug and completely burned.

Sankesh, Edsell, Mazlan, & Lappas (2017) studied the effect of injection timing on the CNGDI engine performances. At part-load, early injection after the valve closure increased combustion rate due to enhanced turbulence. The increased work output, however slightly offset by pumping losses. At full-load, late injection improved volumetric efficiency and hence increased the work output. The improved combustion rate due to late injection is present at all load points. The results suggested that both the early and late injection strategies are applicable for the DI technique as long as the injection is held after the valve closure. But the increased pumping load due to high injection pressure reduced the net work.

A comparative study between the CNGDI and CNGPFI engine by Song, Choi, & Park (2017) showed that the injector configuration did not influence the volumetric efficiency (VE) at early injection timing before the intake valve closure (IVC). The VE were similar; about 38.62% for both CNGDI and CNGPFI. However, as the fuel injection timing was slightly retarded after the IVC, the VE of CNGDI increased while the

volumetric efficiency of CNGPFI was almost constant. It is because a larger amount of air occupied the cylinder volume if the injection commenced after the IVC. Song, Choi, & Park reported that the combustion was stable for all the test conditions. Thus, the CNG-DI could have higher volumetric efficiency by applying the late fuel injection timing after IVC than the CNGPFI.

2.4.3 Effect of CNGDI Combustion System Configuration

The two-stroke SI engine produces a higher emission than the four-stroke engine due to incomplete mixing, combustion, and short-circuiting of the induced air-fuel mixture into the exhaust. Kumarappa & Prabhukumar (2008) reported that the maximum brake thermal efficiency (BTE) is 9.1% higher than the carburetted engine at 3500 rpm. There is a 79.3% reduction in hydrocarbon (HC) and 94.5% reduction in CO emission at that condition. The maximum value of BTE is equal to 24.3%, achieved by using a CR of 12:1 with an optimum spark timing at 30° BTDC.

SPFI CNG engine results showed the VE are more than 80%, higher than the port injection operations. The highest VE, brake power and BMEP obtained at SOI of 190° BTDC. SPFI operation is found to be very sensitive towards injection timing and in agreement with the findings by Huang et al. (2003) and Zeng et al. (2006). It yields earlier and higher peak pressure compared to the port injection engine. However, as the combustion proceeds longer than 30° CA ATDC, the cylinder pressure falls below port injection, which results in slightly lower performance. The significant advantage of SPFI direct injection operation is its burning rate characteristics, where the combustion duration in SPFI direct injection operation is shorter than the one of port injection (Mohamad et al., 2010).

Kalam and Masjuki (2011) reported on the performance comparison of CNGDI engine, CNG throttle body injection (CNGTBI) and gasoline port injection (GPI) engine. The CNGDI engine produced 4.26% lower power than GPI and 19.10% higher power than the CNGTBI engine. The CNGDI engine reduced fuel consumption by 0.28% and 7.87% compared to GPI and CNGTBI. In terms of emission, the CNGDI engine reduced by 42% NO_x emissions compared to the GPI engine. The CNGDI engine produced 25% higher and 56% lower HC as compared to GPI and CNGTBI engine, respectively. The CNGDI engine produced higher CO emissions as compared to GPI and CNGTBI engines.

In general, it can be stated that CNGDI engine performance was on the same par as the GPI engine and better than the CNGTBI engine. The performance of CNGDI reported by Kalam and Masjuki is considered the best performance recorded for CNGDI compared to the gasoline port injection engine.

The EGR is regularly used to reduce NO_x emission in engine combustion. Since the direct injection engine possessed a significant formation of NO_x, Wasiu, Aziz, & Sulaiman (2011) analysed the effect of EGR rates on CNGDI engine power and emission. The results showed that as the EGR is increased, the brake torque and the BSFC were decreased. On the emission results, NO emissions reduced drastically at various fractions of EGR while at the same time the HC emissions increased. EGR has no significant effect on CO emission. The addition of EGR reduced cylinder gas temperature and pressure. It effectively reduced the formation rate of thermal NO_x while reducing the combustion temperature and, consequently, combustion pressure. It can be concluded that in introducing EGR in CNGDI engines, there is a trade-off between the engine's performance and NO_x emission, while it is difficult to realise stable combustion at high temperatures.

Based on the work of Lee et al. (2019), who attempted to produce a truly diesel-like CNGDI engine, it was found that the ignition only occurred in the form of a partially premixed flame rather than a diffusion flame for all tested conditions. The gross MEP varied from 2 bar to 5.5 bar. The total number of particles (PN) from CNGDI operation exceeded diesel at an equivalence ratio of 0.74 because of incomplete combustion. However, the total mass of the particulate matter (PM) was approximately only 15% of the diesel because the average particle size from CNGDI was approximately one third smaller than that of diesel. The high combustion temperature for the auto-ignition of CNGDI resulted in a high combustion peak temperature, resulting in approximately 2000 ppm NO_x under all test conditions.

2.4.4 Essential Remarks on CNGDI Engine Performance

Based on the literature in Section 2.4.1, the current performance of CNGDI is comparable to the gasoline port injection (GPI) engine. But in detail, it has not yet surpassed the maximum performance of gasoline based on the power and torque comparison for the same capacity engine. It is possible to outperform the baseline GPI

engine by the use of a turbo-charge (TC) unit (Chala, Aziz, & Hagos, 2017). Without the TC method, the highest recorded power for the CNGDI was still 5% lower than GPI engine.

CNG fuel has a high octane number which permits it to tolerate the high CR without facing knocking problems. The maximum CR tested for the CNG operation is about 14:1, as demonstrated by (Aljamali et al., 2016; Liu et al., 2010). The brake thermal efficiency was found to increase with the increased compression ratio (Fang et al., 1998). However, the increased compression ratio must be traded-off with the injection pressure used as at excessively high pressure, knocking combustion may occur.

Early and late injection timing is the common injection strategy for CNGDI engines, similar to the GDI mixture formation strategy. The early injection is used to produce a homogenous mixture, whereas late injection is used to form a stratified mixture. Besides, a typical direct injection strategy requires the overall injection process to be performed within the duration of the all-valves closed. The important reason is to ensure that the injected amount of fuel is fully mixed and combust with air. Hence no fuel is wasted (or short-circuited) to the exhaust (Kumarappa & Prabhukumar, 2008).

Another critical issue related to direct injection timing is the time available for direct injection. The direct injection time window is significantly shorter than that available for ported injection. The injection window must be reduced to avoid injection during the exhaust or intake stroke (intake of exhaust valve opened) and ensure its completion before ignition. Because if a high injection pressure is used, there is a possibility that backflow of the air-fuel mixture into the intake port occurred. Moreover, during the exhaust stroke, the unburnt fuel may short circuit straight to the exhaust or the fresh air charge may be displaced from the engine cylinder.

On the other hand, the high-pressure injection of gases directly into the cylinder during the all-valves-closed period introduces starting difficulty due to the higher resistance on the upward piston motion. It will increase the pumping load on the engine. The injection pressure utilised in the previous study is limited to a certain value. Mohammed et al. utilised 14 bar, Mohammed, Baharom, Aziz, & Firmansyah (2011), Kalam and Masjuki (2011), and Hassan et al. (2009) were all equal to 20 bar, and Wasiu et al. (2011) were equal to 18 bar. They mainly were utilising injection pressure up to 20

bar only. The CNGDI engines utilised a high-pressure gas injection primarily converted based on the platform of compression ignition engine. These were demonstrated by the work of Miura & Honjou (2000), which utilised 50 bar, and Cowan, Bushe, Hill, & Munshi (2003), which was equal to 300 bar. The higher mass and inertia of the diesel engine enabled the engine to overcome the increased pressure build-up in the cylinder.

Ignition timing is advanced and retarded to control the start of combustion in an internal combustion engine. In the CNGDI engine, ignition timing control is becoming more significant as the CNG burns slower than gasoline fuel. It always found that the ignition timing must be advanced more than 10 deg compared to the gasoline engine in order to extract the maximum work from the CNG combustion gases.

An optimum CNGDI engine operation is attainable if the following issues can be resolved; they could be answered at first. Is the injector able to supply the fuel mass requirement at each engine speed and load? What is the appropriate injection pressure that should be utilised for the direct injection of gases? Can the engine withstand a higher injection pressure which is vital to maximising the gas flow rate? What is a suitable range for the engine compression ratio? What are the optimum injection timing, injection duration, and ignition timing for the CNGDI engine for maximum engine performance? Some of the answers have been provided in the reported literature. However, all the parameters must be tuned to meet the baseline engine design used in the current study.

2.5 Engine Modelling using Analytical Approach

Engine modelling is the *state of art* approach used for engine design, development, and parametric analysis. It can be classified into a few categories with different complexities, usage, and built. They are the analytical, mean-value, and data-driven models (Zweiri, Whidborne, Seneviratne, & Althoefer, 2002). The analytical engine model is the thermo-fluid dynamic model and derived from the energy (first law of thermodynamics), mass continuity and momentum conservation equation. They are coupled with numerous sub-models of engine processes and usually derived in the crank angle domain. The engine strokes are solved progressively from intake, compression, power and exhaust. Often, The analytical engine model produced one torque pulse per one calculation (Sitthiracha, 2006). If the model solves a single-engine cycle, it is called

cycle modelling. The model can be extended to cycle-to-cycle engine modelling and cylinder-to-cylinder engine modelling.

The mean value approach simplified certain engine processes by replacing the in-cylinder processes with empirical models. The in-cylinder processes modelled was set as a mean value of the pulsating torque over one or more engine cycles and/ or engine cylinders. The torque generation model is derived empirically based on other parameters such as ignition timing, injection timing and dynamic airflow (Pezouvanis, 2010). The reduction of thermo-fluid dynamic equations and crank slider representation in the overall model reduced calculation time. Time delay is introduced as a function of engine speed to represent the dynamic effect of the engine processes in contrast to the analytical approach, where the changes are modelled as a function of crank angle.

The black-box or data-driven models are usually used in control and optimisation related studies. It is built upon input-output data pairs from experimental research and formulated by statistical method. However, it can also be developed from a well-validated first principle engine model to produce surrogate models. The system identification model is the simplest among these models. Hence its offer the fastest calculation time and proven to be suitable for real-time application (Zweiri et al., 2002). Plus, its often give the best accuracies in term of model prediction provided that correct input-output parameters are included. Figure 2.5 presents the classification of engine modelling applied in engine research and development.

The analytical engine model is the most complex model with multiple non-linear governing equations and sub-models. It gives insight information between the engine parameters. It is widely used to analyse the fundamental aspect of flow, mixing, combustion, and pollution formation. In the context of mapping, calibration, and control-oriented application, A model is preferred to be mathematically simple. Hence it can be solved in rapid calculation time and comply with real-time analysis and online monitoring as well as actual control implementation (Guzzella & Onder, 2010).

The current use of the mean-value engine and data-driven might fit with the mapping, calibration, and control purpose, but these models result in a set of data that cannot be used on the other engines due to rigorous calibration. At the same time, some phenomena cannot be expressed at all because it is too simplified (Pezouvanis, 2010).

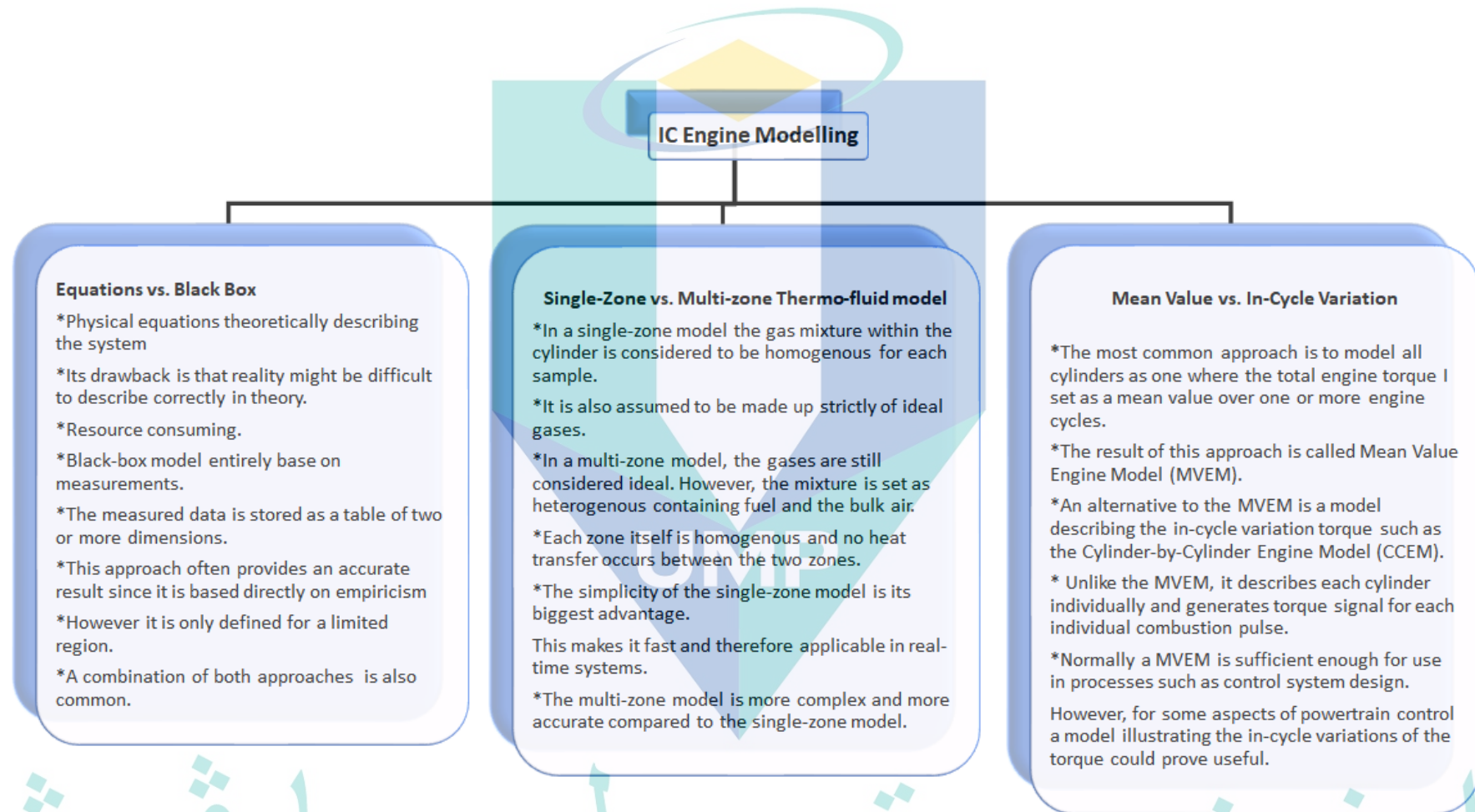


Figure 2.5 The classification of engine modelling technique

Source: Pezouvanis (2010)

Analytical modelling is the best option for parametric study in the absence of experimental engine data. It is because all the established model equations, when coupled together, become a fully predictive model with the condition that good inputs are provided. The calibration work of the model is far less than the mean value engine model. More importantly, the model provides explainable relations between the input, the intermediate parameters and the output. However, the most challenging part is to assemble and implement a complete model from various sub-models.

Most of the engine models are generally suffered from two major drawbacks. The first is a certain model too complex in which it cannot be applied for control and optimisation process due to increased computational cost. At the same time, they retain massive information about engine processes and their properties. Other types of models are too simple, even sometimes developed without solving the intermediate engine processes and just relying upon the engine's input-output data pair. At the same time, they provide greater accuracy.

2.5.1 Modelling Technique using Analytical Approach

This section reviews and discusses the analytical engine modelling technique for transient operating conditions. The main purposes of this review are to highlight basic approaches and equations involved concerning the modelling of throttle dynamics, intake manifold dynamics, in-cylinder calculations, friction modelling, and engine kinematics and dynamics solutions for transient engines operation. Figure 2.6 presents the components of an analytical engine modelling technique.

The idea of analytical modelling is to represent the physical components/ systems of the engine by a set of mathematical equations which are coupled altogether: such elements are intake and exhaust manifold and valves, turbocharger, crank-slider mechanism, piping systems and catalytic converter. These led to the introduction of various models such as the filling and emptying model, gas dynamics model, and simplified crank-slider model.

Additional sub-models are required for solving the in-cylinder processes such as heat transfer, combustion, heat release, heat losses and cylinder pressure/ temperature progression. The whole models are used to solve the governing equations of energy, mass

continuity and momentum. The model interactions with the surrounding are described by the heat energy supplied to the cylinder, heat losses to the cylinder wall, boundary work due to piston-cylinder gas interaction, and the mass transfer through the intake and exhaust gas flow. If the engine dynamic to be considered, the throttle dynamic, crankshaft dynamic, and the variation of reciprocating part's inertia must be accounted.

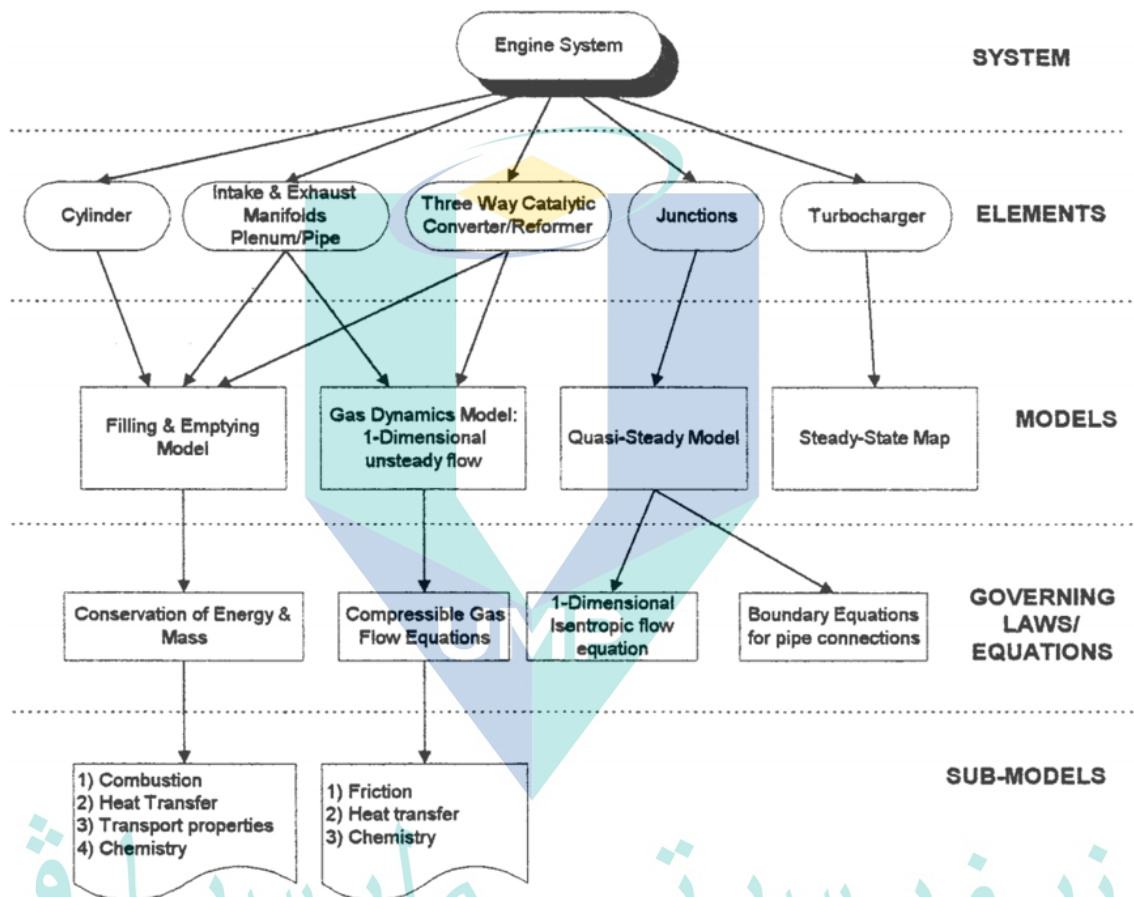


Figure 2.6 Components of an analytical engine model and governing equations

Source: Chow & Wyszynski (1999)

UNIVERSITI MALAYSIA PAHANG

2.5.1.1 Air Flow Dynamics

The main objective of the airflow dynamics model is to solve the mass flow rate of air into and out of the combustion chamber. The mass flow rate parameter is calculated at the throttle and valves. Modelling of the dynamic engine processes must require the inclusion of throttle dynamics. The changes in the throttle flow area with time introduced the dynamic effect on the overall airflow inside the air intake system. The difference

between the intake mass flow and the throttle's mass flow is used to calculate the manifold absolute pressure using the speed-density method.

Pezouvanis (2010) proposed a throttle area model and its rate of change, which is the key variable for transient engine control. Instantaneous effective throttle flow area was calculated and substituted in the compressible flow equation to solve the throttle mass flow rate. However, to aim for real-time application, another approximation for the throttle model is required due to the increased calculation time.

A similar approach has been employed by Yoon, Park, & Sunwoo (2000) to solve the throttle flow dynamics. The only difference is the formulation for the effective flow area. The discharge coefficient of the throttle valve is modelled as a function of the throttle angle and the pressure ratio across the throttle body. The solution of throttle mass flow is vital since the difference between the throttle mass flow and intake valve flow will be used to calculate the manifold absolute pressure by using the ideal gas state equation (Arsie, Pianese, & Rizzo, 2000).

The intake manifold includes the plenum, runner and poppet valve mechanism. The gas flow is modelled through every section and solved by using a one-dimensional compressible flow equation. Sittiracha (2006) demonstrated the solution of intake valve dynamics by physically model the intake valve, valve lift function, valve opening, and valve closing timing. An empirical model of the discharge coefficient as a function of the valve lift and pressure ratio across the valve based on a polynomial equation is used.

In conclusion, the focus on the intake manifold dynamics is to solve the intake air mass flow rate into the system. The same approach is applied to the exhaust flow but in a reverse direction. The critical part is the definition of the effective flow area of the throttle valve, the description of the valve lift profile and the definition of the flow discharge coefficient at different valve lift and pressure ratio conditions.

2.5.1.2 Fuel Flow dynamics

The objectives of the fuel flow dynamics are to calculate the fuel mass flow rate into the engine cylinder. The fuel mass flow rate is used to determine the amount of fuel mass and, consequently, the energy supplied for the combustion process. The mass flow

rate calculation must consider the physics or the fuel types and the method by which the fuel is delivered to the engine cylinder.

Fuel flow dynamics modelling is crucial for the detailed modelling of liquid fuel. The mixture preparation process involved the injection, atomisation, and mixing of the air-fuel mixture found in the port injection gasoline engine. Yoon et al. (2000) utilised a first-order lumped parameter model, which considers the total injected fuel from the injector, the fraction of fuel that forms a fuel puddle on the cylinder walls, the mass of fuel in the fuel puddle. The actual fuel flow rate which enters the cylinder is the sum of the evaporated fuel from the film and the rest of the fuel that was not formed in the puddle on the manifold wall. Therefore, the modelling of gas fuel flow is less complicated if compared to the modelling of liquid fuel flow dynamics. By assuming that the properties of the gas are consistent before the chemical reaction, the only important parameters of the fuel flow dynamics of gases fuel are the mass flow rate or mass of the fuel. The mass of fuel can be directly introduced in the heat release calculation, which is then included in the pressure and temperature calculation.

A simpler approach has been employed by Tirkey, Gupta, & Shukla (2010). They utilised a zero-dimensional knock model, a two-zone combustion model and a dynamic gas model. For simulation involving CNG fuel, they just provided the AFR without really solving the fuel flow dynamics of the engine. They even incorporated the kinetic rate reaction model to solve the exhaust emission formation. Thus, the fuel flow dynamics solution can be derived from either the AFR instead of the detailed calculation of fuel mass supplied to each of the cylinders. It has been demonstrated by the work of Kodah, Soliman, Abu Qudais, & Jahmany (2000), and Kesgin (2004).

To conclude this discussion, for a gases fuel simulation using an analytical engine model, the complexity of fuel flow dynamics modelling can be omitted by selecting the appropriate AFR value as simulation input. Another viable means is to directly use the injector mass flow rate from measured data as the input to the model if the value is known. In combination with the opening time of the injector, it can be easily used to calculate the mass of fuel provided to each of the cylinders.

2.5.1.3 The In-Cylinder Processes

In-cylinder processes modelling is essential to solve every fundamental process: boundary work, combustion (often modelled as heat release), heat losses, and mass transfer into and out of the cylinder. These resulted in the temperature and pressure variations in the cylinder. The pressure variation is used to solve the variation of gas force and, consequently, torque transferred from the cylinder to the crankshaft. The mass transfer into and out of the cylinder have been discussed in section 2.5.1.1 and 2.5.1.2. Hence this section focus on the solution of the boundary work, combustion and heat losses modelling.

The standard solution to model the dynamic variation of combustion chamber volume and surface area is to solve the kinematics of the crank slider mechanism, and numerous reports have demonstrated such applications. Examples are the work of Zweiri, Whidborne, & Seneviratne (2001), Falcone et al. (2003) and Abu-Nada, Al-Hinti, Al-Sarkhi, & Akash (2006). The essential requirement for the solution of the crank slider model is the availability of the engine geometrical information such as the bore and stroke size, the length of the connecting rod, and the engine rotational speed. In steady-state engine modelling, the speed may be defined as a constant value. However, in dynamic and transient engine modelling, the speed is changing and produced due to a difference between the driving torque minus the load torque (inertia and external load). The dynamic variation of combustion chamber volume and surface area is vital for the definition of boundary work produced by the piston motion inside the cylinder, which also contributes to the cylinder and pressure variations.

A complete and realistic in-cylinder process must always account for the combustion processes. In general, the combustion model can be classified as a model with detailed chemistry or simplified chemistry. The detailed chemistry model incorporated chemical kinetic modelling. Then special solver for stiff chemical kinetics is often coupled with an analytical engine model to solve the detailed chemistry. *CHEMKIN* has been used to formulate stiffed chemical kinetics within a complete engine cycle simulation (Fiveland & Assanis, 2000; Olsson et al., 2002). A similar approach has also been performed by (Narayanaswamy & Rutland, 2004), where they conduct a parametric to examine the effect of combustion timing on control parameters of a Direct Injection (DI) Diesel Homogeneous Charge Compression Ignition (HCCI) engine.

Another more straightforward approach is an established model, namely Stochastic Reactor Model (SRM), a spatially zero-dimensional model based on probability density function (pdf) transport methods. The cylinder charge is split into an ensemble of particles that make up the pdf of temperature, pressure and composition space. In work based on SRM models, Etheridge, Mosbach, Kraft, Wu, & Collings (2010) managed to simulate the transition from spark ignition (SI) to homogeneous charge compression ignition (HCCI) combustion mode in a direct-injection SI engine. They claimed that the transition from SI to HCCI could be solved in very short computation times.

Detail chemistry always taxes higher computational times compared to other methods, even for an established chemistry solver. Additionally, stiff chemistry will require an adaptive time step to achieve convergence at each time step. Even though the actual chemical reaction rates for fuel combustion are so fast, tracking down each of the elementary reactions is expensive. It is why detail chemistry is not a viable option for dynamic, cycle to cycle engine modelling.

The single-zone model is the simplest model for engine cycle calculation. The most popular model is the Wiebe heat release model (Serrano, Climent, Guardiola, & Piqueras, 2009; Sitthiracha, 2006; Zweiri, Whidborne, & Seneviratne, 1999). Sitthiracha performed cylinder to cylinder engine modelling for performance prediction of a spark-ignition engine. He employed the Wiebe Function to model the combustion progress in the cylinder. He managed to successfully validate the model with experimental engine torque and power of six different engine data. Karkamkar (2013) had employed the same model to analyse the effect of advanced and retarded spark timing on the burn fraction variation, cumulative heat release rate, and cylinder pressure variation. Abd Alla (2002) stated that by using the Wiebe Function, the modelling process is obviously getting closer to reality and is now worth pursuing as a design aid in engine performance prediction

Based on the three examples before, it can be concluded that the single-zone model suffices for the prediction of cylinder pressure, indicated work, heat transfers, heat losses, friction losses, and pumping losses from the in-cylinder processes. An important input for the single zone type model, particularly the Wiebe function, is the amount of heat supplied to the engine, which can be deducted from the mass of the fuel supplied and the burning duration of the fuel.

A more detailed model in the analytical modelling framework is the multi-zone model. The multi-zone model usually divided the combustion chamber mixture into two parts, the unburn and the burned mixture (Alla, Soliman, Badr, & Rabbo, 2001; Bayraktar & Durgun, 2004; Hosseini, Abdolah, & Khani, 2008; Ma et al., 2008; Narayanaswamy & Rutland, 2004; Rakopoulos, Antonopoulos, & Rakopoulos, 2007). However, such a model will increase the computational cost since it includes multiple mixture materials. However, the model is useful to simulate diffusive combustion such as diesel combustion since it involves liquid spray evaporation. In addition, it can be adopted with detailed chemistry calculations.

In the framework of the multi-zone model, the pressure and temperature build-up are control by the combustion speed, which is defined by the turbulent flame speed and the laminar flame speed. Both are the properties of the fuel. The chemical properties of the fuel influence the laminar flame. In comparison, the turbulent motion level inside the cylinder controls the turbulent flame speed. The turbulent flame speed more influences the combustion speed (Hosseini et al., 2008).

Another important in-cylinder process solution is the heat loss modelling, which considers the convective heat transfer process from the burned gases to the cylinder wall. In most of the studies, the radiation heat transfer and the conductive heat transfer are often omitted. It is because the duration of the luminous flame period, which contributes to the radiative heat transfer, is very short and thus form a small percentage of total heat transfer. On the other hand, the conductive heat transfer process is only relevant for the engine structural design or in the cooling related problem. Thus, the radiative and conductive heat transfer mechanisms are mostly neglected in thermodynamic modelling of in-cylinder processes.

The convective heat transfer from the gas to the cylinder wall can simply be express by the Newton cooling law. The only difference between various heat transfer models is the definition of the empirical heat transfer co-efficient. The surface-averaged heat transfer coefficient, which is defined in terms of the bulk gas temperature, is used to calculate surface averaged heat losses or total heat flux. Among established correlations for the heat transfer coefficient are the Annand correlation (Hosseini et al., 2008; Rakopoulos et al., 2007; Şahin & Durgun, 2008; Tirkey et al., 2010), Woschni correlation (Yusaf, Hoe, Fong, & Yusoff, 2005), and Hohenberg correlation (Sitthiracha, 2006).

Other available heat transfer models but are uncommonly used are Assanis and Heywood model (Jung & Assanis, 2001) and Chang model (Neshat & Saray, 2014), and Eichelberger correlation (Kodah et al., 2000).

Hosseini et al. (2008) concluded that the empirical correlation of Annand was found to have a better influence on matching experimental data than models of Woschni and Eichelberg. Hohenberg empirical correlation is the improved Annand correlation (Sitthiracha, 2006). Sitthiracha et al. utilised the Hohenberg correlation to simulate the torque and power prediction of 8 engine models and verified by experimental data. It can capture torque and power characteristics very well. The overall errors are between -6% to 4%.

Kodah et al. (2000) stated that The Eichelberger equation is simple, accurate and easy to use in a step-by-step computer program. Chang model is a modified version of Woschni empirical correlation. The founder optimised the model parameters such as the characteristics length, temperature terms and various constants of Woschni correlation to suit different engine strokes (Neshat & Saray, 2014). In comparing various heat transfer correlations to suit the HCCI engine operation, Neshat and Saray concluded that Annand and Hohenberg correlations had over-predicted the heat transfer coefficient causing incomplete combustion or misfiring. Whereas, at the same time, they have underpredicted the in-cylinder pressure lower than actual data. The value of CO and HC were calculated higher than the actual data. They concluded that these models are not suitable for HCCI engines convective heat transfer prediction. On the other hand, Chang and Woschni models estimated a lower heat transfer coefficient than their actual values, leading to overpredicted the in-cylinder pressure higher than the corresponding experimental values.

Based on the presented discussion, Annand and Woschni correlations are the most widely validated correlation for modelling of engine's convective heat transfer process. It is parallel with the fact that both were among the earliest correlations developed for modelling purposes. Both were modified in later studies for prediction improvement. Later, both were identified as Hohengberg and Chang correlations, respectively. However, the Chang and Eichelberger correlation are seldom used and reported in the literature. In comparison, the Hohengberg correlation was tested for various engines and

fuel types. The HCCI engine concept is not within the scope of the current study; hence the finding of Neshat and Saray (2014) is not significant to the current study.

This section reviewed the common methods to solve the in-cylinder processes, namely, boundary work, combustion, and heat losses out of the cylinder, which contributes to the temperature and pressure variations in the engine cylinder. The pressure pulse is used to solve the torque pulse acting on the crankshaft. The existing methods and formulation are sufficient to solve each of the processes. The actual challenges based on the review are selecting correct models and integrating all the sub-models into a complete in-cylinder model. The next section discusses the modelling of crankshaft dynamics.

2.5.1.4 Crankshaft Dynamics

The crankshaft dynamics modelling is used to solve the instantaneous crankshaft torque and its rotational speed/ acceleration. Its detailed modelling mainly required only when dealing with a transient problem. The model in use should consider the inertia load, especially the inertia of reciprocating parts and external load. The external load must be coupled with the crankshaft. A significant effect of the coupling is the torque produced by the engine cylinder must overcome these resistance loads. Otherwise, the engine cannot rotate accordingly.

Mathematical modelling and simulation have paved the way for an in-depth study of engine processes under steady-state and transient conditions. However, the majority of research mainly focused on the steady-state thermodynamics processes. It is because this directly affects heat release predictions and consequently performance and pollutants emissions. On the other hand, issues concerning engine dynamics that incorporate connecting rod complex movement, kinematics, and dynamics of the crank-slider mechanism, crankshaft deformations, and torsional vibrations are often disregarded or over-simplified, possibly for the sake of speeding up thermodynamic simulation program execution time (Rakopoulos & Giakoumis, 2006).

Detailed dynamic engine models solve the instantaneous torque of the engine as a function of time from one cycle to another cycle. Many methodologies can model the crankshaft dynamics that solve the cycle to cycle progression with different complexity and accuracy. The updated values of crankshaft rotational speed and angular acceleration

during transients operation are derived from the conservation of energy principle applied to the total engine system and engine load.

Rakopoulos and Giakoumis (2006) classified the crankshaft dynamics modelling approaches into a few techniques; 1) The quasi-linear models applied once per-cycle or per-firing interval using the respective mean torque values. The crankshaft is usually assumed to be a rigid body. The stiff crankshaft model considers the engine torque, related inertia torque, and gravitational forces contribution. The model also considered the friction torque, the torsional stiffness torque, and the damping torque. The load torque can be assumed to be a function of linear or quadratic load type. 2) A more detailed crankshaft model that defined energy balance, which includes all possible crankshaft deformation between each pulley, cylinder and flywheel.

Sittiracha (2006), Gogoi and Baruah (2010) performed a cycle simulation that only solves a single cycle. They use the pressure profile of that single cycle to calculate the mean torque and power of the cycle. They modelled the friction and pumping as mean quantities and neglected the effect of inertia and the inertia changes of the components. Thus, their model is considered a steady-state model since the predicted brake torque and power are constant with time along that single operating cycle (Jagadish, Kumar, & Madhu, 2011).

Zweiri et al. (2001) had proposed a non-linear model for a single-cylinder diesel engine to aid engine control system design and fault diagnostics. The model does not use any empirical inputs where every component was physically modelled. The model treated the dynamic effects by solving instantaneous friction of every engine sub-system, which included the piston ring assembly, the piston skirt etc. The model also considered the inertia variations and piston pin offset. The model is validated using experimentally measured cylinder pressure and instantaneous engine speed under transient operating conditions and gave good agreement. In Zweiri et al.'s work, the cylinder's instantaneous pressure profile is directly transferred to the crankshaft to calculate the torque at the crankshaft.

Yoon et al. (2000) had developed a nonlinear dynamic engine model to represent an SI engine over a wide range of operating conditions. The dynamic crankshaft model is much simpler compared to the model used by Zweiri et al. (2001). The crankshaft is

modelled under the assumption of a lumped parameter system with constant inertia by using Newton's Second Law. Kamaruddin & Darus (2012) employed an engine model that was validated against dynamometer testing to produce random engine data based on pseudorandom binary sequence (PRBS) input. The data is used to generate a more accurate model representation which able to eliminate complicated formulation of the model by applying a system identification method.

The model developed by Crossley and Cook (1991) consisted of empirical models of engine dynamics, including the throttle body, the mass of air inducted into the cylinders and torque generation model. The intake manifold dynamics are solved by the use of the exact equation for one-dimensional compressible flow. The crankshaft dynamics, on the other hand, is model by the Newton Second Laws of dynamic. The rotational motion of the engine crankshaft is given in terms of the engine polar moment of inertia, angular acceleration, and the difference between the net torque generated by the engine and the load torque applied to the output shaft.

In conclusion, the crankshaft dynamic modelling is vital for transient simulation. In a steady-state simulation, crankshaft dynamics can be easily simplified or almost unnecessary with the availability of empirical models for the brake torque and friction torque. And this is in agreement with the control-oriented modelling requirements. However, when detail interaction between engine parameters is needed, there is a need for detailed crankshaft modelling. Or, the existing empirical model may not be generalized enough to represent the current engine design. However, this is a rare case since the IC engine design is hardly evolved.

2.5.1.5 Injector Dynamics

The dynamic injector model is used to predict the transient mass flow rate of the fuel supplied to the engine. The knowledge of injector mass flow rate is important to evaluate the suitability of the injector at various engine operating points. Common GDI injector is a peak and hold type. Regular construction of an injector consists of the nozzle tip, pintle which is connected with the armature, solenoid drive, compression spring, and a fine fuel filter. In practice, the input to the injector is the driver signal voltage and pressurized fuel. The basic injector control parameters are the injection duration and injection timing (Cheng, Zhang, & Xie, 2015).

A coupled model based on one-dimensional hydraulics with a two dimensional (2D) axisymmetric electromagnetic finite element code had been developed by Digesu, Ficarella, Laforgia, Bruni, & Ricco (1994) to calculate the magnetic force and injection quantity. The electromagnetic solver is used to solve the electromagnetic magnetic force, which became the input to the one-dimensional hydraulic model. The model is considered computationally expensive.

Coppo, Dongiovanni, & Negri (2002) and Coppo & Dongiovanni (2007) developed a model of a common-rail injector with a combined pipe, fluid, mechanical and electromagnetic model. Good agreement was observed between calculated and experimental profiles of rail pressure, needle lift, and injection quantity. Hu, Wu, Stottler, & Raghupathi (2001) model excluded the use of the electromagnetic sub-model. Their model was able to correlate the pressure profile with the measured one. Both, Coppo et al. and Hu et al. models used the measured data as the input to the models. Coppo et al. used exciting current signals as the model input, whereas Hu et al. used a measured magnetic force profile as the input. Both parameters are proven to be effectively used as the model input, and the modelling results well agreed with the measured data.

Ando, Koizumi, & Ishikawa (2001) developed a one-dimensional injector model coupled with the electromagnetic model, simplified rigid body model, and fluid models. The model is used to study the electromagnetic effects, including magnetisation time lag. Both models were developed based on the commercialised *AMESIM* software.

Antunes (2010) developed a model for a hydrogen fuel injector. The model provided a detailed relation between each injector component and process. Even though the injector is hydraulic controlled, the detailed information is helpful and worth studying further. It is subdivided into the following features; orifice area, inlet valve, exhaust valve (return line), total force calculation, solenoid, critical pressure ratio, choked flow and subsonic flow calculation, injected flow calculation, hydraulic actuator, and cylinder pressurisation.

Zhang et al. (2014) conducted a study to optimize the injector power driver system for improved fuel injection quantity and timing control. They performed a coupled simulation of electromagnetic and rigid body model using an Electromagnetic solver

coupled with a computational fluid dynamics (CFD) model to generate the optimal values based on the multiple driver signal profile.

Based on the discussed works on the injector modelling, the model developed in the previous studies has been used for independent injection simulation on diesel and gasoline fuel. The studies provided detailed information on required sub-models for injector modelling to solve the interaction between injector components and parameters. It also offered theoretical trends of injector mass flow rate when each of its parameters was excited. However, the analytical model of the injector for CNG was hardly found. Besides, no study demonstrated the combined use of an analytical injector model with an engine model to produce a comprehensive engine model.

2.5.2 Previous Work on Analytical Engine Modelling

A comparison of various types of transient diesel engine models has been presented by Rakopoulos and Giakoumis (2006). They categorised transient engine modelling as nonlinear modelling as the engine dynamics are taken into consideration. The lowest requirement of the transient engine model can be achieved by utilising the filling and emptying sub-models. In addition, the inclusion of crankshaft dynamics is vital since it imposed the main inertia terms of the drivetrain and external load. Furthermore, throttle dynamics is also needed for varying load problems (Pezouvanis, 2010; Yoon et al., 2000)

Sittiracha (2006) had developed a mathematical model of spark ignition engine based on a cylinder-by-cylinder engine model, which combines both physical model and empirical model (as model closure). The engine model, however, neglected the existence of the exhaust valves. It is sufficient to neglect the exhaust process if the model used to predict the engine torque and power. The model used a simplified friction model as a function of engine speed and neglect the solution of crankshaft dynamics. Overall, the model is simple and computationally low cost but can provide adequate in-cylinder information. The approaches are proven to be effective in solving in-cylinder engine processes with a simplified method to predict engine torque and power. Plus, it can be coupled with a knock model, two-zone combustion model, or kinetic rate solver (Fiveland & Assanis, 2000; Kesgin, 2003, 2004; Tirkey et al., 2010) to obtain greater insights on more realistic combustion.

Metallidis and Natsiavas (2003) analysed the dynamics of the reciprocating engine by solving sets of the equation of motion for single and multi-cylinder engines by considering the dependence of the engine moment of inertia, driving torque, and resisting torque on the crankshaft rotation. These improved the model accuracies and introduced strong nonlinearities in the equation of motions due to the complexity of the equation. They found out that the dependence of the engine moment of inertia on the crankshaft rotation was found to have a weak effect on the average rotational speed, but it was shown to affect the instantaneous speed fluctuations significantly.

A detailed analytical, non-linear dynamic model for a single-cylinder diesel engine had been proposed (Zweiri, 2003; Zweiri et al., 2002; Zweiri et al., 2001; Zweiri et al., 1999). The model explained the dynamic behaviour of the engine system, such as the fuelling dynamics, non-linear air intake dynamics, crankshaft dynamics, dynamometer dynamics, instantaneous friction dynamics and the engine thermo-fluid dynamics. The friction model was expressed in detail and taken into consideration the viscosity variations with temperature. The complete model can solve cycle calculations and treat the cylinder strokes and the manifolds as thermodynamic control volumes by using the filling and emptying method. The model application can be extended for steady-state and transient engine problems.

Karlsson and Fredriksson (1999) had compared the characteristics of a cylinder-by-cylinder engine model, CCEM and a mean value engine model, MVEM required for use in powertrain control applications. The investigation showed that the mean value engine model is sufficient for powertrain simulations and powertrain control design. The dynamical behaviour for the two models is found to coincide. In the CCEM approach, the fundamental events are modelled as a function of crank angle degrees and the torque output during the power stroke is approximated by a mathematical function to capture the shape of the torque pulse. One calculation is performed for each torque pulse. In the MVEM approach, these events are replaced by time delays which are set as a function of the engine speed. The torque output is continuous and represents a mean value of the pulsating torque. Hence, the real challenge of the MVEM is the determination of the engine delays, and often, the calibration of the delays function is done by experimental setup, which is relatively difficult.

A more comprehensive model has been proposed by Arsie et al. (2000) for control-oriented simulation of SI engine. The model predicted engine and driveline states by considering air and fuel flow, crankshaft, transmission, and vehicle dynamics. The model output is ranging from the throttle position, engine speed, engine torque, vehicle speed, Air-Fuel ratio, HC, CO, NO_x. It is considered the most comprehensive model. It adopted different classes of models, ranging from black-box ANN to grey-box mean value dynamic models. However, the engine model was simplified to reduce calculation time. Additionally, certain parts based on black-box and grey-box cannot be easily generalised for other types of the engine even though they produce accurate predictions.

In summary, developing an analytical, comprehensive engine model is possible by considering all aspects of engine dynamics. The throttle and crankshaft dynamics, the inertia of reciprocating parts and external load, and the progression of in-cylinder processes are important dynamics aspects that must be taken into account. Integration of the sub-models is the most critical factor. In-cylinder processes are often formulated as a function of crankshaft angle, whereas transient process often describes in the time domain. In addition, the complex solution process, the interaction between models, and the numerous parameter involved required an accurate design of the modelling algorithm. Table 2.2 presents related works using analytical modelling of vehicles and engines for performance prediction.

2.6 Engine Modelling using Artificial Neural Network (ANN)

Artificial Neural Network (ANN) has been successfully used for engine modelling, control and optimisation study. It is constructed of parallel distributed processors inspired by the structure and functions of living creatures' brains and nervous systems. ANN is composed of a large number of simple processing units (artificial neurons). These units are fully connected by one-way, directly linked synapses. The Multi-Layer Perceptron (MLP) model is the most popular network type and constructed using several layers of interconnected perceptron nodes. These nodes are connected in a feed-forward manner between the input and the output layer (Janakiraman, 2013).

Table 2.2 Previous work on analytical modelling of vehicle for performance prediction

Author	Type & application	Techniques	Validation parameters & method	Major findings	General remarks
Zweiri et al. (2010)	Dynamics model of a diesel engine	Detailed dynamometer and friction dynamics.	Comparison with measured engine speed under steady-state and transient conditions	The suitability of the models for various control applications	Detail friction model for analytical analysis
Sitthiracha (2006)	Cycle model of SI engine	Tuning variables based on physical parameters	Verification with commercial engines in terms of engine brake torque and power	The overall errors are in between -9% to +5%.	The model only consists in-cylinder process and simplified friction and brake torque model
Pezouvanis (2010)	Cycle-by-cycle model for cyclic engine mapping	Dynamics crankshaft model.	ECU calibration and real-time engine control simulation.	Single cyclic variables can represent all moving engine components.	Consider realistic engine parameters but able to meet the real-time condition.
Zweiri (2003)	Parameter estimation of Diesel engine	A novel inverted dynamic model of the Diesel engine	Comparison with static and dynamic engine rotational speed and torque	Dynamic friction of ring assembly, bearing mixed lubrication and valve train.	Analytical model inversion
Yoon et al. (2000)	Nonlinear dynamic model for control optimization	Inclusion of intake manifold, fuel film, and engine rotational dynamics with transport delays.	Validation with engine dynamometer test data from 42 operating conditions of the engine.	The model is compact to run in real-time and can be used as an embedded model within the control algorithm.	Torque generation by using empirical model and constant inertia.
Tirkey et al. (2010)	Model for minimisation of engine emissions and safe knock limit	GENSIM model with gas-dynamic, knock, two-zone combustion, and kinetic rate model.	Parametric analysis of equivalence ratio, spark plug location, CR, and cylinder diameter.	Predicted cylinder pressure, BMEP, BSFC were in closed agreement with those obtained by previous studies	The model only simulated the in-cylinder thermodynamic processes.

Table 2.2 Continued

Author	Type & application	Techniques	Validation parameters & method	Major findings	General remarks
Kodah et al. (2000)	Prediction of cylinder pressure in SI engine.	Combustion modelling using Wiebe function.	Validation with measured engine data.	The model can be adapted to accommodate any combustion chamber shape.	Wiebe constants need to be carefully selected.
Kesgin (2003)	Effects of engine parameters on NO _x emissions	Zero-dimensional with reaction kinetic modelling to calculate the NO _x emissions	Predicted data verified by measurements from a TC CNG engine	Increase in the excess air ratio and engine speed causes a significant decrease in NO emissions.	Focus on in-cylinder modelling with detailed kinetics.
Kesgin (2004)	ANN use to develop surrogate model for NO _x optimisation	ANN (surrogate model) model developed from kinetic modelling and used to predict engine efficiency and NO _x emissions	Validation based on engine NO _x measurement.	This model gives quick and accurate predictions for any input pattern of the engine operating parameters.	Relationship between engine parameters with engine efficiency and NO _x emissions by ANN model.
Zweiri et al. (2001)	Analytical non-linear dynamic model for diesel engines	Dynamic behaviour of fuelling, engine speed, dynamometer and instantaneous friction.	Validation using measured cylinder pressure and instantaneous engine speeds.	Profiles of cylinder pressure and instantaneous crankshaft velocity through transient and steady-state cycles	The dynamometer model enables the study of engine behaviour under loading conditions.
Falcone et al. (2003)	Combustion model using black-box method.	The parameters of both models are identified via a non-linear least-square optimization algorithm.	Identification and validation data based on experiments on a diesel TC with a dynamic test-bench	A benchmark model to estimate the torque and simple enough to be implemented on a commercial vehicle.	Black-box approach solved dynamic engine model.
Abu-Nada et al. (2006)	Otto cycle model with variable specific heats	Temperature-dependant and constant specific heats using analytical model.	Constant and temperature-dependent specific heat	Engine working parameters are affected by variable specific heats significantly.	The model solved the in-cylinder process only.

Table 2.2 Continued

Author	Type & application	Techniques	Validation parameters & method	Major findings	General remarks
Olsson et al. (2002)	Influence of CR on CNG HCCI engine maximum load.	Full-cycle simulation used to resolve ignition timing, thermal boundary conditions, emissions.	Validation against a Volvo TD100 truck engine in a closed-loop technique.	Tighter limits for combustion timing, unstable operational points and physical constraints at high loads.	Full-cycle simulation for parametric study
Fiveland & Assanis (2000)	HCCI four-stroke engine model	A zero-dimensional framework coupled with chemical kinetic mechanism.	Full-cycle simulation used to predict the variation in output parameters due to inlet temperature and CR.	Importance of coupling detailed chemistry descriptions with physical models.	The CHEMKIN libraries used to formulate a stiff chemical kinetic
Narayanawamy & Rutland (2004)	DI Diesel HCCI engine	GT-Power coupled with an external cylinder model	Experimental data from a single-cylinder truck engine modified for Diesel HCCI operation.	Cycle simulation used to demonstrate the capability to develop closed-loop control strategies.	A multi-zone model implemented to account for temperature and fuel stratifications

اونیورسیتی ملیسیا قهق

UNIVERSITI MALAYSIA PAHANG

2.6.1 Advantages of Artificial Neural Network (ANN)

The main advantages of artificial neural network (ANN) modelling are its learning and generalising capability, the ability to approximate nonlinear system, a minimum requirement of prior fundamental knowledge, nonlinear parallel inherent structures, and its ability to identify the unknown or less understood dynamical system (Afrashteh, 2000). It is beneficial in situations in which there is no detailed or complete information about the problem and which there are only sets of data as inputs and outputs of the system.

ANN can be used for pattern classification, speech synthesis and recognition, adaptive interfaces between humans and complex physical systems, function approximation, image data compression, associative memory, clustering, forecasting and predicting combinatorial optimisation, and nonlinear system modelling and control. In the context of engine calibration, Turkson, Yan, Ali, & Hu (2016) concluded that the combination used of ANN with the design of the experiment (DoE) outperformed other data-driven modelling methods in the engine's ECU calibration. It overcomes the curse of dimensionality primarily if used together with DoE to reduce engine testing points.

In addition, ANN also outperformed other classical data-driven modelling techniques such as polynomial regression. The polynomial regression modelling can approximate the input-output relationship fairly well for steady-state engine operation but unable to capture the non-linearity in a global engine model satisfactorily. It is normally because the polynomial models could be prone to measurement errors, including noise and outliers (Gutjahr, Kleinegraeber, Huber, & Kruse, 2017; Ropke, 2014).

The advantages and capabilities of ANN presented before are sufficient to prove the advantages of ANN over other modelling techniques. Compared to the analytical modelling technique, the essential advantageous characteristics of ANN are the computing time required to perform a simulation and the accuracy of the ANN model prediction. Besides, it is known that the analytical engine model is limited to predicting ideal engine performances. Therefore, any deviation from the ideal engine processes may not be predictable by such models, but that is not a big deal for the ANN modelling technique.

2.6.2 Challenges for Successful ANN Application

The main challenge of using ANN to model a nonlinear dynamic system is to determine an optimum ANN structure, including the number of nonlinear layers and the number of neurons in each layer (Rutherford & Cole, 2010). In neural network design, the selection of network topology, the trigger function, learning rule and the criteria for stopping the training phase is crucial. However, it is difficult because there is no fixed method to do it. (Garg, Diwan, & Saxena, 2012)

Wu et al. (2004) suggested that it is crucial to consider both fitting accuracy and generalisation accuracy when determining the network structure. They suggested; 1) considering structures with one and more hidden layers, 2) observing the trends of training mean square error (MSE) and validation MSE as the network size grows, 3) selecting the smallest size structure that still provides good fitting accuracy, and 4) verifying a good generalisation. Tan and Saif (2000) proposed a heuristic method to determine the architecture of the hidden layer of the network. The orders of the input variables must be determined at first based on empirical knowledge. The number of the hidden nodes depends upon the minimisation of the criterion concerning the weight.

The neural network requires huge data to give good confidence in the results. Hence they are not suitable for small data sets. With higher numbers of inputs, the number of connections and hence the complexity increase rapidly. Turkson, Yan, Ali, Liu, & Hu (2016) stated that the capability of ANN to generalise satisfactorily depending upon whether the underfitting and overfitting could be eliminated. Under-fitting implies the situation where there is a high degree of statistical bias, and overfitting refers to the situation where there is a high level of statistical variance in the model prediction. Hence, the total model error is composed of bias error and variance error.

The Model-Based Calibration (MBC) toolbox utilises the ANN algorithm from the Neural Network Toolbox (Beale, Hagan, & Demuth, 2018). Modelling of the transient engine response will require a behaviour number of inputs compared to steady-state engine modelling. Based on the Neural Net Toolbox manual, increasing the number of model parameters reduces the bias error while increasing the variance error. On the other hand, a decrease in the number of model parameters increases the bias error.

Based on the presented discussion, the most critical procedure in applying ANN in engine modelling is the selection of the optimal neural network structure. Tan and Saif and Wu et al. have proposed the heuristics method more systematically for determining the optimal network structure. Both directions suggested the MSE and validation MSE for the evaluation of the selected structure. The selection of the trigger function, learning rules, stopping criteria, and permissible errors are expected to be problem dependent. A review of previous works of ANN application for engine modelling is required to select the best practice which able to provide the best model prediction.

2.6.3 Classification of ANN

Artificial Neural Network (ANN) has been developed, applied, and modified for various purposes since it was first introduced in the early 80s. Since that, it had evolved to meet each of the application purposes. The variant of ANN is quite versatile in which it can be classified based on the network structure, the hierarchy level number, and the learning method. This classification is important to suit the ANN variant with the purpose, data type and the number of factors involved in the study.

Tan and Saif (2000) classified the neural network types into two broad categories. The first category is called global neural networks, and the second category is called local neural networks. In the global network, the neurons are affected by all inputs. Therefore, the new information (input) coming in may destroy the old information that the network has learned, including the weight and bias of each neuron. However, in the local network, each neuron only responds to the corresponding particular region of the input. If a problem involves dynamic system modelling, feedback or auto-regressive terms must be introduced into the neural network to derive temporal memory or dynamics. Such a neural network is called a recurrent neural network (RNN) or a dynamic neural network.

Sangha, Gomm, Yu, & Page (2005) categorised the neural networks based on the training approaches. There are two major categories of ANN based on the training method, which are the supervised and unsupervised networks. A supervised ANN learns from input-output pair examples to build an external relationship between the input and output. Under unsupervised training, the network is provided with inputs without the desired outputs. The process is called self-organisation or adaption, where the system continually learns on their own as they encounter new environments. Nevertheless, at

present, the vast bulk of neural network work is in systems with supervised learning. Supervised learning is easier and faster to achieve convergence (Beale et al., 2018).

Turkson et al. (2016) classified the ANN into two broad categories; 1) the feedforward neural network and 2) the recurrent neural networks (RNN). Feedforward neural networks could further be classified into single-layer perceptron networks, multi-layer perceptron networks, and radial basis function networks. Similarly, RNN could also be classified further into Competitive and Hopfield type networks. The recurrent neural network is usually applied for dynamic engine modelling using the real-time approach..

Nowadays, engine modelling tends to be used for a more realistic operating condition, hence encouraging the use of RNN. It is found that RNN to be more difficult for dynamic modelling but provided greater accuracy at limited data pairs. Arsie, Pianese, & Sorrentino (2008) reported that the RNN could be further divided into three other categories depending upon the structure of the feedback link. The feedback link may involve the neurons in the input and output layer only or involve all the topology neurons. The RNN may be further classified into global, local, or external recurrent neural networks.

Based on the classification of ANN, it is known that a global RNN must include autoregressive or feedback terms. This additional structure allows the network to detect and generate time-varying patterns where time plays a significant role in the modelling. It differs from conventional two-layer networks by the addition of a feedback/ recurrent connection. The delay terms store value from the previous time step, which can be used in the current step. (Beale et al., 2001). It makes the RNN useful in signal processing and prediction where time plays a dominant role. Sometimes, they also inherit the ability to fit any input/output function with a finite number of discontinuities.

The recurrent neural network may be a better choice to represent the transient engine operation compared to a standard MLP. However, no comparison between the MLP and RNN effects on the dynamic engine modelling has been found. However, in rainfall forecasting, Chiang, Chang, & Chang (2004) concluded that (1) the static-feedforward neural network could produce satisfactory results (in the case of dynamic process modelling) only when there is a sufficient and adequate training data set, (2) the dynamic neural network generally could produce better and more stable flow forecasting

than the static network, and (3) the RTRL algorithm helps to update the dynamic network for learning continually.

2.6.4 ANN Application in Engine Modelling, Control and Optimization

The ANN modelling technique has been widely used for internal combustion applications. Various types of engine modelling studies demonstrated its applicability of modelling various types of engine configurations.

He and Rutland (2004) utilized ANN to model a turbocharged direct injection (DI) diesel engine and performed simulations over a wide range of engine operating points. Janakiraman et al. (2013) used ANN-based methodology to predict HCCI combustion behaviour during transient operation. They concluded that the ANN modelling technique is a low cost and quick alternative to traditional physics-based modelling. Tan and Saif (2000) developed a procedure for using neural networks to identify a nonlinear dynamic model of the intake manifold and the throttle body in an automotive engine. A variance of the dynamic neural network called external recurrent neural network was used for dynamic mapping and model construction.

Zhao & Xu (2013) developed nonlinear models for the Atkinson cycle engine based on the ANN technique. The ANN models were trained and tested using the data computed by a precisely calibrated commercial engine simulation model in a meta-modelling exercise. He performed an optimisation to maximise the fuel economy under the WOT torque reduction percentage, knock intensity, and exhaust temperature. Zhao & Xu (2013) proved that the ANN is applicable for modelling the various types of engine design at different engine operating points. The ANN is also applicable for modelling based on static and transient engine data in an offline or online engine condition and can be modelled based on measured or well-validated engine simulation data.

The ANN models were also intensively used for various types of control and optimisation studies. Atashkari, Nariman-Zadeh, Gölcü, Khalkhali, & Jamali (2007) used polynomial type neural networks (PNN) to determine the effects of intake valve-timing on both engine torque and fuel economy at different engine speeds. Sangha et al. (2005) utilised a radial basis function neural network (RBFNN) for fault diagnosis and fault pattern classification in the air path of an automotive engine. Its included air leakage

factor in the intake manifold, EGR valve at different positions, intake manifold pressure, and temperature sensor faults factors.

Arsie et al. (2008) utilised the recurrent neural network (RNN) for real-time prediction and control of AFR in spark-ignited engines. The training and validation data sets obtained from transient measurements by imposing throttle and load perturbations. In the succeeding work, Arsie, Pianese, & Sorrentino (2009) performed an experimental identification using RNN for virtual sensing of NO emissions in engines. Network training is performed by minimising a cost function based on the MSE. A weight regularisation term is added to improve model generalisation. In order to obtain a proper RNN structure, Arsie et al. suggested that the training data set must be generated large enough to guarantee an acceptable generalisation of the knowledge retained in the training examples. Then one needs to select proper stopping criteria to prevent overtraining. The last rule is to define the network structure with the minimum number of weights.

The work flow for the general neural network design/modelling process has seven primary steps; 1) data collection, 2) network creation, 3) configuring the network, 4) initialisation of the weights and biases, 5) network training, 6) network validation (post-training analysis), and the last stage 7) network implementation. The training data will influence the accuracy of the ANN modelling performance. The experimental design must ensure that the measured data becomes maximally informative, subject to constraints at hand (Hamad, Yu, Gomm, & Sangha, 2011). The accuracy of the ANN model depends upon the data used to train because it is hard to set a comprehensive limit, standard or prior knowledge to the network. The data must cover the range of inputs for which the network is expected. The ANN can be trained to generalise well only within the range of inputs that have been trained. Beyond the range, they can't extrapolate accurately. It can be concluded that the coverage and size of the data pairs play a significant role in affecting ANN accuracy.

The data is best divided into the training, validation, and test set. The training set is used for computing the gradient and updating the network weights and biases. The training and validation error should be monitored, and error normally decreases during the initial phase of training. The increased validation error indicated that the network begins to overfit the data. The network structure, weights, and biases should be saved at

the minimum of the validation set error. The test set error is used to compare different models (Beale et al., 2018).

Data pre and post-processing are important steps in ANN training, and most of the most common data processing is provided automatically in the solver, such as MBC Toolbox. They became part of the standard procedure so that all the incoming data is pre-processed similarly. In general, the two-layer feedforward networks are sufficient to learn any input-output relationship. However, feedforward networks with more layers are expected to learn complex relationships more quickly. Thus, the practice starts with two layers and then increases to three layers, if required.

The training process involves tuning the weights and biases values of the network to ensure optimal network performance. The input-output data pairs are used as examples of proper network behaviour during the training, especially in the supervised learning process. The essential performance measure for ANN is the MSE. There are two different ways of training. It is either incremental mode training and batch mode training. For most problems, batch training is significantly faster and produces smaller errors than incremental training.

In summary, ANN has all the advantages for engine modelling purposes, including steady-state and transient problems applications. Table 2.3 presents the application of ANN in automotive engine modelling. The issues related to ANN application are determining optimal ANN topology, the use of MLP for transient engine problems, the number and arrangement of input to the ANN learning process, data size and coverage, data pre and post-processing, and suitable parameters for evaluation of ANN modelling accuracy. Several studies mentioned in this section have proposed a few techniques such as; using RNN for dynamic problems, using a more systematic heuristics method for optimal topology selection, model identification using metamodelling, the needs for estimation of proper model inputs, and the use of MSE for modelling error evaluation and optimal structural optimization.

Table 2.3 Previous work on ANN application in automotive engine modelling

Author	Model type	Purpose/ Problems	Methods & parameters	Algorithm/ structure	Major findings
Janakiraman et al. (2013)	ANN coupled with principal component analysis (PCA)	Prediction of transient HCCI engine combustion behaviour	MISO model for IMEP, combustion phasing, maximum in-cylinder pressure rise rate and AFR	MLP and radial basis network PCA for pre-processing	ANN is a powerful approach for transient, non-linear identification
Afrashteh (2000)	Recurrent NN (RNN)	On-board failure detection and isolation (FDI) in SI engines	EGR, MAP, and MAF subsystems of the engine as ANN input.	Back-propagation and Levenberg-Marquardt learning algorithms	ANN is a strong candidate for application in the OBD-II control strategy.
Turkson et al. (2016)	GMDH-ANN, and NSGA-II	Modelling and optimization of BMEP and HC emissions.	BMEP and unburned HC emissions.	1D GT-Power for data generation use in ANN modelling (meta-modeling).	Validated 1D engine model can be used to generate a data-driven modelling.
Turkson et al. (2016)	Review of ANN and its variant (SLP, MLP, and RNN)	Overview on ANN applications in calibration of SI engines.	Rapid prototyping, virtual sensing, look-up table by surrogates' model, emerging control strategies and OBD	SLP, MLP, feedforward network, RNN, and various activation functions.	Inputs within 5–10 factors considered appropriate for engine calibration tasks.
Gutjahr et al. (2017)	Gaussian NN regression with Bayesian approach.	Optimisation of fuel consumption, combustion stability (CoV), soot, and NOx emissions.	Injection and ignition timing, fuel pressure, rate of EGR, the timing of exhaust and inlet camshaft, and the swirl control valve (SCV).	The hyperparameters determined based on maximum likelihood optimization.	Standard physics-based models unable to predict with sufficient accuracy, computational demand and real-time incapable.

Table 2.3 Continued

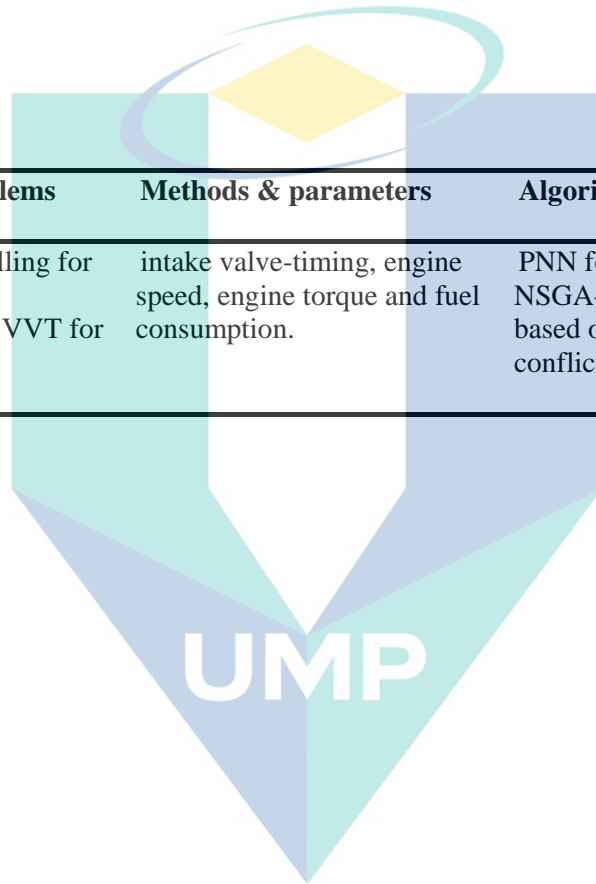
Author	Model type	Purpose/ Problems	Methods & parameters	Algorithm/ structure	Major findings
Gutjahr et al. (2015)	Demonstration of Gaussian ANN	Transient emission prediction, real-time HiL system, and meta-modelling.	Diesel engine inputs such as engine speed, torque, SOI, EGR, throttle, rail pressure, boost pressure and the NOx	Gaussian technique for data sets training and NARX model structure	Methods were used to meet the requirements for ease of use and high-quality plant modelling.
Rutherford & Cole (2010)	Standard MLP-ANN for vehicle dynamics	Investigation on the network size, structure, and initial weights.	The network's inputs are the fed back outputs of the network (parallel training)	Standard MLP with NARX structure and Levenberg Marquardt algorithm.	As the number of neurons in the layer increased, the modelling error reduces asymptotically.
Wu et al. (2004)	Standard MLP-ANN	Transient airflow rate with independent intake and exhaust camshaft-phasers	Intake camshaft position, exhaust camshaft position (ECL), engine speed and MAP	Systematic selection of the optimal network structure	Multi-layer feedforward networks can be regarded as universal function approximators.
Tan & Saif (2000)	External RNN	Identification of dynamic model for intake manifold and the throttle body.	MAP, MAF, throttle plate angle, EGR valve position, idle air control (IAC) valve, throttle geometry, and engine speed	Levenbert-Marquardt algorithm is applied to the weight-estimation problem	The ANN model is comparable if not better, than the first-principle-based models.
Sangha et al. (2005)	RBF-ANN used to detect and diagnose faults and to indicate fault size	Fault detection and isolation in automotive engine air path using an ANN.	Leakage, EGR valve and sensor faults with different fault intensities.	Gaussian transfer function in used for learning proces	A single, large neural network is more accurate instead of five smaller separate networks.

Table 2.3 Continued

Author	Model type	Purpose/ Problems	Methods & parameters	Algorithm/ structure	Major findings
Arsie et al. (2008)	Recurrent Neural Network (RNN)	Real-time prediction and control of AFR in spark-ignited engines.	Transient AFR, injection time, engine speed, MAP data sets by imposing throttle and load perturbations	ANN-based control systems are classified as a) Direct Control Systems and b) Indirect Control Systems	High accuracy and generalization capabilities guaranteed by RNN
Chiang et al. (2004)	The standard BP, conjugate gradient (CG), the recurrent learning (RTRL)	Comparison of two ANN variants for static and dynamic problem	23 storm events, 1632 rainfall and runoff data sets	The standard BP, and CG used for the static network, RTRL used for the dynamic-feedback network.	(1) the static-feedforward neural network could produce satisfactory results only when there is a sufficient training data set
He & Rutland (2004)	MLP-ANN	Meta-modelling based on CFD simulation of TC-DI diesel engine	Engine speed, load, SOI, injection pressure, mass of first injection pulse, boost pressure and EGR.	ANN-MLP as a surrogate model based on CFD engine cycle prediction.	ANN modelling accuracy improved by incorporating prior knowledge into ANN design
Zhao et al. (2012)	MLP-ANN modelling	Atkinson cycle model for MBC optimization of CR and operating parameters	Intake valve closure, CR, spark timing, AFR, WOT torque, knock intensity and exhaust temperature	Meta modelling using a precisely calibrated GT-Power engine simulation model	Significant fuel improvement of 6–13% at WOT operating conditions is obtained.
Zhao & Xu (2013)	MBC using GA for Atkinson cycle engine	Optimization of fuel economy for part load Atkinson cycle engine.	Intake valve closure, electrically throttling control (ETC), exhaust valve opening, spark angle and AFR	Each speed-load control map were optimized. The maps were embedded into the ECU	The fuel economy was greatly improved with the maximal improvement up to 7.67%.

Table 2.3 Continued

Author	Model type	Purpose/ Problems	Methods & parameters	Algorithm/ structure	Major findings
Atashkari et al. (2007)	GMDH-ANN and evolutionary algorithms (EA)	Part load modelling for SI engines and optimization of VVT for torque and fuel.	intake valve-timing, engine speed, engine torque and fuel consumption.	PNN for modelling, NSGA-II used for Pareto based optimization of two conflicting objectives	GMDH type models produced better prediction over feedforward ANN



اونيور سيئي مليسيا قهغ

UNIVERSITI MALAYSIA PAHANG

2.7 Electronic Control Unit (ECU) Maps Calibration and Its Requirement

This section presents the review of the model-based calibration technique for the ECU's lookup table by using a model-based calibration (MBC) Toolbox of Matlab-Simulink. Important issues reviewed are traditional calibration versus model-based calibration, optimization-based calibration using genetic algorithm (GA), and GA parameters tuning.

2.7.1 Traditional Calibration Versus Model-based Calibration (MBC)

Essential calibration of ECU maps consists of the calibration for various maps parameters. Usually, calibration is performed based on the engine operating modes. The objective of calibration is to select and define the optimum value of control parameters at each operating point (Niedernolte, Klöpper, Mitterer, & Schwarzer, 2006). The traditional calibration process is called engine tuning. As the new engine technologies introduced, the number of tuning variables increased. Since these variables are dependent on speed and load, the tuning burden rises significantly. It includes extra variables and combinations of the variables (Rask & Sellnau, 2004).

The traditional tuning combined a steady-state test with a transient engine test. The steady-state test is used to tune the optimised variables at a specific operating point. In contrast, the transient test is used to evaluate the overall engine performances. For each of the basic variables, the tuner needs to consider at least 32×32 operating points (based on the size of the maps). Besides, traditional engine tuning depending upon tuner expertise and entirely based on heuristic approaches where months could be spent to accomplish the task (Wong, Tam, Li, & Vong, 2010).

Thus, the challenge of traditional calibration is the experimentation cost due to enormous testing points. A new ECU maps calibration method is needed to eliminate the expensive cost and time for engine tuning and the need for a specialist to perform the tuning process. Model-based calibration of engine control is a state-of-art for modern engine performance optimisation. Moreover, it can be completed online or offline depending upon the available hardware and software facilities (Hafner, Jost, & Isermann, 2002).

The application of model-based calibration has reduced the total development cycle time through reduced experimentation costs. The core success factor is the availability of an accurate engine model. Furthermore, the design of the experiment (DoE) is employed to determine the significant operating points during testing. The calibration process initiated by defining optimal test plans, fitting statistical models, and generate calibration lookup tables, as presented in Figure 2.7. The calibration process can be carried out manually from point to point or by using an automated process. However, the DoE mostly suits steady-state tests only and rarely reported for transient engine testing.

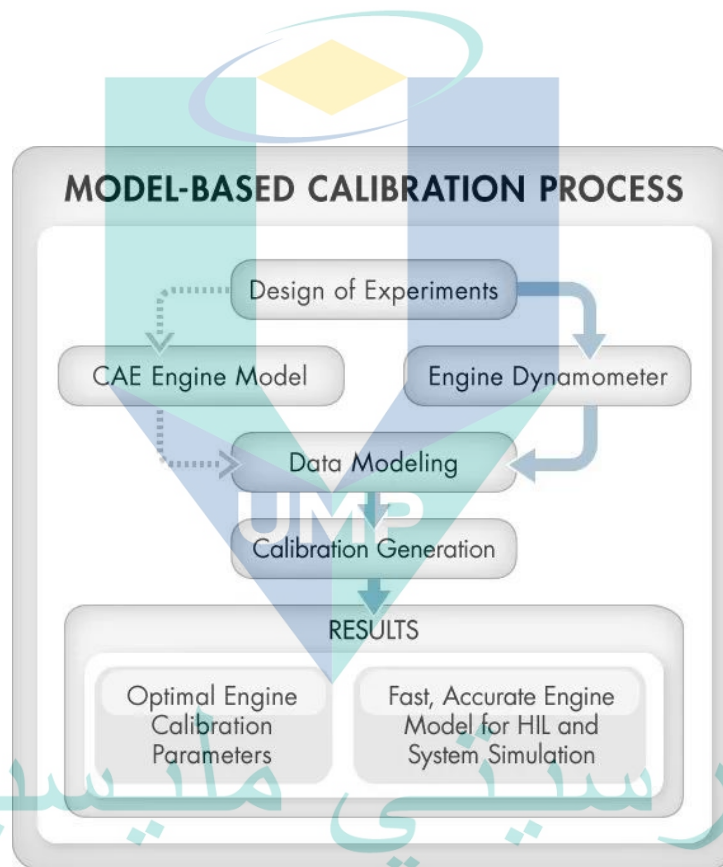


Figure 2.7 Standard procedures of MBC based on MBC Toolbox of Matlab
Source: MathWorks (2018)

2.7.1.1 Model-based Calibration using MBC Toolbox

MBC Toolbox consists of two major applications: Model Browser for the design of experiment (DoE) and statistical modelling, and Calibration Generation (CAGE). The CAGE dedicatedly designed for calibrating lookup tables or maps of ECU. The MBC toolbox offers analytical methods for calibrating lookup tables. The majority of the methods utilised a validated statistical model as a comparator to the optimized results

produced by CAGE. Thus, it eliminates the requirement of expertise to carry out the ECU tuning while at the same time accelerate the overall tuning process. There are at least three methods available to accomplish the calibration process (MathWorks, 2018). The methods are Feature Calibration, Trade-off Calibration and Automated Trade-off and Optimization Based Calibration. Table 2.4 presents the comparison of those three methods.

2.7.1.2 Essential Advantages of MBC Technique

Major advanced features of the model-based calibration (MBC) procedure are its ability to perform online calibration and calibrate the vehicle's transient operating mode. The latter part is made feasible using a transient vehicle model. The majority of the MBC applications are mostly focused on the steady-state operating mode where the steady-state models were developed based on a steady-state data testing (Ho & Karri, 2011; Morales, Hernández, & Carrillo, 2013; Wong et al., 2010; Wong, Tam, & Ke, 2012). It is primarily due to the DoE limitation, which is more appropriate for the steady-state testing process.

With the advent of computing technologies, recent studies show that the online calibration process is also available. Online calibration means that the calibration process is performed in real-time. When the engine performance is measured, the ECU control parameters are optimized, and the optimum parameters are sent back to the ECU and stored in the maps or lookup table. The online calibration procedure reported primarily involved steady-state testing only (Berger, 2012; Hardie et al., 2002; Mohammadi, Manzie, & Nešić, 2014). The end targets of online calibration are optimal and adaptive control strategies. The online calibration is advantageous if the model requirements are obsolete and the process can be executed in real-time, on-board, and include transient engine operation (Sharafi, Moase, & Manzie, 2018).

Table 2.4 Comparison of calibration methods offered by MBC Toolbox

Method	Characteristics	Advantages & disadvantages
Feature calibration	Use a comparative approach between a model and an estimated signal that utilises an algebraic collection of tables called the calibration strategy.	It is required that the calibration strategy inputs are similar to the model inputs for validity reason. However, it is problematic as there is a lack of reported calibration strategies and hence narrowing its success rate.
Manual trade-off calibration	The lookup tables are filled by manually comparing models of different engine characteristics at key operating points. It required multiple models for different engine characteristics. It is identical to a manual calibration process.	The significant advantage is the response of each model can be inspected instantly by a graphical method when the input is varied. However, the method is more useful for specific point tuning only, and it is problematic when considering hundreds of operating points simultaneously. Plus, it requires multiple models for different characteristics of the engine
Automated trade-off and/or optimization based calibration	Trade-off calibration in automatic mode by the combined usage of trade-off calibration and optimisation calibration. It allows the use of various optimisation algorithms, including the gradient-based and non-gradient based approach.	The easiest way to automate the calibration of multiple maps and multiple competing objectives. It allows simultaneous optimisation of all operating points within lookup tables and updating multiple trade-off tables in a single run. It can optimise multiple models, including single and multi-objective optimisations, sum optimisations and user-defined optimisations.

Source: MathWorks (2018)

اونيور سيني مليسيا فھق

UNIVERSITI MALAYSIA PAHANG

Online multi-objective optimization-based calibration of diesel engine controller was performed by using a multi-objective genetic algorithm (MOGA) technique by Sakawaki, Kaji, Yamamoto, & Sakoda (2009). However, in this work, an approximation model was still required for noise filtration and fitness evaluation. Other relevant results related to the online calibration include the steady-state calibration of spark advance for alternative fuel engines by using extremum seeking control by Mohammadi et al. (2014). The calibration was based on feedback torque. A similar work which is based on online and steady-state optimisation of spark advance for alternative fuel CNG engine by using multiplexed extremum seeking, was carried out by Sharafi, Moase, & Manzie (2018). Earlier, online calibration was presented by Hardie et al. (2002). The objective of his work is to automate the engine tuning process by using tuning software to communicate with the dynamometer controller and the ECU to create a closed-loop engine tuning system in real-time. These reported works are all based on online tuning for steady-state engine conditions.

Another advanced feature of MBC, the calibration can be performed using a transient engine model, which is developed based on transient engine data to optimize transient engine operating mode. However, the calibration of transient operation mode was mostly performed using an offline calibration procedure. (Atkinson & Mott, 2005; Atkinson, Allain, & Houshun Zhang, 2008; Atkinson, Allain, & Zhang, 2010; Atkinson, 2014). The use of a transient engine model to optimized transient characteristics in an online procedure is hardly found. It is due to the MBC process required a certain calculation period, thus hindered the transient mode calibration in real-time. Thus, the availability of an online, transient calibration procedure is a major step forward to reduce the enormous calibration time. The enabling technology which allows this progress is the excellent communication and data transfer technology between the hardware.

Corti et al. (2014) conducted transient spark advance calibration by an offline and online method. The proposed approach was based on transient tests coupled with a statistical investigation while allowing reliable performance analysis. They utilised a combination of field-programmable-gate-array (FPGA), real-time controller and host-personal computer for the transient optimisation process. The method was successful even with a low number of engine cycles. They also utilised the speed-sweep test method for the transient test by assuming that the speed-sweep test is comparable to the sequence

of steady-state tests. However, the sampling procedure indicated that they were still heavily relied on the offline optimization strategy for dealing with transient operating mode calibration. In addition, they were still dependent upon the statistical model during the calibration process.

Atkinson et al.(2008) had elaborated an approach to perform an off-line, transient engine calibration for fuel efficiency, emission output, and engine performance by using an MBC technique. He utilized ANN to model the measured data by considering engine operating history. They found that it is only by considering the immediate history of the engine operation that the dynamic behaviour of the engine can be predicted effectively. Furthermore, the choice of model inputs should be based on the fundamental engine control and operating variables which are measured and recorded, excluding any calculated parameters and mathematically constructed. The engine torque or the engine state model should be utilised as the calibration limit to ensure that any control inputs do not cause the engine to be operated beyond its mechanical limit. Later, Atkinson et al. (2010) had proposed a model which feasible to calibrate the engine transient emission even with a limited amount of data. Transient engine emissions and performance models are created by using ANN. The engine calibration is then executed offline using the transient models in conjunction with a set of optimisation and constraint functions. Several transient experiments allowed the engine to be exercised through a wide range of transient engine operations using random perturbation and the use of a rapid-prototype engine control system.

Brahma and Chi (2012a, 2012b) had proposed a steady-state and transient engine model for a turbocharged multi-cylinder diesel engine calibration. They had addressed that the transient engine testing required fast-response data acquisition especially for the exhaust gas emission sampling. The use of transient data for data-driven modelling produced a more accurate FTP cycle prediction. Furthermore, the steady-state model cannot predict the transition state mainly when the cycle-to-cycle variations existed. The transient model can be produced with a very much less amount of data and required lesser experimentation time. However, synchronisation of transient data together with other engine events was crucial to estimate the time delay. Their work also indicated that a steady-state model could be used to optimise transient driving cycles by optimising the response variables at discrete operating points within the cycle. It is merely an

approximation of transient cycle solutions. All the points within the cycle can be optimised in sequence or simultaneously optimised. However, the effect of dynamic behaviour depends strongly on the dynamic parts of the driving cycle. These dynamic parts include acceleration, deceleration, sudden stopping, or transition. Therefore, to consider the dynamic effects, the best option is to use a transient model.

Discussion on the method of model-based optimisation for driving cycles (which utilised transient engine models) was elaborated and clarified by Sequenz, Mrosek, & Isermann (2010); Sequenz & Isermann (2011); and Isermann and Sequenz (2016). The important conclusion is that data-driven modelling is the best choice for model-based calibration since it is a strongly nonlinear process. It is primarily part of parameter estimation methods by applying methods such as least squares and their modifications. Steady-state and transient models can be produced by two different methods, which are steady-state and transient testing, respectively. In order to model a transient engine response, the dynamic behaviour the process must be excited by appropriate test signals like step functions, fast ramp functions, sinusoidal or pseudorandom binary signals (PRBS). The sampling time, the present and past input and output must be recorded at each instantaneous response. It is obvious that the execution of the online calibration process in combination with transient operation mode testing is a hardware-dependent process, and the hardware integration is expected to be expensive. A cheaper calibration method is the combined use of transient engine model and offline calibration process. The offline calibration with transient models can even be performed for stationary (or steady-state) engine conditions which were corrected for transient operation. Table 2.5 presents numerous works of models-based calibration work, which progressed from the year 2002 to the year 2018.

Table 2.5 Application of MBC for automotive engine calibration study

Author	Model & technique	Test and Optimisation method	The objective of the study	Major finding
Hardie et al. (2002)	No modelling involved, manual tuning with digital interface	Develop own tuning algorithm for point to point testing.	Tuning algorithm tested on master fuel injection durations setting	Simple online tuning algorithm but still required expertise as manual tuning.
Wong et al. (2012)	MIMO-LS-SVM for ECU parameter and one-to-n remapping	Steady-state, constant speed test using a chassis dynamometer. Optimisation using GA, QNM and PSO	Developed model-based optimisation by considering nominal and numerical setting	Improvement of engine torque and part selection method
Wong et al. (2010)	MIMO-LS-SVM for engine idle speed modelling	Steady-state and transient loading testing of Idle speed and optimisation using GA and PSO	Developed a methodology of idle-speed modelling using LS-SVM for model-based optimisation	LS-SVM outperforms ANN for idle speed modelling. LS-SVM-PSO outperforms LS-SVM -GA
Morales et al. (2013)	Steady-state MIMO model based on LOLIMOT-ANN for HC, NOx, and CO modelling	Stationary testing for almost 60 points and optimisation using NSGA-II and multi-objective PSO (MOPSO)	Minimisation of exhaust emission for 1.6 L SI engine	MOPSO algorithm reductions are reached at least 13.68%, 83.8%, and 7.67% and outperform NSGA II
Ho & Karri (2011)	Two-stage model using polynomial spline for local model and various technique for global model	Steady-state, constant load speed (at 25%, 50%, 75% and 100% throttle opening) based on ISO 15550:2002 .	Multi-objective optimisation technique to maximise torque and minimising NOx emissions.	Desired performance optimisation at all engine operating states were successfully achieved by map calibration.

اوپنیورسیتی ملیسیا قہق

Table 2.5 Continued

Author	Model & technique	Test and Optimisation method	The objective of the study	Major finding
Turkson et al. (2016)	1D GT-Power model used to generate data and GMDH-ANN for surrogate modelling.	Used of the design of experiments (DoE) on stationary GT-power modelling for data generation.	Modelling and multi-objective optimisation of BMEP and HC emissions for a spark-ignition engine retrofitted to run on LPG	Trade-off between BMEP and brake specific HC emissions are solved.
Atkinson & Mott (2005)	A fully predictive dynamic engine model by combination of analytical and ANN method.	Transient test and regulatory cycles on dynamometer by perturbed input to produce a dynamic engine data.	Model-based calibration optimisation that reduced time and effort opposites to the DoE based systems.	High-fidelity transient model for performance and emissions prediction and applicable for model-based calibration.
Atkinson, Allain, & Zhang (2008)	Transient model based on MLP-ANN with externally tapped time delays or history.	Limited data collection using transient Federal Test Procedure (FTP) as the target transient cycle.	Offline calibration using the MLP-ANN model that able to simulate transient performance, emissions, and fuel consumption.	Reductions of 4.5% in measured FC, and 15-20% reductions in NOx, PM, and HC with no degradation in engine performance.
Atkinson (2014)	ANN model is used with the engine operating history to capture transient engine operation.	Limited data collection using FTP emissions test cycle to produce high-fidelity dynamically predictive, engine emissions models.	Demonstrate calibration optimisation procedure using fully predictive, transient engine and after treatment models	Used of an accurate transient forward predictive and inverse control models together with real-time optimisation.

اونيورسيتي ملايسيا قهغ

UNIVERSITI MALAYSIA PAHANG

Table 2.5 Continued

Author	Model & technique	Test and Optimisation method	The objective of the study	Major finding
Berger (2012)	Gaussian process used to model fuel consumption and exhaust emission and compared to other modelling technique	Stationary engine testing - For the initial data with 483 measurements were taken at 33 operating points.	Multi-objective online optimisation of consumption, NOx and soot and combine used of NSGA II and hypervolume measure for optimisation	Establishment of online optimisation method for stationary engine.
Mohammadi et al. (2014)	No modelling required but has to fulfil the extremum seeking requirement	Constant speed, load, and AFR with closed-loop feedback from oxygen sensor to optimise engine torque.	A tuning procedure for grey-box extremum seeking (ES) controller parameters to maximise the brake torque by finding the best spark advance at varying AFR.	Feasibility of applying grey box extremum seeking framework in practical engineering problems.
Sharafi et al. (2018)	Standard ES cater for optimisation of steady-state test. Multiplex ES considered transient test caused by exogenous input disturbances.	The New European Driving Cycle (NEDC) was used for transient driving scenario.	A novel multiplexed ES scheme to track time-varying extremum caused by a measurable disturbance. It accommodates the rigorous practical stability results of the standard ES approaches.	Under proper tuning, the proposed controller can improve engine fuel efficiency for unknown CNG compositions.

اونيفرسيتي ملايسيا قهق

2.7.2 Optimisation Based Calibration using Genetic Algorithm (GA)

The MBC approach allows the optimisation technique to calibrate the ECU maps as described in Section 2.7.1. One of the optimisation methods which the MBC Toolbox offers is the Genetic Algorithm (GA). Genetic algorithms (GA) are part of evolutionary algorithms. The search for the optimal values or optimisation process is based on the population-based approach that uses biology-inspired mechanisms and survival of the fittest theory. The objective of the genetic algorithm process is to refine a set of a solution by an iterative process (Malhotra, Singh, & Singh, 2011). This binary string defines the fitness of each individual in the population space. In practice, this fitness is defined by the objective function of the study.

The genetic algorithm has the advantage of solving complex optimisation problems. It can be applied to the problems that are not well suited for standard optimisation algorithms, including problems in which the objective function is discontinuous, non-differentiable, stochastic, or highly nonlinear. It can also address problems of mixed-integer programming, where some components are restricted to be integer-valued. The genetic algorithm techniques are derivative-free optimisation techniques and do not depend on gradient information. Thus, GA only considers the fitness functions that do not need to be differentiable or even continuous, no matter the problem.

Furthermore, since GA is a global optimisation technique, they are not likely to become trapped in the local optima (Wu, Lin, & Duan, 2006; Zhao & Xu, 2013). In addition, the genetic algorithm optimisation process can be performed based on the online and offline approaches. The offline approach is the most widely used and successful means. In contrast, an online approach is still a rare approach due to the difficulties with GA application in an online optimisation (Fleming & Purshouse, 2002). The GA optimisation process always requires finite computation time and is not suitable for online optimisation and transient engine operation.

As per other usual GA operations, it requires the use of standard GA operators. Based on Chebbi and Chaouachi (2015), the standard GA will need at least four essential elements for complete problem definition: the representation of a problem, the fitness function, termination criterion of the algorithm, and the different parameters and variables to control. One needs to define the crossover function, crossover fraction,

mutation function, selection function, population size, generation number, and stopping criteria for proper operation. The selection of these parameters affects the overall performance of GA. The primary input to any GA-based optimisation process is the objective function. The GA's output is the fitness function values of the system with the corresponding optimised controlled parameters (Malhotra et al., 2011).

Genetic algorithms begin with the generation of a set of solutions represented by a group of chromosomes, called population. The genetic algorithm selects individual chromosomes at random from the current population, mutated, crossed over, and mixed to be parents and uses them to produce the children for the next generation. This process is motivated by the possibility that the new population will be better than the old one. Besides, new solutions are selected according to their fitness to form new solutions called offspring. Over successive generations, the population is expected to evolve toward an optimal solution. The above process is repeated until some condition is satisfied (Senecal, Montgomery, & Reitz, 2000).

Based on the working principle, each iteration of the GA optimisation shall consist of the stated processes; selection, reproduction, evaluation and replacement. The algorithm stops when its population converges to an area in the search space that contains the best solution to a problem (Chebbi & Chaouachi, 2015). However, in practice, the GA will also possibly stop when any of the criteria specified in Table 2.4 are met. Thus, this also explained the importance of the criteria selection, and premature convergence should be carefully avoided. The iterative process for the searching of promising solutions by GA solver is presented in Table 2.6.

Table 2.6 The Genetic Algorithm iterative process

Process	Description
Selection	The individuals are generated through random selection within the search space for each control factor. A population is produced from a set of individuals. In creating the initial population, the best practice is to know the suitable range for the initial population. The range in the vicinity of the maximum or minimum point of the function is optimised.
Reproduction	The fittest individuals are allowed to reproduce, resulting in a new generation called the off-springs. The selections are made on the members, called parents, based on their expectation values. The algorithm usually selects individuals that have better fitness values as parents. These parents will contribute their genes (the entries of their vectors) to their children. The genetic algorithm creates three types of children for the next generation. 1. Elite children are the individuals in the current generation with the best fitness values. These individuals automatically survive to the next generation. 2. Crossover children are created by combining the vectors of a pair of parents, and 3. Mutation children are created by introducing random changes, or mutations, to a single parent.
Evaluation	A model (which may be empirical or multi-dimensional) is used to evaluate each individual's fitness. This model is called the objective or cost function of the problem. The scores of each individual in the current population is determined by computing its fitness values using the model. These scores are called raw fitness scores. The solver then scales the raw fitness scores to convert them into a more usable range of values. These scaled values are called expectation values.
Replacement	The fitness criteria are also used to filter out the population by terminating less suitable solutions. The characteristics of the individuals tend to converge to the most-fit solution over successive generations. The process continued, and the solver shall replace the current population with the children to form the next generation. In general, the algorithm will stop when one of the stopping criteria is met. The standard stopping criteria used are the number of generations, time limit, fitness limit, stall generations, stall time limit, stall test, function tolerance, constraint tolerance.

Source: Fleming and Purshouse, (2002)

2.7.3 Setting and Tuning of GA Parameters

In practice, several parameters must be appropriately set to ensure that the solver successfully fulfils the optimisation objective. It includes the crossover function, crossover fraction, mutation function, selection function, the population size, the number of generations, and the stopping criteria.

A larger population size created a larger search domain and provided a greater possibility for optimal solutions. However, it affects the computing time at each generation. The general rule is to set the population size to be at least the value of the number of variables so that the individuals in each population span the space being searched (Mathworks, 2018). Fleming & Purshouse (2002) suggested that a population size between 20 to 100 individuals are sufficient for most applications. Malhotra et al. (2011) recommended that the population size be about 20 to 30 chromosomes since a large population consumes a longer searching time which may deteriorate the performance of GA. Both studies agreed that the minimum number or the population size should not be less than 20.

Crossover and mutation are essential features in GA. Crossover enables the algorithm to excerpt the best genes from other individuals and reunite those different genes into new, potentially superior children. On the other hand, the mutation adds to the diversity of a population by modifying specific individual genes, thereby increasing the likelihood that the algorithm will generate individuals with better fitness values. GA may suffer problems related to premature convergence due to improper selection of crossover rates. These two values are important for controlling the balance between exploration (mutation-based) and exploitation (crossover-based) (Yuan & Gallagher, 2005).

The crossover rate and mutation rate are both continuous variables within $[0, 1]$. Typically, the crossover fraction was given a value of 0.8. A higher crossover rate of about 85% to 95% is recommended to minimise premature convergence problems. In contrast, a low mutation rate of about 0.5 % to 1% is generally recommended to avoid ad-hoc and random behaviour. The mutation is an artificial and forced method of changing the chromosome. Low mutation rates prevent genetic algorithms from falling into local maxima or minima (Malhotra et al., 2011).

Local maxima or minima is where the function value is smaller or larger than at nearby points but possibly greater than or smaller than a distant point in the search space. However, Zhao & Xu (2013) stated that the use of mutation operation could provide additional genetic diversity, and it is more likely to avoid the local optimum solution. Mutation operations are performed according to some probability for the generated child vector by the crossover operations. It is imperative to prevent premature convergence and prevent directionless search late (Fleming & Purshouse, 2001). It is concluded that the mutation is required to add the solution diversities, but a low mutation rate should be used.

Elite children required nor mutation neither crossover function process. They are fully reproduced similarly to the same parents with the highest fitness scales in the previous generation. The typical value of elite count is 2. When the elite count is at least 1, the best fitness value can only decrease from one generation to the next. Setting the elite count to a high value causes the fitness individuals to dominate the population, which can make the search less effective (Mathworks, 2018).

The selection function chooses parents for the next generation based on their scaled values (or expectation value) from the fitness scaling function. The scaled fitness values are called expectation values. The typical selection option, for example, is the Stochastic uniform. Other than Stochastic, a more deterministic selection option is Remainder. Wu et al. (2006) have discussed three other selection functions that are often used for parent selection; the roulette wheel, ranking, and deterministic tournament selection.

2.7.4 Application of GA for ECU Maps Calibration

Genetic algorithm (GA) has been applied for engine structural design optimisation (Ge, Shi, Reitz, Wickman, & Willems, 2009; Mattarelli, Perini, & Rinaldini, 2009; Park, 2010; Senecal et al., 2000), ECU design and optimisation (Sakawaki et al., 2009), and engine operational parameters optimisation (Dempsey & Reitz, 2011; Z. Yang, Wang, & Li, 2008). In most of the studies, the objective of GA application moving around three engines crucial factors, output power and torque, emission and fuel economy. This section focuses on the application of GA for ECU maps optimisation in the framework of model-based optimisation. The crucial element to be reviewed is the setting up of GA

parameters in ECU maps optimisation, especially the objective function, the constraint, the GA operators setting, stopping criteria etc.

Zhao & Xu (2013) performed the minimisation of brake specific fuel consumption (BSFC) as a function of engine speed and fitness function in order to reduce the fuel consumption of a spark-ignition engine running on an Atkinson cycle. The fitness function is derived as a function of optimisation variables which include the electrical throttle control valve (ETC), intake valve closure (IVC), exhaust valve open (EVO), spark angle (SA) and AFR. Morales, Palacios-Hernández, & Carrillo (2013) proposed an objective function formed by an ANN that represented the hydrocarbon (HC), carbon monoxide (CO) and nitrogen oxides (NO_x) emission in an exponential form and compared the optimised emission with the maximum allowable limits of that specific emission. All the objectives are optimised by adjusting the engine control parameters. The parameters also became optimisation constrained based on the engine operating envelope.

Desantes, Benajes, Molina, & Hernández (2005) developed an objective function which consists of BSFC and emission terms. The emissions to be minimised are the particulate matter (PM) and the nitrogen oxides (NO_x) emission. The BSFC term is normalized with the average BSFC for all test cases, and the emission terms are compared to the allowable emission values based on the EURO IV standard. The emission terms are also expressed in exponential forms. Yang et al. (2008) employed a multi-objective genetic algorithm technique to produce an optimal setup for a hydrogen engine controller. He classified the operating region of the hydrogen engine into four distinguished regions: the start and idle speed state, the full load state, low to mean load, and finally, the transition state. The objective function was based on the power and fuel consumption rates of the engine at each state. Hence there will be at least eight different objectives in the study. However, Yang et al. had combined all those other objectives into a single weightage objective which consists of power and fuel consumption terms. The objective combination and the use of weightage simplified the optimisation problem and made the optimal control with GA practical.

As discussed in section 2.7.3, the control and tuning of GA parameters have a crucial impact on the GA optimisation results. Wong et al. (2012) proposed the Quasi-Newton method (QN), genetic algorithm (GA) and particle swarm optimisation (PSO) to

determine the optimal engine setup. On the GA specific operators, they specified values of 1000, 50, 80%, 40% and 0.2 for generation number, population size, crossover probability, mutation probability, and standard deviation, respectively. They also used standard proportional selection, simple crossover method and hybrid static Gaussian method. Guo et al. (2017) proposed an adaptive model-based optimal control algorithm based on Multi-Objective Genetic Algorithms (MOGA). It targeted online engine calibration and control to improve engine performance and reduce greenhouse gas (GHG) emissions. Guo et al. utilised NSGA-II, which was implemented in MATLAB with a population size of 50, crossover probability of 0.9, and mutation probability of 0.005.

In an idle speed optimisation study, (Wong et al., 2010; Wong et al., 2008) proposed an idle speed optimisation study using GA. They utilised a generation number of 1000, a population size of 50, a standard proportional selection method, a simple crossover method and a Hybrid static Gaussian for mutation method. The crossover probability used is equal to 80%, the mutation probability of 40% and a standard deviation of 0.2. Eiben, Hinterding, & Michalewicz (1999) highlighted the root of complexity in parameter tuning because GA parameters are not independent. Instead, they are related to each other. Hence, even if we trying all different parameter combinations systematically, it is still practically impossible. The process of parameter tuning is time-consuming, even if parameters are optimised one by one, regardless of their interactions. For a given problem, the selected parameter values are not necessarily optimal, even if the effort made for setting them was significant.

Based on the cited studies, the BSFC is considered the most prominent parameter used to define the objective function. It became popular because it considers both the rate of fuel consumption and the engine brake power. Minimisation of BSFC can be achieved either by reducing fuel consumption or by increasing the engine brake power. The BSFC term is primarily suitable for global optimisation where every single operating point are optimised simultaneously. The BSFC parameter also combined with the emission terms to cater for the emission limit regulated by the authorities. In a condition where there are multiple competing objectives, the usage of the weighted objective function may simplify the overall problem's objective. Table 2.7 provide the suggested setup for GA parameters used in the previous study.

Table 2.7 Suggested setup for GA application in MBC calibration

Author	Applications	Suggested setup
Fleming & Purshouse (2002)	Optimisation for controller design and model identification	Population size between 20 to 100 individuals are sufficient for most applications
Malhotra et al. (2011)	Concept and design procedure of GA as an optimization tool	Crossover rate of about 85% to 95%, the mutation rate of about 0.5 % to 1%
Wu et al. (2008)	Multi-objective genetic algorithms for engine optimization	Roulette wheel selection, the ranking selection, and the deterministic tournament
Zhao and Xu (2013)	Fuel consumption reduction in a SI engine running on an Atkinson cycle	Minimisation of BSFC as a function of engine speed and fitness function
Morales et al. (2013)	Minimization of exhaust gas emission	Multiple objective functions based on the ANN model for hydrocarbon, carbon monoxide, and nitrogen oxides emissions in exponential form
Desantes et al. (2005)	Minimisation of particulate matter (PM) and nitrogen oxides (NOx) emission	The objective function consists of BSFC and emission terms
Yang et al. (2008)	Optimisation of optimal setup for a hydrogen engine controller	Single objective function with which consists of power and fuel consumption terms for different engine operating regions.
Wong et al. (2012)	Modelling and optimisation of engine performance using numerical and nominal data.	The generation number: 1000, population size: 50, crossover probability: 80%, mutation probability: 40% and standard deviation: 0.2
Vong and Wong (2010)	Engine idle speed optimisation problem.	The generation number: 1000, the population size: 50, standard proportional selection method, simple crossover method and Hybrid static Gaussian for mutation method. The crossover probability: 80%, mutation probability: 40% and standard deviation: 0.2
Wong et al. (2008)		
Guo et al. (2017)	Online engine calibration and control to improve engine performance and reduced GHG	The population size: 50, crossover probability: 0.9, and mutation probability: 0.005.

2.8 Gaps in the Study

Chapter 2 has reviewed the following topic: 1) the properties of CNG, 2) existing configurations of CNG direct-injection engine, 3) existing CNGDI engine performances, 4) engine modelling using an analytical approach, 5) engine modelling using ANN, and 6) ECU maps calibration. Based on the review, the following are considered the significant gaps of study that reflect the current study novelty. The direct injection system configuration must be critically assessed to ensure its advantages are fully recovered. The injector flow specification must first be determined to evaluate its new specification and suitability with the engine capacity for the whole engine operating range, especially if the injector is converted from a GDI injector. There is a need to reduce the engine test point in the calibration procedure. Moreover, a more convenient method should be proposed for calibration. Additional benefits are obtained if the calibration could be executed using standard hardware in the automotive workshop since the proposed technique could be readily applied using existing facilities. The use of an analytical model is considered an established approach to predict engine performance. However, a solution for a comprehensive, dynamic model is rarely found. In the context of ANN application, it is necessary to determine the applicability of the MLP approach for transient vehicle operation. Special consideration shall be given to the number of dataset size, model inputs and optimal network structure. In applying GA for ECU maps optimization, The issues are the definition of the objective function that best suits the calibration problem, GA parameters tuning, and the description of the optimization constraint. The next chapter presents the methodology used throughout the study.

اونيور سيني مائيسيا قهغ

UNIVERSITI MALAYSIA PAHANG

CHAPTER 3

METHODOLOGY OF THE STUDY

3.1 Introduction

This chapter presents the methodology used throughout the study. The main contents of the chapter are divided into Section 3.2 on the flow chart of the study, Section 3.3 on the injector analytical modelling, and Section 3.4 on the vehicle analytical modelling. It follows Section 3.5 on the independent injector testing, Section 3.6 on the speed-sweep test using chassis dynamometer, and Section 3.7 on model-based calibration procedure. Finally, in Section 3.8, the chapter presents the error quantities for results evaluation.

3.2 Flow Chart of the Study

The flow chart of the study based on the task sequences and based on the study's objectives are presented in Figure 3.1 and Figure 3.2, respectively.

3.3 Analytical Injector Modelling

The injector sub-models are divided into four different types; 1. the electromagnetic, 2. mechanical, 3. flow model, and finally, the description of the simulation setup. These models are coupled and simulated in Matlab/Simulink. The ODE45 solver is selected to solve the parametric problem because it performed well with most of the ODE problems and considered a first choice solver. A higher order can be more efficient than ODE45 for problems with looser or tighter accuracy requirements.

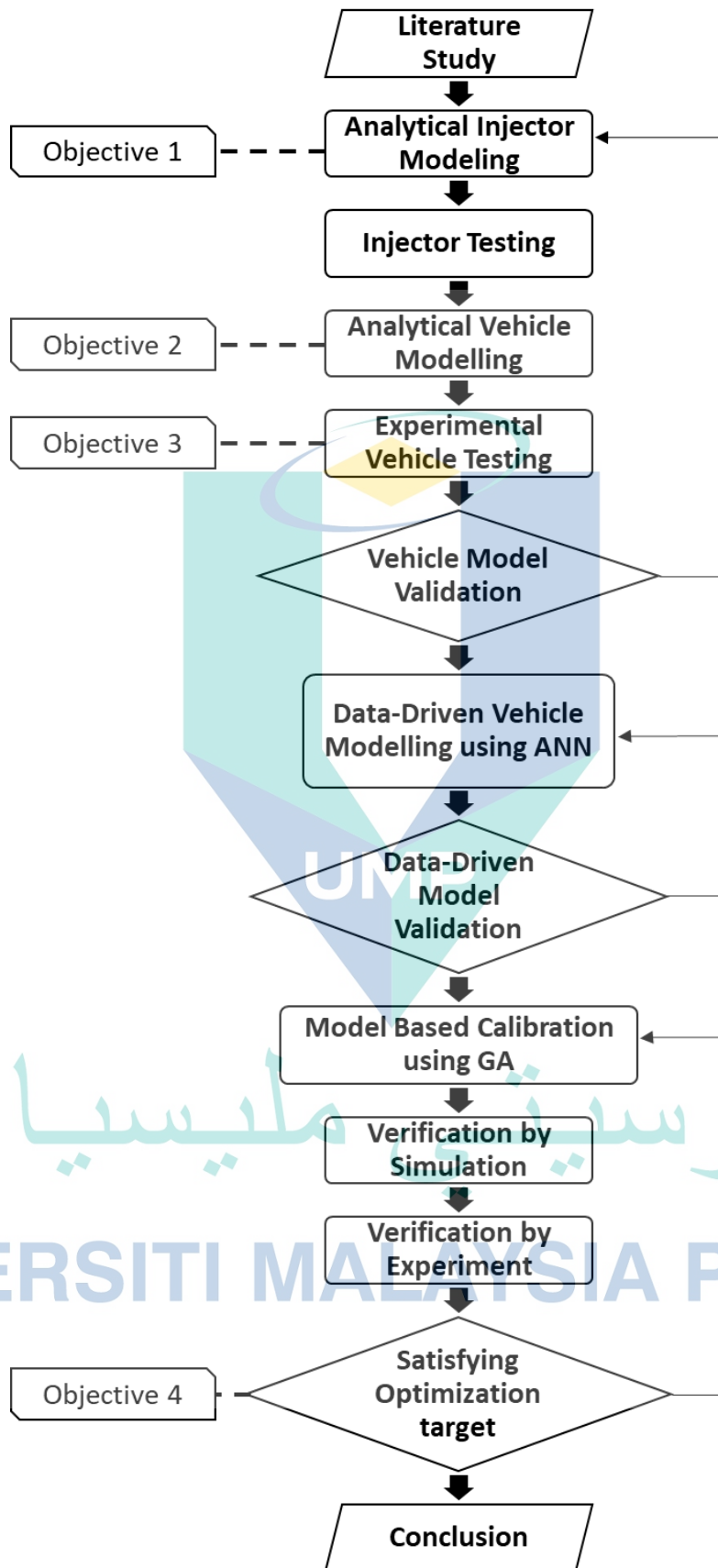


Figure 3.1 Flowchart of the study based on the task sequences

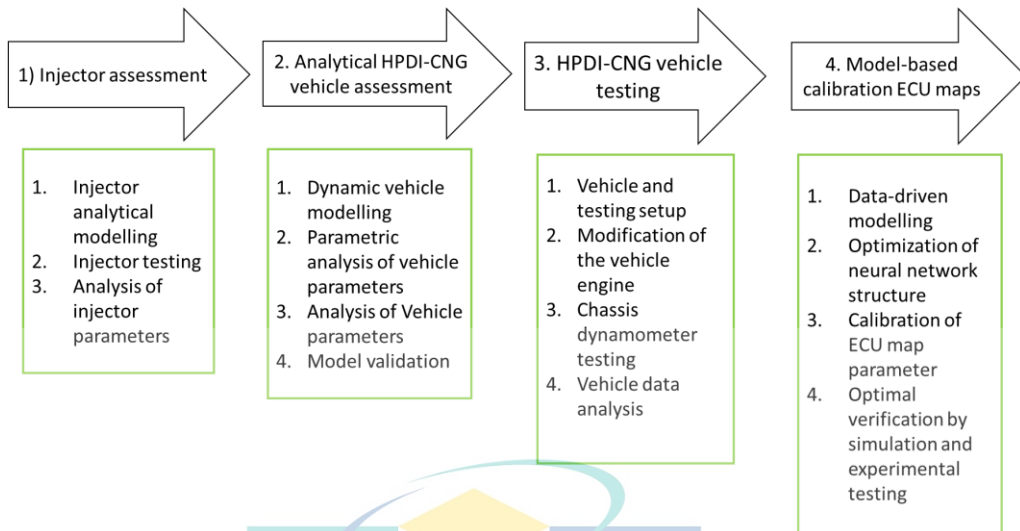


Figure 3.2 Major task based on the study's objective.

3.3.1 The Electromagnetic Model

The electromagnetic model is based on the work of Schimpf (2013). The solenoid driver presented by Schimpf is a derivation of electromagnetic force in terms of coil diameter, coil length, wire gauge, supply voltage, packing density, and the number of turns. This model eliminated the current factor, which is challenging to solve. The electromagnetic force is given by Equation 3.1 and 3.2:

$$F_{mag} = \frac{-V^2 \mu_r \mu_o}{8\pi\gamma^2 l^2} \left(\frac{r_o}{r_a}\right)^2 \alpha e^{\frac{\alpha}{l^x}} \quad 3.1$$

or in terms of winding factor, is given by:

$$F_{mag} = \frac{-V^2 \mu_r \mu_o}{8\pi\gamma^2 l^2} W_f \alpha e^{\frac{\alpha}{l^x}} \quad 3.2$$

where

- V: Supply voltage
- μ_r : The relative magnetic permeability of armature/pintle material
- μ_o : Air gaps magnetic permeability
- r_o : The inner radius of coil cross-section
- r_a : The average radius of coil cross-section
- γ : Ratio of coil material resistivity to coil wire cross-section area
- W_f : Winding factor, equal to the square of r_o/r_a ratio
- l : Length of the coil body

- α : Ratio of inductance to relative permeability of armature material
- x : Instantaneous position of the armature
- τ : Time factor

The model required detailed information about the coil materials such as coil material, coil material resistivity and coil wire cross-sectional area. In general, the larger the coil wire cross-section area, the larger the generated force. In the study, the selected coil wire is estimated to be AWG 43, which has a diameter of 0.07874 mm and copper type.

3.3.2 The Mechanical Model

The mechanical system of the direct injector is modelled as a mass-spring-damper system. The needle valve is assumed at rest on the valve seat in its initial state. In this initial stage, five forces act on the pintle; the gas pressure force, contact friction force, gravitational force, initial spring force, and finally, the normal reaction force is considered. Figure 3.3 presents the free body diagram of the pintle in the study.

The gas force is due to the CNG fuel pressure, the contact friction force is due to the contact between the pintle and surface of the valve seats, and the gravitational force is due to the mass of the pintle. The initial spring force is due to the compression of the spring at the initial state. Additional spring force is generated as the pintle is pulled by the solenoids. The normal reaction force defines the existence of the lower (and upper) stopper of valve seats. This force is represented by virtual spring and damper unit, which is equal and opposite to all other forces when the pintle rest or hit the bottom and upper stopper.

The pintle acts as a plunger that opens and closes the nozzle flow area. During the opening state of the injector, the pintle overcomes all the resistant forces by withdrawing the required current from the power supply. Typically, the larger the resistance load, the larger current is required to overcome the load.

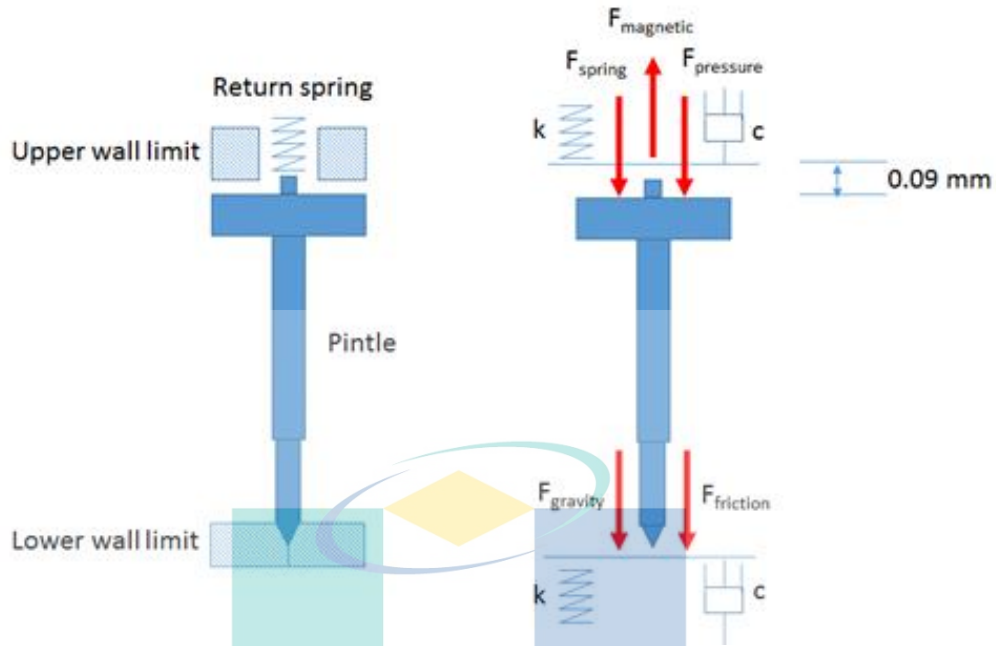


Figure 3.3 Pintle free body diagram based on a mass-spring-damper system

The relationship between all forces is described by the dynamic equation of motion of the pintle given by Equation 3.3. Based on the equation, the displacement of the pintle, x , can be obtained by a twice integration of the acceleration. The mass considered in the equation is the moving mass of the rigid pintle body.

$$m \cdot \ddot{x} = F_{sol} + F_{spring} + F_{contact\ friction} + F_{upper\ wall} + F_{bottom\ wall} + F_{pressure} \quad 3.3$$

The spring compression force, F_{spring} is defined as the sum of initial compression force and the additional compression force during the solenoid activation. The equation for the spring compression force is given by Equation 3.4.

$$F_{spring}(x) = F_0 + K_{spring} \cdot x \quad 3.4$$

where,

F_0 : the initial compression force, N

K_{spring} : spring constant, N/m

x : Pintle displacement

The initial contact friction force is a constant value of 13.8 N at its rest position (for the upper stator or lower stator). The value reduces to zero as the position of the

pintle surpassed a threshold distance of 0.001 mm. The mathematical form of the contact friction force is given by Equation 3.5.

$$F_{initial\ contact\ friction}(x) = \begin{cases} -13.8N & \text{if } x \leq 1e-3mm \\ 0 & \text{if } x > 1e-3mm \end{cases} \quad 3.5$$

Based on Zhang et al. (2014), the displacement of the pintle is limited by the existence of the bottom and upper stator. The maximum displacement allowable for the pintle is estimated to be 0.09 mm upward. Farther than that, a barrier is enforced by imposing a stiff spring and damper. It is to simulate a condition where the pintle hits the stator. The reaction forces imposed on the pintle at the upper wall is expressed mathematically by Equation 3.6.

$$F_{upper\ wall}(x) = \begin{cases} -K*(x-0.09mm)-c*x & \text{if } x < 0 \\ 0 & \text{if } x > 0 \end{cases} \quad 3.6$$

As the pintle moves back to the initial position and hit the lower stator, another barrier is imposed to simulate the reaction force from the bottom stator. The mathematical expression for the lower stator reaction force is given by Equation 3.7.

$$F_{bottom\ wall}(x) = \begin{cases} -K*x-c*x & \text{if } x < 0 \\ 0 & \text{if } x > 0 \end{cases} \quad 3.7$$

where,

K: the wall stiffness, N/m

c: the damping coefficient, N·s/m

3.3.3 The Flow Model

A one-dimensional compressible flow equation constructs the flow model for mass flow rate calculation. The model considers choking and non-choke flow situations determined by the critical pressure ratio. Choked flow occurs when the ratio P_1/P_2 exceeds the critical pressure ratio, P_c , given by Equation 3.8.

$$P_c = \left(\frac{\gamma+1}{2}\right)^{\frac{\gamma}{\gamma-1}} \quad 3.8$$

The mass flow rate through the orifice for non-choked and choked flow conditions are given by Equations 3.9 and 3.10, respectively. The only varying parameter in both

equations is the effective area of the nozzle, which calculated as a function of pintle displacement.

$$\dot{m} = C_d A p_1 \sqrt{\frac{2M}{RT} \left(\frac{\gamma}{\gamma-1} \right) \left[\left(\frac{p_2}{p_1} \right)^{\frac{2}{\gamma}} - \left(\frac{p_2}{p_1} \right)^{\frac{\gamma+1}{\gamma}} \right]} \quad 3.9$$

$$\dot{m} = C_d A p_1 \sqrt{\frac{\gamma M}{RT} \left(\frac{2\gamma}{\gamma-1} \right)^{\frac{\gamma+1}{\gamma}}} \quad 3.10$$

where,

- C_d : the discharge flow coefficients
- A : the orifice area
- p_1 : the CNG upstream pressure
- p_2 : the in-cylinder/ downstream pressure
- T : the CNG upstream temperature

The crucial part of the flow model is the definition of the nozzle's effective flow area. Figure 3.4 presents a schematic illustration of the effective flow area for the pulled-in injector. The effective flow area is defined as a surface area for a truncated cone. It is formulated based on Antunes, Mikalsen, & Roskilly (2009) and Antunes (2010).

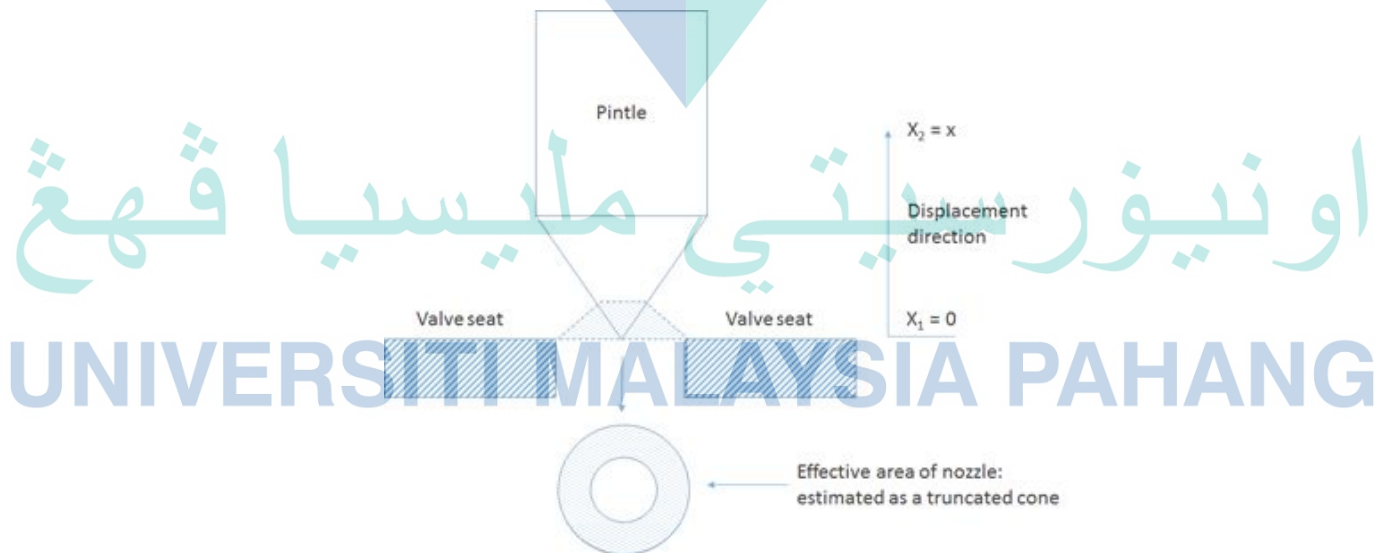


Figure 3.4 Definitions of effective flow area for nozzle flow calculation

Source: Antunes (2010)

The effective area for the nozzle flow, as illustrated in Figure 3.4, can be calculated by using Equation 3.11.

$$A_o = \pi \left(\left(R \sqrt{R^2 + (R \sin \varphi)^2} - (R - x \sin \varphi \sin \varphi) \sqrt{(R - x \sin \varphi \sin \varphi)^2 + (R \tan \varphi - x \sin^2 \varphi)^2} \right) \right) \quad 3.11$$

where,

R : the nozzle hole radius (m)

θ : the needle tip angle (rad)

φ : is equal to $\theta/2$

The maximum flow area of the nozzle is given by Equation 3.12.

$$A_{o \text{ Max}} = \pi R^2 \quad 3.12$$

3.3.4 Injector Simulation Setup

The simulations were carried out to replicate the two cases of the experimental study. A significant amount of inputs is required to ensure the model can predict the measured data. Table 3.1 listed all the inputs needed by the model. Table 3.2 presents the case study simulated using the analytical injector model. For Case 1, the injection pressure is a varied parameter, whereas in Case 2, the injection duration is varied. The electro-magnetic inputs and mechanical inputs are mainly based on Zhang et al. (2014). The pulse generator produced a square wave signal representing the output of the injector controller and PWM driver.

3.4 Vehicle Analytical Modelling

The analytical vehicle model is based on two modelling approaches; 1) a regular Simulink-based model and 2) a SimScape-based model. These two modelling techniques differ because Simulink blocks symbolise basic mathematical operations. A linked Simulink block together is equivalent to a mathematical representation of a system under study. In comparison, the Simscape model is dedicated to the modelling of physical systems. Simscape utilises the physical network approach such as physical coupling and particularly suited for simulating real physical components.

Table 3.1 Injector simulation model input

General Input Parameter (unit)	Values
Actuator radius (m)	0.005
Gas pressure (bar)	20, 30,40,50, 60
Nozzle Diameter(m)	0.00068
Spring Constant (N/m)	12140 N/m
Electro-magnetic Input Parameters (unit)	Values
Length of air gap (m)	0.00009
Magnetic Permeability of Air (H/m)	1.256×10^{-6}
Magnetic Permeability of Steel (H/m)	3290
Magnetic circuit length (m)	~0.001
Number of Turns	160
Coil Resistance (Ohm)	0.9
Resistance (ohm)	1.5
Inductance (mH)	1.9 mH @ 1kHz 3.9 mH @0.12 kHz
Voltage (Volt)	90
Peak Current (Amps)	20
Mechanical Input Parameters (unit)	Values
Static Spring Force (N)	40
Spring mass (kg)	0.001
Actuator Mass (kg)	0.003
Actuator Damping Constant (Nm/s ²)	14.97 N.s/m
Overall Weight (kg)	0.078
Flow Input Parameters (unit)	Values
Gas specific heat ratio	1.32
Gas valve flow co-efficient	0.65
Universal gas constant (J/kg.K)	8314
Gas Molecular Mass (kg/kmol)	16.04
Gas Supply Temperature (K)	300

Table 3.2 Definition of case study for injector testing

Case Number	Controlled variables:	Dependent variables:
Case 1: Effect of different CNG injection pressure on the CNG mass flow rate	CNG injection pressure is varied from 20 bar to 60 bar. The injector drive signal (square wave type)	Injector mass flow rate
Case 2: Effect of different injection duration on the CNG mass flow rates	CNG injection duration is varied from 2 ms to 28 ms. The injector drive signal (square wave type)	Injector mass flow rate

3.4.1 Integration of Simulink and Simscape Model

The Simulink engine model consists of the following; throttle dynamics (Pezouvanis, 2010), intake manifold (Pezouvanis, 2010), intake and exhaust valve (Sitthiracha, 2006), combustion (Rousseau, Lemoult, & Tazerout, 1999), heat transfer (Sitthiracha, 2006), and empirical submodels of convective heat transfer coefficient (Sitthiracha, 2006). The cylinder volume and cylinder surface area variation is solved by the crank slider mechanism submodel (Zweiri et al., 2001). All the submodels are incorporated within the modified first law of thermodynamics to solve the in-cylinder pressure and temperature.

The SimScape model consists of the clutch, simple manual transmission, final drive, and vehicle submodel. The input to these models is the acceleration and torque from the crankshaft. Based on the physical network approach, each system consists of functional components that interact with each other by exchanging energy through their physical conservation ports/coupling, not by a mathematical operation such as in a purely Simulink-based system. They are equivalent to the connection between real components such as pumps, valves, shafts, etc. As a result, the connection between the real physical components did not require any input boundary, such as flow direction or velocity. The most significant advantage is that they automatically resolve all the traditional issues with variables and directionality.

Since there is no variable defined in physical modelling, there is a special method to obtain the required variable properties from the model. The study proposed the use of virtual sensors attached to the physical elements. There are two types of sensors supported, which are *through-sensor* that is connected in series to a component, and *across-sensor* that is connected in parallel connection. In the study, such sensors are used to define the connection between the crankshaft and the clutch, namely the rotational speed sensor and the torque sensors.

3.4.2 The Gas Flow Dynamics

The airflow dynamics model consists of the throttle valve, intake/ exhaust manifold, and intake/exhaust valves. The one-dimensional compressible flow equation is used to calculate the mass flow rate of air at throttle-valve, intake valves and exhaust

valves. The model's output influenced by the pressure ratio of the upstream and downstream of each component.

The opening area of the throttle's butterfly valve following the work of Pezouvanis (Pezouvanis, 2010) is given by Equations 3.13-3.19. The maximum throttle flow area, A_{th}^{max} is given by the area of both circular segments which exclude the restriction of the throttle shaft. This is defined by Equation 3.13.

$$A_{th}^{max} = \frac{D_{th}^2}{4} 2\theta_{seg} - \frac{1}{2} D_{th} D_{sh} \sin(\theta_{seg}) \quad 3.13$$

where

$$\theta_{seg} = \cos^{-1} \frac{D_{sh}}{D_{th}} \quad 3.14$$

and given that:

D_{sh} : the throttle shaft diameter
 D_{th} : the throttle bore diameter

The close plate angle is the angle of the throttle plate when the throttle plate is fully closed. This parameter is required in the future calculation of the varying throttle flow area. Pezouvanis defined the throttle plate angle by using the expression in Equation 3.15.

$$\theta_{thc} = \cos^{-1} \frac{D_{th}}{D_p} \quad 3.15$$

where

D_p : the plate diameter

The throttle flow area is modelled as an elliptic area which has one of its sides varying with the throttle angle. Thus, the plate height, $h_p(\alpha)$ is a function of throttle angle, α and the throttle plate diameter, D_p and is given by Equation 3.16.

$$h_p(\alpha) = D_p \cos(\theta_{thc} + \alpha) \quad 3.16$$

The elliptic throttle flow area, excluding the area covered by the shaft, is given by Equation 3.17.

$$A_{th}^{plate}(\alpha) = \frac{h_p(\alpha)D_{th}}{4} 2\theta_{seg}^{plate} - \frac{1}{2}D_{th}D_{sh}\sin(\theta_{seg}^{plate}) \quad 3.17$$

where

$$\theta_{seg}^{plate} = \cos^{-1} \frac{D_{sh}}{h_p(\alpha)} \quad 3.18$$

Finally, the effective throttle flow area is obtained by deducting the elliptic throttle flow area from the maximum flow area and is given by Equation 3.19.

$$A_{th} = A_{th}^{max} - A_{th}^{plate}(\alpha) \quad 3.19$$

Figure 3.5 presents the geometrical description of the throttle valve model used in the throttle dynamics model. To simulate a realistic engine breathing process, a model of filling and emptying the cylinder is used. This study assumes the valve cam shape is designed based on the cosine function. Based on the work of Sittiracha (2006), the valve lift function is given by Equations 3.20-3.21:

$$L_{iv}(\theta) = \frac{L_{iv,max}(1 + \cos \varphi)}{2} \quad 3.20$$

where φ is given as:

$$\varphi = \frac{\pi(IVO - IVC + 2\theta + 540)}{IVO - IVC + 180} \quad 3.21$$

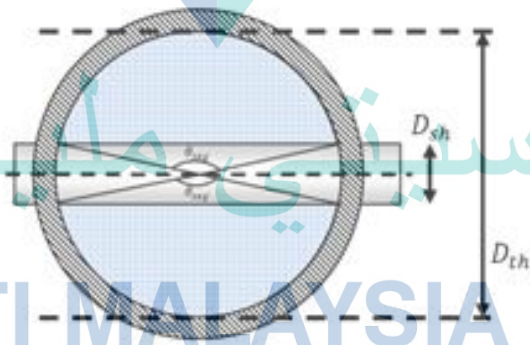
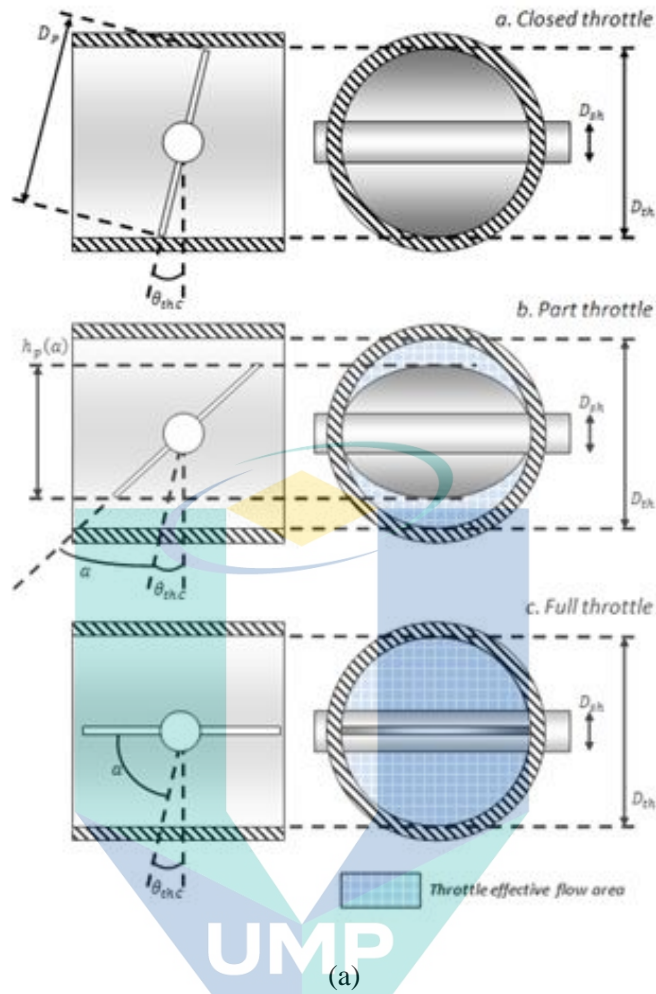
and

IVO : intake valve opening crank angle

IVC : intake valve closing crank angle

Intake air induced into the cylinder is calculated using the compressible flow equation for a flow through a restriction as given by Equation 3.22.

$$\dot{m}_a = \frac{C_d A_{cur} p_o}{(RT)^{0.5}} \left(\frac{p_{st}}{p_o} \right)^{\frac{1}{k}} \left\{ \frac{2k}{k-1} \left[1 - \left(\frac{p_{st}}{p_o} \right)^{\frac{k-1}{k}} \right]^{\frac{1}{2}} \right\} \quad 3.22$$



(b)

Figure 3.5 Illustration of the throttle model valve
Source: Pezouvanis (2010)

where

C_d : discharge flow co-efficient

p_o : upstream stagnation pressure

p_{st} : static downstream pressure

$\left(\frac{p_{st}}{p_o}\right)$: the pressure ratio that determines the flow condition.

A_{cur} : Valve curtain area. A_{cur} is given by Equation 3.23.

$$A_{cur} = \pi D_{iv} L_{iv}(\theta) \quad 3.23$$

where

D_{iv} : diameter of the inlet valve

The mass flow rate of air into the engine is also dependent upon the intake valve opening, closing and engine crank angle. Differentiation of equation (3.22) yields Equation 3.24.

$$\frac{dm_a}{d\theta} = \frac{C_d A_{cur} p_o}{6N(RT)^{0.5}} \left(\frac{p_{st}}{p_o}\right)^{\frac{1}{k}} \left\{ \frac{2k}{k-1} \left[1 - \left(\frac{p_{st}}{p_o}\right)^{\frac{k-1}{k}} \right]^{\frac{1}{2}} \right\} \quad 3.24$$

Equation 3.24 for the exhaust valve flow. The only difference is the definition of the pressure ratio, $\left(\frac{p_{st}}{p_o}\right) = P_r$. Equation 3.24 is differentiated with the crank angle because the flow over the valve is dependent on the valve opening, while the valve opening is dependent upon the instantaneous crank angle.

For the intake flow process, Sub-sonic inflow, $p_r < \left(\frac{2}{k+1}\right)^{\frac{k}{k-1}}$, Equation (3.24)

becomes

$$\frac{dm_a}{d\theta} = \frac{C_d A_{cur} p_{im}}{6N} \sqrt{\left(\frac{p_{cyl}}{p_{im}}\right)^{\frac{2}{k}} \left(\frac{2k}{(k-1)RT_{im}}\right) \left(1 - \left(\frac{p_{cyl}}{p_{im}}\right)^{\frac{k-1}{k}}\right)} \quad 3.25$$

where

p_o : intake manifold pressure, p_{im}

p_{st} : cylinder pressure, p_{cyl}

$\left(\frac{p_{cyl}}{p_{im}}\right)$ = the pressure ratio, p_r

Whereas in sonic and supersonic inflow, $p_r \geq \left(\frac{2}{k+1}\right)^{\frac{k}{k-1}}$, Equation (3.24)

becomes

$$\frac{dm_a}{d\theta} = \frac{C_d A_{cur} p_{im}}{6N} \sqrt{\left(\frac{k}{RT_{im}}\right) \left(\left(\frac{2}{k+1}\right)^{\frac{k+1}{k-1}}\right)} \quad 3.26$$

For the exhaust flow process, Sub-sonic outflow, $p_r < \left(\frac{2}{k+1}\right)^{\frac{k}{k-1}}$, Equation (3.24)

becomes

$$\frac{dm_{exh}}{d\theta} = \frac{C_d A_{cur} p_{cyl}}{6N} \sqrt{\left(\frac{p_{exh}}{p_{cyl}}\right)^{\frac{2}{k}} \left(\frac{2k}{(k-1)RT_{cyl}}\right) \left(1 - \left(\frac{p_{exh}}{p_{cyl}}\right)^{\frac{k-1}{k}}\right)} \quad 3.27$$

where

p_o : cylinder pressure, p_{cyl}

p_{st} : exhaust manifold pressure, p_{em}

$\left(\frac{p_{em}}{p_{cyl}}\right)$ =, pressure ratio, p_r

Whereas in sonic and supersonic outflow, $p_r \geq \left(\frac{2}{k+1}\right)^{\frac{k}{k-1}}$, Equation (3.24)

becomes

$$\frac{dm_{exh}}{d\theta} = \frac{C_d A_{cur} p_{cyl}}{6N} \sqrt{\left(\frac{k}{RT_{cyl}}\right) \left(\left(\frac{2}{k+1}\right)^{\frac{k+1}{k-1}}\right)} \quad 3.28$$

The difference between the throttle flow and the sum of intake valve flow is used to calculate the MAP. The MAP is vital to estimate the intake manifold flow and used as the ECU map's primary reference. This method is called the speed-density method, and its formulation is given by Equation (3.29).

$$\dot{m}_{manifold} = \eta_v \frac{MAP \cdot V_d \cdot N \cdot \left(\frac{1}{60}\right)}{C_{ps} \cdot R_{air} \cdot MAT} \quad 3.29$$

Rearrange Equation 3.29 yields the following form:

$$MAP = \frac{\dot{m}_{manifold} \cdot C_{ps} \cdot R_{air} \cdot MAT}{\eta_v \cdot V_d \cdot N \cdot \left(\frac{1}{60}\right)} \quad 3.30$$

By defining the $\dot{m}_{manifold} = \dot{m}_{intake} - \dot{m}_{throttle}$, the final equation becomes the following.

$$MAP = \frac{(\dot{m}_{intake} - \dot{m}_{throttle}) \cdot C_{ps} \cdot R_{air} \cdot MAT}{\eta_v \cdot V_d \cdot N \cdot \left(\frac{1}{60}\right)} \quad 3.31$$

3.4.3 In-Cylinder Thermo-Fluid Process

A zero-dimensional thermodynamic model combines the theoretical and empirical model of in-cylinder processes. Elementary submodels for the in-cylinder processes are the model for crank-slider, pressure and temperature, combustion, heat release, and heat loss. The empirical models are used as a closure to the theoretical expression. They include empirical burning duration, convective heat transfer coefficient, and flow discharge coefficients. Finally, a fuel supply model is required to estimate the fuel supplied to each cylinder. However, it is often simplified by using known AFR, as Sitthiracha (2006) and Rashedul et al. (2014) demonstrated.

3.4.3.1 Overall Model Assumption

The assumptions used in current modelling are:

1. The combustion chamber mixture is mixed homogeneously and uniformly distributed throughout the combustion chamber.
2. The temperature of the piston surface, cylinder head, and combustion chamber wall are constant.
3. The compression and expansion processes are assumed to follow isentropic processes.
4. The mixture occupied the chamber, and its volume is defined as a single zone.
5. The volume mixture is assumed to behave as an ideal gas mixture throughout the processes.
6. The cylinder volume is defined as an open system, where the system interacts with the environment via intake and exhaust mass transfer.

7. The heat loss mechanism considered is the convective heat transfer process from the gases to the wall only. The conjugate heat transfer between the cylinder wall to the coolant is beyond the scope of the current study.
8. The combustion of the volume mixture is assumed to be complete
9. The fuel properties assumed to be based on the pure methane properties.
10. The pressure and temperature throughout the processes are assumed to be uniformly distributed across the cylinder.

3.4.3.2 Crank Slider Dynamics

The crank slider mechanism is used to determine the combustion chamber's instantaneous volume and volume surface area as a function of crank angle. The instantaneous volume is important for state estimation, whereas the surface area is used to estimate the heat loss through the chamber wall. The equation for instantaneous cylinder volume and combustion chamber surface area as a function of crank angle is given by Equations 3.32 and 3.33.

$$V(\theta) = \frac{V_d}{CR - 1} + \frac{V_d}{2} \left[\frac{\iota}{a} + 1 - \cos\theta - \left(\left(\frac{\iota}{a} \right)^2 - \sin^2\theta \right)^{\frac{1}{2}} \right] \quad 3.32$$

$$A(\theta) = \frac{\pi B^2}{2} + \frac{\pi BS}{2} \left[\frac{\iota}{a} + 1 - \cos\theta + \left(\left(\frac{\iota}{a} \right)^2 - \sin^2\theta \right)^{\frac{1}{2}} \right] \quad 3.33$$

where

- B : cylinder bore, S : stroke
- V_d : Displacement volume
- ι : connecting rod length
- a : crank radius (taken as 0.5ι)
- CR : compression ratio

Equation (3.32) and (3.33) are differentiated to obtain $\frac{dV}{d\theta}$ and $\frac{dA}{d\theta}$. Both terms are substitutions for the solution equation of pressure and heat transfer.

3.4.3.3 Total Energy Equation

The first law of thermodynamics is used to formulate the equation of cylinder pressure and temperature. The variation of chamber internal energy, dU is determined by the three processes across the control volume boundary. The first is the net heat release into the chamber, $\frac{dQ_n}{d\theta}$, which considers the heat released by the fuel burned and the heat losses through the cylinder. The second term is the net changes of mass in the system. This term considers the air induced and exited the chamber through the valves and the fuel mass supplied, $\dot{m}_f h_{inj}$. Finally, the internal energy of the system is also affected by the boundary work of the system, $p \frac{dV}{d\theta}$. Derivation of the modelled equation is given as Equation 3.34 and graphically explain by Figure 3.6:

$$\frac{dQ_n}{d\theta} - p \frac{dV}{d\theta} + \dot{m}_f h_{inj} = \frac{dU}{d\theta} \quad 3.34$$

where

$\frac{dQ_n}{d\theta}$: the net heat release

$p \frac{dV}{d\theta}$: the variation of energy due to boundary work

θ : crank angle degree

$\frac{dU}{d\theta}$: variation of internal energy

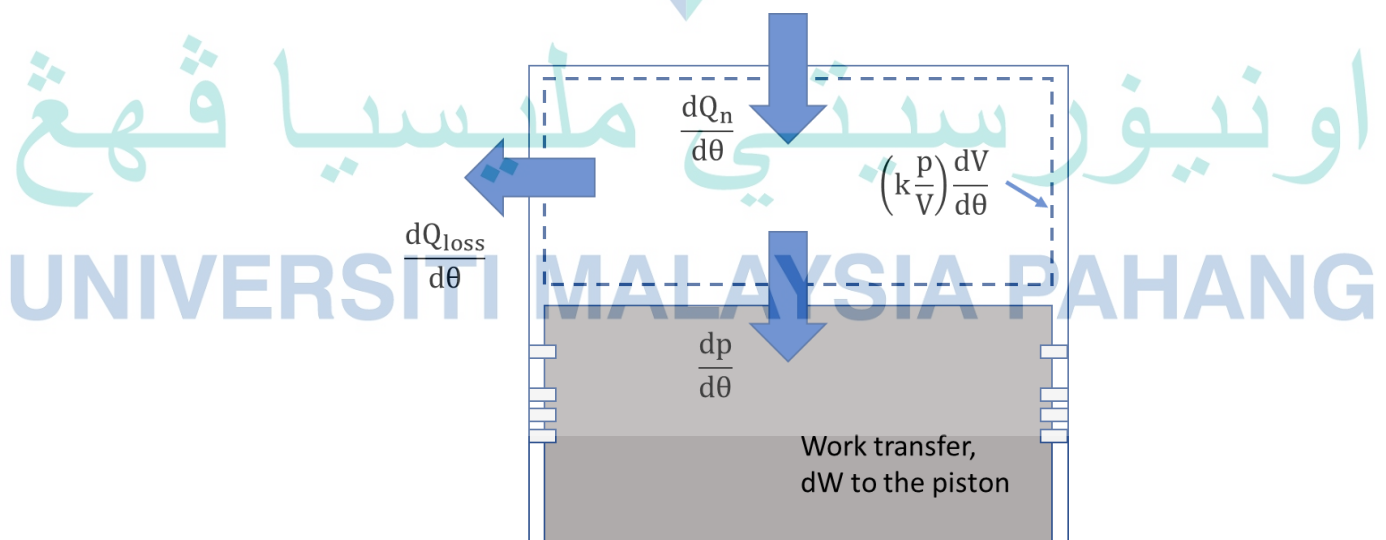


Figure 3.6 Open system boundary of the combustion chamber

From the ideal gas relation of internal energy and the rate of temperature changes, the net change of mass due to intake and exhaust valves flow is treated by Equation 3.35:

$$\frac{dU}{d\theta} = mc_v \frac{dT}{d\theta} \quad 3.35$$

where

m : the total mass of the cylinder

c_v : constant volume-specific heat

$\frac{dT}{d\theta}$: variation of temperature over the crank angle

and from the ideal gas equation of state, the relation between pressure, volume and temperature can be written as Equation 3.36.

$$\frac{dp}{p} + \frac{dV}{V} = \frac{dT}{T} \quad 3.36$$

Substitution of Equation 3.36 and 3.35 into equation 3.34 and by using ($R = c_p - c_v$), with neglecting the enthalpy component, Equation 3.34 will become:

$$\frac{dQ_n}{d\theta} = \left(1 + \frac{c_v}{R}\right) p \frac{dV}{d\theta} + \frac{c_v}{R} V \frac{dp}{d\theta} \quad 3.37$$

where

R : Specific gas constant

Finally, by using $k = c_p/c_v$, and by re-arrangement of Equation 3.37, the expression for the cylinder pressure in the chamber volume is obtained as:

$$\frac{dp}{d\theta} = \left(\frac{k-1}{V}\right) \frac{dQ_n}{d\theta} - \left(k \frac{p}{V}\right) \frac{dV}{d\theta} \quad 3.38$$

where

k : specific heat ratio

3.4.3.4 The Heat Release Rate Model

The combustion or the heat release process is modelled by applying the Wiebe function. The Wiebe function describes the mass fraction burned as a function of a crank angle given by Equation 3.39.

$$f(\theta) = 1 - \exp \left[-a \left(\frac{\theta - \theta_o}{\Delta\theta} \right)^{m+1} \right] \quad 3.39$$

where

$f(\theta)$: the fraction of heat added

θ_o : the start of heat release or ignition timing

$\Delta\theta$: the burning duration

The values of model constant a and m are given as 5 and 2, respectively. These values define the s-shape of the mass fraction burned curve. Changes on any of these values will change the curve shape. Substitution Equation (3.39) into the net heat release term has resulted as Equation 3.40.

$$\frac{dQ_n}{d\theta} = Q_{in} \frac{df}{d\theta} \quad 3.40$$

where

Q_{in} : the total heat input

$\frac{df}{d\theta}$: derivative of equation (3.39) over crank angle degree

The total heat input is calculated based on the AFR and estimated air mass flow rate using the following relation.

$$Q_{in} = \frac{HV \int_{IVO}^{IVC} m(\theta) d\theta}{1 + m_{air,stoic}} \quad 3.41$$

3.4.3.5 The Heat Loss Model

The heat transfer mechanism considered in the study is the convective process from the bulk cylinder gases to the cylinder wall. The net heat release terms, $\frac{dQ_n}{d\theta}$ in

Equation (3.40) is obtained by summing the +ve total heat input to the cylinder and –ve total heat loss to the wall, dQ_{loss} .

$$dQ_{loss} = hA(T_{b,g} - T_w) \quad 3.42$$

where

h : Convective heat transfer co-efficient

A : Exposed area of cylinder liner, cylinder head and piston face

$T_{b,g}$: Bulk gas temperature

T_w : Wall surface temperature

By taking derivative of equation (3.42) over crank angle degree, the equation becomes:

$$\frac{dQ_{loss}}{d\theta} = \frac{hA}{6N} (T_{b,g} - T_w) \quad 3.43$$

Now, the final form for cylinder pressure Equation (3.38) has become Equation 3.44:

$$\frac{dp}{d\theta} = \left(\frac{k-1}{V}\right) \left[Q_{in} \frac{df}{d\theta} - \frac{hA}{6N} (T_{b,g} - T_w) \right] - \left(k \frac{p}{V}\right) \frac{dV}{d\theta} \quad 3.44$$

3.4.3.6 Zero-Dimensional Thermodynamic Model Closure

Based on the mathematical models resented in Section 3.4.4.1 until 3.4.4.5, unknowns from the equations can be listed as below. The equations are closed by defining empirical relations for the unknowns, which are basically derived from experimental data.

1. $\Delta\theta$, the burning duration
2. h , convective heat transfer co-efficient
3. $T_{b,g}$, bulk gas temperature
4. C_d , flow discharge co-efficient
5. p_o , upstream stagnation pressure
6. p_{st} , downstream static pressure
7. FMEP, friction mean effective pressure

The model inputs are listed below. The exhaust gas pressure and the wall surface temperature is assumed to have constant values throughout the engine processes. Sources for each of the approaches were cited in the successive subsection.

1. T_w , wall surface temperature
2. B , bore
3. S , stroke
4. l , connecting rod length
5. CR , compression ratio
6. L_{iv} , maximum valve lift
7. D_{iv} , valve diameter
8. IVO , intake valve opening angle
9. IVC , intake valve closing angle
10. N , engine speed
11. θ , engine crank angle

3.4.3.7 The Burning Duration

The burning duration, $\Delta\theta$ in Equation (3.39) is derived based on the measured trace of mass fraction burned curve. In this study, the expression in Equation 3.45 for the burning duration is employed (Sitthiracha, 2006). It has been tested for CNG combustion in cycle engine modelling and validated against experimental data:

$$\Delta\theta = -1.6189 \left(\frac{N}{1000} \right)^2 + 19.886 \left(\frac{N}{1000} \right) + 39.951 \quad 3.45$$

where

N : engine speed

3.4.3.8 The Convective Heat Transfer Co-efficient

The model in the current study is employing the Hohenberg correlation for the convective heat transfer coefficient, which is provided by Equation 3.46 (Sitthiracha, 2006).

$$h = 130 x V(\theta)^{-0.06} x P(\theta)^{0.8} x T^{-0.4} (\bar{U}_p + 1.4)^{0.8} \quad 3.46$$

where

$V(\theta)$: Cylinder volume as a function of crank angle
 $P(\theta)$: Cylinder pressure as a function of crank angle
 \bar{U}_p : Mean piston speed

3.4.3.9 The Bulk Gas Temperature

The bulk gas temperature is calculated using the ideal gas equation of state. It is given by Equation 3.47 (Abd Alla, 2002).

$$T_{cyl} = \frac{P_{cyl}(\theta)V(\theta)MW_{cyl}}{R_u m_{cyl}} \quad 3.47$$

3.4.3.10 Flow Discharge Coefficient

The flow discharge co-efficient for intake and exhaust valve is given by Equation 3.48 (Sitthiracha, 2006).

$$C_d = 107.78 \left(\frac{L_{iv}}{D_{iv}}\right)^4 - 77.204 \left(\frac{L_{iv}}{D_{iv}}\right)^3 + 14.1 \left(\frac{L_{iv}}{D_{iv}}\right)^2 - 1.01 \left(\frac{L_{iv}}{D_{iv}}\right) + 0.6687 \quad 3.48$$

3.4.4 The Crankshaft Dynamics

The solution of engine dynamics requires that the intake and in-cylinder model be coupled with the crankshaft dynamics model. This includes the conversion of indicated pressure to indicated torque pulse, reciprocal torque, and inertia of the crankshaft assembly. The rate of change of inertia of the crankshaft assembly and instantaneous friction models are also required. Finally, the model shall include the net mean brake torque model and the dynamic crankshaft acceleration and rotational speed. Based on Zweiri et al., the generated force due to interaction of gas pressure and piston surface produced indicated torque which is calculated by Equation 3.49.

$$\mathbf{T}_{ind} = (P_{ind} - P_{atm})A_{pis}rG(\theta_1) \quad 3.49$$

The engine geometry function, $G(\theta_1)$ is given by Equation 3.50.

$$G(\theta_1) = \frac{\sin(\theta_1 + \beta)}{\cos\beta} = \sin\theta_1 + \sqrt{\frac{1 - \lambda(\theta_1)}{\lambda(\theta_1)}} \cos\theta_1 \quad 3.50$$

and the geometry function, $\lambda(\theta_1)$ is given by Equation 3.51.

$$\lambda(\theta_1) = 1 - \left[\frac{\delta + r \sin(\theta_1 - \phi)}{L} \right]^2 \quad 3.51$$

where

- β : angle of connecting rod
- r : the crank radius, equal to half of the stroke
- L : Connecting rod length
- δ : piston pin offset
- ϕ : Connecting rod angle when the piston is at TDC

The reciprocating torque produced by the reciprocating motion is given by Equation 3.52.

$$\mathbf{T}_r = M_{pass}rG(\theta_1) \left[G_1(\theta_1)\dot{\theta}_1^2 + G_2(\theta_1)\ddot{\theta}_1 \right] \quad 3.52$$

The geometric functions, $G_1(\theta_1)$ and $G_2(\theta_1)$ are given as Equation 3.53 and 3.54, respectively.

$$G_1(\theta_1) = r \left\{ \cos(\theta_1 - \phi) \left[1 + \frac{(r/L)\cos(\theta_1 - \phi)}{\sqrt{\lambda(\theta_1)^3}} \right] - \sqrt{\frac{1 - \lambda(\theta_1)}{\lambda(\theta_1)}} \sin(\theta_1 - \phi) \right\} \quad 3.53$$

and

$$G_2(\theta_1) = r \left\{ \sin(\theta_1 - \phi) + \sqrt{\frac{1 - \lambda(\theta_1)}{\lambda(\theta_1)}} \cos(\theta_1 - \phi) \right\} = rG(\theta_1 - \phi) \quad 3.54$$

These two terms are then substituted into Equation 3.55 of the crankshaft dynamics to solve the acceleration of the crankshaft.

$$\ddot{\theta}_1 = \frac{1}{\tau \dot{\theta}_1} \left\{ T_{ind} - \left[M_{pass} r G(\theta_1) G_1(\theta_1) + \frac{1}{2} \frac{\partial J(\theta_1)}{\partial \theta_1} \right] \dot{\theta}_1^2 - \sum_{k=1}^5 T_{fk} - T_S - T_D - T_L \right\} \quad 3.55$$

This equation can be coupled to any coupling mechanism, as demonstrated in the original work of Zweiri et al. (2001). The terms which construct Equation 3.55 are:

τ : the moment of inertia of the engine and crankshaft assembly. This value is given by Equation 3.56.

$$\tau = J_{cran}(\theta_1) + M_{pass} r G(\theta_1) G_2(\theta_1) \quad 3.56$$

$\ddot{\theta}_1$ and $\dot{\theta}_1$: crankshaft rotational acceleration and rotational speed, respectively

$M_{pass} r G(\theta_1) G_1(\theta_1)$: portion of the reciprocating torque of the engine

$\frac{\partial J(\theta_1)}{\partial \theta_1}$: the rate of variation of engine inertia due to inner components

$\sum T_{fk}$: the sum of friction torque due to internal engine assemblies

$\sum T_S$: the sum of stiffness torque at the coupling

$\sum T_D$: the sum of damping torque at the coupling

$\sum T_L$: The sum of external load implied on the engine

Equation 3.55 is the final equation that produces the engine output from the pure Simulink type-based model. From this point onwards, a few engine output variables are transferred to the physical network model of SimScape via signal transformation. The utmost essential variables are net mean brake torque and the crankshaft acceleration. Since the actual engine on the vehicle is a four-cylinder engine, the net mean torque and acceleration are summed up before subtracting the external load and inertia of the load.

3.4.5 Multi-Cylinder Synchronization

The baseline engine design is a four-cylinder inline engine configuration. Therefore, the formulations of thermo-fluid and crankshaft dynamics must be accounted for the four-engine cylinder which acting on the same crankshaft. The starting crank angle was set as -360° and the final crank angle was set as 360° (with reference to cylinder

number 1 following the firing order of 1-3-4-2). The zero crank angle represents the firing TDC of a specific cylinder. In order to simulate the phasing of each cylinder, the crank angle input to each cylinder must be phased out relative to the reference cylinder given by Equations 3.57 to 3.60.

$$\text{Cylinder 1: } \theta_1 \text{ (reference cylinder)} \quad 3.57$$

$$\text{Cylinder 3: } \theta_1 + \pi \quad 3.58$$

$$\text{Cylinder 4: } \theta_1 + 2\pi \quad 3.59$$

$$\text{Cylinder 2: } \theta_1 + 3\pi \quad 3.60$$

3.4.6 The Net Mean Brake Torque Solution

The actual form of torque transferred from the piston-connecting rod assembly to the crankshaft is in the form of torque pulse. The highest magnitude of the pulse is generated during the power stroke. In a multi-cylinder engine, the number of pulses acting on the crankshaft will increase. These torque pulses created moments and torsional vibration, and damping of these effects is compulsory to provide a smooth power transfer. In practice, the damping is accomplished by using counterweights and balancing procedures until a mean torque is produced. Throughout the study, a cycle-averaging approach has been utilised to obtain the mean brake torque. It is assumed that the results of the averaging process are equal to the smooth mean torque at the crankshaft. A variable frequency mean-value quantifier from the Simulink Simscape toolbox has been used. The instantaneous frequency of the engine is determined from engine speed based on the following expression:

$$f = \frac{\dot{\theta}_1}{4\pi} \quad 3.61$$

where

$\dot{\theta}_1$ = the crankshaft rotational speed in rad/s

As a result, throughout the simulation, there are three terms of torque that are produced. These three different torques are presented in Figure 3.7. The pulsating torque is representing the torque pulse at the engine crankshaft, which has deducted with the friction torque and the inertia of piston-connecting rod and crankshaft assemblies. The mean brake torque is the cycle-averaged values of the pulsating torque which has been calculated by the variable frequency mean value quantifier. Finally, the net mean brake torque is the mean brake torque that has been deducted with the external load inertia imposed by the engine driveline, including the inertia of the clutch system, gears, final drive and the vehicle body. By theory, the value of mean brake torque will always be the mid-value of the pulsating torque, and the net mean brake torque value will always be lower than the mean brake torque value.

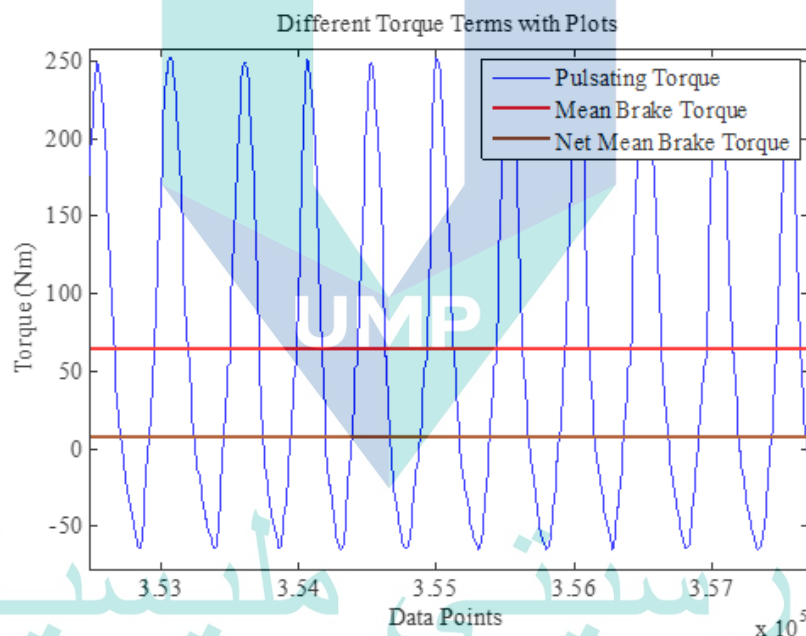


Figure 3.7 The plot of different torque produced by the analytical model

APPENDIX A presents other equations for the vehicle model. **APPENDIX B** shows the model flow chart and detailed relationships between the model equations. The equations are required mathematical models for a complete vehicle modelling procedure. However, the equations are mainly lengthy equations that are derived and utilised in the cited studies.

3.4.7 The Coupling between Engine and Drivetrain

The vehicle simulation is performed to represent the prototype vehicle dynamics. Moreover, it must be able to replicate the vehicle testing procedure using a chassis dynamometer. Therefore, the engine model must be coupled to a driveline model, which is proposed to be based on the SimScape modelling approach. In the coupling definition, the mean brake torque signal has been converted to a physical signal by the use of a Simulink-Physical Signal (S-PS) converter. On the physical side, the load torque imposed by the drivetrain load is measured by a virtual torque sensor downstream of the clutch. The measured physical torque is converted to a Simulink signal by PS-S converter and fed to the engine. The signal is then deducted from the instantaneous value of mean brake torque. Once converted, the Simulink signal can be coupled with the clutch shaft. The outcome of the coupling is an effective torque called the net mean brake torque. The net mean brake torque is used to calculate the acceleration of the vehicle. Positive and larger net mean brake torque values will produce higher acceleration and speed of the vehicle and vice versa. This is mathematically expressed by Equation 3.62.

$$\begin{aligned} \text{The net mean brake torque} & \qquad \qquad \qquad 3.62 \\ & = \text{the mean brake torque} - \text{The external load torque} \end{aligned}$$

A simplified clutch model, which consists of the torsional spring-damper element is used. The lack of actual clutch's attributes hinders a more realistic and complex clutch model. In the current study, the simple clutch model only consists of spring and damper properties which are referred from the previous study of Ding and Pan (2009). All the values of the clutch model are presented in Table 3.3. The damping force is the sum of viscous and Coulomb friction forces.

Table 3.3 The clutch spring-damper model properties

Properties	Values
Restoring spring stiffness (Nm/rad)	763
Viscous friction coefficient (Nms/rad)	14
Coulomb friction Torque	0
The ratio of static to kinetic friction	1.1
Velocity tolerance (rad/s)	0.001
Initial deformation of spring (deg)	0

Sources: Ding & Pan (2009)

3.4.8 The ECU Look-Up Table

The throttle input governs the operational engine state. The action of the throttle affects the MAP, the amount of air intake, and consequently the amount of fuel injected into the cylinder. This is accomplished by the use of a lookup table in a feedforward control strategy. As in the actual ECU, the references in the lookup table are based on the MAP and engine speed. The model architecture is designed so that the model becomes fully predictive. The lookup table contents are similar to the actual table in the prototype vehicle.

3.4.9 Simulation Procedure

A parametric analysis has been conducted to analyse the effect of control parameters on the mean brake torque output. In addition, by using parametric analysis, one can analyse the level of influence of each control parameter on the engine output. The analysis can also be used to predict the maximum extends of vehicle performance. In this study, four control parameters were manipulated and studied. The selected parameters are presented in Table 3.4.

Table 3.4 Description of the cases for the parametric study

Case	Description	Manipulated parameter ranges
1	Effect of throttle opening rate	2 secs to 18 secs period
2	Effect of ignition timing advance	-5 to -20 deg BTDC
3	Effect of injection pressure variation	20 bar to 60 bar (defined in terms of corresponding mass flow rate)
4	Effect of increased injection duration	0.02 secs to 0.1 secs

UNIVERSITI MALAYSIA PAHANG

In order to simulate a realistic dynamic event, the vehicle had been simulated in an acceleration mode, mimicking the speed-sweep test procedure on a chassis dynamometer. The ramp input through the throttle angle parameter is given to the engine, and the default simulation time was 30 seconds. The specification of the baseline case of the simulation is provided in Table 3.5.

Table 3.5 Specification of the baseline case for vehicle simulation analysis

Description	Magnitude
Throttle opening rate	0.6885 rad/s
ignition timing advance	default
injection pressure	40 bar (mass flow rate = 0.7 g/s)
injection duration	Default fuel map
vehicle mass	1015 kg
initial speed	0 mph

Table 3.6 provides the vehicle specification which is used in the study. It is inspired by a vehicle product of Proton and modelled as Gen. 2, a hatchback passenger vehicle. The car is powered by a Campro engine, codenamed as S4P, an engine originally made by Proton. The engine is produced with multipoint electronic fuel injection (EFI), which is run based on gasoline fuel. The engine was modified to enable the high-pressure direct injection of CNG by the addition of high-pressure direct injectors. **APPENDIX C** provides detailed input to the analytical vehicle model.

Table 3.6 Vehicle and engine specification use for analytical modelling

Vehicle dimension	
Overall length	4310 mm
Overall width	1725 mm
Overall height	1435 mm
Wheelbase	2600 mm
Tracks	1475 mm/1470 mm
Weight	1175 kg (Auto = 1195 kg)
Engine dimension and configuration	
Type:	4 cylinders, 4 valves per cylinder
Bore/stroke	76/78 mm
Displacement: 1597 cc	1597 cc
Compression ratio:	10:1

Source: S4P Service Manual (2004)

3.5 Independent Injector Testing

Independent injector testing is performed to measure the actual mass flow rate of the injector. The mass flow rate at each injection pressure setup and injection duration are analysed. The results are compared with theoretical injection simulation and previous injection studies, and discrepancies from both comparisons are discussed in the results and discussion.

3.5.1 Experimental Apparatus

The physical layout of the baseline injector is shown in Figure 3.8. The injector is made of Bosch, modelled as HDEV 5, a direct injector for gasoline direct injection (GDI) engine. General specification of the injector and flow characteristics for gasoline fuel operation is provided in Table 3.7. The maximum allowable fuel pressure for the injector is 200 bar. Calibration of the injector with gasoline fuel at 100 bar produced an estimated volumetric flow rate of 30 cm³/min or 0.36 g/s (by taking gasoline density as 719.7 kg/m³). In this study, CNG fuel pressure was regulated between 20 bar to 60 bar. The range is selected because it is the range where the prototype vehicle is operable. The mass flow rate for different pressure and injection duration is to be determined.

Table 3.7 General injector specification, model HDEV 5, made of Bosch

Mechanical specifications	
Allowable maximum pressure (bar)	200
Volume flow rate (gasoline fuel/cm ³ /min) at 100 bar	30
Weight (g)	78
Length (mm)	85
Electrical specifications	
Resistance (Ohm)	0.9 @ 1.5
Voltage (Volt)	90 V
Allowable peak current (Amp)	20 A
Operating Condition (Gasoline fuel)	
Fuel Input	Axial (top feed)
Operating Temperatures (°C)	30-120
Permissible Fuel Temperatures (°C)	<80

Source: HP Injection Valve HDEV 5.2 (2014), Erfan et al. (2015)



Figure 3.8 Bosch single-hole gasoline direct injector

The experimental setup for the injector testing is shown schematically in Figure 3.9. This setup comprises a CNG supply tank, fuel pressure regulator, pressure gauge, test injector, injector microcontroller, and a control computer. The microcontroller acts as a pulse generator to provide square wave signals with adjustable frequency and amplitude to a PWM motor driver, driving the injector in different modes. A digital scale is used to record the cylinder mass tanks after a number of injections is completed. The mass changes are used to determine the mass flow rate of the injector. The time factor is calculated by the total length of the “ON” signals produced by the microcontroller. In the experiment, a constant 12 V supply is provided through the PWM driver. The supply current is limited to 8 Amp in order to replicate the saturated current limit used in the actual electronic control unit (ECU) of the prototype vehicle.

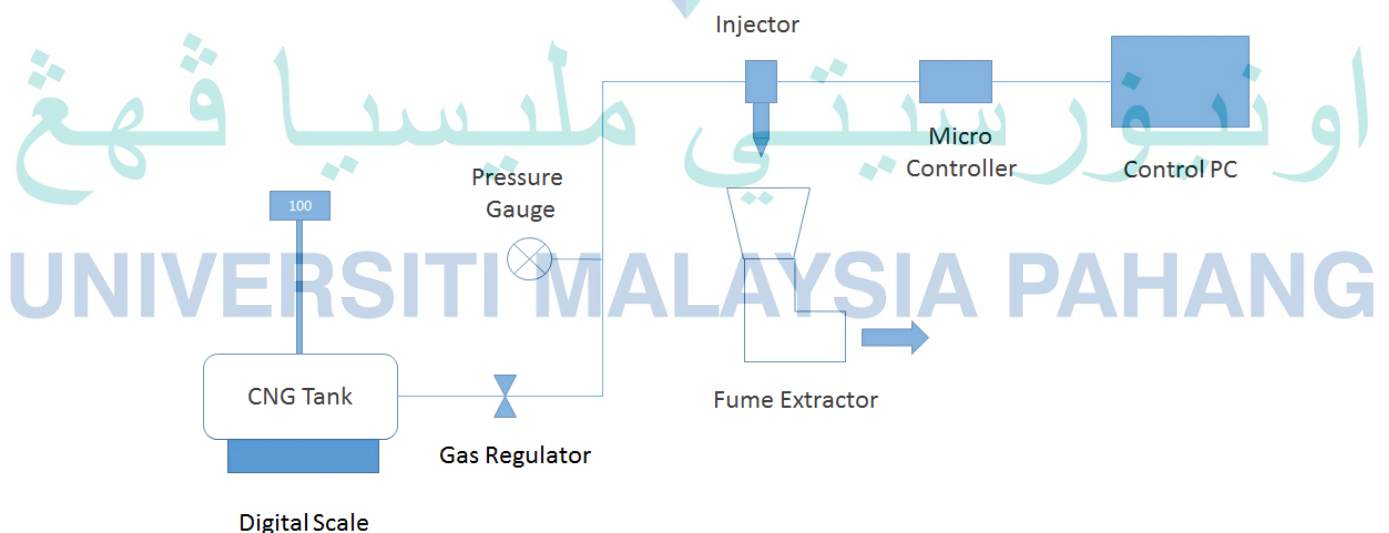


Figure 3.9 Schematic diagram of the experimental setup.

3.5.2 Experimental Procedures for Injector Testing

The varied parameters in the study are the injection pressure for Case 1 and injection duration for Case 2. In Case 1, the injection pressure is varied from 20-60 bar with an increment of 20 bar. The actual HPDI-CNG operation is in between 45 bar to 60 bar. The minimum pressure limit of 20 bar is selected based on the common injection pressure used in the previous study (A-Rashid & Firmansyah, 2009; Kalam & Masjuki, 2011; Taib Iskandar Mohamad & Geok, 2009). At each pressure setting, the CNG fuel is injected at a duration of 25 ms for 1000 counts. The fuel is injected into ambient conditions to replicate the actual HPDI-CNG operation. The ambient condition is assumed to be the downstream pressure because the injection is completed during the valve opening period. In Case 2, the injection duration is varied in the range of 2 to 26 ms. This corresponds to the measured duration in HPDI-CNG operation. At each duration setup, the injection count is set to 500 counts. Table 3.8 presents a detailed setup for injector testing.

Table 3.8 Experimental conditions for the injector testing

Parameters	Values
Number of nozzles	Single-hole injector
Spray Angle (Degree)	11
Injected gas	Compressed natural gas (CNG)
CNG molar mass kg/kmol)	18.12
Chamber temperature (K)	295.5
Ambient temperature (K)	295.5
Ambient pressure (bar)	1
Injection pressure (bar)	20,30,40,50,60 (Case 1)
Injection time duration (ms)	25
Varied time duration (ms)	2-26 (Case 2)

3.6 Vehicle Speed-Sweep Test Using Chassis Dynamometer

The prototyped vehicles are tested using chassis dynamometers. This section presents the vehicle baseline specification, the modification made on the prototype vehicle and the experimental setup of the testing. This study proposes the use of a speed-sweep test procedure to reduce the test points. The speed sweep test procedure implied that the vehicle test is performed in an acceleration mode. It is comparable to the quarter-

mile acceleration test except that the start and stop test limit used is the engine speed and not the travelled distance.

3.6.1 The HPDI-CNG Prototype Vehicle Specification

Table 3.9 presents the specification of the baseline vehicle converted to run on the CNG. The car is made of Proton, modelled Gen2 which is powered by 1.6 litres 4-cylinder inline spark-ignition engine named Campro. Each cylinder is designed with two intake valves and two exhaust valves. The engine is powered by a sequential multi-point injection (MPI) system. In the port injection gasoline version, the vehicle's top speed is 190 km/h, whereas the maximum power is 82 kW at 6000 rpm. The maximum torque is produced at 4000 rpm with a value of 148 Nm.

3.6.2 Modification of Cylinder Head for Direct Injection CNG

Modifications of the cylinder head are compulsory for the conversion of a CNG-DI engine. The physical changes were completed in the previous stage of the project. Based on the observation, a major consideration during the conversion is to minimize the modification made to the original engine configuration. But a crucial modification on the engine's cylinder head is inevitable to provide sufficient spaces for the new direct injector. The second challenge is the new combustion system was expected to be designed to produce a swirling charge flow where the high-pressure injector is located at the side location of the cylinder. It is different from a standard GDI engine, where tumble and squish flow motion is designed as the main flow structure. Figure 3.10 presents the schematic configuration of the new CNG direct injectors, which utilised a side-positioned cylindrical throat geometry that protrude into the combustion chamber. Each of the injectors itself is fixed by an external bracket. The bracket was located separately from the engine body.

Table 3.9 Specification of the vehicle and engine used for HPDI-CNG conversion

Engine Specification	
Code name	S4P
Type	In-line 4 cylinders, DOHC, 4 valves per cylinder
Bore/stroke	76/78 mm
Displacement	1597 cc
Compression ratio	10:1
Fuel delivery	Multipoint EFI
Fuel cut-off point	7000 rpm
ECU	Proton EMS700
Engine dimensions	581 mm (L) x 605 mm (H) x 650 mm(W)
Benchmarked Performance	
Top speed	190 km/h (Auto=185 km/h)
0 – 100 km/h	10.5 secs (Auto=13.0 secs)
Fuel consumption at constant 90 km/h	17.1 kms per litre/48.9 mpg (Auto= 15.9 kms, 45.5 mpg)
Max power	82 kW/110 bhp @ 6000 rpm
Max torque	148 Nm @ 4000 rpm

Source: S4P Service Manual (2004)

Figure 3.11 presents the actual arrangement of the direct injectors after the modification. It is visible how the injector protruded the engine combustion chamber from the side position. From the outer view, the direct injectors for CNG were located just below the intake manifold. The electrical connections of the ECU to the injectors were made interchangeable for either CNG or gasoline operation. The CNG injection system has utilised four units of high capacity GDI injectors made of Bosch to supply the CNG fuel directly into the cylinder. The CNG and gasoline injectors are governed by the same electronic control unit (ECU). The gasoline injectors are saturated type, and CNG injectors are peak and hold injectors. The maximum ECU current (saturated current) is limited to 8 Amp in order to support the peak and hold injectors at 12 Volt voltage. The saturated injector has high impedance and thus produces a much lower current than peak and hold injectors.

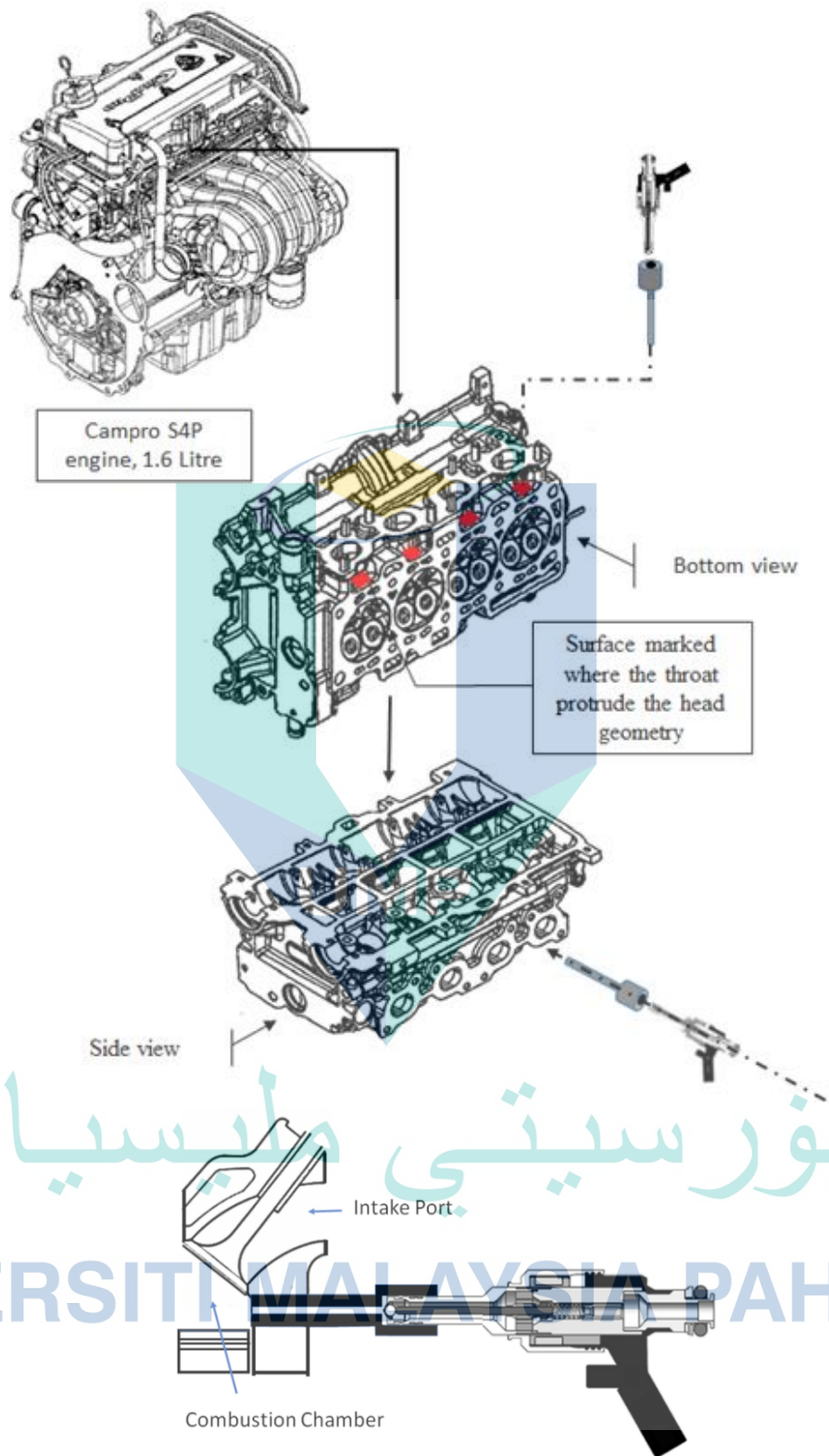


Figure 3.10 Schematic of HPDI-CNG system configuration with added fuel path
 Source: S4P Service Manual (2004)

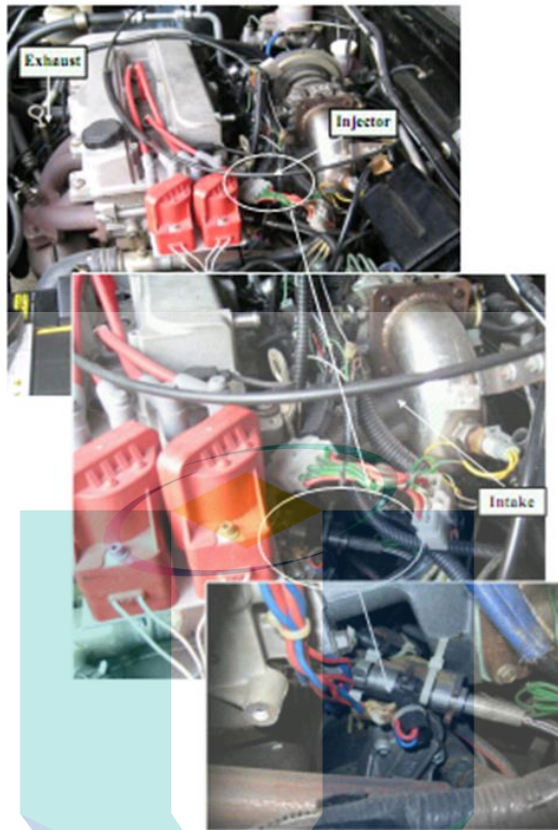


Figure 3.11 The actual configuration of the HPDI- CNG system

The CNG fuel storage is located externally from the vehicle. The system includes the tank pressure gauge, the delivery pressure gauge and regulator, the filling valve, the purge valve and the supply shut off valve. The delivery pressure regulator is used to control the supply pressure of CNG gas to the gaseous fuel common rail. The valve is manually regulated, becoming a true challenge to select the most appropriate pressure setup for the vehicle/engine. Up to this stage, by the combined use of the unique direct fuel injection concept and pressure regulation, the combustion can be sustained at a pressure setup of 45 bar – 60 bar only. Beyond the stated range, the engine/vehicle driving becoming highly sluggish and jerking. Therefore, throughout the study, the pressure setups of 45 bar, 50 bar, 55 bar, and 60 bar were chosen to become the adjustable variables during the testing. Since the current injection pressure is higher than 20 bar, this direct-injection configuration is called a high-pressure direct-injection CNG (HPDI-CNG) engine. The present injection pressure is higher than the pressure setup in previous studies (Abdullah, Kurniawan, Ali, & Mohamad, n.d.; Aziz, Firmansyah, & Shahzad, 2010; Kalam & Masjuki, 2011; Mohamad & Geok, 2008)

The original Proton EMS700 ECU has been replaced with a new programmable ECU made of Haltech, model E8. The Haltech E8 ECU is used to control both the gasoline and CNG injector and the spark ignition unit. **APPENDIX F** provides a detailed specification of the Haltech ECU. The critical stage during the development of the HPDI-CNG is the tuning of the base map. The base maps here consist of the ignition timing, the injection duration, and injection timing maps. The base maps tuning process was completed in the project's first phase by an ECU tuning specialist using a traditional method. The traditional calibration involves constant speed or load testing at each operating point. The specialist, based on his experience, have tuned every control parameter to obtain optimum engine performance. It is essential to highlight that the current study is executed with the assuming that the ECU base maps have been tuned to their best limit in the earlier phase of the project. Therefore, this study is primarily carried out because there is a need to reduce the test point further, improving the calibration method while searching for an additional chance of performance improvement.

3.6.3 Experimental Setup

3.6.3.1 The Two-Wheel Chassis Dynamometer

The chassis dynamometer used in the study is a Mustang MD250, with inertia weight, as presented by Figure 3.12. The dynamometer is utilised in the first stage of the study. It is the most critical instrumentation throughout the study. The maximum absorbable horsepower of the dynamometer is 1118.55 kW. The maximum lateral speed of the dynamometer is about 281.635 km/h. The output from the chassis dynamometer includes the component of torque, power, vehicle speed, vehicle acceleration, engine rotational speed, and roller speed. The data from the dynamometer are measured and calculated continuously, and the data resolution is fully adjustable. The interface of the dynamometer controller to the data-logging PC is made possible by the use of interface software named PowerDyne. **APPENDIX E** provides detailed dynamometer specifications.

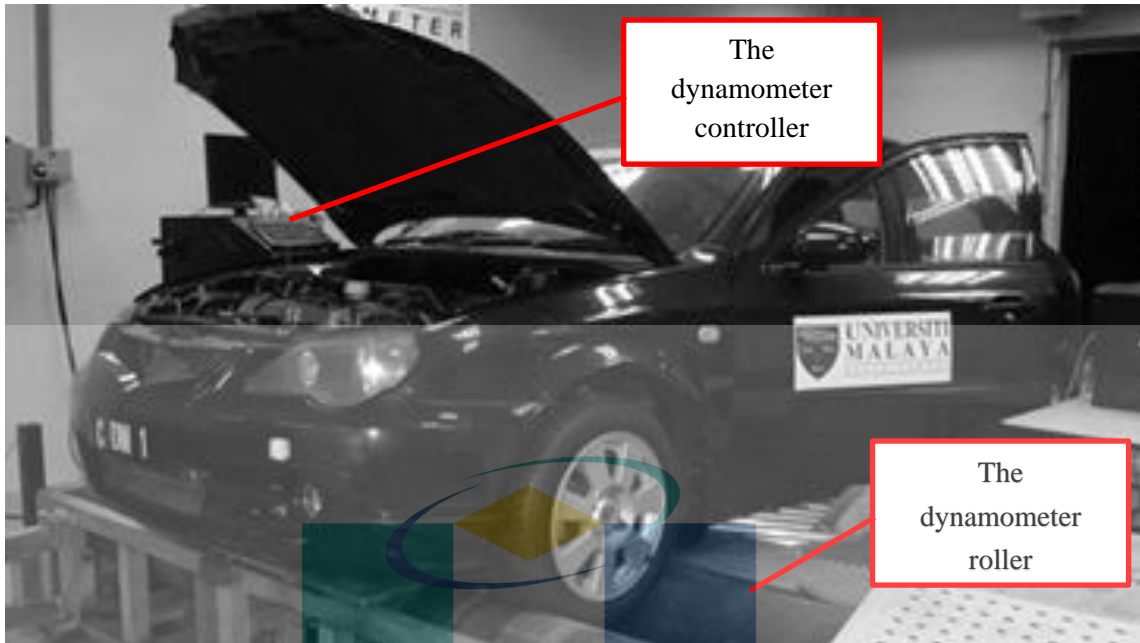


Figure 3.12 The actual HPDI-CNG vehicle on the chassis dynamometer

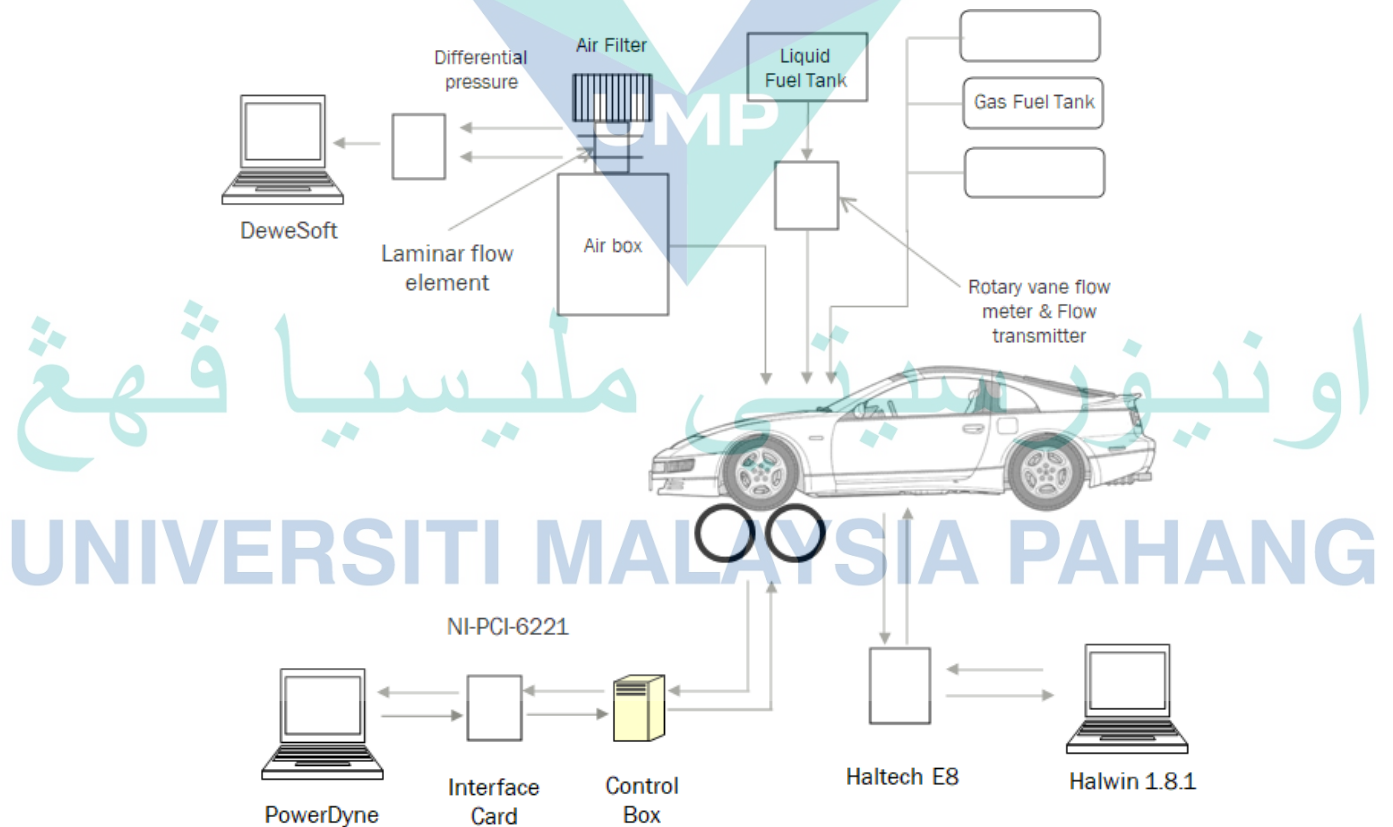


Figure 3.13 The schematic of the data acquisition system and the test layout

Figure 3.13 presents a schematic of the data acquisition system and a test layout for the chassis dynamometer test. There are two main instruments in use on the dynamometer: a load cell as torque sensor and a roller rotational speed sensor. The load cell is calibrated with a standard weight unit every time the test is made. Necessary steps during this linear calibration process include checking up the length of the calibration arm and the deadweight value correctly, zeroing the reading of the load cell before the calibration process, and calibration spanning over the load cell range, and calculate the load cell sensitivity value. A pickup sensor, magnetic type, is used for roller speed measurement. Both data is vital to determine the value of engine torque. Once the transmission gear ratio is fixed, the system can easily calculate the engine torque through reverse calculation. This calculation is performed by using the relation in Equation 3.63.

$$\text{Engine Torque} = \frac{(\text{Dynamometer Shaft Torque} \times \text{Shaft RPM})}{\text{Engine RPM}} \quad 3.63$$

The engine rotational speed measurement can be performed using a few methods such as analogue rpm input (based on the roller rotational speed), pulse-inductive method and an optical method. This study utilised the pulse-inductive method for engine rotational speed measurement.

The data recording resolution is quite a major factor being considered during the testing. Since there are at least three major instruments used during the test, there must be a synchronisation between the logged data of each device. Hence, the dynamometer data resolution is used as the main reference for the other instruments in the test. The sampling interval of 0.019 was applied to all other measurements. The value is applicable for the ECU and AFR data logger. Finally, measured power and torque were corrected based on the SAE J1349 standard (SAE, 2011). The test code is a standard for power measurement in a spark-ignition engine.

3.6.3.2 The Air Intake Measurement System

The engine's throttle and intake manifold system is connected to a surge tank equipped with a laminar flow element (LFE). This LFE is used initially to measure the mass flow rate of the air intake by using the differential pressure approach. However, it was found out that the use of LFE has resulted in an excessive restriction of the air intake flow, thus lowering the maximum engine torque and power. The unit is finally abandoned

since the tests were carried out in WOT condition. As an alternative, the intake airflow was estimated by using the speed-density method.

3.6.3.3 The Programmable ECU and Data Logging Features

The instantaneous ECU parameters can be monitored and logged by the use of an interface software named Halwin. Almost 20 parameters were monitored and logged from the ECU in each test. Among the parameters are engine speed, injection duration, ignition timing, injection timing, injector duty cycle, coolant temperature, air intake temperature, throttle position, intake air manifold absolute pressure, correction factors, etc. The ECU parameters are critical since the study intends to analyse the effect of the ECU parameters on the vehicle output. The study proposes to optimise these ECU parameters to maximise engine performance.

3.6.3.4 The Portable Air to Fuel Ratio Meter

There are two types of AFR measurement methods; the first is based on exhaust analysis, and another method is based on the direct measurement of air and fuel mass. In the current study, the AFR data is measured based on exhaust gas analysis. The Innovate AFR meter has been used for AFR measurement. **APPENDIX G** provides a detailed specification of Innovate AFR meter. The location of the oxygen sensor used is placed before the three-way catalytic converter (TWCC) in order to avoid alteration in the gas composition.

The use of TWCC in original vehicle specification requires the engine to be operated in stoichiometric AFR for maximum TWCC conversion efficiency. This is assisted by the feedback function of AFR measurement data to the ECU. However, the feedback function was turned off, and the ECU was operated in a complete feedforward control strategy. The study truly concentrates on the engine's performance due to the installation of the new direct injection of CNG. Hence, it is important to avoid any ECU corrective function interference during the measurement.

3.6.3.5 The Speed-Sweep Test Procedure

The current study intended to minimise the number of operating test points. Therefore, the speed-sweep test procedure has been selected as the test method. This

method offers a very significant advantage over other test methods since the torque curve or the power curve can be produced instantly when the engine speed is allowed to sweep across the engine's operating range in a single run. If the engine is operated at WOT condition, the engine's maximum performance shall be obtained. The speed-sweep test method requires some information on the tested vehicle, such as the vehicle mass and the engine power at 50 mph. The vehicle simulation loading mode will most accurately reflect the actual power that the vehicle will deliver in use (Mustang, 2005).

The current study has imposed the vehicle simulation-loading mode during the test procedure. The tester needs to define start speed, equal to the lowest speed at which the vehicle runs in the selected test gear (if single-gear testing is to be performed). The *stop speed* is equal to the highest speed at which the vehicle is to be tested. This should be the highest speed at which the vehicle can be operated in the test gear. In the current study, the start speed and stop speed are equal to 25 km/h and 40 km/h, respectively. The selection of the values is made based on the lateral speed range of the vehicle examined before the actual test. The maximum throttle opening tested is 100%, equal to the WOT condition.

In brief, during the testing, the vehicle may be started from a still condition at idling mode. When the driver pushes the gas pedal until the desired throttle opening, the vehicle will accelerate, passing the start speed, and the vehicle speed continuously sweeps throughout the test window until the stop speed is achieved. During the test window, the force acting on the load cell and the dynamometer roller speed will be recorded. These data, along with the engine rotational speed, will be used to determine the engine brake torque. The calculation is performed in a backward manner by the dynamometer controller.

3.6.4 Data Collection Procedure

The experimental data collection was carried out by testing the prototype vehicle on a chassis dynamometer using the speed-sweep test procedure. Based on the procedure, the collected data can be categorized based on the four primary sources, which are the 1) dynamometer, 2) ECU, 3) intake airflow, and (4) AFR meter data. It is quite important to state that the intake airflow data collection was incomplete as the air intake unit could

only supply sufficient air at part-opened throttle opening. Therefore, only the three categories of data are considered in the current analysis at a wide-opened throttle opening.

Initially, a total of 55 variables are available from the data acquisition unit employed during the testing. After selection, about fifteen variables have been used for the modelling purpose. The selection was made based on the literature, the sensitivity analysis conducted on the analytical model of the HPDI-CNG engine performed in the previous stage, and correlation analysis. Generally, in comparison with steady-state engine modelling, transient engine modelling required a greater number of inputs. Some of them are required to represent the rate of change of primary input with time, for example, the rate of change of throttle opening angle and the vehicle acceleration. These two variables are highly correlated with the engine's brake torque. The model is designed to consist of the engine brake torque as the output response, and the rest of the fourteen variables are becoming the input factor.

3.7 Model-based Calibration of ECU Parameters

The data-driven modelling technique provided by MBC Toolbox is widely validated for a steady-state engine's modelling and calibration. This study had proposed a transient engine response modelling by using transient engine data. The transient engine model is expected to be more realistic and more representative of actual engine characteristics during actual driving conditions. The transient models are then used as the basis for the optimization-based calibration of the engine ECU maps. Hence, one important question here is whether the toolbox, particularly the MLP-ANN technique is applicable for the transient engine modelling.

3.7.1 Correlation Study between Engine Torque with Other Engine Parameters

A correlation study was conducted with the purpose of 1) to rank the parameters based on the degree of influences or the correlational strength with the engine brake torque output. This is to determine the sequence of inputs to the model. Table 3.10 presents the list of variables selected for the correlational study.

Table 3.10 Selected variables for correlation analysis

Engine parameters	Symbols
Acceleration	a
Injection pressure	p_{inj}
Barometric pressure	p_{baro}
Air to fuel ratio	AFR
Coolant temperature	T_{cool}
Manifold abs. Pressure,	MAP
Throttle position	θ_{thr}
Ignition timing	t_{ign}
Duty cycle,	DC
Air temperature	T_{air}
Throttle position rate	$\dot{\theta}_{thr}$
Injection timing	t_{inj}
Injection duration	t_{dur}
Engine speed	$\dot{\theta}$
Vehicle speed	V_{veh}

3.7.2 Selection of Model Types for ECU Calibration

There are two types of models offered by the Model Browser in the MBC Toolbox. The first is 1) the one-stage model, and the second is 2) the two-stage model. The one-stage model directly relates the output to the list of model inputs. It fits a model to all the data in one process. The second stage model (or point to point model) fits the model in dual-stage processes where the model consists of local and global models. A specific model is developed at each operating point which is called the local model. Based on these local models, a global model is produced.

The current study is focused on measuring and modelling the torque response of the engine when a ramp input is provided to the throttle pedal. Therefore, based on the data and the nature of the data collection process, the one-stage model is more appropriate for modelling engine brake torque response. While the number of inputs and output are retained, the modelling technique used to relate the input and output data can be changed and evaluated for the best accuracies.

3.7.3 Artificial Neural Network and Optimization of Network Structure

Data-driven modelling was proposed to compensate for the drawback of the analytical model developed earlier in the study. The analytical model cannot capture the abnormal phenomena in the actual HPDI-CNG engine operation; hence it only provided an ideal prediction of engine processes. Contrary to the analytical model, the data-driven modelling did not require intermediate processes and only focused on the input and output changes. Determination of the relationship between the input and output is purely statistical and did not reflect the intermediate processes and variables. It was decided that the MLP-ANN has been chosen for the optimization calibration purpose.

3.7.3.1 Network Optimization Definition

The structure of the ANN model of the HPDI engine has been optimized by using the MBC toolbox. The objective function of the optimisation problem accounted for two important characteristics of ANN topologies. Namely, the total number of neurons ($TNEU = HL1 + HL2$) and the root mean square error (RMSE). The RMSE is divided into two types: the training RMSE and the validation RMSE (VRMSE). The HL1 and HL2 are the numbers of neurons in the first and second hidden layers, respectively.

In order to solve the optimum structure problem, multiple RMSE and VRMSE predictions were modelled by using a few combinations of neurons in the first and second hidden layers. Based on RMSE, VRMSE and TNEU, error models were developed for both the RMSE and VRMSE. Both are modelled using the Radial Basis Function (RBF) technique since it gives the lowest RMSE. The TNEU is defined as a function model in the MBC toolbox. Hence, the optimisation problem is defined as the multi-objective optimisation problem; to minimise the RMSE, VRMSE and TNEU function model. The optimisation algorithm of Normal Boundary Intersection (NBI) was used to perform the optimisation process.

Therefore, the objective functions are defined as:

1. Objective 1: Minimize RMSE
2. Objective 2: Minimize VRMSE
3. Objective 3: Minimize TNEU

The optimisation problem constraints are defined as:

1. Constraint 1: $1 \leq HL1 \leq 40$
2. Constraint 2: $1 \leq HL2 \leq 40$
3. Constraint 3: $RMSE \leq 2$
4. Constraint 4: $VRMSE \leq 4$

Matlab's Neural Net Toolbox manual (MathWorks, 2015) states if the RMSE on the training set is good, but the test set RMSE is significantly worse indicates an overfitting condition. Furthermore, the suggested steps are to reduce the number of neurons to improve the results. However, if training performance is poor, increasing the number of neurons might improve modelling accuracy. It might be easy when considering a single layer, but the judgment will become harder when more than one hidden layer involves.

3.7.3.2 Network Optimization Setup

The Normal Boundary Intersection (NBI) method is an algorithm proposed to find Pareto optimal points for the optimal network optimisation. The advantage of the NBI technique compared to the continuation-type algorithm is it can handle more than two objectives while retaining the computational efficiency of the continuation-type algorithm (Das & Dennis, 1998). The default setup of the NBI algorithm was used and given in Table 3.11.

Table 3.11 The default setup of NBI solver for the optimisation study

Parameters	Setup
Trade-off points per objective pair	10
Shadow minima option	
Display	final
Constraint optimisation algorithm	Active-set
Maximum iteration	2000
Maximum function evaluations	10000
Function tolerance	1×10^{-6}
Variable tolerance	1×10^{-6}
Constraint tolerance	1×10^{-6}
NBI subproblem option	
Display	iter
Constraint optimisation algorithm	Active-set
Maximum iterations	2000
Maximum function evaluations	10000
Function tolerance	1×10^{-6}
Variable tolerance	1×10^{-6}
Constraint tolerance	1×10^{-6}

Source: MathWorks (2018)

3.7.4 Definition of ECU Optimization Maps

The ECU maps or look-up tables were defined in CAGE. Figure 3.14 presents an example of maps with zero-initialized values for all operating points. The X and Y-axis norm were engine rotational speed, RPM and manifold absolute pressure, MAP, respectively. These variables are selected to resemble the actual maps in the ECU. In the study, there are three free variables and nine fixed variables. Therefore, three free variable's lookup tables were created, and the other nine variables were set as constant. The three free variables are the injection duration, the injection timing and the ignition timing. The vertical axis in Figure 3.14 could be either one of these three variables.

It is noticeable from Figure 3.14 that the axis of rpm and manifold absolute pressure is out of the common range for a typical natural aspirated internal combustion engine. The maximum engine speed for a standard vehicle of a four-cylinder engine might exceed 7000 rpm, and the range of MAP is within -90 kPa to 4 kPa. It is because the optimisation work proposed in this study is limited to the measured operating range of the engine, which was achievable and recorded during the speed-sweep test procedure at the earlier stage. The measured maximum engine speed was about 3000 rpm. In comparison, the manifold pressure would not have exceeded -90 kPa since the test was

started from a running vehicle in the third gear. Overall, when the data was recorded, the vehicle speed range was between 25 km/h to 40 km/h.

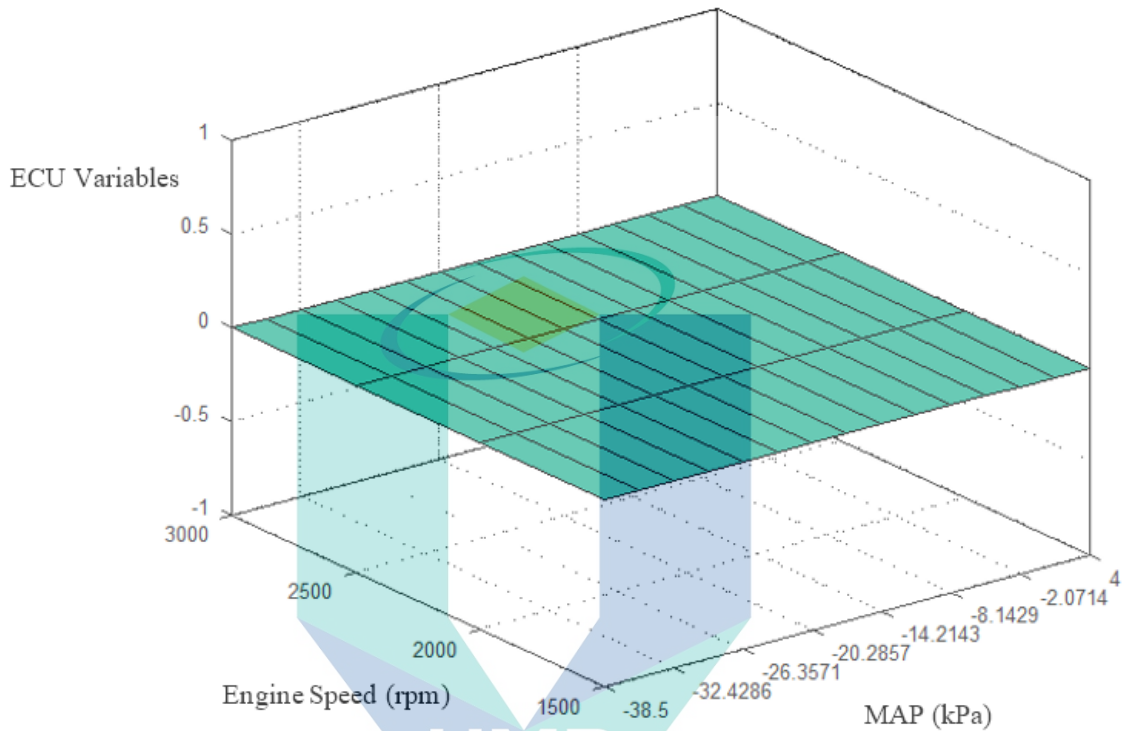


Figure 3.14 The surface plot of the ECU maps when initialised with zero values

3.7.5 Objective Function for the Optimization Based Calibration

The objective function is vital since it determines the results of the optimisation. The first option is to directly use the brake torque response model (imported from Model Browser) as the objective function. This method is applicable, as demonstrated by (Guo et al., 2017; P. Wong et al., 2012). The second option is to use the term for brake power (BP), as demonstrated by (Z. Yang et al., 2008). The last option is to use the normalised term of fuel consumption or the brake specific fuel consumption (BSFC), as demonstrated by (Senecal et al., 2000). The following expression provides the equation which defines the brake power and the brake specific fuel consumption:

$$P_b = \frac{2\pi NT_b}{60} \quad 3.64$$

$$BSFC = \frac{\dot{m}_{fuel}}{P_b} \quad 3.65$$

There are three utmost important performance considerations: torque or power, fuel consumption, and exhaust gas emission. The emission data is not available; hence, the emission factor is not considered. The minimisation of BSFC has been selected as the optimisation problem objective since its combined two main goals; either maximising the power or minimising the fuel consumption. The optimisation objectives were produced for different injection pressure setups: 45 bar, 50 bar, 55 bar, and 60 bar. The BSFC function required additional functions, which are the averaged CNG consumption rate. This study employed functions based on the injection mass flow rate at 45, 50, 55 and 60 bar injection pressure, respectively. The mass flow rate quantities were measured and calculated from the independent injector testing.

The optimization-calibration objective function can be written as:

$$\text{Minimization of BSFC} = f(P_b, \dot{m}_{fuel}) \quad 3.66$$

where

P_b is given by Equation 3.64 and T_b terms (in Equation 3.64) is given by Equation 3.67. This function is the torque function modelled by the Model Browser based on the initial data collected in the study.

$$T_b = f(a, p_{inj}, p_{baro}, AFR, T_{cool}, MAP, \theta_{thr}, t_{ign}, DC, T_{air}, \dot{\theta}_{thr}, t_{inj}, t_{dur}, \dot{\theta}, V_{veh}) \quad 3.67$$

UNIVERSITI MALAYSIA PAHANG

3.7.6 Selection of Optimization Constraint

One of the crucial requirements affecting the success of optimisation is the definition of optimisation constraint. The constraint type used in the study is the range of each variable, but the more critical is the free variable range. Based on the practical experience during the verification testing of the optimal setup, inappropriate selection of the variable range had resulted in a sluggish and jerking motion of the vehicle. In brief, the optimized results are not feasible to be used in actual operation.

The selected constraint provided in Table 3.12 was considered the best range for each free variable suited to the current engine condition. Based on the table, for the optimisation to be workable in real hardware, the limits for the optimisation must not be selected as a single set of values for the whole operating range. However, the limits must be selected based on the specific operating point. In the current study, for the existing operating range, each variable's upper and lower limits were determined based on engine rotational speed. The range values were determined based on the observation of the measured maximum and minimum variable values at $1500 \pm 100 \text{ rpm}$, $2000 \pm 100 \text{ rpm}$, $2500 \pm 100 \text{ rpm}$ and $3000 \pm 100 \text{ rpm}$ in all tested cases.

Table 3.12 The optimisation constraint for the free variables

Engine Speed	Free Variables	Variables Range
1500	t_{ign}	$12.4 \leq t_{ign} \leq 14.1$
	t_{inj}	$473.6 \leq t_{inj} \leq 473.7$
	t_{dur}	$16.173 \leq t_{dur} \leq 19.971$
2000	t_{ign}	$12.6 \leq t_{ign} \leq 15.8$
	t_{inj}	$473.8 \leq t_{inj} \leq 481.7$
	t_{dur}	$15.679 \leq t_{dur} \leq 19.473$
2500	t_{ign}	$14.7 \leq t_{ign} \leq 20.2$
	t_{inj}	$481.1 \leq t_{inj} \leq 489.1$
	t_{dur}	$16.739 \leq t_{dur} \leq 19.091$
3000	t_{ign}	$21.7 \leq t_{ign} \leq 23$
	t_{inj}	$504.6 \leq t_{inj} \leq 515.3$
	t_{dur}	$15.939 \leq t_{dur} \leq 17.445$

3.7.7 Fixed Variables Setup

The fixed variables were given constant values throughout the optimisation process except for the engine speed and MAP. Table 3.13 presents the fixed variables and associated setpoint values for the optimisation problem. The setpoint values are the median for each variable based on measured data. The value of engine speed and MAP are varied in a predetermined order based on the lookup tables setup.

Table 3.13 Example of fixed variables setup for 45 bar case

Parameters	Setpoint Values
Vehicle acceleration, (km/s)	0.534
Injection pressure (bar)	45
Barometric Pressure (kPa)	1021.535
AFR	13.03
Coolant temperature (°C)	71.45
Manifold absolute pressure (kPa)	-38.5
Throttle position (deg)	100
Duty cycle (%)	60.25
Air temperature (°C)	43.75
Throttle positioning rate (deg/s)	9.7

3.7.8 Genetic Algorithm (GA) Operators Setup

There are two model options for multi-objective optimisation: Non-Intersection Boundary (NBI) and Multi-Objective Genetic Algorithm. Most of the time, the Multi-Objective Genetic Algorithm works better than NBI methods. This study focuses on a single-objective optimisation problem. The standard algorithm (GA) has been selected as the sole method for the constraint optimisation problem of ECU maps. Table 3.14 presents the GA operator and parameter setup used throughout the study. The setup was chosen with the purpose to maximise efficiency and accuracy. This setup was produced based on a repetitive optimisation process and compared with previous studies of a similar optimisation problem.

The optimisation procedure can be performed at a single point per run (point-by-point) or by simultaneous run (sum optimisation). This problem has been executed by the sum approach at each engine speed setup. In addition to increasing the population size and number of generations, the stall time limits and stall generations have been added to 100 s and 100, respectively, to ensure a longer calculation time provided to the solver. For solution accuracy, the function and constraint tolerance has been reduced to 1e-9 and 1e-9, respectively. Figure 3.15 presents the standard procedure for the GA optimisation process.

Table 3.14 The Genetic Algorithm Operators and Parameters

Parameters	Value
Crossover function	Scattered/ Simple Crossover
Crossover fraction	(0.8)/ 80%
Mutation function	Adaptfeasible/ Hybrid Static Gaussian
Selection function	Tournament/ Standard Proportional
Population size	50
Generations	1000
Hybrid function	none
Stall generations	100
Stall time limits	100
Function tolerance	1e-06
Constraint tolerance	1e-06
Time limit	infinity

3.8 Error Quantities for Results Evaluation

The modelling prediction and optimisation quality have been evaluated based on a few calculated error quantities, as presented in Table 3.15.

3.9 Summary of The Chapter

This chapter presents all the techniques, testing procedures and assumptions associated with the study. In the first section, the model equations for analytical injector modelling is presented. The following section explained the model equations for the vehicle analytical model. The model equations mainly represent the dynamic engine processes since the drivetrain are physically model in SimScape. The subsequent section described the independent injector testing for the injector flow calibration. The method and procedure for vehicle testing using a chassis dynamometer are presented in the following section. Next, the chapter presents the model-based calibration procedure using the MBC toolbox. The last section presents the error quantities used in results and discussions. The next chapter presents the results of injector modelling, simulation and its independent testing.

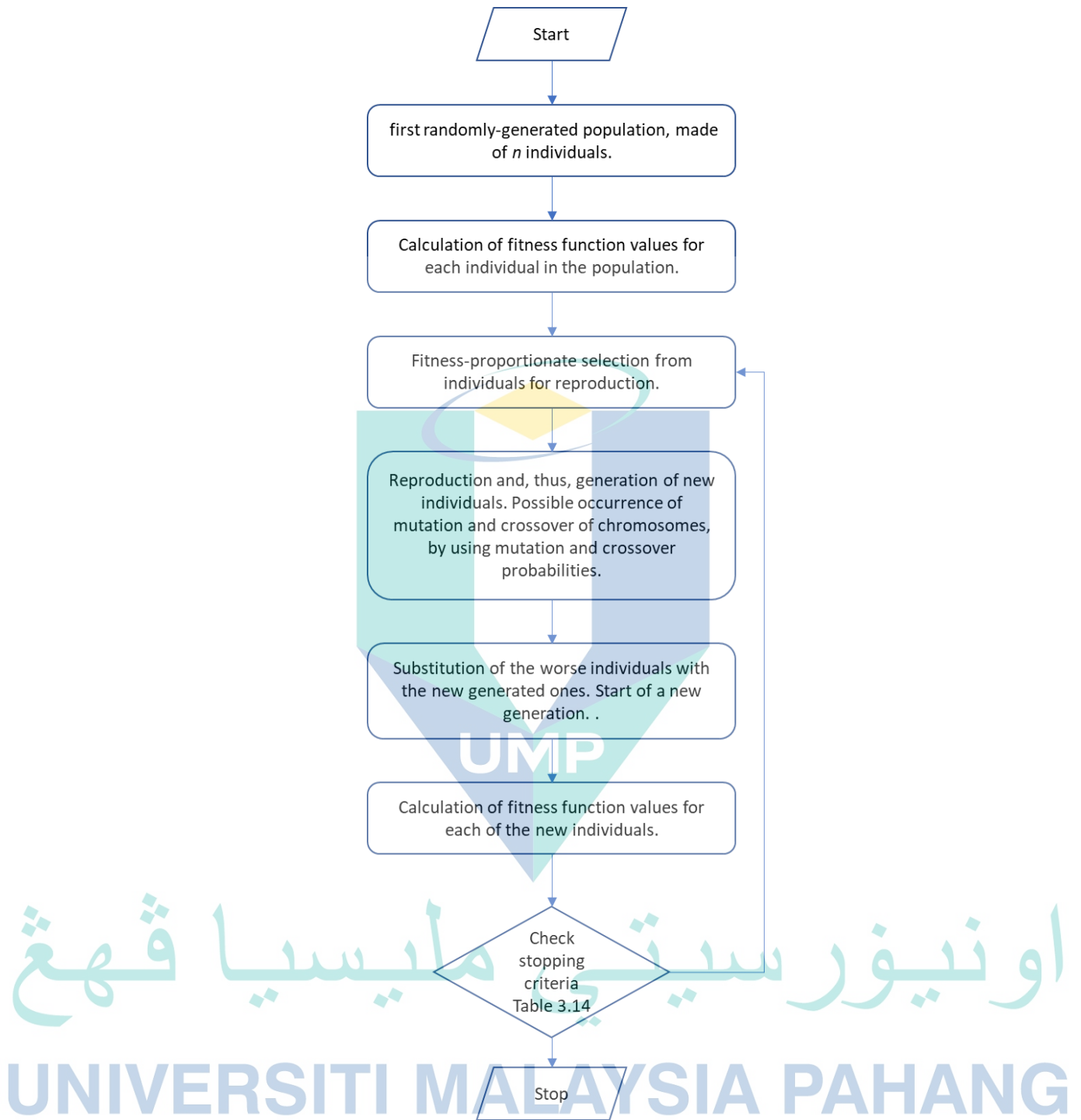


Figure 3.15 Genetic algorithm process flow chart

Table 3.15 Quantities calculated for results evaluation

Pearson correlation formula	$R = \frac{n(\sum xy) - (\sum x)(\sum y)}{\sqrt{[n(\sum x^2) - (\sum x)^2][n(\sum y^2) - (\sum y)^2]}}$	3.68
Sample correlation	$R_{xy} = \frac{S_{xy}}{S_x S_y}$	3.69
	Where S_{xy} : the sample covariance S_x : sample standard deviation S_y : sample standard deviation	
Population correlation	$\rho_{xy} = \frac{\sigma_{xy}}{\sigma_x \sigma_y}$	3.70
	Where σ_{xy} : the population covariance σ_x : population standard deviation σ_y : population standard deviation	
Percentage error	$\text{Absolute error} = x_{\text{predict}} - x_{\text{actual}} $	3.71
	$\text{Percentage error} = \left \frac{x_{\text{predict}} - x_{\text{actual}}}{x_{\text{actual}}} \right \times 100$	3.72
Mean	$\text{Mean}, \mu = \frac{\sum_{i=1}^N x_i}{N}$	3.73
Variance	$\text{Variance}, \sigma^2 = \frac{\sum_{i=1}^N (x_i - \mu)^2}{N - 1}$	3.74
Standard deviation	$\sigma = \sqrt{\sigma^2} = \sqrt{\frac{\sum_{i=1}^N (x_i - \mu)^2}{N - 1}}$	3.75
Coefficient of Variation (CoV)	$\text{CoV} = \frac{\sigma}{\mu}$	3.76
Mean absolute error (MAE)	$\text{MAE} = \frac{1}{n} \sum_{i=1}^n x_i - x $	3.77
Root Mean Square Error (RMSE)	$\text{RMSE} = \sqrt{\frac{\sum_{i=1}^n (x_{\text{predict}} - x_{\text{actual}})^2}{n}}$	3.78
Mean absolute percentage error (MAPE)	$\text{MAPE} = \frac{\sum_{i=1}^n \left \frac{x_{\text{predict}} - x_{\text{actual}}}{x_{\text{actual}}} \right \times 100}{n}$	3.79

CHAPTER 4

RESULTS AND DISCUSSION OF INJECTOR TESTING AND ANALYTICAL SIMULATION

4.1 Introduction

This chapter presents the results and discussion of the injector simulation and testing. The chapter evaluates the injector mass flow rate and assesses its suitability to fulfil engine fuel requirements. Theoretical discussions related to this chapter are presented in Sections 2.3 and 2.5.1.5. Consequently, the related methodologies are presented in Section 3.3 and Section 3.5.

4.2 Independent Injector Testing

The injector testing was performed to measure the injector mass flow rate at different injection pressure and different injection duration. It also covers some observations of the injector characteristics during the testing.

4.2.1 Injector Control Characteristics

The tested injection pressure is in the range of 20 bar to 60 bar, while the injection duration is in the range of 2 ms to 26 ms. Both ranges are selected based on measured pressure and duration in actual HPDI-CNG testing. Throughout the injector testing, it is assumed that the injected mass flow rate is to be equal to the rate of change of mass from the CNG storage tank. Based on Erfan et al. (2015), the injection duration should be less than 50% of the time between pulses. Therefore, in the study, the injection duration cannot exceed 50 ms at a frequency of 8 Hz. However, it was found that the injector has already exceeded 90% of the duty cycle in the actual HPDI-CNG engine operation. The maximum duty cycle recorded for the injector is about 93% at 22 ms at 2820 rpm.

4.2.2 Effect of the Injection Pressure on Mass Flow Rate

Figure 4.1 presents the mean CNG mass flow rate at different injection pressures. Based on the graph, the mass flow rate is found to increase linearly with the injection pressure. The scatter data plot of CNG's mean mass flow rate as a function of injection pressure is best approximated by the equation $\dot{m}_{cng} = 0.0239p_{inj} - 0.182$. However, it is expected that at zero pressure, the mass flow rate of the injector should be equal to zero. Hence, the linear equation is adjusted to intersect the point of zero and produced the corrected equation $\dot{m}_{cng} = 0.0239p_{inj}$. The new equation is expected to represent the actual relation between the mass flow rate and injection pressure. Comparison of the gradient for both graphs shown that there exists a difference of 0.0041 g.bar/s.

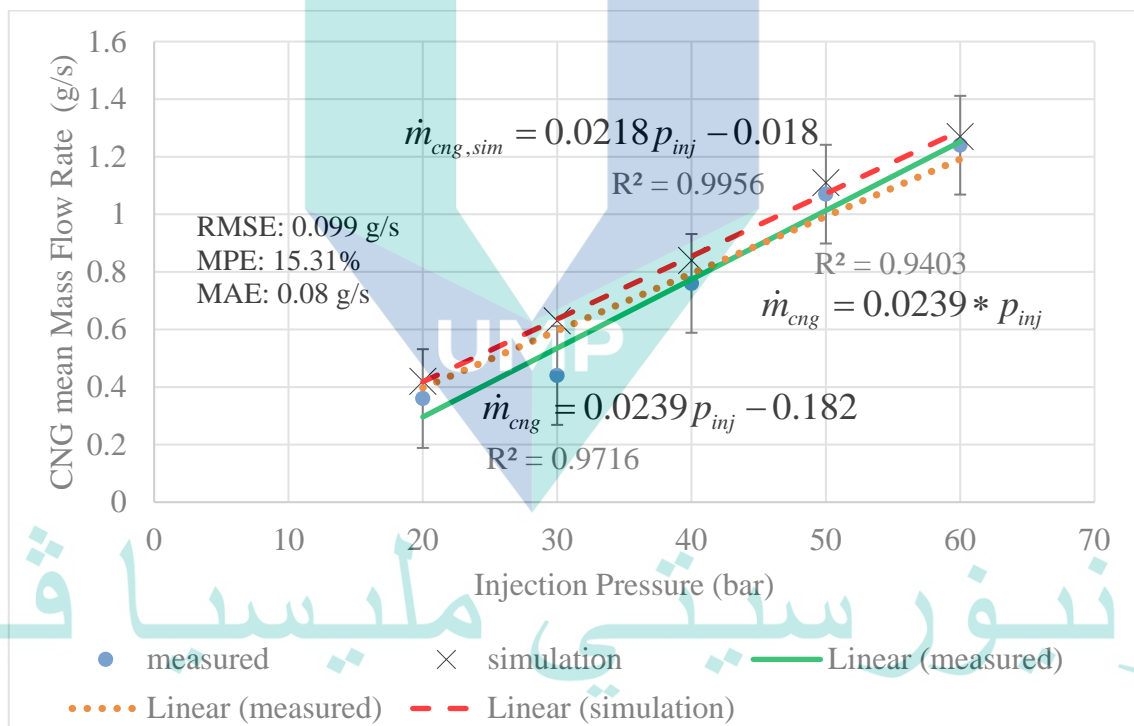


Figure 4.1 Mean mass flow rate of CNG at increased injection pressures

Table 4.1 presents the mean mass flow rate of CNG at the corresponding CNG injection pressure. The injector's maximum and minimum mass flow rate is obtained as a value of 1.24 g/s at the highest injection pressure setup of 60 bar, and 0.36 g/s at the injection pressure of 20 bar. At each data point, a total of 30 data points of the injector mass flow rate were averaged to produce a mean value. Furthermore, each of the data points is produced by performing a total of 1000 injections count. The massive injection

counts are required to provide a measurable CNG tank mass difference due to the low density of CNG gases.

The simulated mass flow rate predicted a higher mass flow rate of CNG compared to the measured data. However, both predict the same trend where the mass flow rate is linearly increased with the injection pressure. It is concluded that the theoretical mass flow rate trend is in agreement with the measured trend. The results support the hypothesis, which states that there is a linear relationship between both parameters. The calculated root mean square error (RMSE), mean percentage (MP), and mean absolute error (MAE) for the comparison are 0.099 g/s, 15.31% and 0.08 g/s higher than the measured data. The error between the measured and simulated data might be contributed by the calculation of the nozzle flow area, which produced a high impact on the calculated values. The discharge coefficient is purely based on the previous study. Since the injector tested is a used injector in the actual vehicle, there is a possibility of the existence of carbon deposits at the nozzle hole, which is hardly detected by naked eyes. The best fit for the simulated data is given by $\dot{m}_{cng,sim} = 0.0218p_{inj} - 0.018$, which has a gradient error of 0.0021 g/s compared to the measured data.

Table 4.1 Tabulated results of injection pressure effect on injector mass flow rate

Injection Pressure (bar)	Mass flow rate (g/s)
20	0.36
30	0.44
40	0.76
50	1.07
60	1.24

Table 4.2 presents the estimated theoretical mass flow rate for stoichiometric operation at various engine speeds. Under a stoichiometric chemical reaction for methane (by assuming methane is the main composition of CNG), we have a stoichiometric fuel-air ratio (FAR) for the engine at about 0.058 or 17.24 of AFR. The required mass of fuel is proportional to the mass of air. By assuming that the engine displacement is 1.6 litre and the average volumetric efficiency of the engine is about 90%, the mass of air for stoichiometric combustion is about 0.36 g. Hence, the required mass of fuel for

stoichiometric combustion is about 0.02g. However, this requirement also needs to consider the engine rotational speed. By considering engine speed, the theoretical fuel requirements are presented in the table based on the method suggested by Erfan et al. (2015).

Table 4.2 Fuel requirement at different engine speed

Engine speed (rpm)	Required mass flow rate (g/s)
1000	0.2
2000	0.4
3000	0.6
4000	0.8
5000	1.0
6000	1.2

Based on the comparison of Table 4.1 and Table 4.2, the maximum requirement of fuel flow rate for a 1.6-litre engine at 6000 rpm is about 1.2 g/s while the minimum requirement is about 0.2 g/s at 1000 rpm (idle speed). Briefly, it seems that the injection pressure and its corresponding mass flow rate suits the engine requirement at all engine speed if the engine needs to be operated in stoichiometric combustion. However, the engine might require a richer mixture at a high load to produce higher torque to overcome the higher load. In addition, the injection pressure must be made entirely variable with the engine speed and load in order to meet the engine control strategy. Thus, it can be concluded that the injector mass flow rate measured from the standalone test only surpassed the engine requirement for stoichiometric combustion.

Based on the observation, the reductions of storage tank mass against injection time are more uniform at higher injection pressure than the low injection pressure. These indicate that there are fewer fluctuations of average mass flow rate at high injection pressure. This fluctuation is mainly contributed by the action and reaction of the solenoid forces, the moving armature, the spring, and the cylinder wall stopper inside the injector, which introduce vibrations when both the moving and stationary components collided. However, at high injection pressure, these oscillations are slightly reduced as the high pressure of gases produced a higher damping force on the moving parts. All those parameters such as the spring, needle valve and armature are assembled together as one

assembly. It interacts with the solenoid force and the stopper and creates vibrational effects. The vibrational effect is the main cause of the fuel supply inconsistencies.

Boretti & Watson (2009) utilised GT-Fuel, a simulation to compute the injector flow rate at different fuel injection pressure and temperature. With an engine speed of 6000 rpm at WOT condition, at CNG injection pressure of 22 bar while injection temperature is 300 K, the direct gas injector can produce 9 g/s - 22 g/s. Douailler et al. (2011) conducted a study to evaluate the potential of a direct injection spark ignition engine based on a Diesel engine platform. The solenoid valve injection system is a prototype injector developed by Orbital. In the range of injection pressure of 13 bar to 29 bar, and downstream nozzle pressure in between 0.3 bar to 2.5 bar, the injector produced a mass flow rate of CNG in the range 4.43 g/s to 11.47 g/s. they tested the injector for a variety of engine capacities in the range of 365 cm³ to 2000 cm³ engine.

Song et al. (2017) analyse a methane direct-injection engine's performance under various fuel injection timings and injection pressures. A single-cylinder optical engine was used to acquire in-cylinder pressure data and flame images. An outward-opening injector was installed at the centre of the cylinder head. The engine capacity is about 338 cm³ and the injector mass flow rate is measured at 5.19 g/s. Zhang et al. (2014) simulate the CNG flow through a direct injector nozzle with the purpose to investigate the pressure distribution around the nozzle and pintle valve during the pintle opening event. In order to ensure the accuracy of this fluid model, mass flow rates between calculated and measured data were compared at different inlet pressures. The CNG injection pressure is in the range of 20 bar to 200 bar. And the predicted mass flow rate through the injector nozzle is in the range of 5 g/s to 14 g/s.

Based on the results (Song et al., 2017; Zhang et al., 2014), it is very conclusive to say that the current injector mass flow rate is very low compared to the specification of the CNG direct injector provided in the literature. A high flow rate injector is essential to ensure the injector is operated at a short injection duration, thus hindering the overloading on the solenoid driver. If a low flow rate injector is used, to obtain a comparable amount of fuel, the injector needs to be operated at a long injection duration which increased the injector duty cycle and might cause overheat of the solenoid.

A CFD simulation by Lei et al. (2019) produced a comparable mass flow rate of the CNG injector when CNG injection pressure in the range of 0.1 bar to 10 bar is used. The mass flow rate produced by the injector is in the range of 0.9 g/s to 1.0 g/s. Erfan et al. (2015) however produced a lower mass flow rate compared to the current results even though they are using a comparable CNG injection pressure in the range of 30 bar - 40 bar. The injector only managed to produce a flow rate of CNG in the range of 0.0852 g/s to 0.152 g/s. It is too lower compared to the current results. Erfan et al. used the same single-hole injector specification compared to the current study. Zhang et al. also using a similar injector model but with a different variation of the nozzle hole number. Thus, it may be further concluded that the single hole, direct injector such as the one used in the current study is a high-pressure (up to 200 bar) but moderate flow rate type. This specification may be suited for gasoline engine application for its higher energy density but inappropriate for the use of CNG fuel. Plus, in GDI application, the high-pressure fuel supplied is very critical for liquid fuel atomization.

4.2.3 Effect of Injection Duration on Mass Flow Rate

The injector is operated by varying the injection duration from 2 to 26 ms at an injection pressure of 50 bar, and injection frequency of 8 Hz. The results are calculated by taking the mass flow rate at each injection duration setup. At each injection duration, a total of 1000 injection counts is performed to obtain a measurable difference of CNG storage tank mass. Based on Figure 4.2, the averaged mass flow rate of the injector is found to fluctuate at the overall injection duration setup. The maximum and minimum mass flow rates are 1.33 g/s and 0.2 g/s, respectively. However, the mass flow rate trend line (the green line) shows that the averaged mass flow rate poses a linear trend with a constant mass flow rate at about 0.75 g/s against the increased injection duration.

It is initially expected that the mass flow rate is close to 1.07 g/s as in Case 1 for injection pressure of 50 bar. But the expectation deviates based on the measured data. The highly fluctuated mass flow rates have occurred, especially at short injection duration. As the injection duration increased, the degree of fluctuation is reduced. Based on the results, the fluctuation is due to a collision between the needle valve and the needle seat. The collision has caused severe vibration during the opening and closing of the nozzle hole, introducing an inconsistent flow area at the nozzle throat.

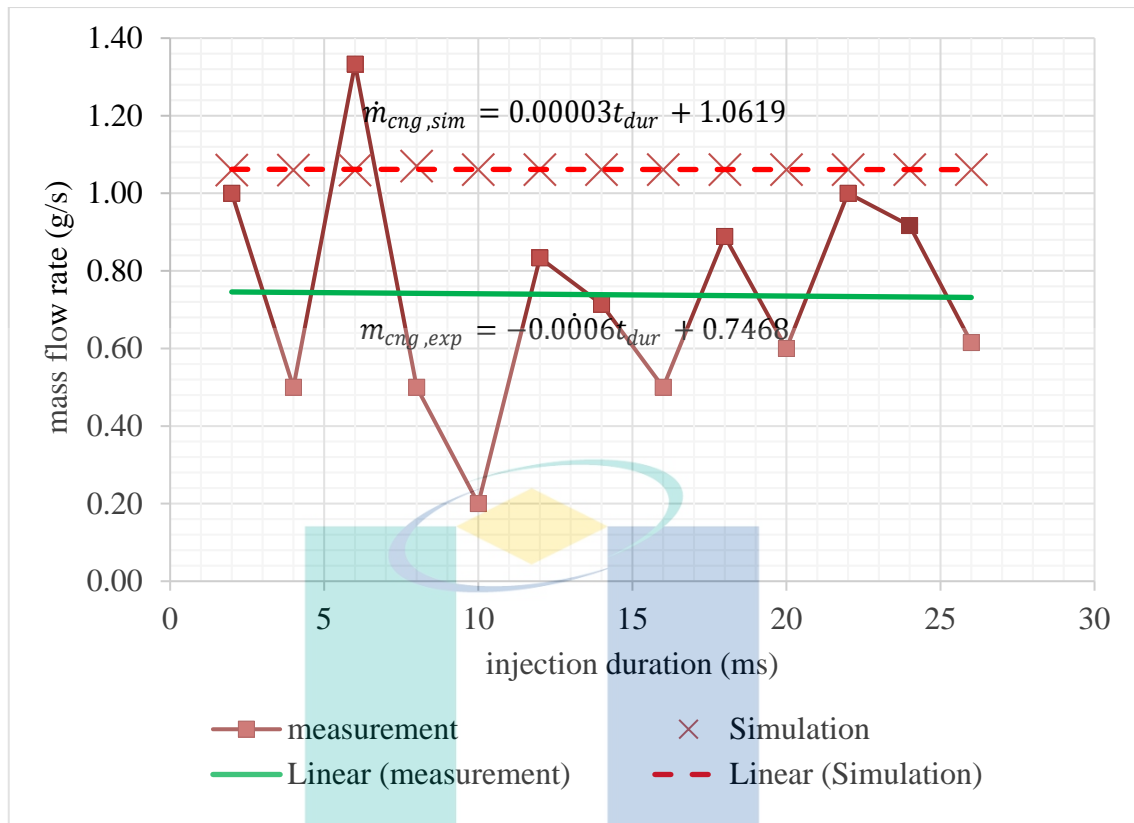


Figure 4.2 The mass flow rate of CNG at an increased injection duration

Cammalleri, Pipitone, Beccari, & Genchi (2013) have identified the existence of a nonlinear zone in the injected mass diagram of a common gas injector. The nonlinearities arise by the injector outflow area variation caused by the needle impacts and bounces during the opening and closing transients and may seriously compromise the mixture quality control, thus increasing both fuel consumption and pollutant emissions. A common finding between the previous study with the current results is that the fluctuation of the injected mass is significant at the minimum injection duration. As the injection duration is increased, the pulsation of the injected mass is reduced, and the mass increment as a function of injection duration became linear again. This supports the suggestion that the fluctuation is affected by the dynamic interaction between the needle valve and the needle seat, which caused severe bouncing and incomplete closing and opening of the injector.

In a consecutive work, Beccari et al. (2014) performed a model-based optimization on the driver signal in order to reduce the non-linearities in the short injection duration regime. They employed multiple injection and *peak and hold* injection

strategies on the injector drive signal. Both methods are proven to be effective in damping the injected mass pulsation in the non-linearities region.

The analytical model of the injector predicted an almost constant CNG mass flow rate at increased injection duration. The simulated data points are well fitted by a linear equation of $\dot{m}_{cng,sim} = 0.00003t_{dur} + 1.0619$. At the y-axis intersection, the simulation trendline gives a mass flow rate of 1.0619 g/s. If the measured data are fitted by a linear equation produced by the theoretical results, the best linear equation to represent the measured data is given by $m_{cng,exp} = -0.0006t_{dur} + 0.7468$. Thus, the simulated mass flow rate is overpredicted by the measured data with an estimated error of 0.31 g/s. It is equal to 41.33% higher than the measured data.

Based on the simulated results, it is concluded that the simulation is confirmed to be capable of predicting the trend of the measured results but still unable to predict the mass flow rate at different injection pressure and different injection duration. The discrepancy is the high-fluctuating trends of measured data that deviated away from the averaged, measured trend line of the theoretical prediction. The model simulated an ideal fuel injection process. The model did not counter any losses associated with the process as well as the hysteresis of the electromagnetic material. Another vital remark from the comparison is that the theoretical characteristics of the mass flow rate obtained from the simulation have confirmed the measured data trend.

Table 4.3 presents a statistical description based on the measured data of Case 2. The standard deviation of the measured mass flow rate is about 0.284 g/s. The standard deviation indicates the dispersion of the data set in relative to the mean value, whereas the co-efficient of variation (CoV) explain the degree of dispersion of the data set around the mean value. The CoV of 38.5% indicates that the injection mass flow rate may fluctuate up to 38.5% at every injection duration set up during the actual injection process.

The independent injector testing was carried out to evaluate the mass fuel delivery trend and its suitability to fulfil engine fuel requirements by using independent injector testing and analytical modelling technique. Based on the presented results, a few conclusions can be made.

Table 4.3 Statistical results for the effect of injection duration study

Parameter	Quantities
Mean value	0.75 g
Standard deviation	0.284132
Coefficient of Variation (CoV)	0.384686
Coefficient of Variation (%)	38.46856

Based on the results of Case 1, the injector seems to be sufficient to provide the required mass flow rate of fuel to the engine up to 6000 rpm, primarily when it is operated at an injection pressure of 60 bar. At this injection pressure, the mass flow rate of the injector is about 1.2 g/s. The results matched the fuel requirement of the engine at 6000 rpm for stoichiometric combustion. However, in actual engine operation, there is a particular condition where the engine requires a rich mixture, for example, during full-load or WOT operation. The calculated fuel requirement only considers a stoichiometric mixture requirement, and thus, the measured injector flow rate only able to supply up to the stoichiometric operation. In addition, the test and simulation setup omitted the effect of the downstream nozzle pressure, which affected the resultant mass flow rate. However, Erfan et al. suggested that the impact of the downstream pressure is minimal, primarily when an inwardly opening or pull-in injector needle is used. Nevertheless, Majczak, Barański, Sochaczewski, & Siadkowska (2017) suggested that the direct CNG injector must have a mass flow rate capacity in the range of 0.87 g/s to 12.38 g/s to ensure the maximum potential of CNG direct injection is obtained.

The mass flow rate varies with pressure by a linear proportion, and it supports the first hypothesis of the study, which predicted that the CNG injection pressure is linearly proportional to the mass flow rate of the injector. For optimum engine performance, it is best to operate the injector with a variable injection pressure of gases to meet the fuel requirement in an automated fashion. It may require automatic pressure regulation for the supplied gas fuel since the engine mainly operates in dynamic operation. Another viable option is to regulate the injection duration at different engine operating points continuously. Besides, the fuel must be supplied at the correct timing to provide sufficient mixing time to form a combustible air-fuel mixture.

In case 2, when the fuel was injected at different injection duration, the injector mass flow rate possessed an unexpected trend. Mass flow rate fluctuations are strongly noticeable at short injection duration when the effect of opening and closing injector nozzle is significant. When the injection duration has increased, the instability of the mass flow rate is minimized. It is also apparent that using a higher injection pressure reduced the fluctuation of mass flow rate out of the injector. This reduction is because the high-pressure gases dampen the vibration of the needle valve. The ideal mass flow rate should be constant regardless of the injection duration because it will penalise the engine's air-to-fuel ratio and consequently affect the engine brake torque (Cammalleri et al., 2013).

4.3 Summary of Results

Based on the results, at the mass flow rate range of 0.36 g/s to 1.24 g/s, it is expected that the engine can be operated steadily in a steady-state operation until a stoichiometric condition. However, at full load, the engine will suffer to fulfil the engine load requirement. The maximum mass flow rate of 1.24 g/s cannot comply with rich mixture conditions ($AFR < 17$). Moreover, the engine might face consistency and stability if used in transient or dynamic situations. It is because, in transient engine operation, the injection duration is continuously adjusted to varying the fuel supply and undoubtedly will be operated at various durations lower than 25 ms. It might introduce a fuel consistency problem and fluctuations of the mixture's AFR. The effect of injector mass flow specification is vital to engine performance. The prediction on the engine performance is made solely based on the completed injector testing. The next chapter presents the results of analytical vehicle modelling and vehicle testing.

CHAPTER 5

RESULTS AND DISCUSSION ON ANALYTICAL VEHICLE MODELLING AND CHASSIS DYNAMOMETER TESTING

5.1 Introduction

This chapter presents the results of analytical vehicle modelling and vehicle testing. The analytical model is used to simulate a parametric study of the vehicle and engine control parameters. The results correspond to the theory reviewed in Section 2.5 and the methodology explained in Section 3.4. The chassis dynamometer testing results consist of measured engine input and output parameters. The results correspond to the theory reviewed in Section 2.3-2.4 and the methodology explained in Section 3.6. It follows by descriptions of resulted HPDI-CNG operating envelope and detailed analysis on influential parameters.

5.2 Parametric Analysis of Control Parameters using Vehicle Simulation

The parametric analysis of the HPDI-CNG vehicle is carried out with the purpose to analyse and clarify the effect of vehicle and engine control parameters on the engine brake torque response. The adjusted parameters are throttle position rate, ignition timing, injection pressure, and injection duration.

The ramp input provided through the throttle position angle represents a pedal ramp by a driver of a vehicle. The highest rate of throttle position angle is 0.6855 rad/s (baseline case), and the lowest rate is 0.0762 rad/s. Since the actual test on the prototyped vehicle mostly started at the idle start with vehicle speed less than 25 km/h, it was assumed that the starting throttle angle is already opened at about 0.2 rad (at about 14.5%), and the maximum throttle angle is 1.371 rad (100%). Figure D.1 in **APPENDIX D** presents the varied throttle position angle rate for the five cases. The highest rate was selected as the baseline case. The highest rate represents the fastest action of ramp action given to the throttle and vice versa.

Figure 5.1 presents the engine mean brake torque variations due to different throttle opening rates. Based on the figure, the increased throttle rate opening affected the maximum mean brake torque timing but did not affect the magnitude of maximum brake torque. The maximum brake torque is almost constant at about 60 Nm for all cases. The simulated mean brake torque profile exhibits a rapid increase as the throttle pedal was rammed. Thus, the higher throttle opening rate produces a higher pressure rise rate, hence producing the most rapid maximum torque timing attainment. The maximum brake torque is proportional to the chemical energy supplied by the fuel. It is expected that the same amount of fuel has been supplied in each simulated case hence produced an almost similar peak torque by the engine.

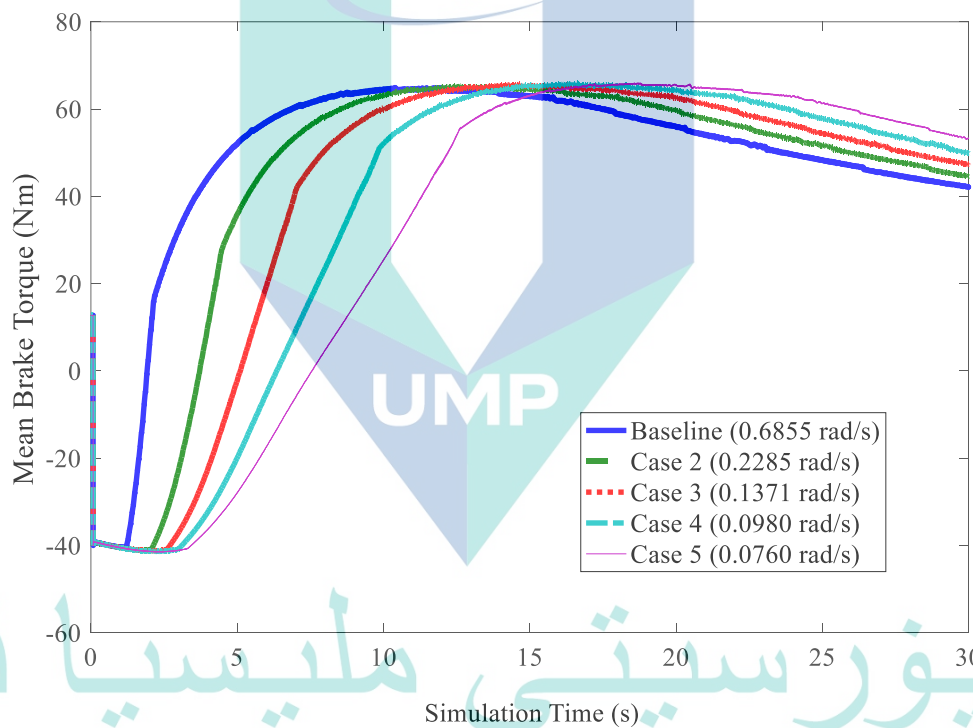


Figure 5.1 The variation of mean brake torque at different throttle opening rates

Figure 5.2 presents the variation of peak torque at different throttle opening rates based on the parametric simulation. In the graph, almost constant values of torque are produced when the throttle opening rate is increased. Even though the plotted graph produced a gradient of $-1.668 \text{ Nm}\cdot\text{s}/\text{rad}$, the throttle opening rate minimally affect the peak torque. The relation between the peak torque and the throttle opening rate is given by $T_{peak} = -1.6684 \cdot R_{throt} + 66.007$. A noticeable effect of reduced throttle opening rate is the delayed peak torque timing, but the peak magnitude is almost constant. The same

amount of energy and air supplied at the same compression ratio and engine rotational speed. Hence, there will be no changes in in-cylinder combustion pressure and, consequently, peak engine brake torque. It has happened because the energy supplied, controlled by the injection duration, is set as a MAP function. The MAP was modelled to follow the actual engine operation, limited to 4 kPa at maximum throttle opening. Therefore, when the MAP value has remained constant, the injection duration will remain constant; consequently, the maximum engine brake torque (Heywood, 1988).

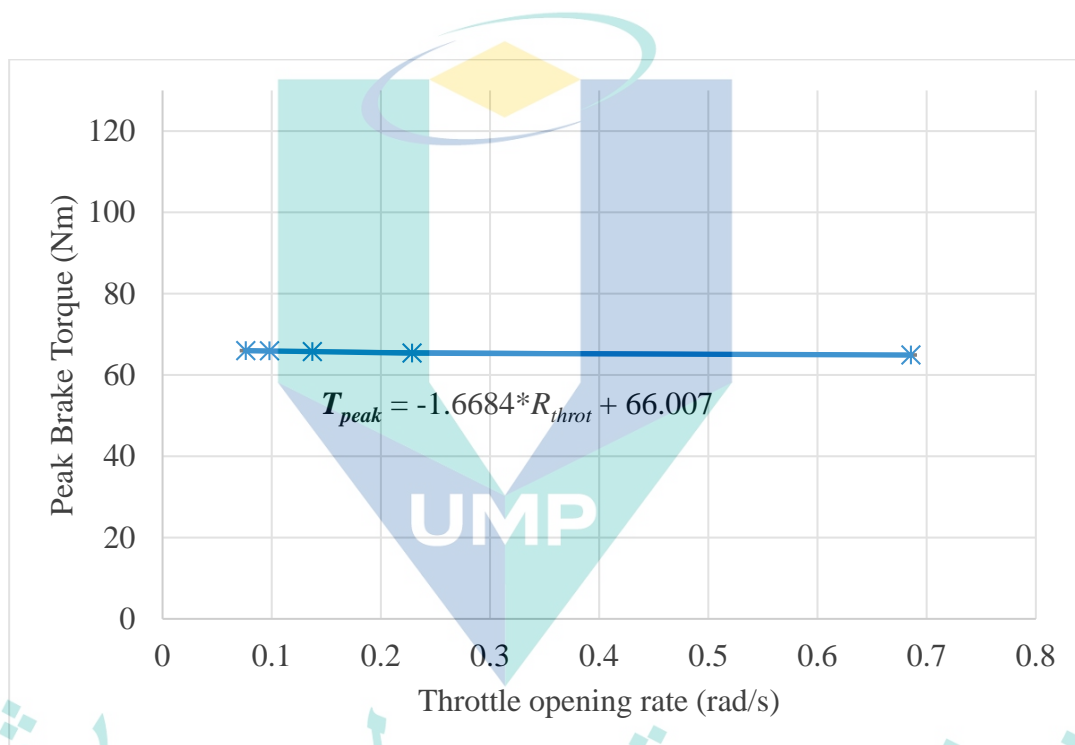


Figure 5.2 Variation of peak torque at different throttle opening rate

The ignition timing is varied by advancing the ignition timing of the baseline case. Advancing means the ignition is occurring sooner than the baseline while retarding means later than the baseline. In the simulated cases, the ignition timing is advanced at an interval of 5° CA starting from -20° CA until -40° CA BTDC. The values are given a negative sign because the ignition timing occurred before the firing top dead centre (TDC), which is used as the reference point, which is given the value of zero degrees.

Figure D.2 in **APPENDIX D** presents the varied ignition timing for this study. Since the ignition timing map was set as a function of MAP and engine speed, the timing

abruptly increased following the MAP increment and speed. It had happened because the vacuum in the intake manifold abruptly increased as the throttle opening increased. The MAP changes are representing the load changes on the engine. In a modern engine control system, the ignition timing is controlled using open-loop schemes that rely on look-up tables. The look-up tables are determined through extensive calibration experiments in either an engine or chassis dynamometer tuning (Flekiewicz, 2009).

Figure 5.3 presents the effect of ignition timing on the mean brake torque. The torque rises and developed as soon as the throttle opening increased. After the peak pressure point, the torque gradually decreased. There were slightly noticeable changes of maximum mean brake torque when the spark timings were advanced. However, the increased mean brake torque magnitude is considered insignificant. The torque difference is observable until the end of simulation time. Figure 5.4 presents the variation of peak torque at increased spark ignition timing advance. Even though the spark ignition timing advance has a minor effect on the output torque, the increment of torque is still noticeable until a maximum advancement of 10 degrees. Beyond that 10 degrees advance, the torque gradually decreased. Theoretically, the relationship between the ignition timing advance and the brake torque can best be approximated by a quadratic equation, $T_{peak} = -0.0397*(t_{ign})^2 + 0.9007*(t_{ign}) + 64.923$.

The theoretical relationship is also a second-order equation. The best ignition timing that produced the simulation's highest brake torque is expected to be close to the maximum brake torque (MBT) timing. At this MBT timing, the combustion peak pressure is expected to happen in the range of 0-10° ATDC (Heywood, 1988). The maximum brake torque is produced because a maximum work transfer is obtained at this coincidence. The results also indicate that the current setting (equal to the baseline case setup) is not optimized and requires calibration to obtain the optimum peak pressure. Detailed calibration results are presented in Chapter 6.

An earlier spark advance gives typically a higher maximum pressure and temperature, which occurs at an earlier crank angle. However, if too early ignition timing, the pressure rise starts too early and counteracts the piston movement. Additionally, early

ignition timing also increased losses due to heat transfer to the walls and flows into and out of crevices. The temperature rises earlier, and more energy will be dissipated during the cycle. Too late ignition produces a pressure increase that comes too late, so that heat energy is lost during the expansion phase. Even though some work can still be gained at late ignition, it cannot fully compensate for the loss early in the expansion phase (Flekiewicz, 2009). The ignition considered as late when the peak pressure is obtained not in the range of 5-10° CA.

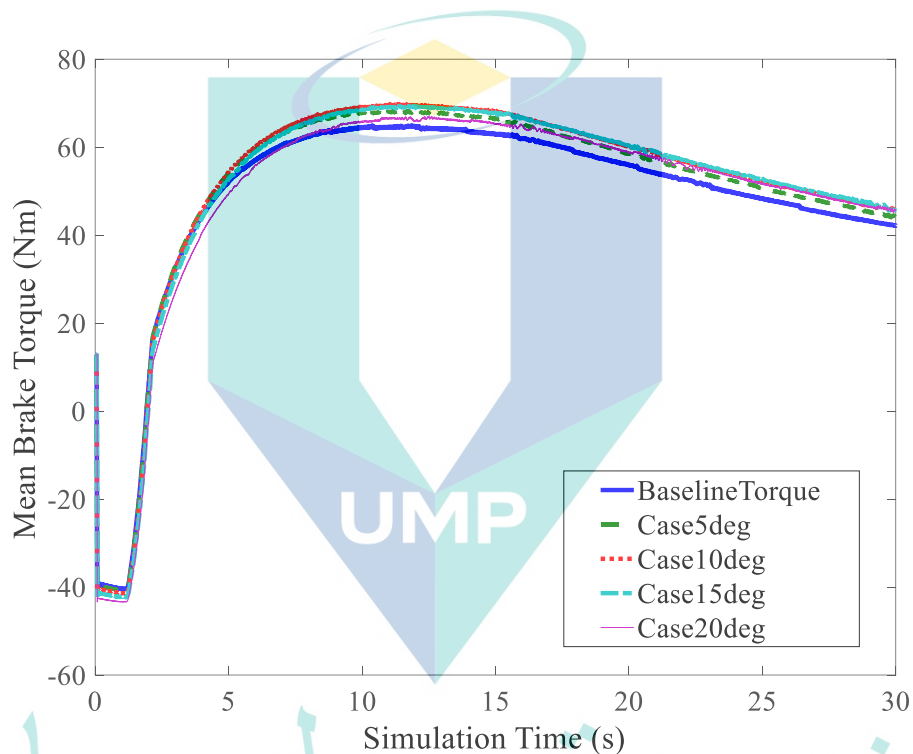


Figure 5.3 The variation of the mean brake torque due to the varied ignition timing

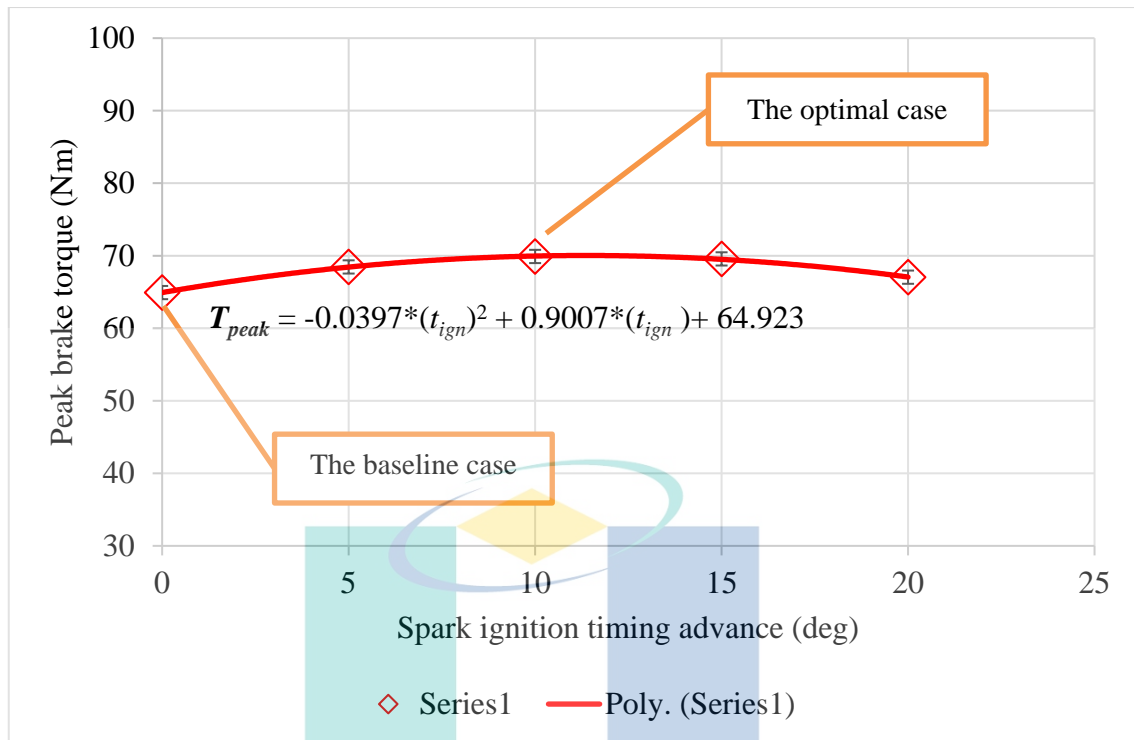


Figure 5.4 Variation of peak torque at increased ignition timing advance

The effect of injection pressure is simulated by imposing the measured mass flow rate of the injector, obtained from the injector testing discussed in Section 4.2.2. Computational load on the model expected to be reduced by using measured results. Table D.1 in **APPENDIX D** presents the mass flow rate of CNG and the corresponding injection pressure used in the current study. The table demonstrated that the mass flow rate increased linearly with the injection pressure.

Figure 5.5 presents the effect of different injection pressure on the mean brake torque. All cases showed that the mean brake torque rises to a maximum value due to maximum ramp input on the throttle pedal before decreasing as the speed increase. The highest mean brake torque obtained by the highest injection pressure of 60 bar is about 123.11 Nm. While the lowest injection pressure of 20 bar produced the lowest brake mean torque at a value of 25.82 Nm. The torque at 20 bar injection pressure exhibits almost a constant value without noticeable decrement after achieving the maximum brake torque point. The maximum brake torque value obtained is 19% lower than the maximum value obtained by the port injection gasoline engine, rated at 148 Nm. The port injection gasoline injector has a measured mass flow rate of 5 g/s at an injection pressure of 3.5

bar. Hence, the HPDI-CNG engine may produce a comparable maximum mean brake torque if the mass flow rate can be further increased by using higher injection pressure.

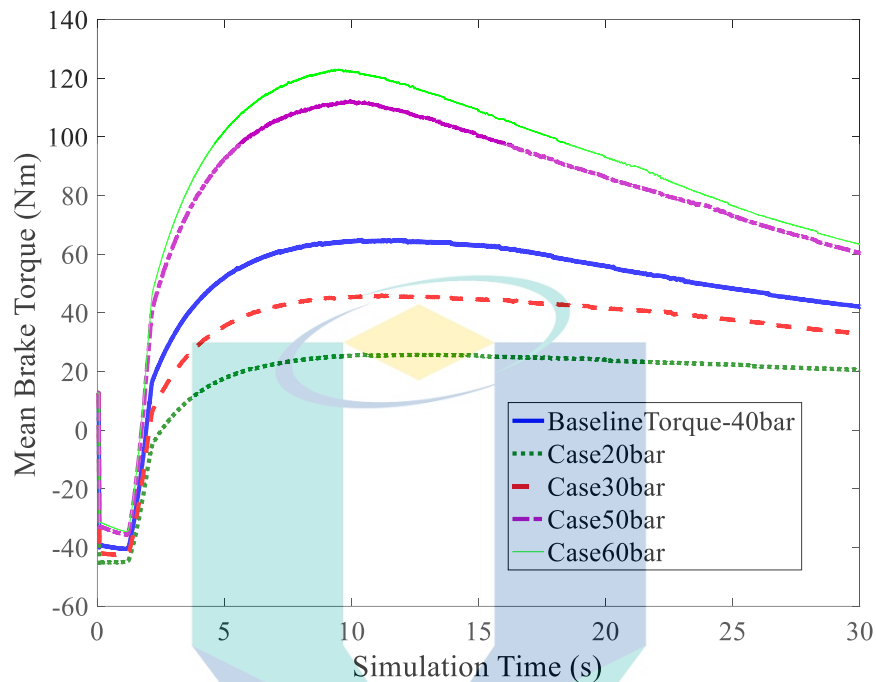
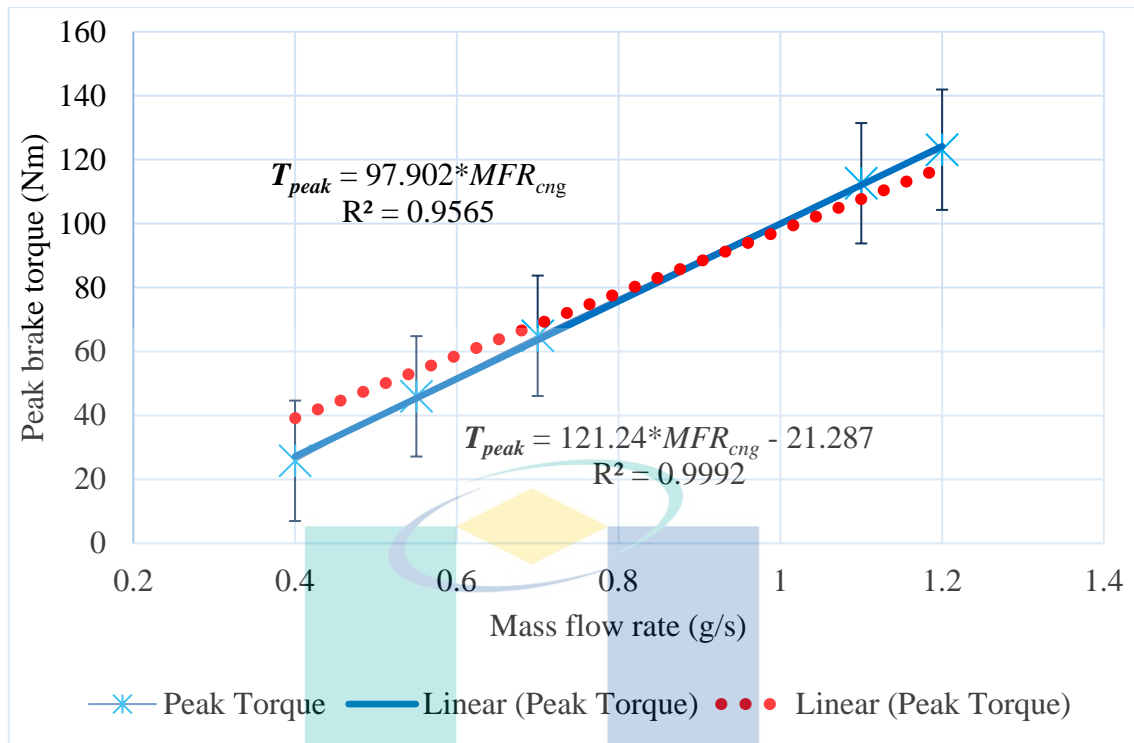
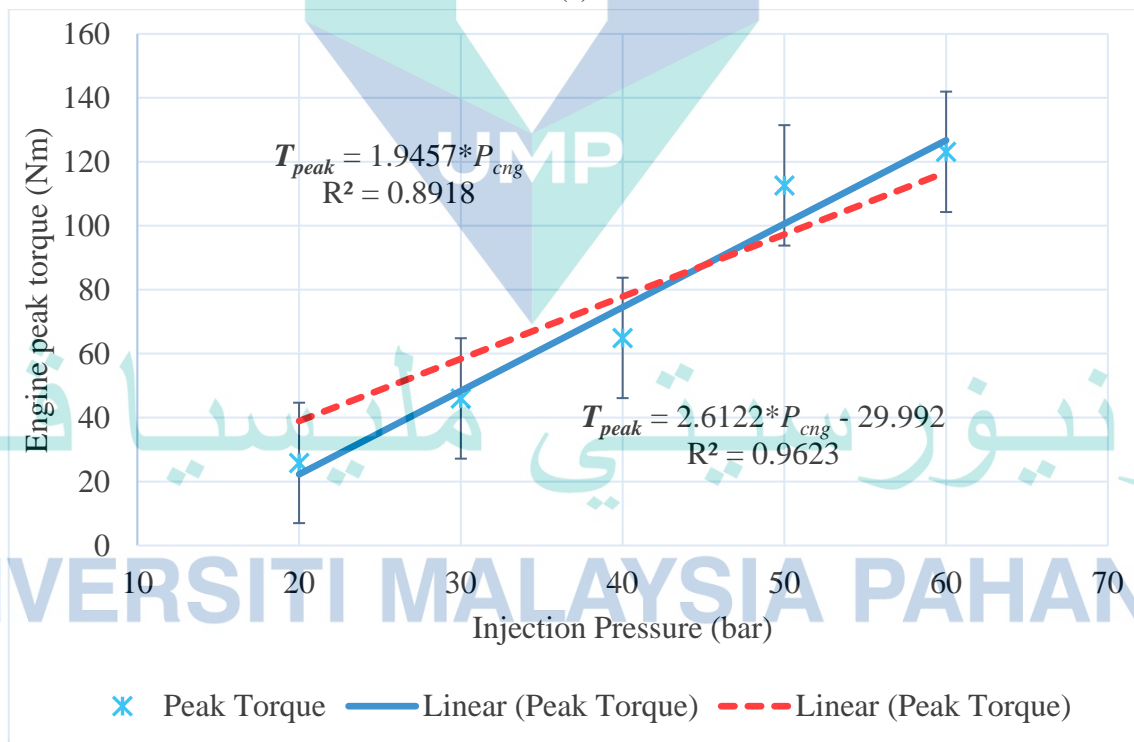


Figure 5.5 The variation of mean brake torque at different injection pressures

Figure 5.6 (a) presents the variation of the theoretical peak torque at an increased mass flow rate of CNG. We can observe that the theoretical engine torque is linearly proportional to the CNG mass flow rate (represented by the dotted line). The rate of increment of the peak torque relative to the mass flow rate is predicted to be 121.24 Nm.s/g. The plot produced a y-axis intersection at -21.287 Nm. However, it is expected that the crossing should be located at 0 Nm for the actual condition. Adjustment on the graph produced a linear graph with a lower gradient and crossed the y-axis at 0 Nm (represented by the continuous line). The new chart is believed to represent the actual relation between the engine brake torque and the mass flow rate of CNG and is given by $T_{peak} = 97.902 * MFR_{cng}$. The relationship is valid in the simulated mass flow rate range, in between 0.4 g/s to 1.2 g/s.



(a)



(b)

Figure 5.6 (a) The variation of peak torque at an increased CNG mass flow rate (b) The variation of peak torque at an increased injection pressure

Since the mass flow rate is representative of the injection pressure, it is valid to replot Figure 5.6 (a) to produce a comparable plot in Figure 5.6 (b). Figure 5.6 (b) presents the engine peak torque as a function of CNG injection pressure. The relation between the peak brake torque to the injection pressure is expressed by the equation of $T_{peak} = 2.6122 * P_{cng} - 29.992$. If the plot is adjusted to intercept at $y=0$, the relation between the peak brake torque and injection becomes $T_{peak} = 1.9457 * P_{cng}$. The results agree with the second hypothesis of the study, which stated that the mass flow rate of the fuel is proportional to the engine output torque. However, this condition is achievable only if the air intake increased at a similar rate with the fuel increment in order to maintain the mixture AFR within the combustible mixture range. This condition is basically met in an ideal combustion process.

The injection pressure of CNG plays a significant role in CNG direct injection process. However, the number of detailed studies related to CNG injection pressure on engine brake torque from the past is minimal. Most of the studies describe the injection pressure with the gas spray characteristics such as gas jet penetration length (Aesoy & Pedersen, 2011), the jet velocity (Huang et al., 2003b), and the mixture formation process (Chiodi, Berner, & Bargende, 2006) only. In the application of direct injection of CNG in engine performance measurement such as reported by Kalam & Masjuki (2011), Aslam et al. (2006), Kalam et al. (2009), Jahirul et al. (2010), Mohammed et al. (2011b), and Mohammed et al. (2011a), they were all limiting the injection pressure up to 20 bar. Most of these studies utilised the injection pressure of 20 bar and solely used a single set of pressure setup throughout the study. Other studies which employed a higher injection pressure include the work (Zheng et al., 2009a) and (Huang et al., 2003b) (90 bar). The high injection pressure of CNG is typically investigated in diesel-built engines. It requires a compressor to achieve high fuel rail pressure.

Rashid & Firmansyah (2009) reported that CNG injection pressure affects a specific range of engine speed differently. In their study, they tried to maintain the injection quantity. Hence they have altered the injection duration for each pressure setup. This approach has led them to inject the fuel during valve opening at a longer injection duration with low injection pressure. Meanwhile, they utilise a shorter injection duration at high injection pressure during all valve closed conditions. They concluded that an optimum direct injection CNG engine performance could be achieved by controlling the

injection pressure. There is a greater possibility that the NGV vehicle can further increase the vehicle travel range, maintain engine performance, and reduce the storage requirement for a light-duty vehicle. The increment of injection pressure from 7.5 bar to 12 bar and 18 bar resulted in increased engine brake torque and power.

Figure D.3 in **APPENDIX D** presents a plot of varied injection duration. The injection duration defines how long the injector needle valve open. In existing architecture, both the injection duration and ignition timing values are predefined in ECU in maps/ look-up tables. The operating point for the maps is selected based on sensed manifold absolute pressure (MAP) and engine rotational speed (RPM). The same architecture has been applied in this model. The varied injection durations are obtained by adding an additional time to the ECU's output value. In this case, the added period is 0.002 s until 0.01 s with an interval of 0.002 s.

Figure 5.7 presents the effect of injection duration on the mean brake torque. Based on the figure, the trend of the torque resembles the results of the injection pressure increment. However, there was no significant increment of torque in each simulated case. The most extended increment of injection duration at a value of 0.01 secs produced the highest maximum mean brake torque at about 68.94 Nm. In contrast, the baseline case produces the lowest maximum mean brake torque at approximately 64.92 Nm. The effect of injection duration and injection pressure increment is similar because both parameters are used to control the amount of fuel supply for combustion.

The larger amount of fuel supplied for combustion increases the heat released by combustion, consequently increasing the mean brake torque. It is true, provided that the airflow is also regulated accordingly to maintain a combustible AFR. It is easily known based on the theoretical cylinder pressure equation for the cyclic engine combustion process. The fuel energy supplied is one of the positive contributors to the pressure build-up. And higher cylinder pressure will result in higher engine's indicated torque (Sitthiracha, 2006). Since natural gas has a low density compared with gasoline fuel, a longer injection duration is always necessary for natural gas injection to obtain a comparable amount of fuel. A typical range for CNG injection duration is between 0-30 ms. It has led to the suggestion of using different types and numbers of CNG injectors to obtain the required injected CNG mass and equivalence ratio (Huang et al., 2003b). If an injector with a large nozzle diameter and high injection pressure is used, the injection

duration could be decreased, and the injection can be performed at a faster injection rate to produce a short period of heat release (Rashid & Firmansyah, 2009).

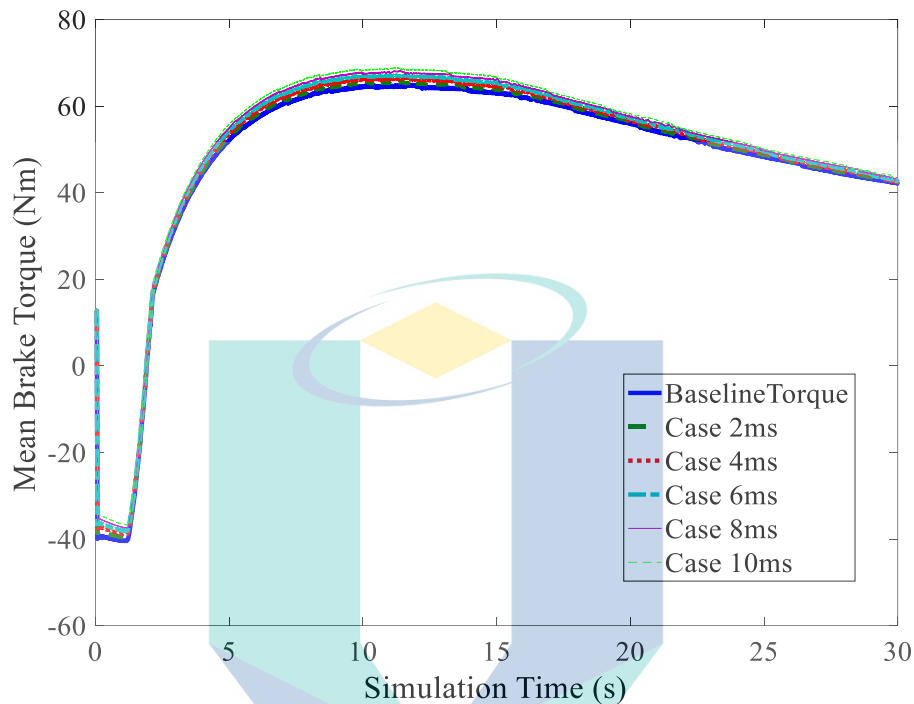


Figure 5.7 The variation of mean brake torque at different injection duration

Figure 5.8 presents the variation of peak torque at increased injection duration. The graph shows that the peak torque linearly increased with the increased injection duration. It is well fitted by a linear trendline of $T_{peak} = 0.4007 * t_{dur} + 64.948$. The increased injection duration increased the fuel and chemical energy supply, consequently increased the output brake torque. However, the gradient of 0.4 Nm/ms indicates that the increment is not significant as 1 ms addition of injection duration increased less than 1 Nm of torque. The selection of duration increment from 2 ms to 10 ms is logically adequate for this case as the default duration in the actual prototype is ranging from 10.04-20.5 ms, based on the vehicle testing results.

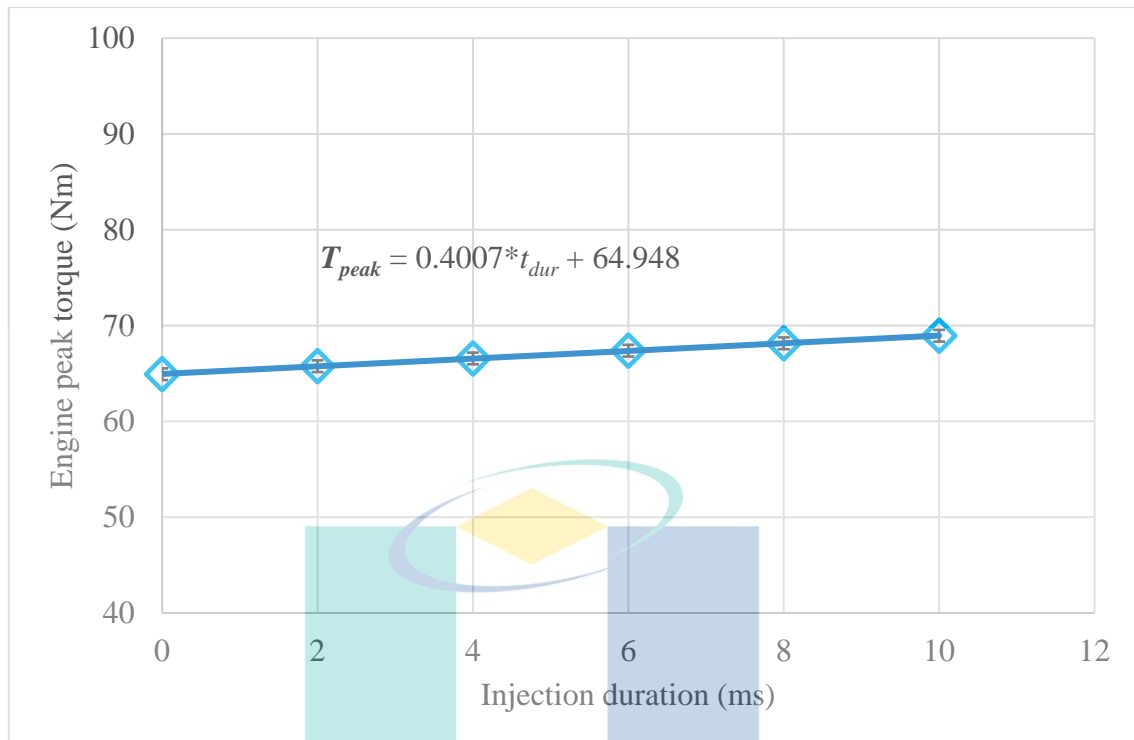


Figure 5.8 The variation of peak torque at increased injection duration

This section presents the characteristics of engine torque response modelling and its comparison against the measured engine torque. The comparison aims to validate the simulation and explain the discrepancies between the ideal trend of simulated and measured engine torque response at the different conditions of the AFR. Figure 5.9 presents the simulation results for two case studies and their comparison with measured engine torque response. First, the case is the simulation of torque response with the inlet fuel boundary based on a constant mass flow rate (Case 3). It is considered the ideal case for the simulation. The model performs at a fully predictive state by assuming that the injector mass flow rate is constant throughout the test window. The second case is the simulation of torque response with the inlet fuel boundary is calculated based on the measured, transient AFR (Case 2). While the actual, measured engine torque is considered as the baseline case (Case1).

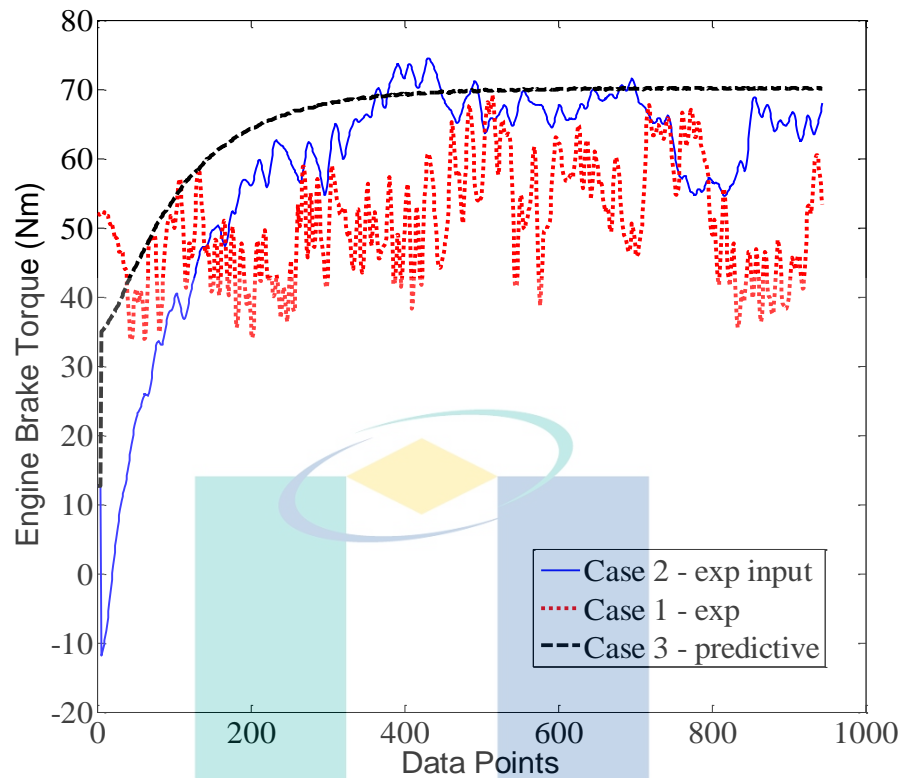


Figure 5.9 Comparison of a different fuel-inlet type boundary on the engine brake torque response

Based on Case 3, where the ideal, constant mass flow rate is used, the response of the brake torque shown an increasing trend at the early test time, but then after the peak torque point, it produced an almost constant torque until the end of simulation time. To explain the results, when a constant injector mass flow rate is used as the boundary calculation, the model produced an almost constant AFR. After the transient period, the engine produced a nearly constant torque response. When the torque is constant, the speed became constant. The speed is feedback into the ECU. It influenced a constant injection duration. Since the injection duration is defined as a function of engine rotational speed and MAP, its behaviour strongly follows the speed and MAP trends.

In Case 2, the use of measured AFR (which has a fluctuated trend), produced a fluctuates engine torque. But the model cannot follow the fluctuated trend of the measured torque closely. However, the prediction still able to capture the increment and decrement trends of the brake torque response with a certain amount of delay, which is estimated to be about 2.5 seconds in the measured data. The delay between the simulated and measured response exists because the torque response is also dependent on other

extraneous parameters such as the engine speed and the ignition timing. The AFR itself is a ratio of two parameters: the air mass flow rate and the fuel mass flow rate. Hence, it cannot be concluded that the fluctuations of the mean brake torque are due to the changes of the AFR alone. However, this result demonstrated the contribution of inconsistent AFR on the resultant engine brake torque.

The inconsistencies of AFR in Case 1 and Case 2 have resulted in inconsistencies of engine brake torque. An increment of AFR, which indicates a leaner mixture resulted in lower engine torque. Whereas a decrement of AFR, which indicates a richer mixture resulted in increased engine torque. This result is in agreement with the previous findings (Rahman, Mohammed, & Bakar, 2009), where AFR and engine speed influences the performance of a hydrogen-fueled engine, especially BMEP, BTE and BSFC. Based on the discussion above, the usage of the model for vehicle and engine control parametric analysis is therefore justified. The parametric simulation and analysis performed in this current stage are vital in predicting the ideal performance of the vehicle and engine. It gives the highest possible performance achievable by the engine.

The analytical modelling of the HPDI-CNG vehicle is performed with the purpose to analyse the effect of the new CNG direct-injection configuration on the engine performances analytically. It also used to assess the influential parameters which contribute to the attained performances. Based on the results presented in Section 5.2 until 5.3, the simulation vehicle simulations have drawn the following conclusion. Based on the highest output performance of the models, at an injection pressure of 60 bar, the HPDI-CNG vehicle is predicted to produce 123.11 Nm of peak torque. Even though this torque is lower than the peak torque of a port-injection gasoline engine at 148 Nm, it is an anticipated outcome since the energy density (energy per unit volume) of the CNG is lower than gasoline fuel, plus it burns slower than gasoline.

However, as stated before, the model simulated an ideal engine operation. The ideal terms refer to a complete combustion process where the mass of fuel supplied is fully utilised to convert chemical energy to mechanical work. So, instead of targeting the 148 Nm of torque, maybe it is more practical to target a 123.11 Nm as the maximum achievable torque by the engine. Parameters such as ignition timing, injection timing, and injection duration are purely replicated from predefined values in the actual lookup table of the ECU. Other setups of the engine model were also based on the exact setup of the

vehicle. Hence, based on the current hardware, we can expect that it is feasible to produce a baseline performance approaching the maximum engine brake torque of 123.11 Nm provided that the combustion process is performing as an ideal combustion process. The most influential parameter on the engine peak brake torque is the injection pressure. Higher injection pressure resulted in higher engine mean brake torque. It is because the higher injection pressure produced a higher CNG mass flow rate, which means higher chemical energy supplied for the energy conversion process. The exact relation between peak brake torque and other adjusted parameters are provided in Table 5.1. These relationships are obtained based on the results plotted and discussed in Figures 5.2, 5.4, 5.6, and 5.8.

Table 5.1 The predicted relationship between parameters based on the simulation

Parameters	Mathematical relationship
Peak torque, throttle opening rate	$T_{peak} = -1.67 * R_{throt} + 66.01$
Peak torque, ignition timing	$T_{peak} = -0.04 * (t_{ign})^2 + 0.9 * t_{ign} + 64.92$
Peak torque, mass flow rate of fuel	$T_{peak} = 97.90 * \dot{m}_{cng}$
Peak torque, injection duration	$T_{peak} = 0.4 * t_{dur} + 64.95$

Based on these equations, the second influential parameter is the ignition timing, where the maximum pressure predicted is 69.9 bar ~70 bar. The result is contrary to the characteristics of a GPI engine where ignition timing is profoundly affected engine torque and speed (Szekely & Alkidas, 2005). This difference is primarily due to the longer combustion period and slower combustion for CNG combustion, resulting in 'less sensitive' response of output torque (Mazlan, 2017). The third influential parameter is the injection duration, where the maximum predicted engine brake torque is about 68.94 Nm. Both the injection pressure and injection duration are related to the controlling amount of fuel injected into the cylinder, which affects the AFR of the cylinder mixture. The engine model is not suited for the control or control and optimization-oriented analysis since it is computationally demanding. A single run of each simulated case will consume at least 45 minutes on a multi-core workstation which is considered computationally expensive. However, its details and comprehensiveness are a significant

contribution to developing a complete vehicle model (from the throttle to the wheel approach).

5.3 Experimental Vehicle Testing using Chassis Dynamometer

5.3.1 Measured Engine Input Parameters

The results of the engine performance test are broadly categorized as the engine input and output parameters. Parameters classified as engine input are throttle position sensor, manifold absolute pressure (MAP), injection timing, injection duration, ignition timing and air to fuel ratio. The plots of the engine data mostly presented by using the moving averaged trendline to improve visibility of the trend since the measured data highly fluctuated. The CNG injection pressure is manually regulated for the existing HPDI-CNG configuration; hence the measurements were made at different injection pressure.

The manifold absolute pressure variation is presented in Figure 5.10. The absolute pressure is strongly correlated with the throttle angle opening and engine speed. As the throttle angle opening increases, the absolute pressure inside the manifold is reduced (became positive) and approaching the surrounding ambient pressure (101 kPa). The highest pressure recorded during the testing is 4 kPa. It is the highest absolute pressure that the MAP sensor can sense. As the speed swept through the test window, the absolute pressure is almost constant, close to 4 kPa limits.

The wide opening throttle represents the maximum load condition of the vehicle. The consequence when the throttle angle opening and the manifold absolute pressure increased are the increment of the engine output and engine speed (Golzari, 2018). The engine speed and the manifold absolute pressure are independent parameters that the ECU utilises to determine the instantaneous operating point of the engine. At low throttle angle opening and low engine speed, the manifold absolute pressure has the most negative values (the vacuum pressure), and the values will increase to become positive (closer to the surrounding ambient pressure) when the opening of the throttle valve and engine speed increased.

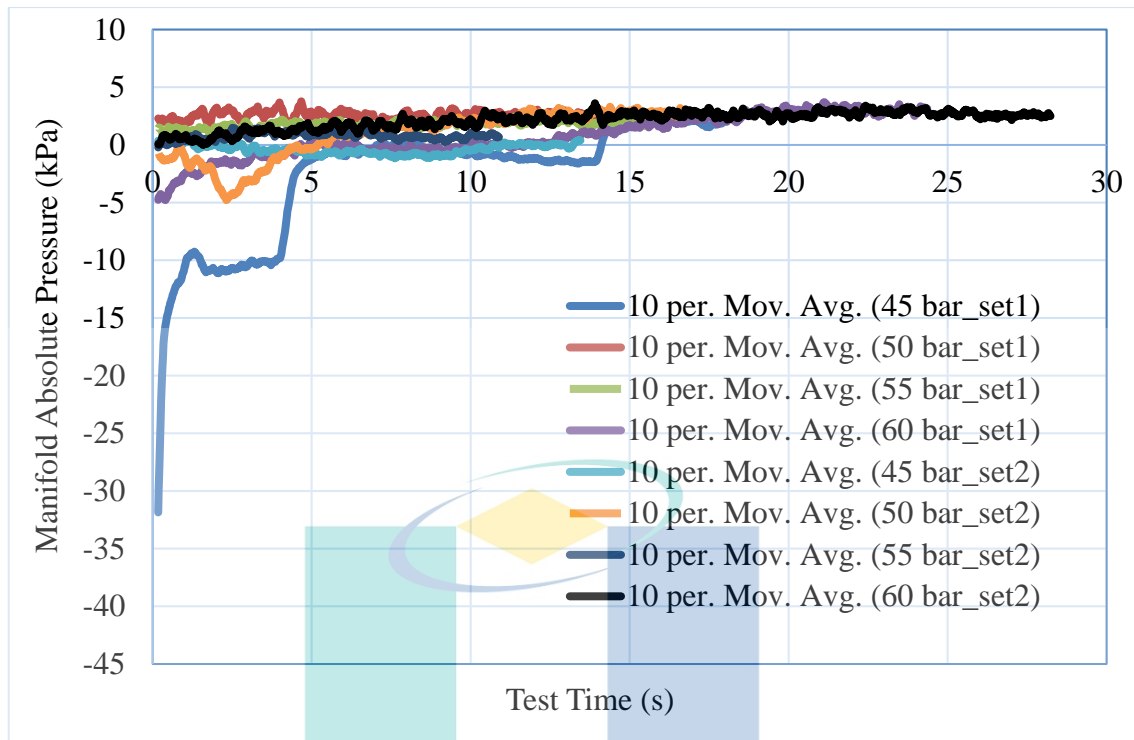


Figure 5.10 Manifold absolute pressure for the speed-sweep test at a different injection pressure

Chang, Yaacob, & Mohsin (2007) stated that the MAP increased with throttle angles at steady engine speed. It is closely related to throttle opening and engine rotational speed. However, at a constant throttle opening, MAPs decreased with increasing engine speeds. And it was valid for all engine speed range at 30° throttle opening. Typical maximum throttle opening is equal to 100°, which is equivalent to WOT condition. However, it was found out from the current testing, at a WOT condition, the MAP is not reduced nor changing at constant throttle opening and increase speed, as demonstrated by Figure 5.10.

The MAP sensor used in the current study is meant for a normally aspirated engine, and the sensing is limited to 4 kPa. Additionally, The maximum MAP could be further increased to a greater constant value and generating higher engine torque if the MAP sensing is limited to a higher value. The finding is formulated based on the solution of ideal engine processes using an analytical engine model.

The end of injection (EOI) timing represents the injection timing properties relative to the compression/power stroke TDC. Based on the results in Figure 5.11, as the

throttle increased, the injection timing advanced further in relative to TDC. In most cases, the most advanced injection timing is about 500 CA before top dead centre (BTDC). Moreover, the most retarded timing is 473 CA BTDC. The values of injection timing for the whole engine operating point defined as a function of engine speed and throttle position. Hence, the injection timing advance increment followed the path and rate of the throttle opening and engine rotational speed increment closely. In further detail, as the speed increased, the cycle period is becoming shorter. Thus the end of injection or the completion of the injection process must be made quickly before the firing TDC. It explains why the injection timing advanced as the speed increased.

In a typical CNG direct injection engine, the effect of injection timing is very significant. Kar and Agarwal (2015) reported that by the advanced start of injection (SOI), the engine gave a relatively lower BSFC and higher BTE and vice versa. It is because advanced SOI provides more time for fuel-air mixing; hence a more homogenous, combustible mixture is formed and results in improved combustion. It also reduced pumping losses during the intake. These factors played an essential role in enhancing engine performance. Whereas retarded SOI reduced available time for fuel-air mixing and decreased the fuel jet penetration distance towards the EOI in the later part of injection, after the IVC in the compression stroke. It happens because of the increased cylinder pressure once the piston starts moving towards TDC during the compression stroke (Mohammed et al., 2011a). This introduced resistance to the fuel injection process, which is still being injected. This resistance finally results in relatively inhomogeneous fuel-air mixing, poor combustion and relatively inferior engine performance.

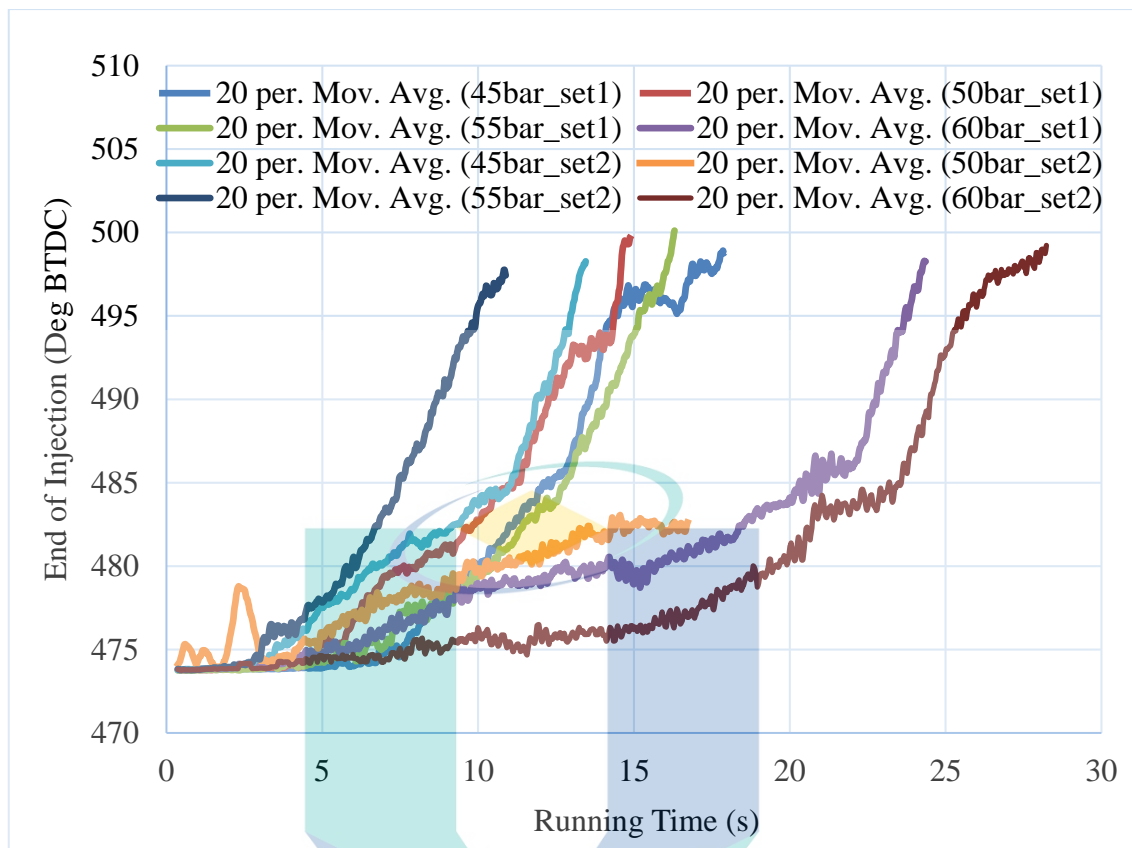


Figure 5.11 Injection timing for the speed-sweep test at a different injection pressure

Figure 5.12 presents a plot of injection duration for the HPDI-CNG vehicle at different injection pressure. The injection duration predefined values are stored in the ECU maps and identifiable based on instantaneous engine speed and manifold absolute pressure (MAP). The controller decides the injector nozzle opening duration based on the measured operating point. Based on Figure 5.15, the injection duration produced fluctuated values throughout the running test time for all injection pressure settings. The maximum and minimum values are about 20.50 ms and 10.04 ms, respectively, between 45 bar and 60 bar of injection pressure. The injection duration value will increase when the engine speed manifold absolute pressure is increased. At this condition, more fuel is required to generate higher torque to overcome the inertia load or accelerate the vehicle. From existing control strategies, the injection pressure and the injection duration are independent of each other, except that more fuel delivered at a higher pressure for a specific injection duration.

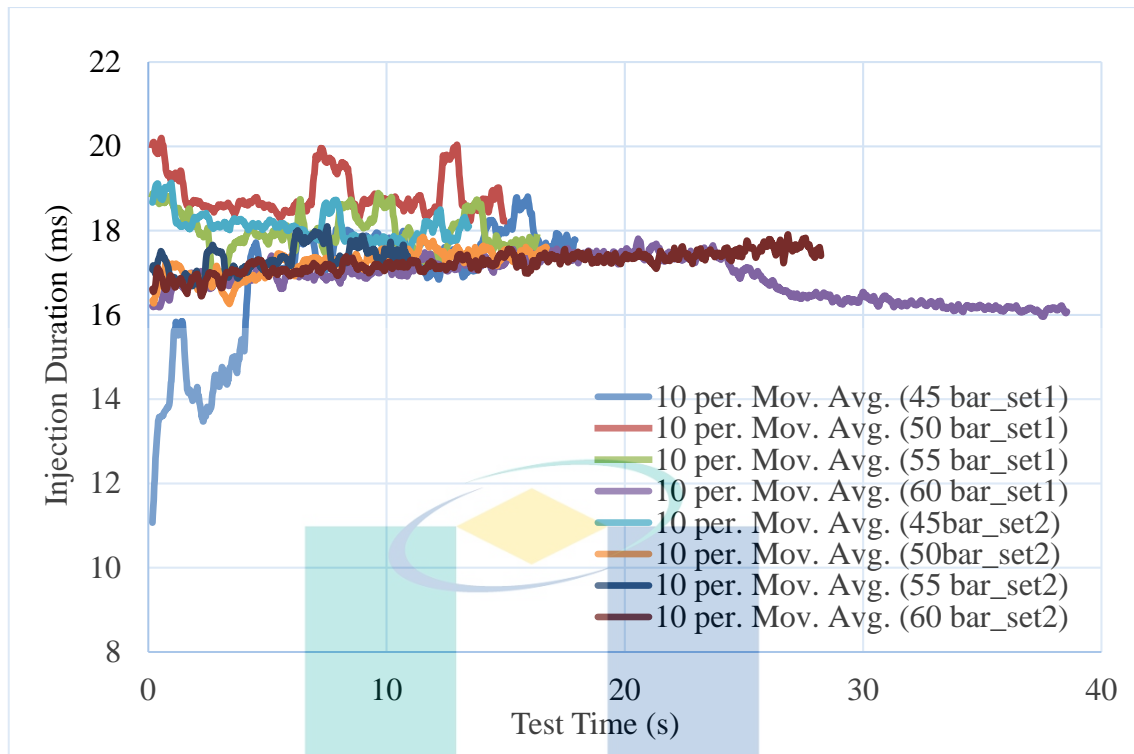


Figure 5.12 Corrected injection duration of HPDI-CNG vehicle at different injection pressures

The predefined injection duration in the ECU maps is actually related to the injector mass flow rate. If the injector is a high flow rate injector, a shorter period is required at a specific engine operating point to obtain a certain amount of fuel. But if the injector is a low flow rate injector, then obtaining the same amount of fuel will require a longer injection duration. Thus, using a high injection rate at low injection pressure is essential for using gaseous fuel to keep the injection duration short and guarantee a longer mixing time (Song et al., 2017).

Figure 5.13 presents the measured ignition timing for the HPDI-CNG engine at a different injection pressure. The ignition timing is defined as the start of combustion in a spark-ignition engine system. Based on the graph, the ignition timing becoming more advanced as the load and speed increased. It is because the ignition timing is controlled by the ECU based on the engine speed and load condition (Khairnar et al., 2015). The ignition timing needs to facilitate a faster combustion period.

Based on the graph, the injection pressure also affect the resultant ignition timing. Different injection pressure produces different mass flow rates, which affects engine torque and, consequently, engine speed. Since the ignition timing is directly selected

based on the instantaneous engine speed and MAP, the ignition advance is chosen according to the change of both parameters.

The combustion initiation must start earlier to ensure that 90 % of the air-fuel mixture as the piston reach the top dead centre (TDC). The completion of combustion for 90% of the mixture is important to ensure the peak cylinder pressure is obtained after 5°-10° after the top dead centre (ATDC). This optimum timing is called the maximum brake torque timing (MBT) (Heywood, 1988). It is where the engine is able to transfer the maximum work to the crankshaft.

Besides, the ignition timing must also occur just after completing the injection process or relatively after the EOI angle. Retarding the injection timing close to or after the spark timing will deteriorate the combustion process, such as incomplete mixing and combustion and increase emission (Chala et al., 2017; Seboldt, 2016). However, too advanced ignition timing is also unfavourable since it can cause knocking combustion. Thus, the determination of the MBT is very important for maximum engine performance.

The most advanced and most retarded ignition timings are about 23 degrees BTDC and 12 degrees BTDC. These are less similar to the trend of ignition timing for CNG direct injection engines. The typical ignition timing range for a CNGDI engine is further advanced than the current results. The usual range of ignition timing for CNG-DI engines is about 22°-34° BTDC (M K Hassan, Aris, Mahmud, & Sidek, 2010). Fukuzawa et al. (2001) showed that retarding the ignition timing lowered the CNG engine's thermal efficiency.

Furthermore, if the ignition advance deviates from the optimum value at a specific operating point, it will also increase the misfire events (Szekely & Alkidas, 2005). However, the current results are still acceptable since the geometrical configuration of the newly HPDI-CNG engine is different compared to the typical direct injection engine. A few in-house trials to advanced the ignition timing further led to unstable combustion and sluggish engine operation. Moreover, the engine ECU maps have been tuned earlier using the traditional calibration method, as explained in Section 3.6.2.

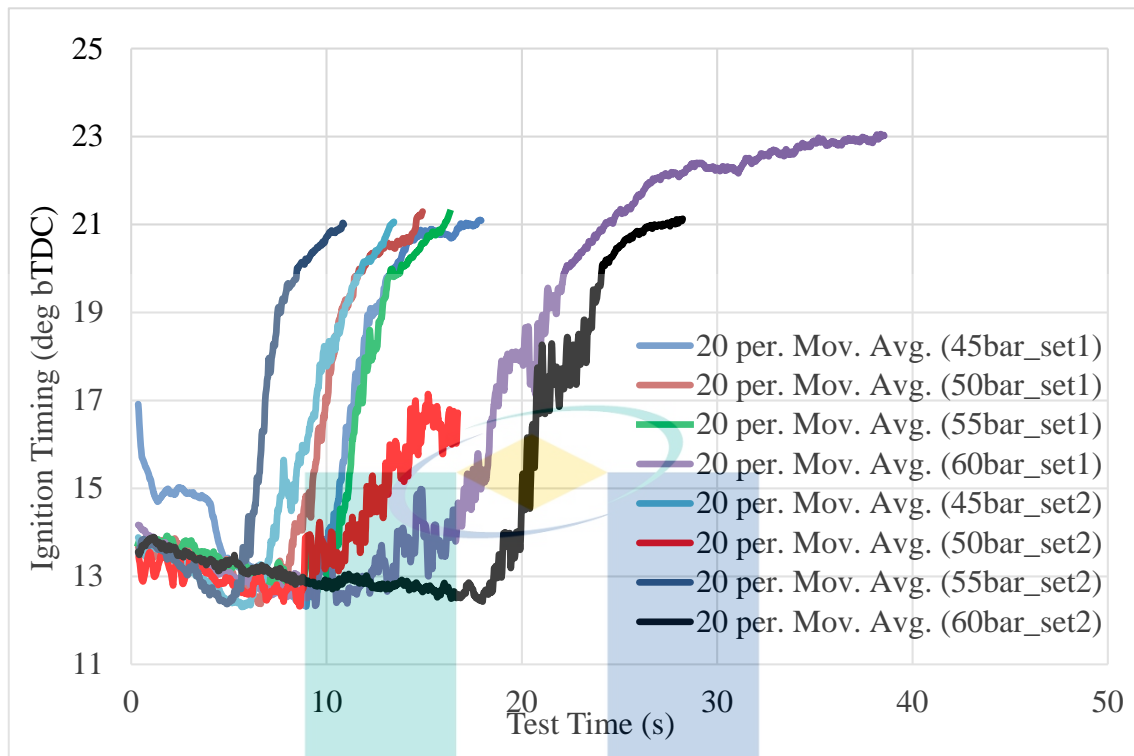


Figure 5.13 Corrected ignition timing of HPDI-CNG vehicle at different injection pressures

Figure 5.14 presents the AFR produced by the mixture formation process of the HPDI-CNG engine at different injection pressure. The trend of the AFR plot showing a slightly increasing trend (becoming leaner) from the test started until the end of the test for most injection pressure setups. It is expected that AFR will become slightly richer as the test started because, at increase engine speed and load, the ECU will intend to provide a richer mixture to the engine in order to produce more torque and power. However, it is essential to highlight that modern engine control tend to adjust the AFR to be closed with the stoichiometric AFR, especially for the vehicle with the three-way catalytic converter (TWCC) system. It is because the pollution control by TWCC is the most efficient at stoichiometric AFR (Zhai & Yu, 2009). A stoichiometric AFR for CNG fuel by weight is about 17.19 (Mohammed et al., 2011a).

At increase injection pressure, The mixture's AFR is observed to become richer. Based on the plot of air to fuel ratio against the test time, the leanest mixture's AFR is produced by the injection pressure of 45 bar at a value of 15.71. In contrast, the richest AFR is produced at an injection pressure of 60 bar with a value of 10.35. At first, this is

reasonable since by increasing the injection pressure, the engine should produce a richer mixture and consequently produced higher torque. However, the highest torque is produced at an injection pressure of 45 bar, and the lowest torque is produced at the injection pressure of 60 bar. This trend is contradicting the earlier understanding where a higher amount of fuel supplied should generate higher torque.

Gasoline engine usually has a combustible mixture's AFR in the range of 12:1 to 18:1. In comparison, the diesel engine can operate at a much leaner condition in the AFR range of 18:1 to 70:1 (Pulkrabek, 2003). The stoichiometric AFR for CNG fuel is about 17.23 (Aljamali et al., 2016). AFR value smaller than the stoichiometric ratio is said to be rich (excess fuel), while a value larger than stoichiometric is said to be lean (excess air). It is common to set up the mixture richer at WOT operation in order to produce the maximum MEP and consequently the highest engine torque in the range of 17.23:1 to 15.66:1 for CNG engine (Heywood, 1988). However, the overall results are considered excessively rich since, at most of the measured points, the AFR is richer than 15.66. This is excessively rich thus lowering the torque produced by the engine.

Therefore, at least two questions need to be answered; 1. why the torque is lowered as the CNG mass flow rate is increased (by understanding that higher injection pressure produces a higher flow rate)? 2. How the AFR produced became rich at all injection pressure? Question number two may be addressed by acknowledging that the engine is operated at full load condition at WOT; perhaps the engine is mostly set up to work at the rich side. However, the overall AFR is still too rich. To address the first question, it may be required to review and compare the results from the injector testing and the air intake measurement.

Based on the injector testing, it was found out that the injector mass flow rate is only able to meet the stoichiometric AFR operation for most of the conditions, and it is almost impossible to produce rich AFR. Next, the amount of air induced theoretically increases with an increment of engine speed and throttle opening. Furthermore, it should be constant at each speed point, regardless of the low or high injection pressure used. However, based on the AFR results, there is a possibility that when the injection pressure is increased, the amount of air intake is inversely reduced, thus causing the overall AFR to be rich and become richer when higher injection pressure is used. If the mixture AFR

is excessively rich, supplying more fuel would not generate a higher torque since the air is insufficient to oxidise all the fuel provided.

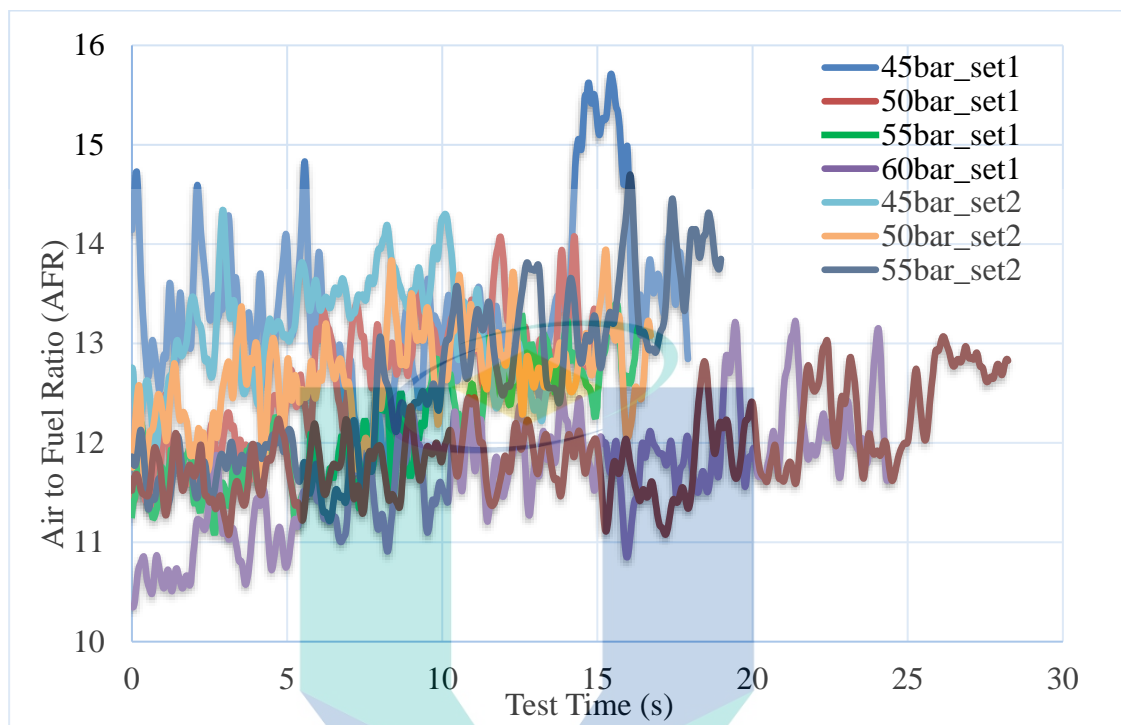


Figure 5.14 Air to fuel ratio of HPDI-CNG vehicle at different injection pressures

5.3.2 The Measured Engine Output Parameters

Parameters classified as the engine output are engine speed, engine brake torque and brake power, engine thermal efficiency (BTE) and brake specific fuel consumption (BSFC).

Figure 5.15 presents the plot of engine rotational speed against test time for different injection pressure. The start engine rotational speed coincident with a vehicle speed of 20 km/h, while the end engine speed coincident with a vehicle speed of 40 km/h. The minimum and the maximum vehicle lateral speeds are the starting and stopping criteria of the speed-sweep test. The maximum vehicle speed of 40km/h is selected as the stopping criteria since it is the maximum speed achievable by the vehicle in most injection pressure setups. Based on the graph, in most cases, the engine rotational speeds are increased at different rates as the throttle is pushed at slightly different rates from partially open throttle opening to the maximum throttle opening. The throttle opening rates are extraneous factors affecting the engine rotational speed increment instead of the different injection pressure of CNG. In most cases, the vehicle achieved the lateral speed of 40

km/h at 2800 rpm of engine rotational speed. The maximum engine rotational speed results are all equal because the tests were carried out at the same gear ratio. The only differences between the graphs are the time required to achieve the test stopping speed at 40 km/h.

Moreover, a different injection pressure setup is used, which produced a different amount of fuel delivered and, consequently, the mixture ratio. Based on the plotted graph, the injection pressure that can achieve the maximum set speed in the shortest time is the low injection pressure setup in between 45 bar to 55 bar. On the other hand, the injection pressure of 60 bar required the longest period to achieve the maximum speed. The lowest injection pressure setup produced the highest torque compared to the highest injection pressure setup. It has generated a higher acceleration ability. Note that the engine rotational speed would be steadily increased during the speed sweep test procedure except during the transmission changes in a normally combusted engine. However, in the current results, it is evident that the rate of speed increment was unsteady. It was due to the unsteady torque and acceleration produced by the engine during the sweep duration.

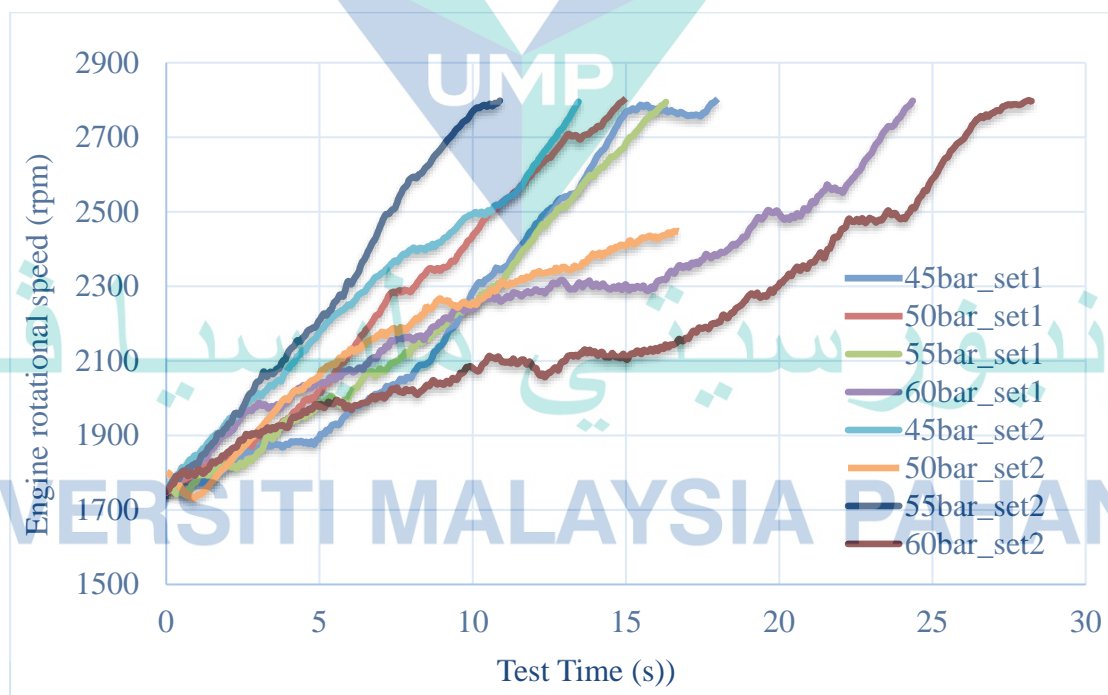


Figure 5.15 Engine speed of HPDI-CNG vehicle at different injection pressures

Figure 5.16 presents the engine total brake torque of the HPDI-CNG vehicle at different injection pressure. Based on the graph, the plotted brake torque showing a highly fluctuated trend without any significant increment or decrement in the mean torque value

at each injection pressure. However, a significant difference is noticeable between brake torque magnitude at each injection pressure. The highest torque was produced by the use of the lowest injection pressure setup (at 69.1 Nm at 45 bar). In contrast, the lowest torque produced by the use of the highest injection pressure setup (15.2 Nm at 60 bar). For a conventional spark-ignition gasoline port injection engine, the typical torque curve should produce a quadratic-like shape where the maximum torque produced at a medium engine rotational speed (Heywood, 1988).

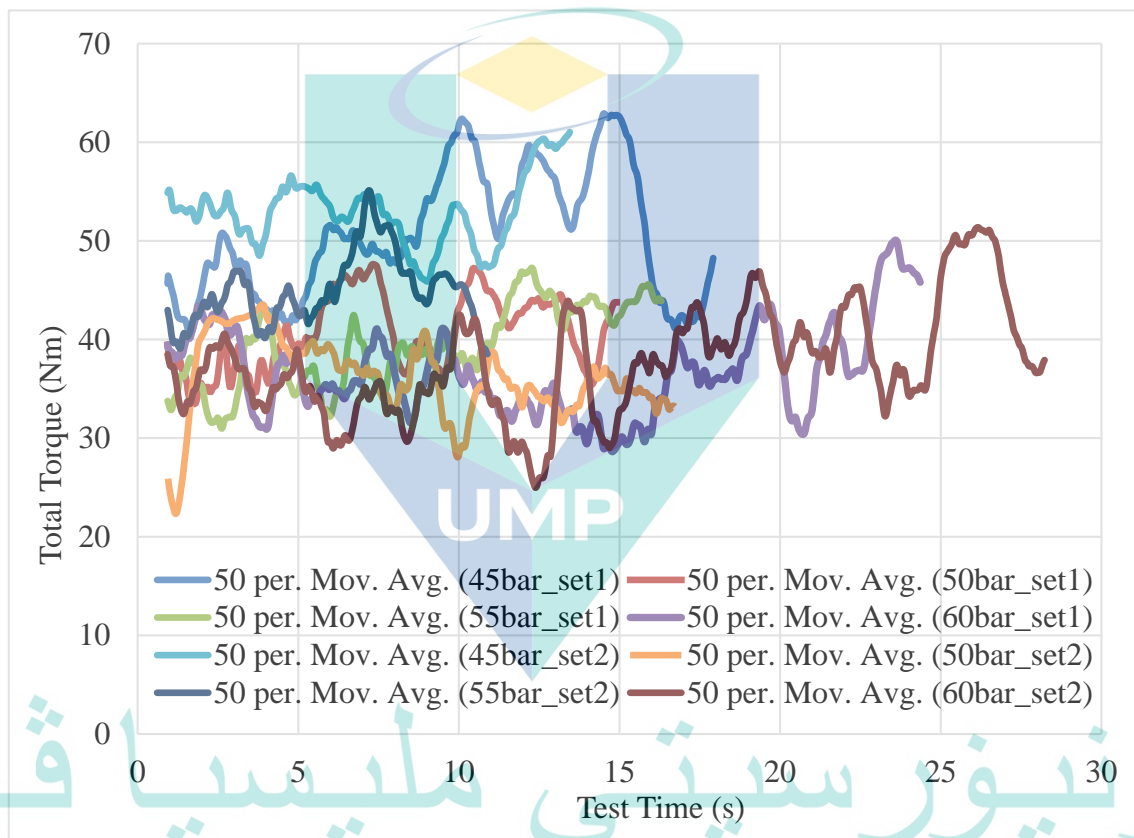


Figure 5.16 Engine brake torque of HPDI-CNG vehicle at different injection pressures

Figure 5.17 presents the total brake power produced by the HPDI-CNG vehicle for different injection pressure. The brake power is a derived parameter calculated based on the engine brake torque and engine rotational speed. Unlike the total brake torque, the total brake power demonstrates a slight increment trend throughout the test time for each injection pressure due to the influence of engine rotational speed. The magnitude of brake power highly fluctuated throughout the test time because it is inherited from the torque characteristics. The use of 45 bar injection pressure produced the highest brake power,

which is about 17 kW during the test. The lowest brake power of about 6 kW is produced by the use of maximum injection pressure, 60 bar (set 2 data). Compared to the baseline engine power in the gasoline port-injection version, the HPDI-CNG engine power is less than half of the peak power of the gasoline engine at about 21.3%. The power drop percentage is much lower than torque because, in current results, both the torque and engine speed are less than half of the standard gasoline engine data. The ideal brake power for HPDI-CNG (based on analytical vehicle simulation) at an injection pressure of 60 bar is about 123.11 Nm.

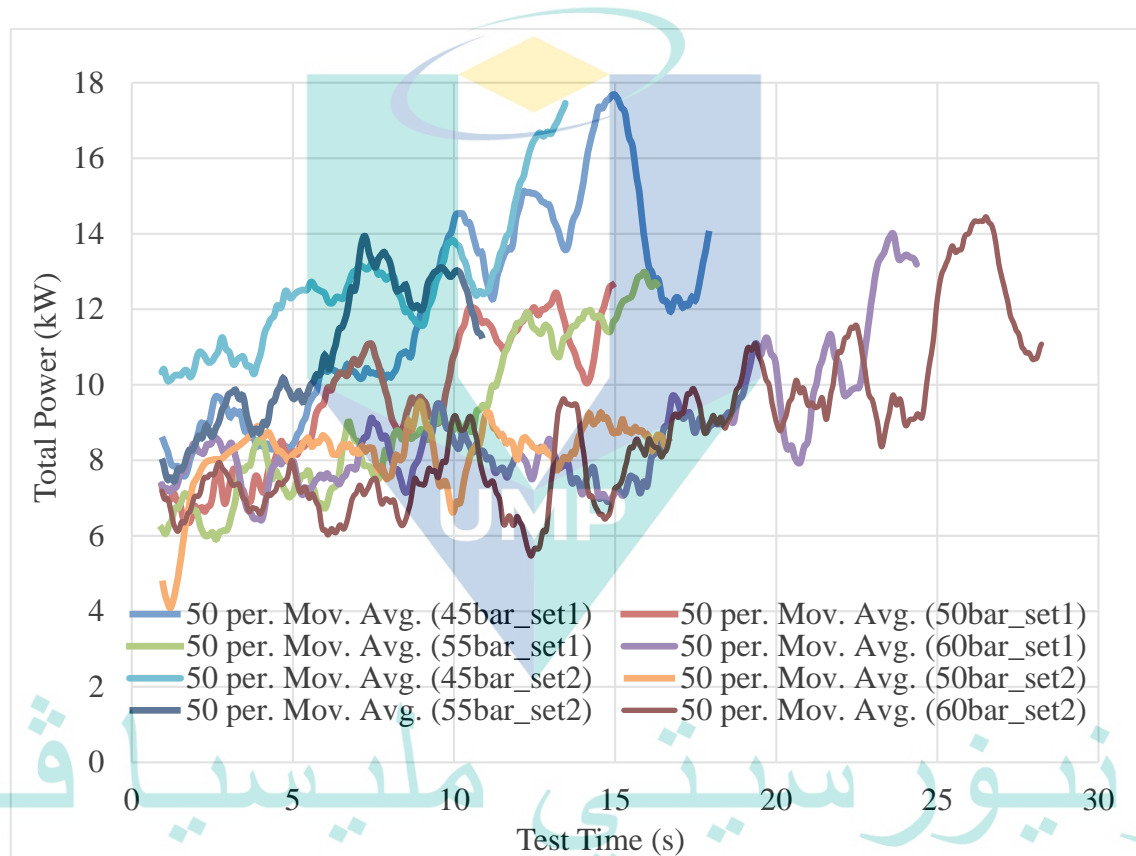


Figure 5.17 Engine brake power of HPDI-CNG vehicle at different injection pressures

As a comparison, the performance of the spark-plug fuel injection (SPFI) engine (Iskandar, 2010) produced a comparable, moderate performance with the current HPDI-CNG results since the conceptual design of both CNG engines feature a common characteristic which includes a throat geometry in the fuel path. The SPFI engine produced about 620 kPa of IMEP and 329.67 g/kWh of indicated specific fuel consumption (ISFC). In comparison, the current study yielded about 704.28 kPa of IMEP (by assuming the mechanical efficiency of 0.75 at WOT) and 226.21 g/kWh of ISFC (at

the best IMEP). The current result of IMEP and ISFC is slightly better than the SPFI engine.

Kalam and Masjuki (2011), which were considered to have achieved CNG-DI's best performance, have produced the BSFC of 243.34 g/kWh at 3500 rpm, and about 123.47 Nm of brake torque at 5500 rpm. The brake torque is only 5% lower than the gasoline port-injection version. In comparison to the current results, HPDI-CNG has produced 169.66 g/kWh of BSFC at 1021 rpm and 69.059 Nm of brake torque at 1790 rpm. The minimum BSFC seems to be better than Kalam and Masjuki, but the overall performance of HPDI-CNG is actually lower. Both the best BMEP and brake torque is obtained at low engine rotational speed (lower than 2000 rpm). The reason for this low performance is discussed in a later section.

Figure 5.18 presents the brake thermal efficiency of the HPDI-CNG vehicle measured by the speed sweep test procedure at different injection pressure. Thermal efficiency is the ratio of the engine output power to the input energy supplied to the vehicle by the fuel. Based on the plot, the thermal efficiency of the HPDI-CNG vehicle slightly increases when the speed progressively developed within the test window. At each injection pressure, the thermal efficiency shows a significant difference in terms of magnitude. The highest thermal efficiency trend is obtained with the use of the lowest injection pressure of 45 bar. In comparison, the lowest thermal efficiency is obtained at the highest injection pressure of 60 bar. Overall, the highest thermal efficiency recorded is about 45.01 %, and the lowest thermal efficiency is about 3.32%. Both are recorded at 45 bar and 60 bar injection pressure, respectively. Higher thermal efficiency is desirable since it indicates a higher amount of power produced by a unit amount of fuel. A comparison of the 45 bar and 60 bar cases shows that at 45 bar, higher torque is produced due to complete combustion in the leaner air-fuel mixture. Whereas at 60 bar, even though more fuel is supplied, the fuel is not fully convertible as useful work. It is believed due to insufficient air intake or excess fuel supplied to each cylinder.

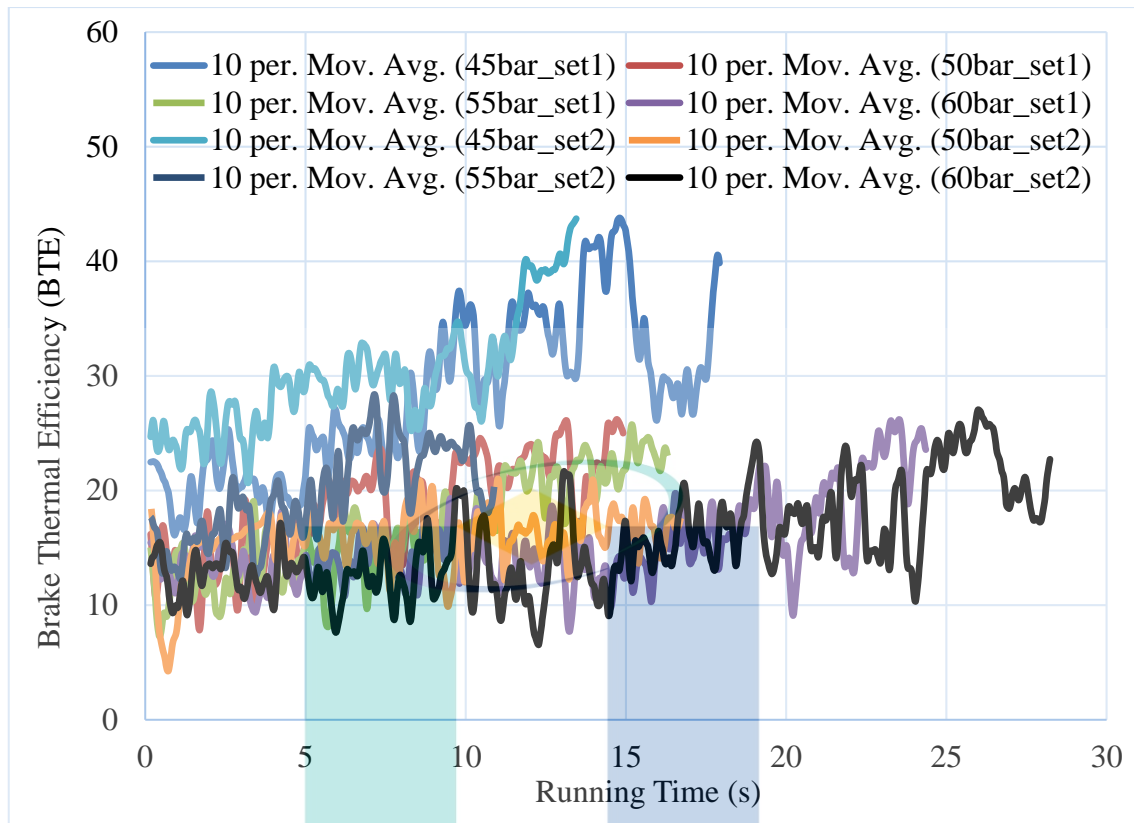


Figure 5.18 Brake thermal efficiency of HPDI-CNG vehicle at different injection pressures

The order of engine brake thermal efficiency for a conventional engine is about 30% to 40%. If the type of engine is considered, the highest thermal efficiency of an internal combustion engine is obtained in compression-ignition, CI (diesel) engine, due to its high engine's compression ratio. Since the spark-ignition SI (gasoline) engine has a lower compression ratio, its thermal efficiency is lower than the CI engine. If the compression ratio for both CI and SI engines is made constant, the SI engine will produce a higher thermal efficiency (Pulkrabek, 2003). CNG engines (regardless of SI or CI platform) typically have a higher thermal efficiency than the gasoline engine and lower than the diesel engine. The best brake thermal efficiency reported for CNG engines is produced at 40% (Fukuzawa et al., 2001), and 47.6% (Goto, Takahashi, Yamada, & Yamada, 2007). However, their work is operated based on the Miller cycle engine on a heavy-duty, large stationary engine. The best thermal efficiency produced by the current study is about 45% at 45 bar injection pressure and 2712 rpm. However, it is understood that the data is generated based on a transient response test of a speed-sweep test procedure. In contrast, all the reported test is believed to be performed based on stationary

testing. Nevertheless, the results demonstrated the high potential of the HPDI-CNG engine.

The BSFC is the ratio of the fuel mass flow rate to the output power of the engine. Figure 5.19 presents the variation of BSFC during the speed sweep test procedure for different injection pressure. Based on the graph, at all injection pressure, the BSFC plots showing a decreased trend as the time prolonged. The decreasing of BSFC is preferable as it indicates reducing fuel consumption. The efficiency of the engine is worst at the start-up, and it increases with the increased speed. The BSFC plots show a significant difference of magnitude at different injection pressure. The lowest injection pressure of 45 bar produced the lowest BSFC. And the highest BSFC is produced by the highest injection pressure of 60 bar. The maximum BSFC measured from the test is about 780 g/kWh at an injection pressure of 60 bar, and the lowest recorded is about 180 g/kWh at an injection pressure of 45 bar.

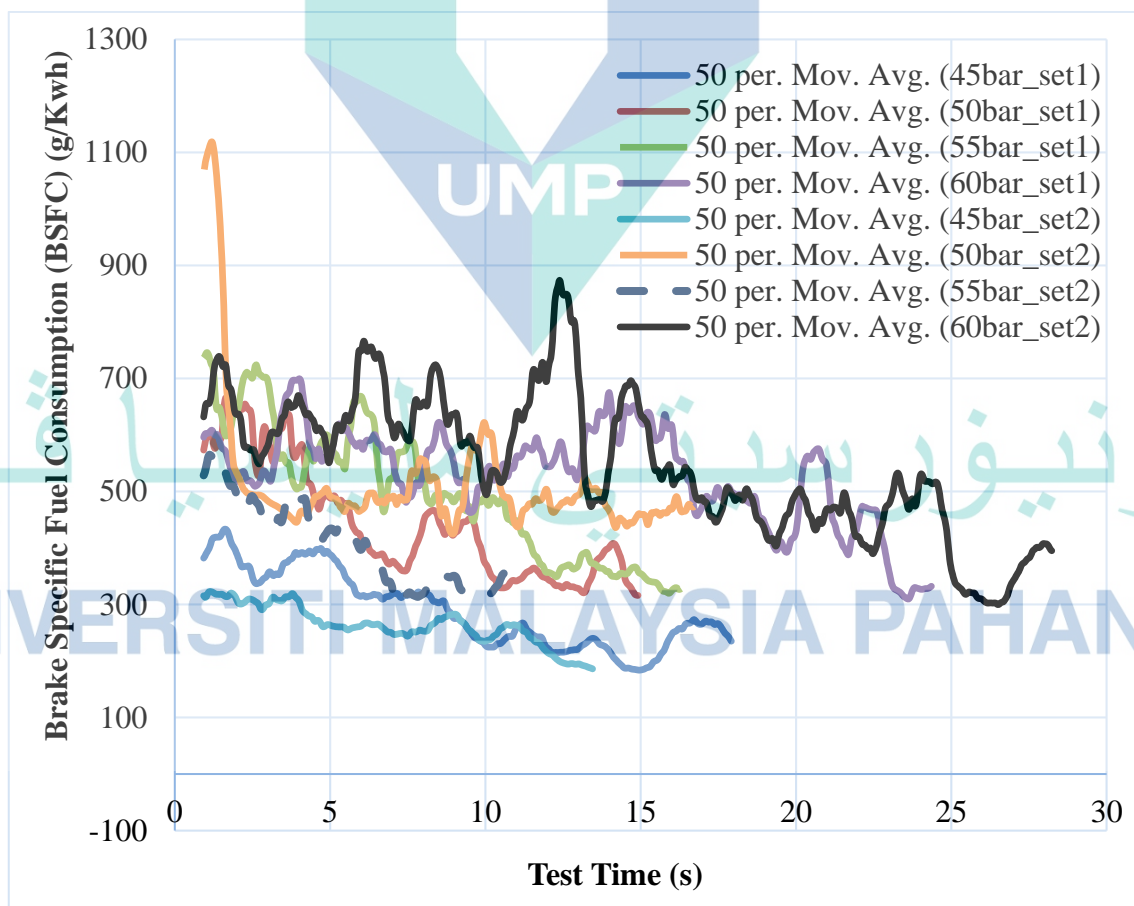


Figure 5.19 Brake specific fuel consumption of HPDI-CNG vehicle at different injection pressures

The BSFC trend of a typical normal aspirated SI engine generally decreases as the engine speed decrease, and it reaches the minimum BSFC point (most of the time coincident with the peak brake torque point) before increase again as the engine speed further increase. The typical trend mimics an inverse quadratic plot. Typically, the BSFC increases engine capacity and is lowest (the most desired) in the largest size engine (Pulkrabek, 2003). In comparison to the current engine results, as the speed decrease, the BSFC has decreased altogether. Still, the trend possessed no late increment since the engine speed and torque were limited to half of the actual gasoline performance.

Duggal et al. (2004) produced the lowest BSFC at a value of about 214 g/kWh. The overall range of the BSFC is between 214 g/kWh to 292.3 g/kWh. They utilise a Cummins ISX engine, six cylinders, 15 litres diesel engine. The engine has a 17:1 compression ratio. It is a conversion of a diesel engine to run on CNG. The engine is equipped with Westport Innovations Inc.'s High-Pressure Direct Injection (HPDI) natural gas fuel system used. The development target is to reduce the nitrogen oxides (NO_x) and particulate matter (PM) emissions while maintaining diesel-like efficiencies at full and part loads. Rashid & Firmansyah (2009) had reported a measurement of BSFC for a four-stroke, spark-ignition, single-cylinder engine. The engine was equipped with a single poppet valve injector, positioned at the centre of the cylinder head and operated within a range of common rail pressure in between 7.5 bar to 18 bar. They recorded BSFC values in the range of 250 g/kWh to 350 g/kWh in a speed range of 1800 rpm to 5000 rpm.

Based on these two previous studies, the current study yielded a better minimum BSFC as the HPDI-CNG engine produced a lower BSFC than the other direct injection CNG engines, either developed based on CI or SI engine platform. However, the maximum BSFC recorded in the current study clearly indicates overuse of fuel supply where the engine efficiency for work conversion is worse. It has happened when the highest CNG injection pressure of 60 bar is used. The over rich AFR is produced, and a large amount of the fuel supplied is wasted. It is expected that the reason for the condition is the lack of fresh air intake to oxidize the fuel.

5.4 The Operating Envelope and Detail Analysis of Influential Parameters

The operating envelope of a vehicle is defined based on the two most important parameters, the engine rotational speed and the manifold absolute pressure (MAP). These

two parameters define the operating point of the engine within the ECU maps. Other variables may be included to provide a more comprehensive definition of the limiting boundary. Table 5.2 provides variable limits, the mean and standard deviation (SD) for major variables measured during engine testing.

Based on Table 5.2, the minimum and maximum vehicle lateral speed of 24.88 km/h and 44.99 km/h corresponds to the starting and stopping test limit defined during the vehicle testing. All the data are recorded and only can be recorded within these limits. If the criteria cannot be met, then the test considered incomplete. Engine total torque is a sum of engine static torque and engine acceleration torque, whereas the static engine torque is a sum of parasitic engine torque and the power absorbing unit (PAU) torque, based on the designation of Mustang Dynamometer, MD250. The same designation is used for power. For the analysis and comparison purposes of the current study, only the total torque and power are considered.

Table 5.2 The measured variables and their descriptive statistics

	Variable Names	Units	Min	Max	Mean	STD
1	Vehicle acceleration	km/h/s	-2.10	3.17	0.74	0.90
2	Vehicle Speed	km/h	24.88	44.99	33.78	5.81
3	Air to fuel ratio	ratio	10.35	15.71	12.50	0.90
4	Air temperature	K	38.10	49.40	45.24	2.90
5	Barometric pressure	mbar	1019.0	1023.9	1022.6	1.57
6	Coolant temperature	deg C	9	8	2	11.22
7	Injector duty cycle	%	51.10	91.80	72.09	11.34
9	Engine Total Power WCF	kW	27.50	93.00	68.10	2.77
10	Engine speed	rpm	1568.0	3175.0	2357.6	396.88
13	Engine Total Torque WCF	Nm	0	0	3	9.05
14	Ignition timing	deg	15.21	69.06	40.87	3.84
15	Injection duration	ms	12.00	23.70	16.64	1.16
16	Injection pressure	bar	10.04	20.50	17.40	5.93
17	injection timing	deg	45.00	60.00	54.30	12.97
18	Manifold absolute pressure	kPa	473.60	521.30	485.63	3.43
19	Test time	s	-39.40	4.00	0.83	9.87
20	Throttle position sensor	Deg	0.00	38.55	13.09	27.28
21	Throttle position rate	deg/s	0.60	18.80	8.34	5.27

*WCF = with correction factor. **All the statistical data are derived by considering experimental data of 45 bar to 60 bar simultaneously.

Based on the presented results before, this section onwards presents a comprehensive discussion of the relationships between the measured engine parameters and engine brake torque. To verify whether all those parameters interacted with the output torque align with the hypothesis or oppose them. The discussion is vital to clarify what is the real cause which affects the low engine performances. It is also crucial to identify whether the system deviates from the ideal simulation results. Since the experimental data possess fluctuating trends, a few statistical variables are used to demonstrate the relationship more suitable. The mean, standard deviation and coefficient of variation of experimental data are calculated and use throughout the discussion.

Figure 5.20 presents the variation of mean engine brake torque at an increased injection pressure of CNG. Based on Figure 5.20, the averaged engine brake torque is inversely proportional to the CNG injection pressure within the tested range of 45 bar to 60 bar. The changes of both parameters can best be approximated by a quadratic polynomial of $T_{mean} = 0.099*(P_{cng})^2 - 11.261*P_{cng} + 356.97$. The relation is contradicted with the earlier theoretical simulation results where the CNG injection pressure (and the mass flow rate of the injector) is linearly proportional to the peak engine brake torque, as presented by Figure 5.6.

One reasonable possibility for the outcome is because the air intake is reduced as injection pressure is increased. As the high injection is used during the intake valve open condition, this directly affects the engine's volumetric efficiency and the amount of air intake. The air intake directly affects the engine brake torque through the mixture formation process. The air-fuel ratio of the CNG-air mixture must be produced within the CNG combustible range. The AFR, lambda, λ or the equivalence ratio, ϕ are commonly used to explain the air-fuel ratio of engine mixture. This proportion affects the combustion characteristics, engine performances and emission (Heywood, 1988).

The results also against the second hypothesis of the study which predicted an increment of engine brake torque if the injection pressure or the mass flow rate is increased. This contradiction indicates that the higher amount of fuel injected at higher injection pressure is not fully utilized and wasted. A more critical issue is to discover what is the reason for such a flaw.

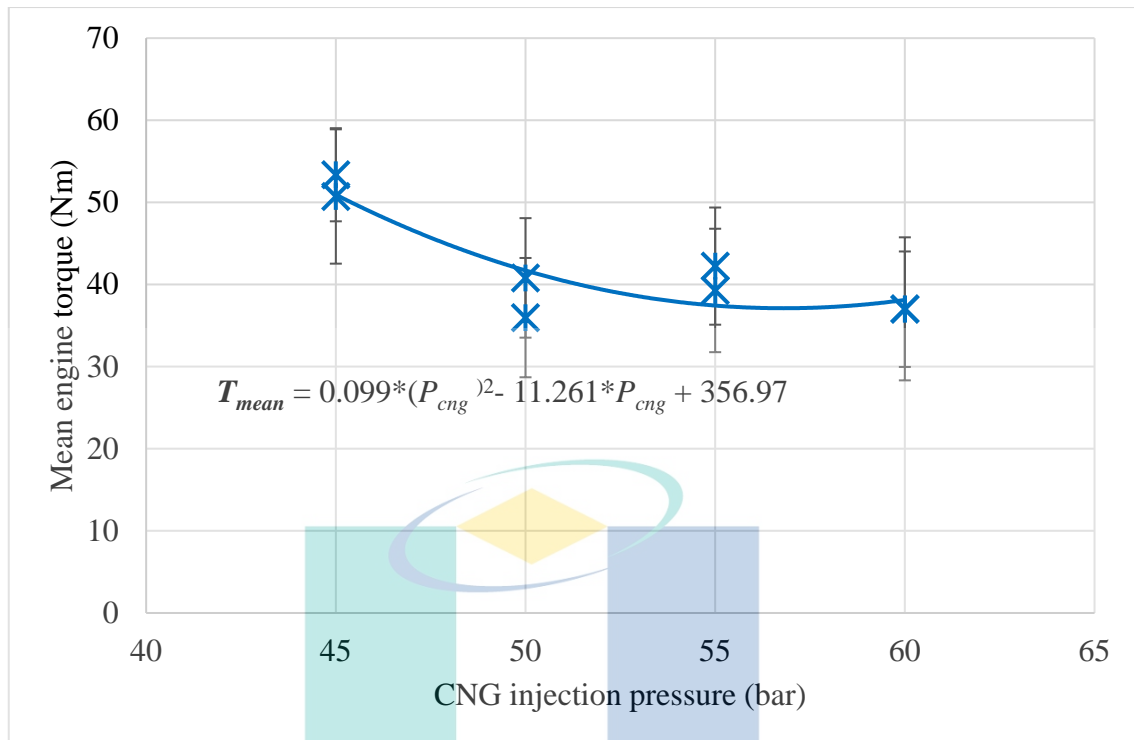


Figure 5.20 Variation of averaged engine torque at an increased injection pressure of CNG

Figure 5.21 presents the mean brake torque plotted against the mean AFR of the engine for injection pressure of 45 bar to 60 bar. Based on the graph, lower mean torque is produced when the mean AFR is rich, whereas higher mean torque is produced when the mean AFR is lean. The mean engine brake torque relation with the mean AFR is best approximated by the quadratic polynomial equation, $T_{mean} = 9.5027*(AFR_{mean})^2 - 229.43*AFR_{mean} + 1422.3$. The relation produced contradiction to the theoretical knowledge that the richer mixture is expected to provide higher torque than a leaner mixture (Pulkrabek, 2003). For gasoline fuel, the stoichiometric AFR for gasoline is about 14.7. At WOT, the AFR is made richer to a value of about ~12:1 (Heywood, 1988). In comparison, CNG has a stoichiometric AFR of 17. At the WOT, the best AFR for maximum torque might be occurring at about ~15:1. In the range of 12-13, the AFR can be considered excessively rich. Thus it is estimated if the AFR can be made leaner until ~15:1, the maximum torque can be obtained.

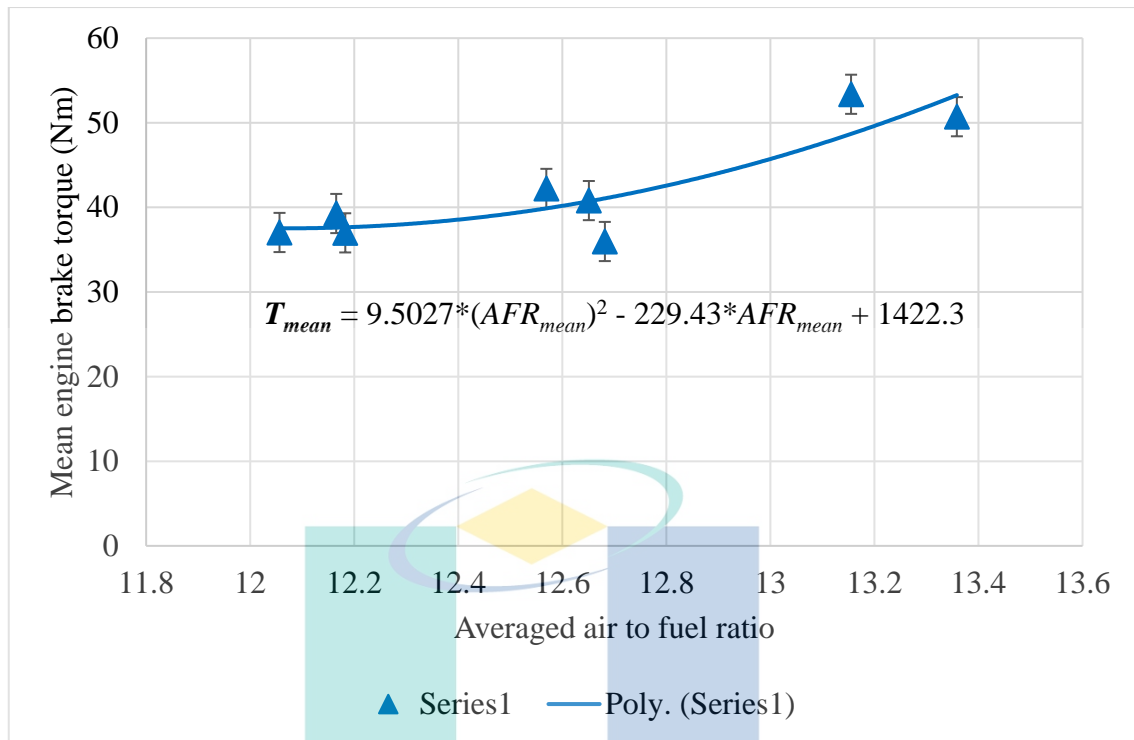


Figure 5.21 Variation of averaged engine torque at increased averaged AFR of cylinder mixture

Figure 5.22 presents the mean engine brake torque plotted against the mean injection duration of the engine measured for 45 bar to 60 bar injection pressure case. The mean engine brake torque poses fluctuation data at an increased injection duration. However, the scattered data is best approximated by a linear trend, $T_{mean} = 1.3098*t_{dur} + 19.087$. The line equation predicted a minor gradient equal to 1.3098 Nm/ms, producing a minor increment of the engine brake torque within the tested range. This minor increment agrees with the theoretical results of vehicle modelling, which produced a minor increment of brake torque when the injection duration increased. Hence, it can be concluded that the relation of engine brake torque to injection duration is following the theoretical trend since both plots demonstrated a minor increment of engine brake torque at increased injection duration.

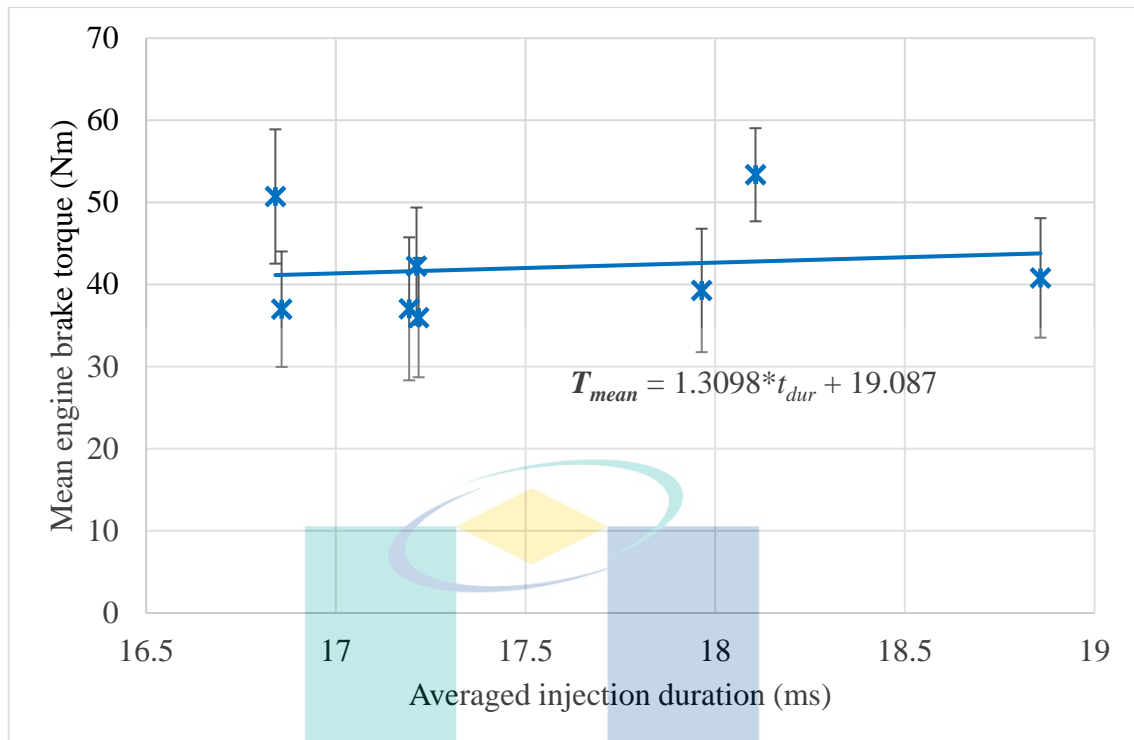


Figure 5.22 Variation of averaged engine torque at increased injection duration

Figure 5.23 presents the mean engine brake torque plotted against the mean spark-ignition timing advance. The mean engine brake torque possesses a fluctuated trend as the mean spark ignition timing is advanced. However, if a quadratic polynomial fits the scattered data, the resultant trendline matches the theoretical results of vehicle modelling (Figure 5.4). The mean torque of the experimental data is lower than the peak torque of theoretical simulation. Nevertheless, the trendline is following the theoretical prediction. The measured data of engine brake torque against ignition timing is best approximated by a quadratic polynomial equation of $T_{mean} = -0.9887*(t_{ign})^2 + 32.53*t_{ign} - 223.7$. An optimum mean spark ignition timing produces the best torque, which is estimated at 16.5 degrees BTDC. The value of the ignition timing advanced is controlled solely by the ECU based on the instantaneous engine rotational speed and manifold absolute pressure

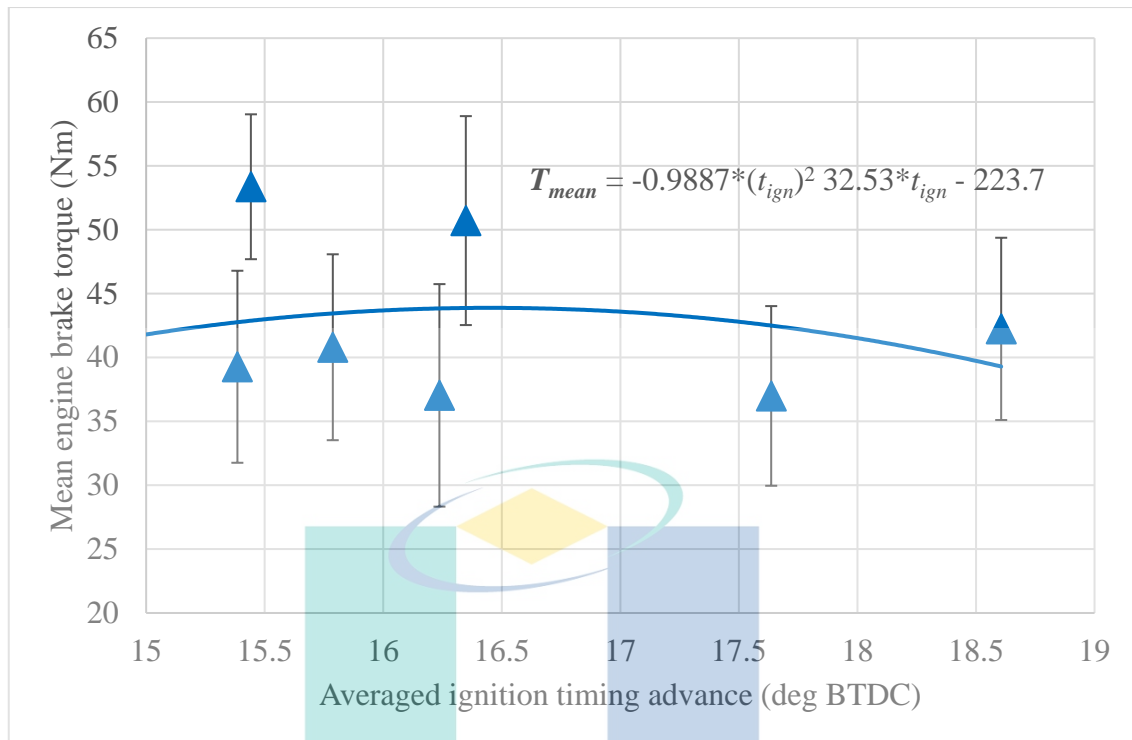


Figure 5.23 Variation of averaged engine torque at ignition timing advance

An engine could produce its best performances at MBT timings (Zheng et al., 2009b). To tune the ignition timing for MBT, one needs to identify the average cycle speed. Then the average cycle speed is set with the MBT. If the engine cycle is slower (low engine speed), the ignition timing must be advanced to speed up the cycle (to increase engine speed). If a cycle is faster (high engine speed) than average and requires slower growth, then the ignition timing should be retarded. Ignition timing also needs to be adjusted according to the mixture preparation strategy, either late or early injection timing. However, too retard timing, causing losses in power and efficiency. In the CNG direct injection engine application, the ignition timing advanced as much as 50° before top dead centre (BTDC) has been employed to compensate for the slow combustion of CNG-air fuel mixture (Mazlan, 2017). In comparison to the current results, the ignition timing set-up is too retarded. The setup is comparable to a spark-ignition gasoline engine at moderate engine speed. However, the selection of proper timing is limited by the hardware configuration. The previous finding during the in house engine testing, modifying the ignition timing far beyond the existing setup resulted in the engine misfiring and severe vibration on engine and vehicle body, and sluggish vehicle motion.

Figure 5.24 presents the theoretical calculation and the measured mean air mass flow rate, which is plotted against the injection pressure of 45 bar to 60 bar. The theoretical mass flow rate of air is calculated based on the speed density method by using the measured MAP engine rotational speed and manifold absolute temperature (MAT). The same formulation is used in the vehicle model for the calculation of MAP. In both usages, the MAP is limited to 4 kPa (abs), corresponding to the maximum sensible absolute pressure of the MAP sensor in the real hardware. On the other hand, the measured mass flow rate of air is calculated based on the exhaust gas analysis of AFR. First, the injector is assumed to produce a constant mass flow rate of CNG (based on the injector measurement) at specific CNG injection pressure. Then the mass flow rate of air is calculated based on the AFR equation using the CNG mass flow rate. The values produced by this method are close to the actual value of air intake since fewer variables are involved in the calculation.

Based on Figure 5.24, both the theoretical and measured results produced an increasing trend of air mass flow rate as the injection pressure is increased following the speed increment. The theoretical and measured AFR data can be represented by a trendline of $\dot{m}_{air,theo} = 0.1917 * p_{inj} + 15.983$ and $\dot{m}_{air,meas} = 0.1057 * p_{inj} + 8.3435$. The gradient for fitted lines are 0.1917 g.bar/s and 0.1057 g.bar/s which are considered close to each other. The major finding from the graph is there is a large difference between the theoretical and measured air mass flow rate, and the difference is almost consistent at all injection pressure. The mean percentage error between the theoretical and measured values are about 43%. This difference explains the difference between the theoretical peak brake torque (120 Nm) and the measured peak brake torque (69.059 Nm), with a mean percentage error of 42.45%. This close error is not merely a coincidence. 43% drop in air intake has resulted in a 42.45% drop of the maximum engine brake torque. Therefore, it can be concluded that the lower engine performance and the excessively rich AFR are because of insufficient air intake to oxidise the CNG fuel. The air intake is an important input of combustion. Its insufficiency will directly affect the mixture ratio and combustion performances (Heywood, 1988).

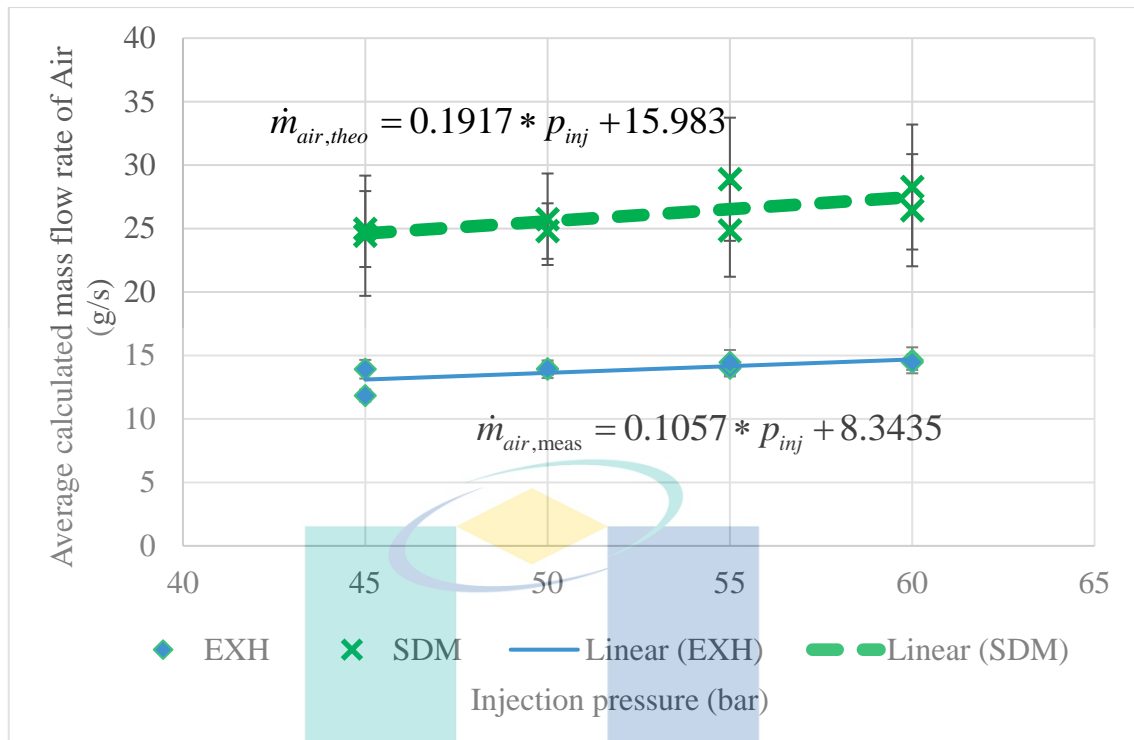


Figure 5.24 The averaged theoretical and measured mass flow rate of air at different injection pressures

Figure 5.25 presents the theoretical and measured mass flow rate of CNG at different injection pressure. Both the theory and measured mass flow rate of CNG produced a positive, proportionally linear trend of theoretical and measured CNG mass flow rate with increased injection pressure. The mean percentage error for the difference between the theory and measurement values is calculated as 47%. The gradient of the trend line for theory and measurement are 0.0263 g.bar/s and 0.019 g.bar/s, respectively. Both values are considered comparable to each other, and best represent the theoretical and measured data.

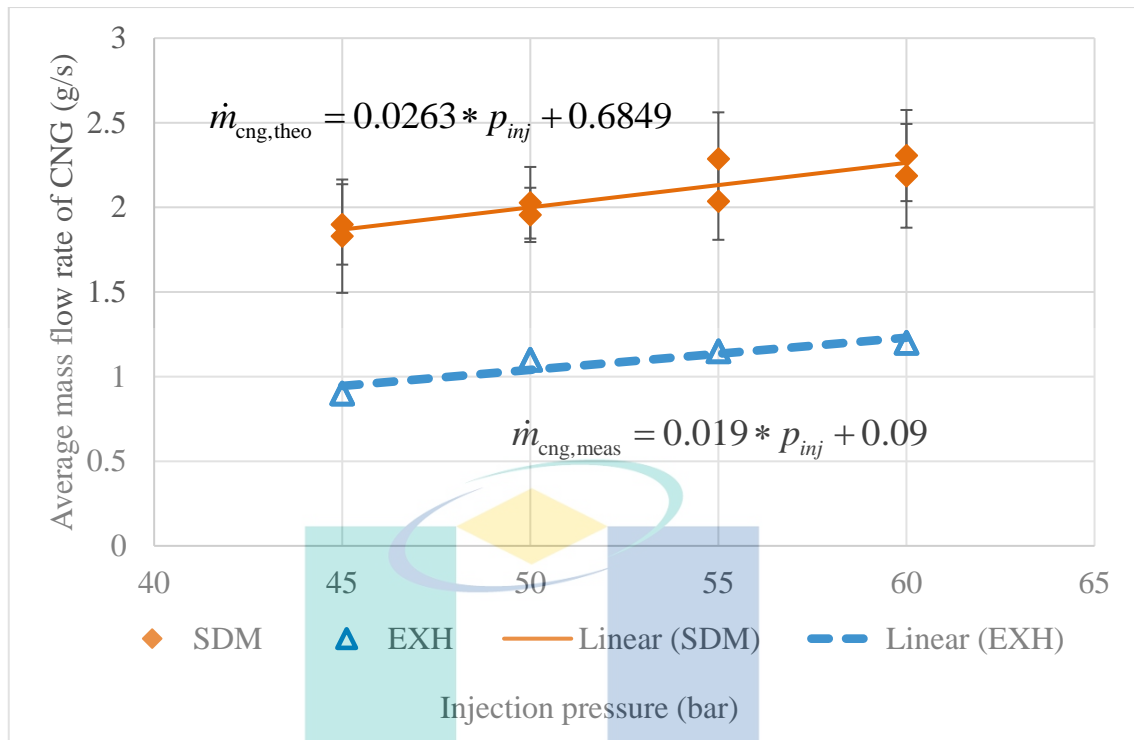


Figure 5.25 The averaged theoretical and measured mass flow rate of CNG at different injection pressures

The current section presents the comparison plot of the coefficient of variation for the engine brake torque and other parameters. There are three main parameters to measure the variability of each variable. They are variance, σ^2 standard deviation, σ and coefficient of variation (CoV). Standard deviation is preferred over variance because it is directly interpretable. However, the COV has an advantage over the standard deviation in multiple variables comparison. In an internal combustion engine, COV_{imep} is often used to characterise the cyclic variability of the engine combustion process. In the current section, the COV compares the degree of variability of engine brake torque and other engine parameters to clarify the parameters that affect the fluctuations of engine brake torque.

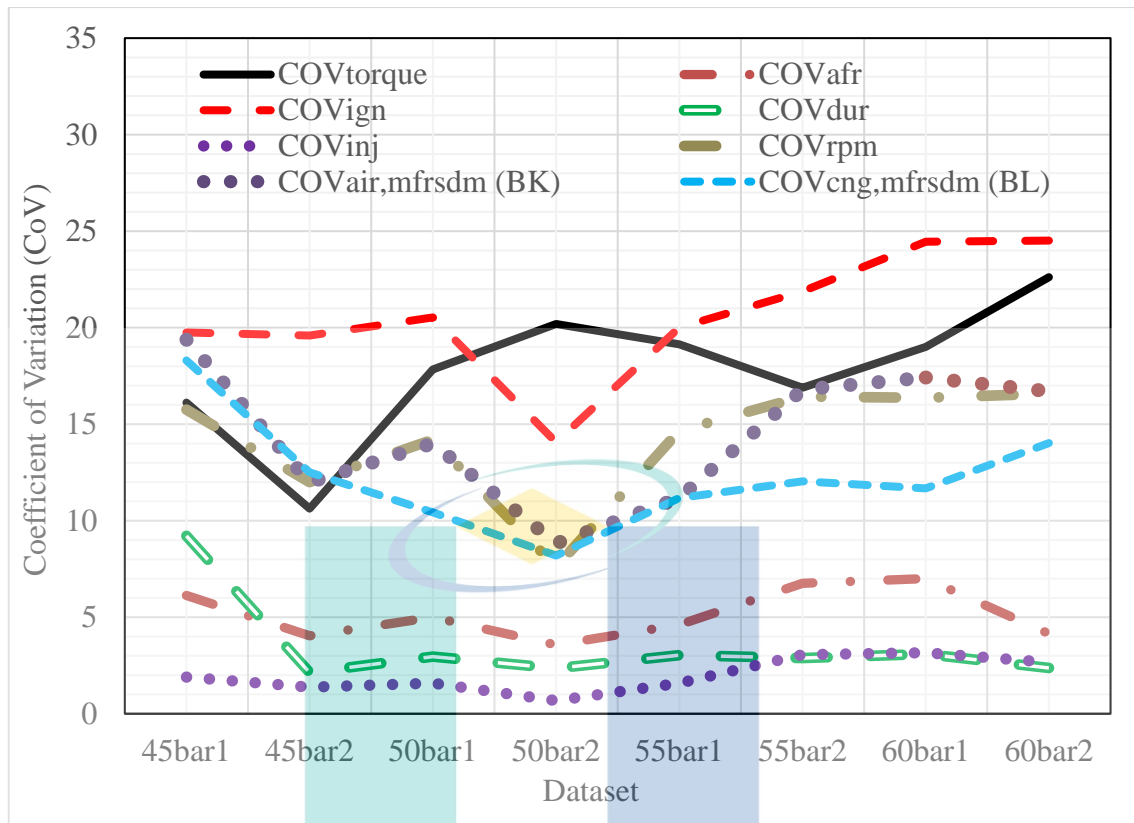


Figure 5.26 The coefficient of variation (COV) of engine brake torque and control parameters

Figure 5.26 presents the plot of the coefficient of variation (COV) of engine brake torque and the other parameters measured in the vehicle testing. Based on the graph, at least four parameters have the magnitude of COV in the same range and comparable to the engine brake torque. Those parameters are the ignition timing, the air mass flow rate, the CNG mass flow rate and the engine rotational speed. Other parameters such as the AFR, the injection duration, and injection timing produced COV values at a different range than the engine brake torque. There such a clear distinction of the COV values of the four parameters compared to the rest of the parameters. The COV of both groups almost does not intercept each other. However, it doesn't mean that they have no relation with the engine torque since the AFR is the air mass flow rate ratio to the fuel mass flow rate. In addition, the injection duration controls the supplied amount of CNG mass for combustion.

Air and CNG fuel is the raw input for the combustion process. Both directly affect the AFR of the cylinder mixture and consequently affect the combustion pressure and the output torque. Ignition timing defines the start of combustion. The beginning of CNG

combustion is very critical since CNG has a lower laminar flame speed. In most CNG applications, the combustion must start earlier than gasoline or diesel application to ensure that the CNG is completely burned close to the top dead centre position in order to extract maximum engine torque from the energy conversion during cylinder combustion. On the other hand, engine rotational speed is the engine output. However, the instantaneous speed output is measured and updated by the crank sensor and send back as the input to the ECU for the next cycle process. If the speed fluctuates, the other parameters such as ignition timing, CNG fuel injection, and even air intake process will fluctuate. Thus, we can conclude that the fluctuation of engine brake torque is not only affected by the fluctuation of AFR, such as hypothesise earlier in the study. But it is affected by multiple parameters since all these parameters, namely the ignition timing, the air mass flow rate, the fuel mass flow rate, and the engine rotational speed, are the major inputs for the combustion.

Based on the graph, however, it is clearly noticeable that there is one point where the COV of brake torque is high, and all the other parameters produced a minimum COV. In other words, all the combustion inputs have minor variability, but the variability of the torque is mounting high. It happened during the second set of data for the 50 bar injection pressure. We predicted the transitional condition between stable combustion at 45 bar injection pressure and unstable combustion at 60 bar injection pressure. The 60 bar injection pressure produce the highest COV for the engine brake torque.

Evaluation on the valve timing diagram, as shown in Figure 5.27, indicates that the end of injection (EOI) completed during/within the exhaust stroke (where the start of injection (SOI) might commence during the exhaust or power stroke). As a result, by the beginning of intake stroke, the in-cylinder pressure, which is already high, is becoming higher due to the mass transfer of CNG gases into the cylinder. Even though the piston moves downwards (the volume expanded), and the in-cylinder pressure is becoming lower, the in-cylinder pressure is still greater than the manifold pressure. Hence, this will end up with reduced suction capabilities and consequently lower the engine's volumetric efficiency. This drawback is the reason why the amount of air is insufficient to oxidize the fuel fully. The worst-case scenario is the backflow from the cylinder into the intake manifold, consisting of burned gases, fresh intake air, and fresh CNG fuel. Based on the experience during the testing procedure, it may happen because there were multiple

events of loud explosion in the intake manifold during stroking conditions at cold start. A probable solution to increase air intake is to boost the intake process (Chala et al., 2017).

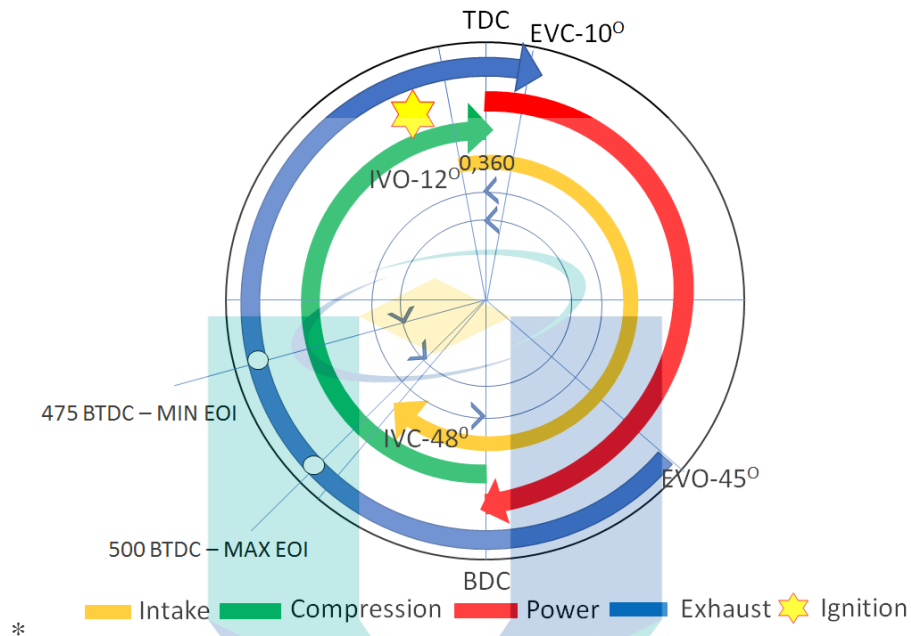


Figure 5.27 Valve timing diagram for HPDI-CNG engine and the location for minimum and maximum EOI

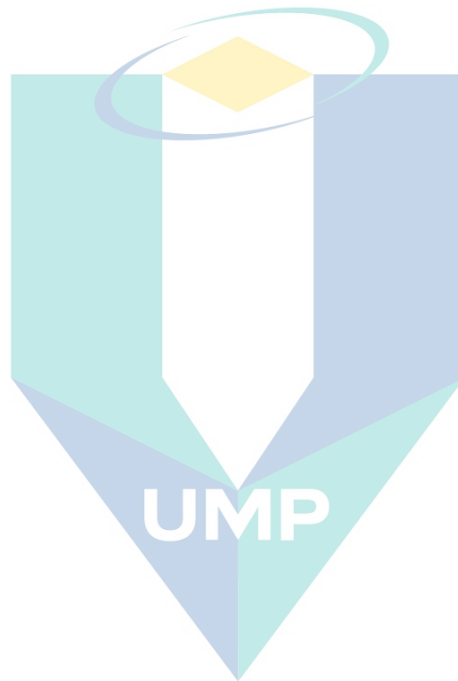
It is expected that the setup of the injection timing used for this direct-injection engine is still made within the framework of the port injection engine, which allows the injection process to commence during the all-valve opened condition. Indeed, this is the control strategy used in the port injection engine. However, it is preferred to start the injection process of a direct injection engine during the all-valve closed condition or during the compression stroke, as suggested by previous research. It will ensure no fuel short-circuiting to the exhaust, and no backflow occurred on the fresh air intake.

5.5 Summary of Results

The HPDI-CNG vehicle performance testing was carried out to assess the prototype vehicle's performance since no data had been documented before. The engine's operating envelope defined by the minimum and maximum MAP are -32 KPa and -4 kPa, respectively. The most advanced and most retarded injection timing are 5000 CA BTDC and 4730 CA BTDC. The shortest and the longest ignition duration are about 11 ms and 22 ms, respectively. The most advanced and most retarded ignition timing advances

are about 23 degrees before the top dead centre and 12 degrees before the top dead centre. And finally, the air to fuel ratios fluctuate in the range of 15.7 and 10.4. These data explain the operating envelope of the HPDI-CNG engine during vehicle testing or particularly the upper limit of the vehicle performance. The HPDI-CNG engine output produced lower performances compared to the same engine with the GPI technique. This low performance is demonstrated by the maximum engine speed, brake torque and brake power recorded as 3175 rpm, 69.06 Nm, and 19.10 kW, respectively. The maximum brake torque is less than half of 148 Nm, which is the maximum brake torque of the gasoline port injection version. The maximum engine speed of HPDI-CNG is also less than half of the maximum engine speed for the gasoline port-injection version, which is about 7000 rpm. One can conclude that the current configuration of CNG direct injection, which utilised the high-pressure CNG injection, is not effective in increasing CNG engine performance. The theoretical relationship between the peak engine brake torque and the mass CNG mass flow rate of the injection pressure is positive and linearly proportional (the same goes with the injection duration). This trend agrees with the second hypothesis, which predicts an increase in the CNG mass flow rate/injection pressure will increase the engine output brake torque. However, the measured results have shown a contradictory relationship with increased mass flow rate/ injection pressure; the engine brake torque was reduced when the tested pressure increased. It has happened because the measured air mass flow rates in the actual engine operation are lower than the theoretical air mass flow rate by 43% and thus resulted in the torque reduction of 42.45%. There are at least two main factors that affected the HPDI-CNG engine performances. 1) the ability of the fuel injection system to deliver fuel at the correct amount and time and 2) the air-breathing capability of the engine to induce the maximum amount of air in each engine cycle. Based on the results and discussions of the standalone injector test presented in Chapter 4, the averaged CNG mass flow rate fluctuated by using the existing driver setup. The air mass flow rate and the ignition timing of the engine also fluctuated. These fluctuations affected the engine AFR. The inefficiency of the fuel delivery due to the existing delay in fuel path resulted in lagged engine response hence lowered the maximum engine torque and engine rotational speed. In order to maximise the engine torque or power, predefined ECU maps can be tuned to obtain the optimal engine's operating setup. However, it is questionable whether the performance can be maximized based on the current injection configuration. However, the effect of delay is not quantified and beyond the scope of the present study. The air-breathing capability of the engine is

affected by the high CNG injection pressure, which is commenced partially from the exhaust and intake stroke at opened valve conditions. This condition creates excess pressure build-up in the cylinder, affecting the cylinder capability to induced fresh air. Hence, a lesser amount of fresh air is managed to be inducted into the cylinder. The next chapter presents the model-based calibration results, which generally consist of the data-driven modelling and model-based calibration results.



اونيورسيتي ملايسيا قهغ

UNIVERSITI MALAYSIA PAHANG

CHAPTER 6

RESULTS AND DISCUSSION OF MODEL-BASED CALIBRATION OF ECU MAPS

6.1 Introduction

This section presents the model-based calibration results, which generally consist of data-driven modelling and model-based calibration. In order of appearance, the optimization of the neural network structure is presented. The results correspond to the theory presented in Section 2.6 and the methodology presented in Section 3.7.1-3.7.3. It follows by verification of model-based calibration by simulation and vehicle testing. The results correspond to the theory presented in Section 2.7 and the methodology presented in Section 3.7.4-3.7.8.

6.2 Data-driven Modelling using Artificial Neural Network (ANN)

The data-driven modelling is performed based on available measurement data of the HPDI-CNG vehicle. A total of 4619 experimental data pairs were exported to the Matlab-Simulink and MBC Toolbox. The 4619 data pairs are the maximum number of data pairs accepted by the MBC Toolbox. The training datasets utilised 70% of the data pairs (corresponding to 3233 data pairs), whereas the validation datasets consist of the rest 30% (corresponding to 1386 data pairs) of the data.

6.2.1 Correlation Study between Brake Torque and Other Parameters

The data variables are analysed for correlation with engine output torque. The purpose is to select only influential factors to become model input. By properly ranked the variables based on the correlation strength, the most influential factor was first utilised as model input, followed by lower rank variables. At the addition of every variable, the modelling RMSE were check. In order to improve the modelling RMSE, more variables

are added. Table 6.1 presents the correlation coefficient calculated for the selected variables. The ranked variables shows that the vehicle acceleration produces the highest correlational strength with brake torque output. The vehicle acceleration is known to be proportional to the engine acceleration.

Measurement made by the chassis dynamometer explained that the acceleration torque dominates the total engine brake torque (during speed-sweep) compared to static engine torque. It explains why the vehicle acceleration has the highest correlational strength. The engine's total torque components consist of static torque, acceleration torque, parasitic torque, and power absorbing unit torque (Mustang, 2005). The rank is followed by injection pressure, barometric pressure, air to fuel ratio, and coolant temperature. The manifold absolute pressure and engine rotational speed are two variables that formed the axis/ norms of the look-up tables. Thus, regardless of the correlation coefficient estimated for the two variables, they must exist as the input factor to the data-driven model. The variables rank is then followed by the throttle position angle, ignition timing, duty cycle of the injector, air temperature, throttle position rate, injection timing, injection duration, and vehicle lateral speed.

Table 6.1 Ranking of the selected variables based on Pearson correlation

	Engine Torque	Engine Torque (abs)
Acceleration, a	0.75	0.75
Injection pressure, p_{inj}	-0.533	0.533
Barometric pressure, p_{baro}	-0.435	0.435
Air to fuel ratio, AFR	0.366	0.366
Coolant temperature, T_{cool}	-0.282	0.282
Manifold abs. Pressure, MAP	-0.198	0.198
Throttle position, θ_{thr}	-0.148	0.148
Ignition timing, t_{ign}	0.077	0.077
Duty cycle, DC	0.053	0.053
Air temperature, T_{air}	-0.04	0.04
Throttle position rate, $\dot{\theta}_{thr}$	0.038	0.038
Injection timing, t_{inj}	-0.035	0.035
Injection duration, t_{dur}	0.026	0.026
Engine speed, $\dot{\theta}$	0.022	0.022
Vehicle speed, V_{veh}	-0.005	0.005

Based on the prearranged approach, it is found that all the variables need to be utilised as the modelling factor to lower the RMSE and validation RMSE of the model. The targeted value of RMSE and validation RMSE were set to be as close as possible to zero. However, the order of modelling input is retained to follow the ranked correlated strength mapped with the engine torque.

6.2.2 Optimization of ANN Structure

This sub-topic presents the results of optimisation for optimum neural network structure. Figure 6.1 presents the contour view of the RMSE error function generated by the Model Browser using the RBF modelling method. X1 represents the number of neurons in the first layer, while X2 represents the number of neurons in the second layer. Based on the RMSE error function in Figure 6.1, the lowest RMSE of the RMSE error function is produced when the highest number of the neuron is used in the first and second layer of the ANN structure. This combination of neuron numbers will be penalised with high computation time as maximum allowable values are selected. Figure 6.2 presents predicted-observed data points for the RMSE error function by using the RBF modelling method. The modelled error function produced the RMSE, R^2 , and validation RMSE of 0.027, 0.024 and 0.027.

Figure 6.3 presents the contour view of the VRMSE error function generated by the Model Browser using the RBF modelling method. X1 represents the number of neurons in the first layer, while X2 represents the number of neurons in the second layer. Based on the RMSE error function in Figure 6.3, the lowest VRMSE is produced when a middle-range value of the neuron is used in the first and second layers of the ANN structure. The optimum range of X1 and X2, which give the lowest VRMSE, is between 10-30 for both layers. The middle of the plot's closed contour indicated the optimum range area for the VRMSE error function. The next plot in Figure 6.4 presents the predicted-observed data points for the VRMSE error function. The modelled error function for VRMSE produced the modelling RMSE, R^2 , and validation RMSE of 0.075, 0.058 and 0.135.

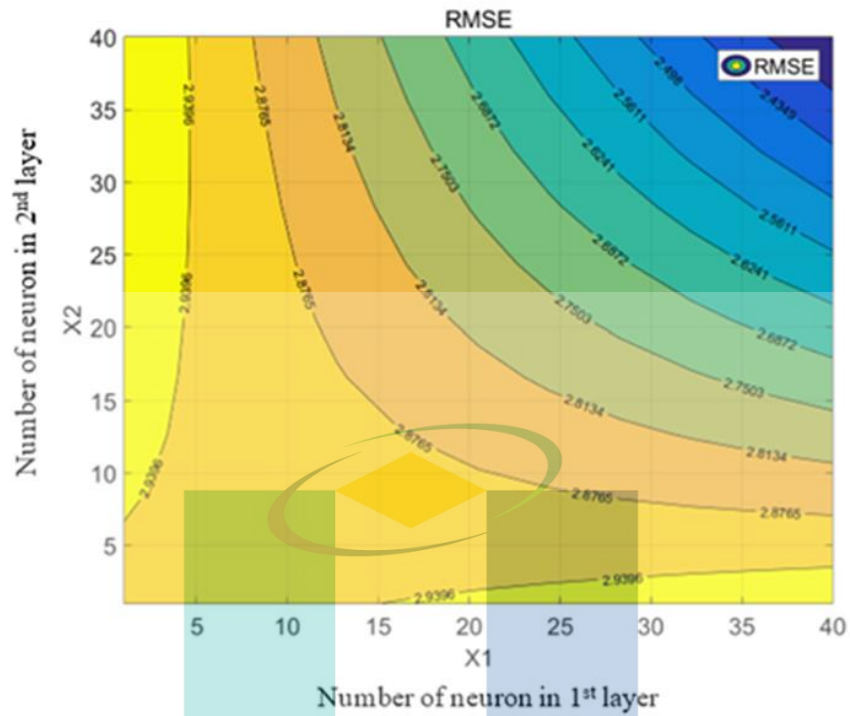


Figure 6.1
Browser

The contour plot of the RMSE error function modelled in Model

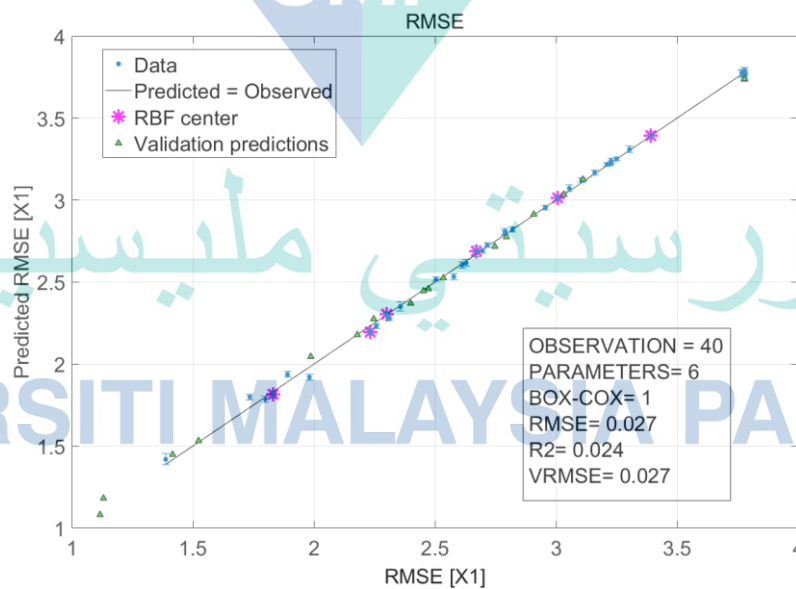


Figure 6.2
function.

Comparison of predicted and observed data points for RMSE error

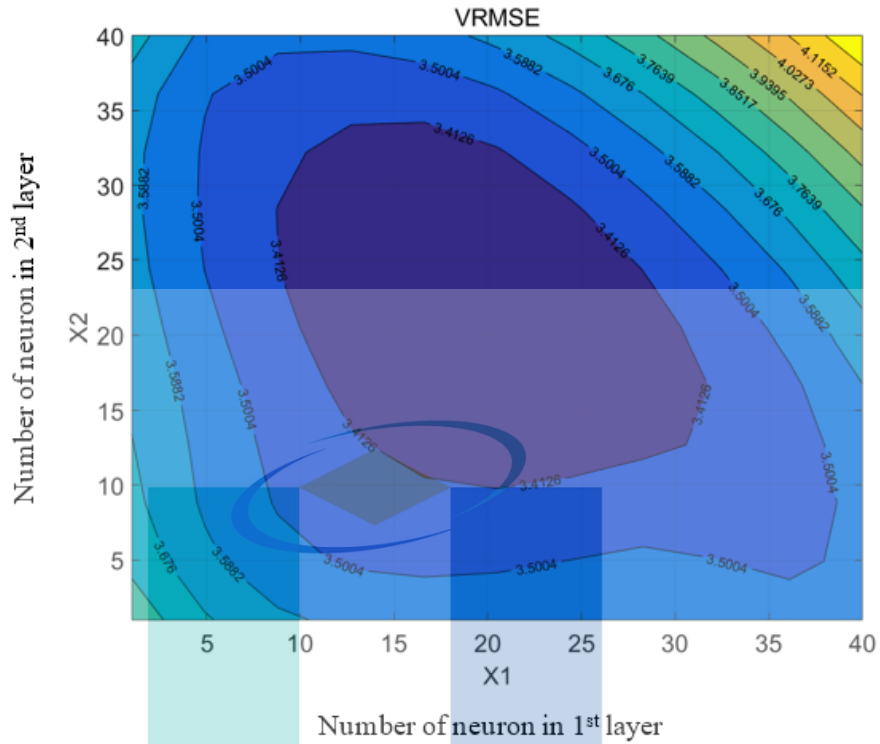


Figure 6.3 The contour plot of VRMSE error function modelled in Model Browser

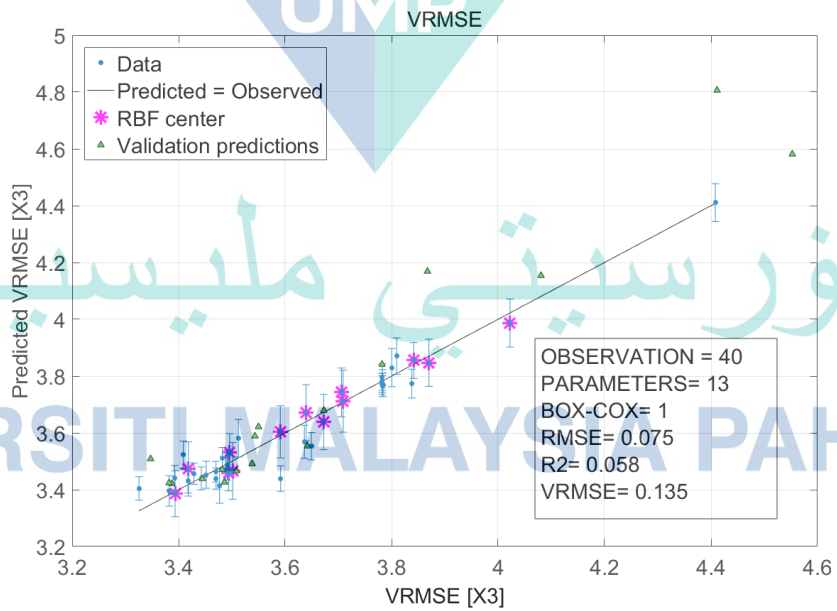


Figure 6.4 Comparison of predicted and observed data points for VRMSE error function

The error function of the training RMSE and validation RMSE produced an excellent agreement between the measured and predicted values. These are because the error distribution trends and values, which have common quasi-linear and quasi-quadratic surfaces, were easily predicted by the modelled function by using X_1 and X_2 as the prediction factors. Both the RMSE and VRMSE are required to be minimised to improve modelling accuracy and model overfitting. However, both error functions indicate a different location of X_1 and X_2 for minimum errors. A balance trade-off is difficult to be determined by using manual calculation; thus, a multi-objective optimisation is proposed to choose the optimum values for X_1 and X_2 . In multi-objective optimisation, the optimisation solver will seek to fulfil the requirement of combating the lowest RMSE and VRMSE while at the same time targeting the smallest number of neurons in both layers of ANN structure or the trade-off between the two objectives (Turkson et al., 2016).

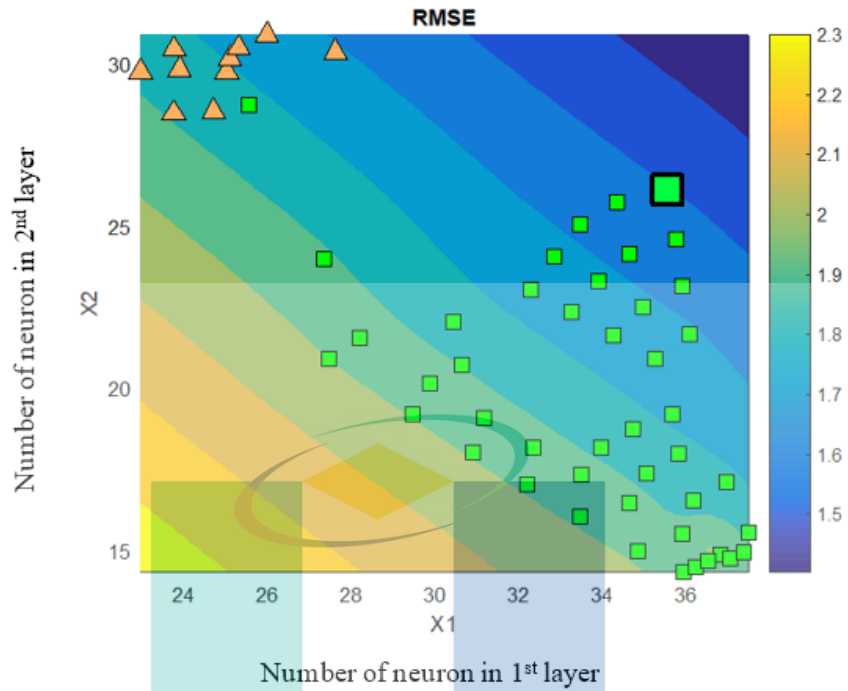
6.2.2.1 Optimum Artificial Neural Network Structure

The determination of an optimum number of neurons for the inner layers of ANN was performed by using Normal Boundary Intersection (NBI) method, as discussed in detail in Chapter 3. The optimisation aims to minimise the error produced by the RMSE and VRMSE error functions and minimise the number of neurons utilised in both inner layers. The optimisation was performed within the Calibration Generation (CAGE) environment. By the use of the CAGE optimisation procedure, the best solutions can be selected as the accepted possible solutions are readily listed in the highest to the lowest ranks. However, other graphical results may provide a broader overview of how the selected solutions are distributed.

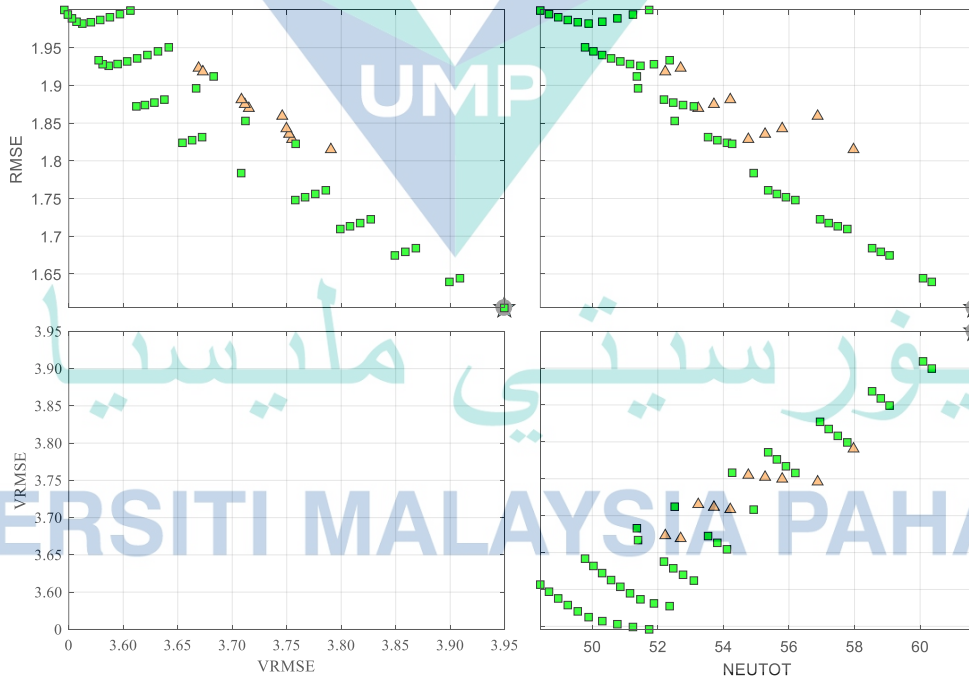
Figure 6.5 (a) presents the contour plot of the minimised RMSE with the accepted solution (green marker) and unaccepted solution (orange marker). The minimised RMSE is plotted as a function of the number of neurons in the first layer, X_1 and the second layer, X_2 . The black-square box marks the best solution. Most of the accepted solutions suggested the number of neurons in the first layers should be in the range of 25-38 neurons. At the same time, the number of neurons in the second layer is in the range of 15-30 neurons. However, the best combinations of neurons (which has the best trade-off of RMSE, VRMSE and NEUTOT) is found to be 35.551 (~36) and 26.103 (~26) for the first and second layers, respectively. The best solution for this optimisation produced the RMSE, R^2 , and validation RMSE equal to 1.605, 0.981 and 4.0, respectively.

Figure 6.5 (b) presents the Pareto diagram of the proposed solutions in terms of the objective functions. All these three objectives were provided with the same weightage. However, the solution is simplified by providing an unequal limit for each error. The limit for the VRMSE error function is made larger than the RMSE limit. Otherwise, no accepted solution can be obtained. This restriction is decided based on the modelling trend of ANN for this problem. Logically, a mid solution for each graph should fulfil each objective, but it is not attainable in practice.

Reproduction of the model with optimum network structure was carried out in the Model Browser and Simulink. The model is used to examine the ANN structure performances further. Figure 6.6 compares predicted and measured engine brake torque tested against the training and validation data sets reproduced within the Model Browser. The black straight line represents the condition where the prediction equal to the measured data. The plot showed that the predictions of the training data (in blue marker) spread along the equality line with the value of RMSE, R^2 , and validation RMSE equal to 1.501, 0.985 and 3.773, respectively. These values are slightly changed as X1 and X2 have been rounded to 36 and 26. The green marker is the validation data prediction which is spread at a greater distance from the equality line and corresponded to the larger value of validation RMSE. The red circled marker represents the outliers data point calculated by the modeller. Removal of this outlier may reduce the RMSE to 1.312 but have increased the validation RMSE to 3.867 as presented by the box in the plot. Based on the observation during the optimization work, dual inner layers improved the training MSE and validation RMSE. This combination is in agreement with the finding from the previous study (Wu et al., 2004). Wu et al. added that networks with three hidden layers do not show any improvement over the two-layer ANN. Thus, the present study suggests that the use of a dual hidden layer is sufficient.



(a)



(b)

Figure 6.5 (a) Contour plot of the minimized RMSE with the proposed solution as a function of neuron in layer 1 and 2 (b) The Pareto front of the optimization which highlight the proposed solutions in terms of the objective function.

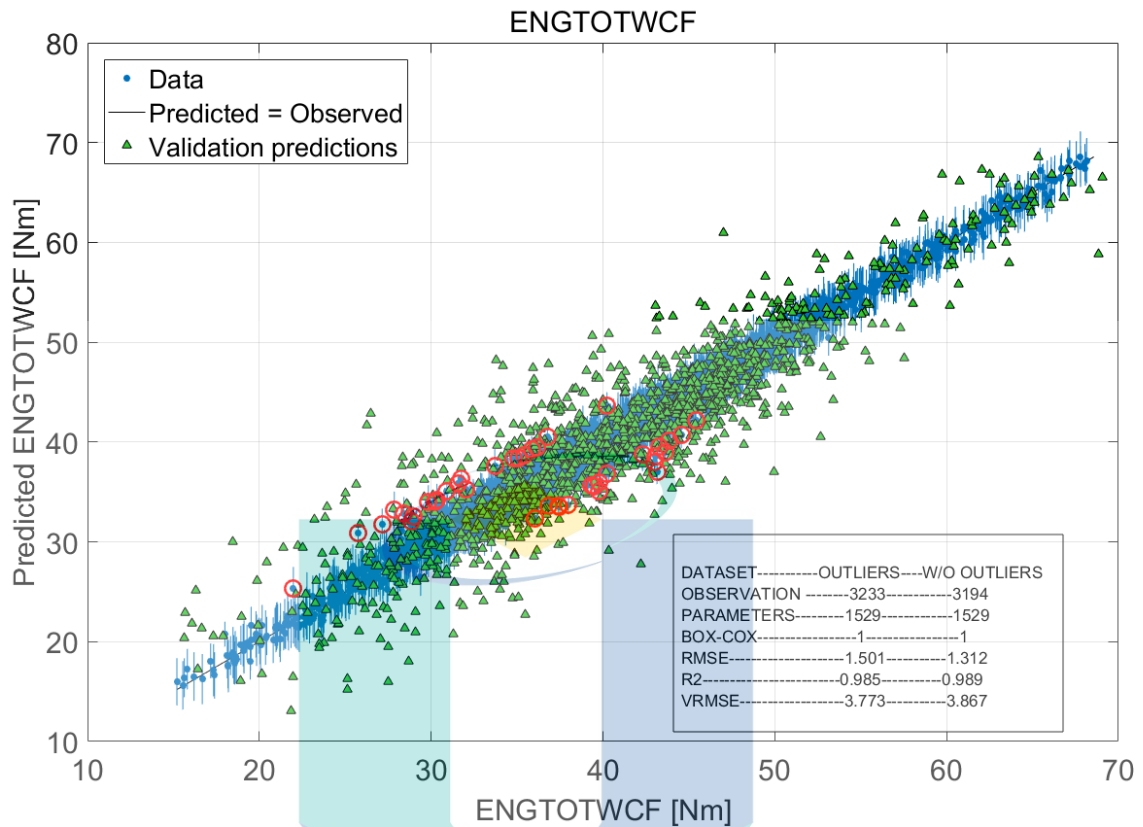
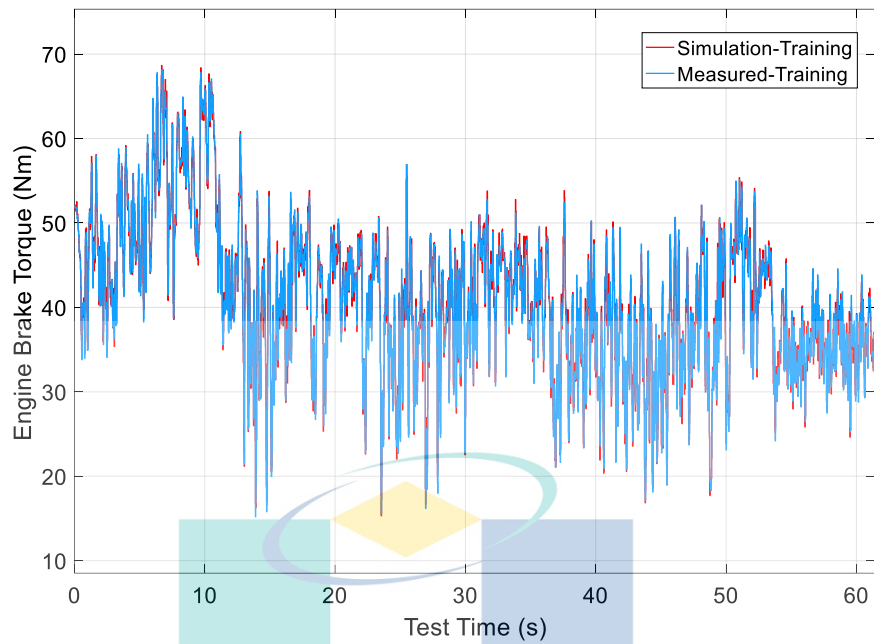


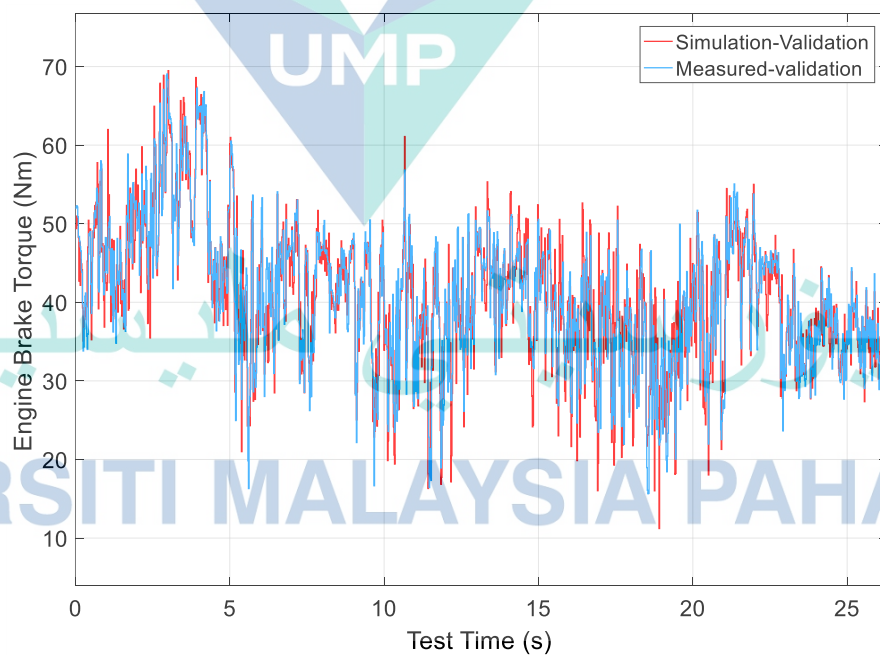
Figure 6.6 Comparison of predicted and measured data points of the best ANN structure using training and validation data sets reproduced in Model Browser

The Simulink model based on the optimum ANN structure were also simulated based on the training and validation data sets. Figure 6.7 and Figure 6.8 presents the comparison of measured and simulated engine brake torque based on the training and validation data sets. It is observed that the simulation has produced a good prediction of the training data sets, as presented in Figure 6.7. Both the measured and simulated data almost overlaid each other. The simulation prediction produced an RMSE of 1.111Nm, which is smaller than the predicted RMSE of the Model Browser. The improved accuracy is due to the rounded of the X1 and X2 values and the different solvers used to simulate the engine's operation. Other factors are expected to have a significant impact on the model calculation. The model's MAPE, MAE and MPE are about 2.182%, 0.8246Nm and 0.12%, respectively.



Training Error			
MAPE	MAE	RMSE	MPE
2.182%	0.824 Nm	1.111 Nm	0.12%

Figure 6.7 Comparison of simulated and measured engine brake torque by using training data sets for the optimum ANN structure



Validation Error			
MAPE	MAE	RMSE	MPE
7.593%	2.798Nm	3.773Nm	0.36%

Figure 6.8 Comparison of simulated and measured engine brake torque by using validation data sets for the optimum ANN structure

The simulation of the optimum model performed based on the validation data sets produced lower accuracies than expected since the original model suggested by the CAGE solver also has lower accuracy for the validation data sets. Based on Figure 6.8, the prediction values are sometimes over predicted and underpredicted the measured data, especially at the peak and bottom point of the torque spike. The RMSE for the simulation prediction is 3.773Nm, equal to the RMSE produced by Model Browser before removing the outliers. Whereas the MAPE, MAE and MPE for the prediction are 7.593%, 2.798Nm and 0.36%, respectively. The recorded accuracy scores for the validation data sets are almost lower than the training data sets.

In summary, the ANN modelling technique is found to be a powerful technique for the prediction of engine brake torque response. It is concluded based on the comparison of engine torque response, produced by ANN technique, offered by MBC Toolbox. Based on the quantitative error evaluation for the ANN prediction in the Simulink simulation, the range of RMSE, MAPE, MAE and MP as presented by Table 6.2 are produced. The results produced by the ANN data-driven model is excellent by considering that the engine is ill-performed where the brake torque fluctuates along the transient test period. The predicted trend follows the measured engine data closely. However, to achieve such accuracies, a total of 14 inputs have been used as the model factor. Comparable accuracies have been demonstrated in the previous study (Atkinson & Mott, 2005; Atkinson et al., 2008, 2010; Atkinson, 2014) based on the ANN modelling technique. The ANNs model was able to capture the transient data fluctuation excellently. The fluctuations happened to be a regular trend in dynamic and transient engine data based on the reported results in these references.

Table 6.2 The quantitative error evaluations for data-driven modelling

Training And Validation Error			
MAPE	MAE	RMSE	MPE
2.182-7.593%	0.8246-2.798Nm	1.111-3.773Nm	0.12-0.36%

6.3 Model-based Calibration of ECU Maps

The optimized ANN structure is transferred to the CAGE environment, and the associated setup, as explained in Section 3.7.4 until 3.7.8, are executed to complete the model-based calibration procedure. The calibration results are visualized to demonstrate the optimized surface of ECU parameters. Surface before and after the optimization are examined. More crucial steps are to verify that the optimized ECU parameters contributed to enhancing HPDI-CNG vehicle performance.

Two verification methods have been selected. The first approach is carried out by using a simulation technique based on the data-driven model in Matlab-Simulink. The second approach is to embed the optimal setup into the actual ECU and performing the vehicle testing on a chassis dynamometer. In both techniques, the effect of optimal ignition timing, injection duration, and injection timing setup have been evaluated and justified. However, implementing optimal setup in the actual hardware is very challenging where several trials failed, and certain components were damaged and replaced. In early tests, the vehicle run in sluggish and shaking motions; hence no data can be recorded. This failure happened for a few reasons; 1. The wrong selection of optimisation constraints, and 2. the absence of data reverse-correction before embedded in the ECU hardware. These findings are important since every data set collected from the ECU during the initial testing has been corrected for ambient and engine conditions.

6.3.1 Visualisation of Calibration Results

The 45 bar injection pressure case plots are selected to demonstrate the visual results of the optimization calibration process. Figure 6.9 and Figure 6.10 present the surface plot of BSFC before and after the optimization calibration process. The BSFC is plotted as a function of engine rotational speed and manifold absolute pressure (MAP), where both are used to define the operating point within the real ECU hardware. By comparing the plot of BSFC, it is evident that the optimisation by GA has successfully minimised the BSFC surface to produce a different BSFC surface contour. The high BSFC area is only produced at a low engine speed region. As the engine speed is increased, the optimiser expected a reduction in BSFC at medium engine speed, especially at medium to full load conditions. Overall, BSFC is expected to be reduced in comparison to the baseline data.

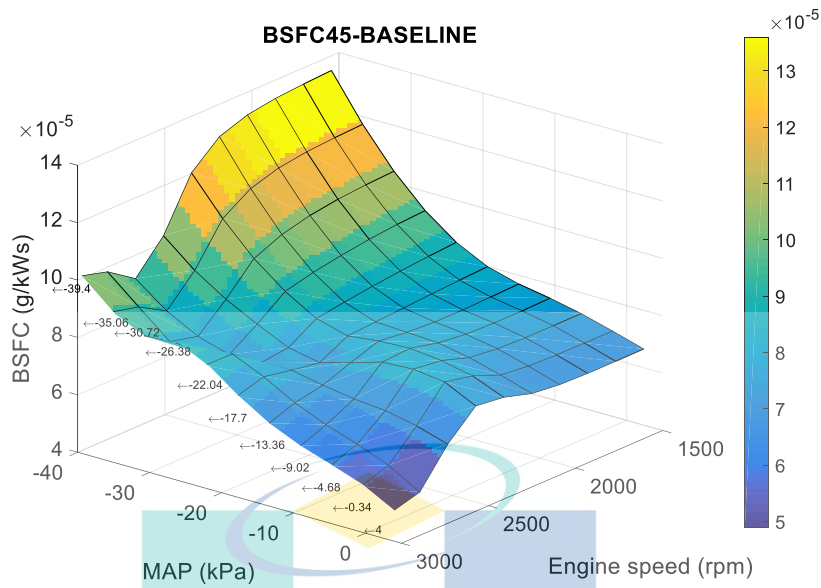


Figure 6.9 Surface plot of BSFC (the objective function) before the optimization-calibration process for the case of 45 bar injection pressure

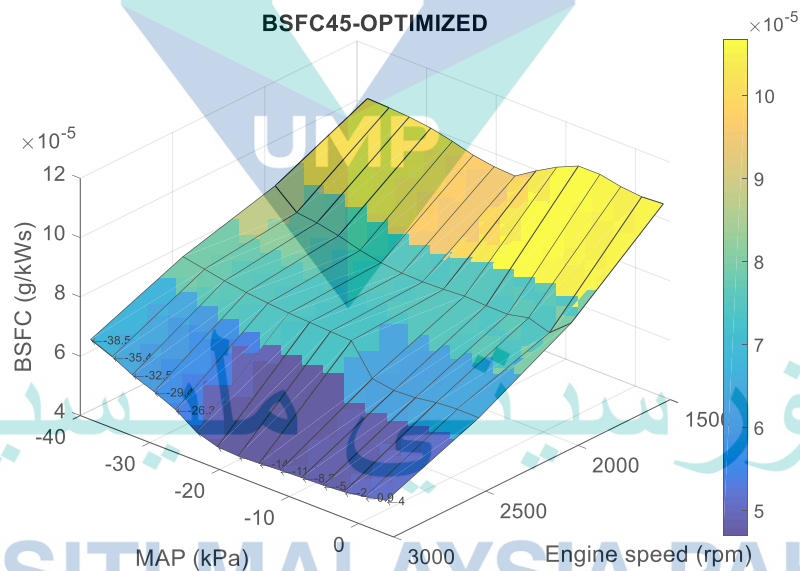


Figure 6.10 Surface plot of BSFC after an optimization-calibration process for the case of 45 bar injection pressure

Figure 6.11 and Figure 6.12 present surface plots of ignition timing as a function of engine rotational speed and MAP before and after the optimization calibration process for the case of 45 bar injection pressure. The trend of ignition timing before and after optimisation is almost similar, where the ignition timing is expected to be advanced as the engine speed is increased. Practically, the spark advanced is required to be advanced to cope with the shorter combustion duration at high engine speed. The only visible difference in spark timing surface is the convex-like surface of ignition timing before the optimisation and the concave-like surface after the optimisation. This difference is related to the rate of ignition timing increased. The optimised maps tend to produce a slower rate of timing increased at low engine speed and a higher rate of timing increased at medium engine speed. This difference is expected to produce a smooth driving condition at a low engine speed where spark timing changes minimally affect the engine torque.

It is known that, as engine speed increases, spark advance for maximum brake torque (MBT) also advanced. Spark timing was retarded as MAP increased. The knock was a limiting factor at lower engine speeds. At speeds higher than 3500 rpm and MAP less than 20 kPa, a spark advance of 40 deg BTDC was necessary to produce significant torque (Everett, 2011). These are in agreement with the current results of optimized ignition timing. Increased engine speed increases/ advanced the ignition timing. Whereas increased (more positive) manifold absolute pressure retarded the ignition timing.

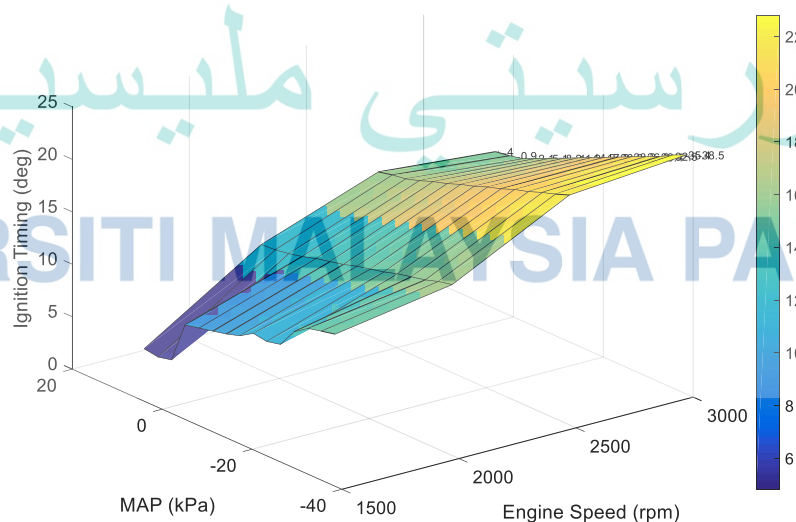


Figure 6.11 Surface plot of ignition timing (the optimise variables) before the optimization-calibration process for the case of 45 bar injection pressure

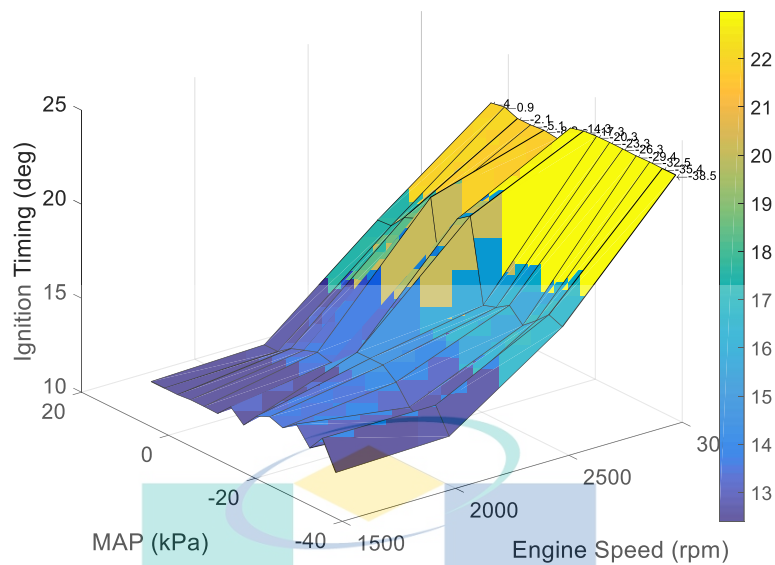


Figure 6.12 Surface plot of ignition timing after the optimization-calibration process for the case of 45 bar injection pressure

Figure 6.13 and Figure 6.14 present the injection duration surface plot as a function of engine rotational speed and MAP before and after the optimization calibration process for 45 bar injection pressure cases, respectively. The surface plot of injection duration before and after the optimization calibration process is slightly a different response surface. Long injection duration is utilised at the maximum MAP at each engine speed in the baseline surface plot. Whereas at the minimum MAP, a shorter duration is used regardless of engine rotational speed. Since the duration is theoretically proportional to the mass of fuel injected and the engine brake torque, it is expected that the peak brake torque should be produced during the maximum MAP condition. It is also corresponding to the WOT condition. It is also noticeable that the injection duration is also increased with the increase of engine rotational speed. The range of baseline duration is within 8-15 ms. The surface trend is likely to be appropriate for the typical operation of a normally aspirated internal combustion engine.

The original response surface is in agreement with the surface of fuel flow by Everett (2011), where the fuel flow is increased with increasing engine speed and engine brake torque. The engine brake torque is comparable to the MAP since MAP is directly proportional to the throttle opening angle in representing engine load. In order to generate higher engine torque or to overcome higher load, the throttle angle must be increased, which resulted in increased MAP before its constant at WOT. And as the brake torque is

increased, the resultant engine rotational speed will increase altogether without any brake or frictional load.

The surface, however, has produced a different surface topology of the injection duration concerning the objective function to minimise the BSFC of the engine and its predefined constraint. In the optimised injection duration surface, the range of injection duration is elevated to the range of 16-19.5 ms. It means that more fuel is supplied in the optimised condition, especially in the mid-range of engine rotational speed. However, at low-range speed and medium-range speed, a lower injection duration is used. Hence, it is expected that the peak torque point is produced in the mid-range region of engine rotational speed.

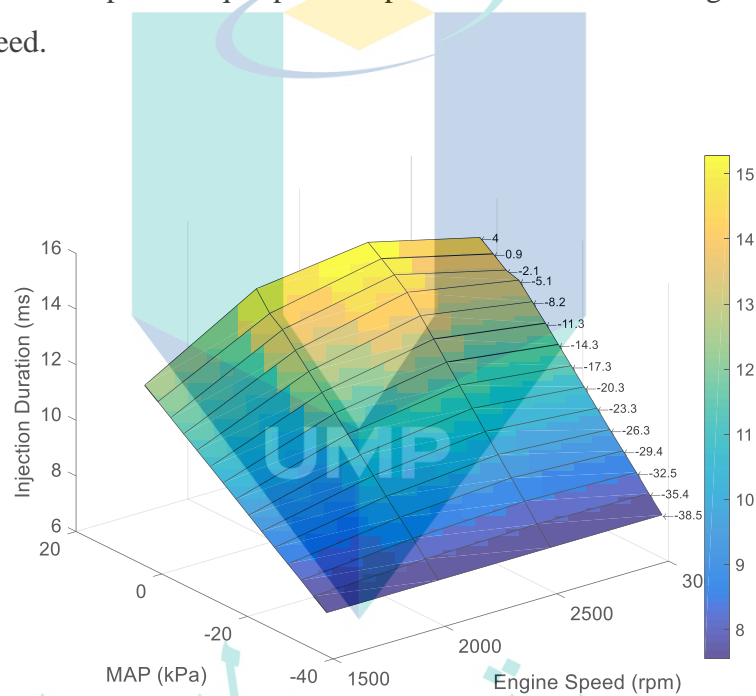


Figure 6.13 Surface plot of injection duration (the optimise variables) before the optimization-calibration process for the case of 45 bar injection pressure

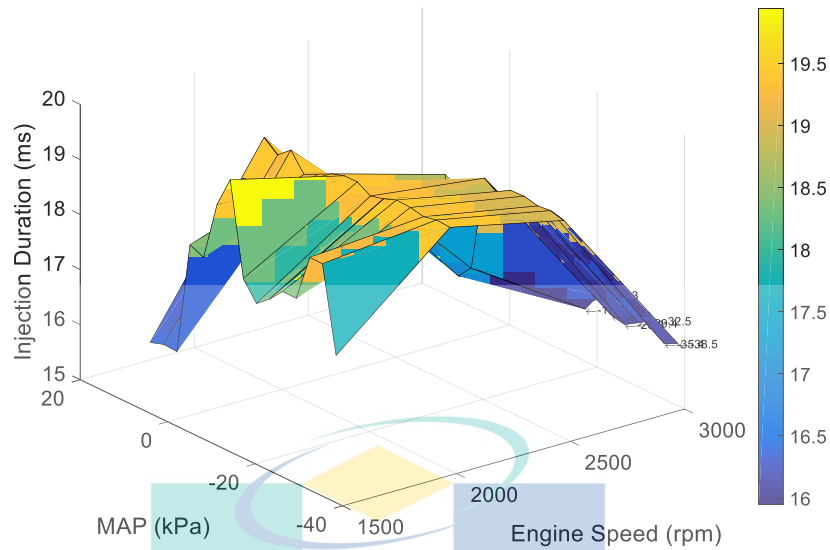


Figure 6.14 Surface plot of injection duration after the optimization-calibration process for the case of 45 bar injection pressure

Figure 6.15 presents line plots of baseline and optimize injection timing (which is defined as the end of injection (EOI) before and after the optimization calibration process for the case of 45 bar injection pressure. Both the baseline and optimised injection timing have the same trend before and after the optimization calibration, where the injection timing was uniformly increased. At 2500 rpm, both setups changed the increment rate, and the baseline injection timing overtook the optimized timing. The immediate effect of increasing the end of injection angle is raised of the time window to complete the injection process. This addition allows the fuel injection process to be executed for a longer time, and more fuel can be injected into the engine. The trend is equivalent to advancing the start of injection (SOI) as the engine speed, or load is increased (Chen et al., 2019; Keskinen et al., 2016)

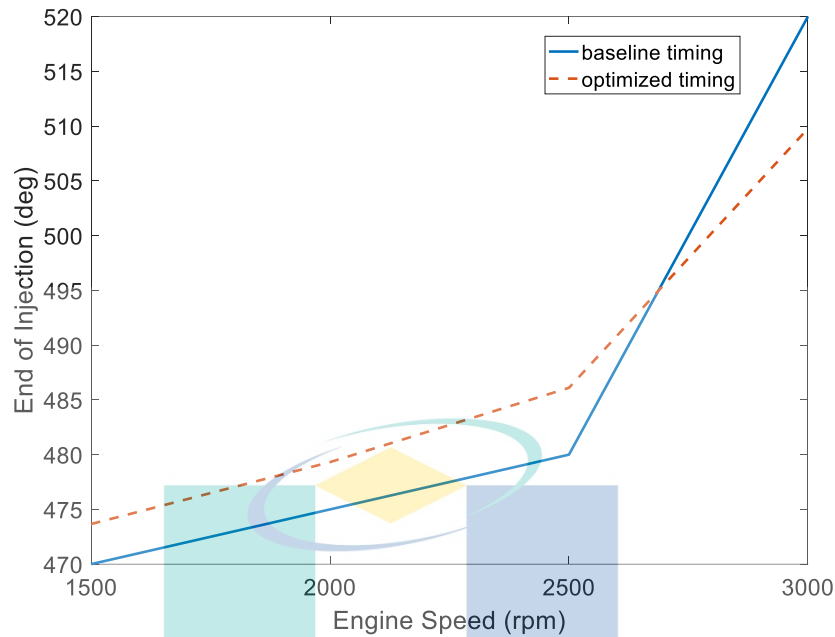


Figure 6.15 Line plot of injection timing (the optimise variables) before and after the optimization-calibration process for the case of 45 bar injection pressure

6.3.2 Verification by Simulation

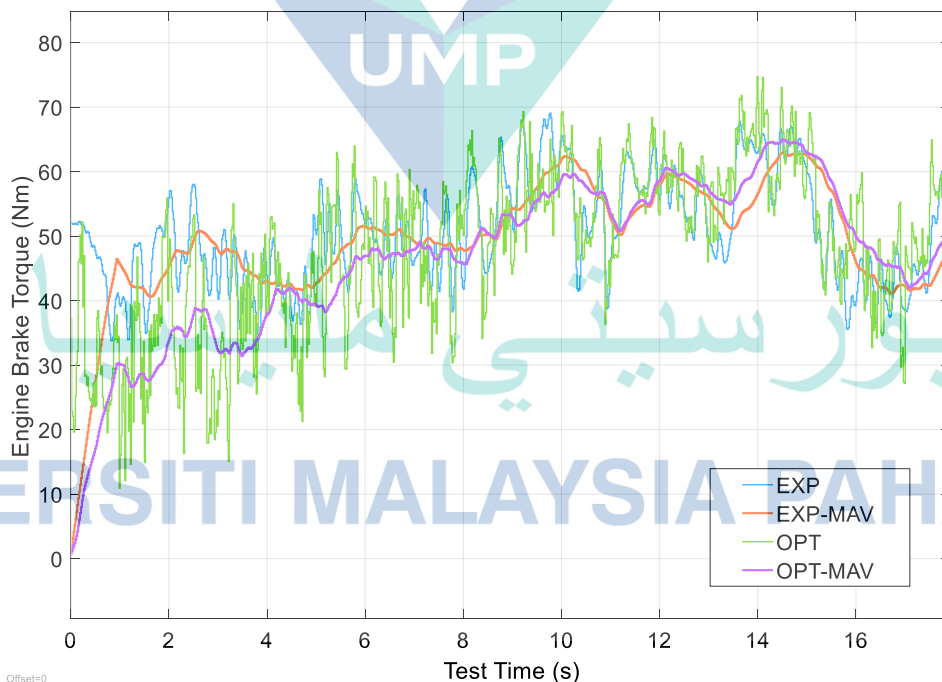
The ANN model was exported to Simulink for verification of ECU base map parameters. The comparisons were made between the measured and optimised engine brake torque. Four cases were selected to demonstrate the effectiveness of the optimisation process for injection pressure setup of 45 bar, 50 bar, 55 bar and 60 bar. To implement the optimal map parameters, the Simulink model is modified to include the look-up table element on the input side.

Figure 6.16 presents the comparative plot of engine brake torque for the optimised and baseline 45 bar injection pressure cases. The optimised engine brake torque is still fluctuating as the optimisation constraint imposed has not included any particular technique for suppressing the fluctuation. Average trendlines are plotted together to provide better visibility for the comparison purpose. In the early test time, the baseline engine torque is higher than the optimised engine torque. However, at about after the 8th second, the optimised engine brake torque started to produce comparable data to the measured engine brake torque. The corresponding MAPE, MAE, RMSE and MPE is 14.25%, 6.80Nm, 9.411Nm and -5.77%.

In a comparison of the modelling prediction and measured engine data, the value of the error matrices is desired to be as small as possible since it indicates a higher

accuracy. However, it is always desirable to have the error as significant as possible in an optimisation comparison, which means a larger improvement. The optimised data is always higher than the baseline. In a case where, at a certain point, the optimised data is lower than the baseline data, the use of absolute or squared error may produce a misled interpretation.

For example, the Mean Absolute Percentage Error (MAPE) in the current plot is valued as 14.25% does not mean an average improvement of 14.25% over the baseline data. This misleading is because the MAPE formulation always sums up the absolute error regardless of whether the optimised engine brake torque is lower than the baseline data. It implicates that the significantly lower optimised torque in the early test time might have dominated the mean absolute percentage error. On the other hand, the Mean Percentage (MPE) always considers positive and negative errors, causing the total error to be balanced. It also resulted in the MPE value becoming smaller most of the time. It also implicates that, even though the negative error might occur in a very short range of time. However, if the negative error value is large enough, it still can produce a huge impact on the final value of the mean percentage error.

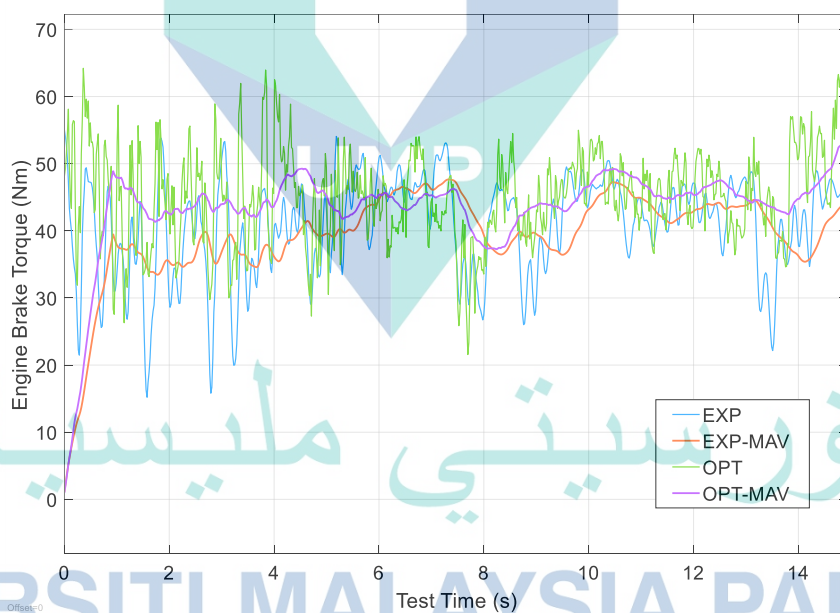


MAPE	MAE	RMSE	MPE
14.25%	6.80Nm	9.41Nm	-5.77%

Figure 6.16 Comparison of optimised engine brake torque with the baseline torque for injection pressure of 45 bar.

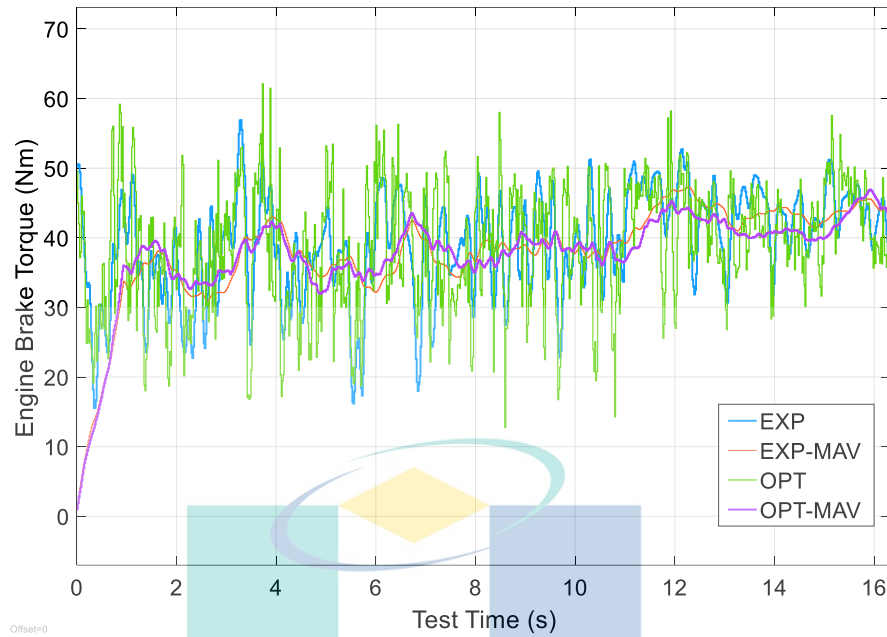
Figure 6.17 presents the comparative plot of engine brake torque for the optimised and baseline 50 bar injection pressure cases. The optimisation outcome shows a significant improvement of engine brake torque for most of the test time. The resultant errors based on MAPE, MAE, RMSE and MPE are 18.86%, 6.846Nm, 8.61Nm and 13.53%, respectively. The tabulated errors for the current case are more convincing since, most of the time, the optimised engine brake torque is higher than the baseline engine torque.

Figure 6.18 presents the comparative plot of engine brake torque for the optimised and baseline case of 55 bar injection pressure. Based on the figure, the case of 55 bar injection pressure produced a minor improvement compared to the baseline engine data. However, the plot of optimised engine brake torque produced an almost similar plot of the baseline engine brake torque. The corresponding MAPE, MAE, RMSE and MPE are 15.03%, 5.5Nm, 7.08Nm and 0.1976%, respectively.



MAPE	MAE	RMSE	MPE
18.86%	6.85Nm	8.61Nm	13.53%

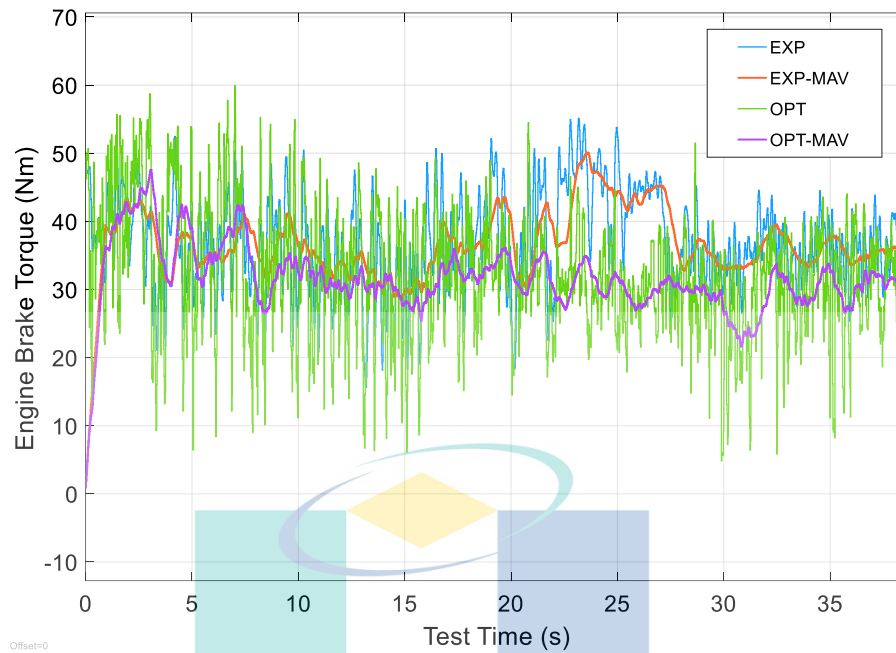
Figure 6.17 Comparison of optimized engine brake torque with the baseline experiment for injection pressure of 50 bar.



MAPE	MAE	RMSE	MPE
15.03%	5.50Nm	7.08Nm	0.1976%

Figure 6.18 Comparison of optimized engine brake torque with a baseline experiment for injection pressure of 55 bar

Figure 6.19 presents optimised engine brake torque with the baseline experiment for the injection pressure of 60 bar. In the current case, a similar condition as injection pressure of 45 bar is found, where after the 5th second test time, the optimised engine brake torque underperforms the baseline engine data at a considerable error distance. It caused the mean percentage error, MPE, to drop to -12.81%. The other quantities, MAPE, MAE and RMSE, are calculated as 21.85%, 8.104Nm and 10.14Nm.



MAPE	MAE	RMSE	MPE
21.85%	8.104Nm	10.14Nm	-12.81%

Figure 6.19 Comparison of optimised engine brake torque with the baseline experiment for injection pressure of 60 bar

These simulations verify that the optimisation procedure is feasible to improve engine performance, at least for the case of 50 bar and 55 bar based on the calculated Mean Percentage Error (MPE). The comparison of simulated results also demonstrated the optimised engine torque trend relative to the measured engine brake torque. However, the brake torque and power curve didn't resemble a typical torque and power for a standard CNGDI engine, such as demonstrated by previous studies (Aslam et al., 2006; Kalam & Masjuki, 2011). This discrepancy existed because the ANN model used in the verification is an accurate model replicating the HPDI-CNG vehicle's ill-performed engine. The improvement made is more vital than the predicted trend. The following verification stage is to implement the optimised engine maps/look-up table data into the real ECU hardware and test using a chassis dynamometer.

6.3.3 Verification by Actual Hardware

Verification of optimal setup has been executed by embedded the optimal ECU parameters into the programmable ECU on the test vehicle. Two cases were selected to demonstrate the effect of optimisation results on actual vehicle performances. The two

cases are the 45 bar (case with a significant error and MP value is equal to -5.77) and the 50 bar (case with the optimised brake torque is higher than the baseline data) injection pressure setup. The biggest challenge of the verification stage was to adapt the vehicle prototype and the instrumentation with a new chassis dynamometer unit.

The new chassis dynamometer is a tuner-class dynamometer made of Dynamite, which has a single roller of 16 inch diameter. The unit equipped with a specialised dynamometer controller and data acquisition system. The verification test setup consists of Innovate AFR meter, dynamometer dedicated controller and data acquisition, and Haltech ECU data logger. Figure 6.20 presents the dynamometer used for the verification test. This dynamometer unit is a different unit compared to the model used in the initial data collection.



Figure 6.20 Experimental engine setup for the verification of optimal setup

The uncertainties due to changing of the chassis dynamometer made and set up during the initial data collection, and optimal verification are evaded by measuring and recording new sets of baseline vehicle data before and after optimal setup implementation. The older data which were used during the modelling stage is no longer valid for comparison purpose.

The verification tests are still carried out by the use of speed sweep test procedures in which the engine is allowed to speed up and accelerate through the test window while the engine parameters such as torque and power, AFR and ECU quantities were recorded. Another crucial challenge was that the ignition coils were repeatedly burned multiple

times. These failures have disturbed the execution of verification tests and limiting the amount of verification data collected at the end of the process. A few months later, it is discovered that every time the maps are updated, the ECU connection to the coil must be disconnected and switched ON at first before restarted for the actual engine operation.

Figure 6.21 presents the throttle opening input imposed on the vehicle during the course of the verification test. These are among the best-recorded throttle input since the throttle input was maintained at 100% throttle angle opening. The problem of preserving the throttle opening is the car's sluggish motion, which shaken the driver's body and finally implicated the pedal position consistency.

Figure 6.22 and Figure 6.23 present a comparison of measured, optimised and baseline engine brake torque for injection pressure of 45 bar and the plot of their corresponding error, respectively. These two cases are the two cases that were selected and entirely recorded during the verification test. The moving averaged trend line is plotted to produce better visibility of the averaged parameters since the actual data of engine torque is fluctuated.

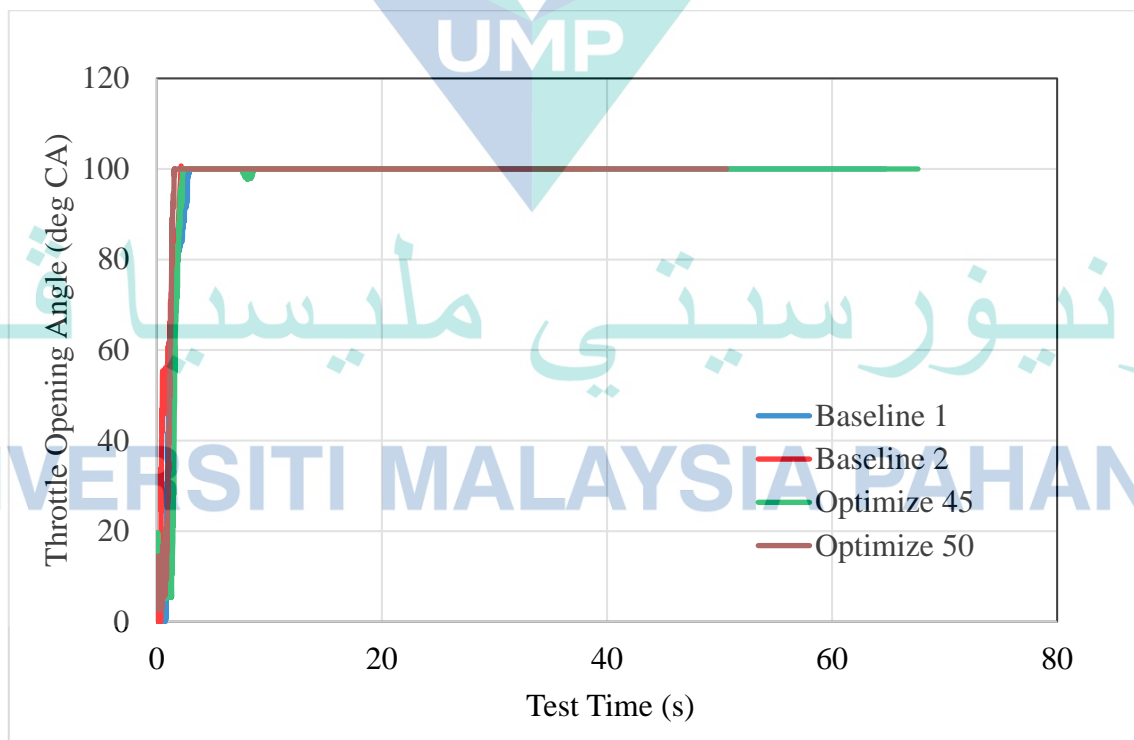
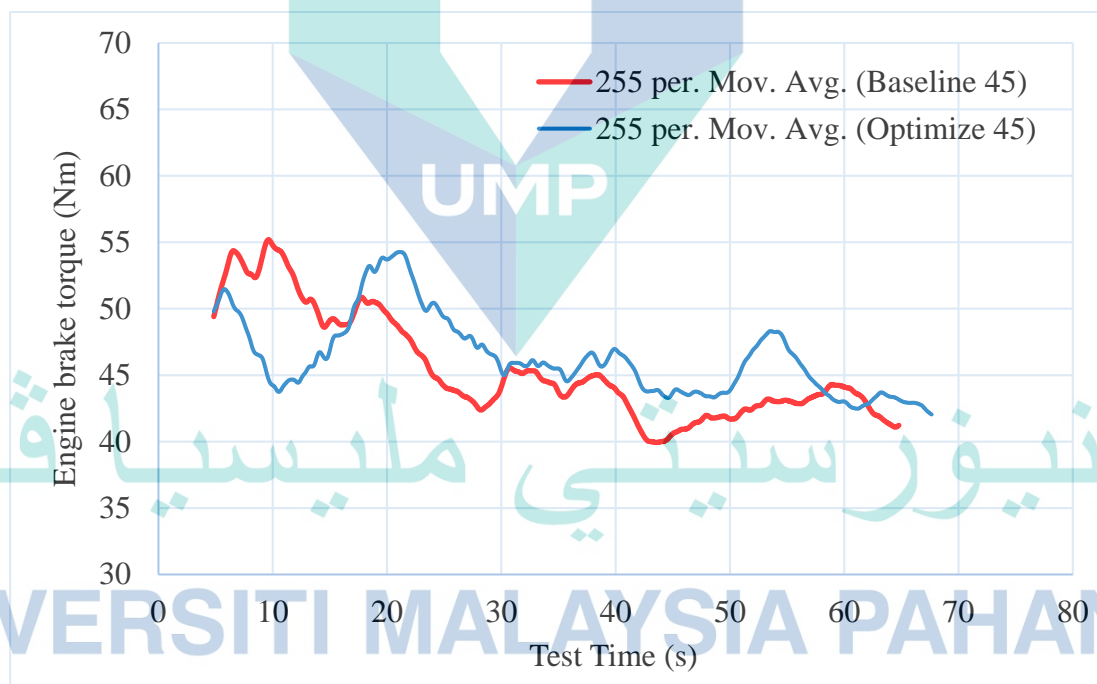


Figure 6.21 The throttle opening recorded during the verification test for the baseline and optimised case

Based on Figure 6.22, the optimal setup torque is considered higher than the baseline torque from an overall view except for the time range of 0-20 sec. Within this range, the maximum torque values produced by the optimal setup is significantly lower than the baseline. This trend is in agreement with the simulation results. The timing for the maximum brake torque in the optimal setup test is shifted later than the baseline case. The shifted maximum torque point is purely due to the changes in the map values after the calibration. Based on the error plot in Figure 6.23, the MAPE, MAE and MPE errors for the comparison are 10.02%, 4.62Nm, and 3.27%. The line plot of the MAPE and MPE is purposely plotted to explain the calculated error. The error trace on the y-axis (dashed line) negative side represents the actual percentage error when the negative error is considered. In contrast, the reflected error (continuous line) is the absolute percentage error. These two errors affected the calculated mean values error.



MAPE	MAE	MPE
10.02%	4.62Nm	3.27%

Figure 6.22 Comparison of the optimized engine brake torque and the baseline case for 45 bar injection setup

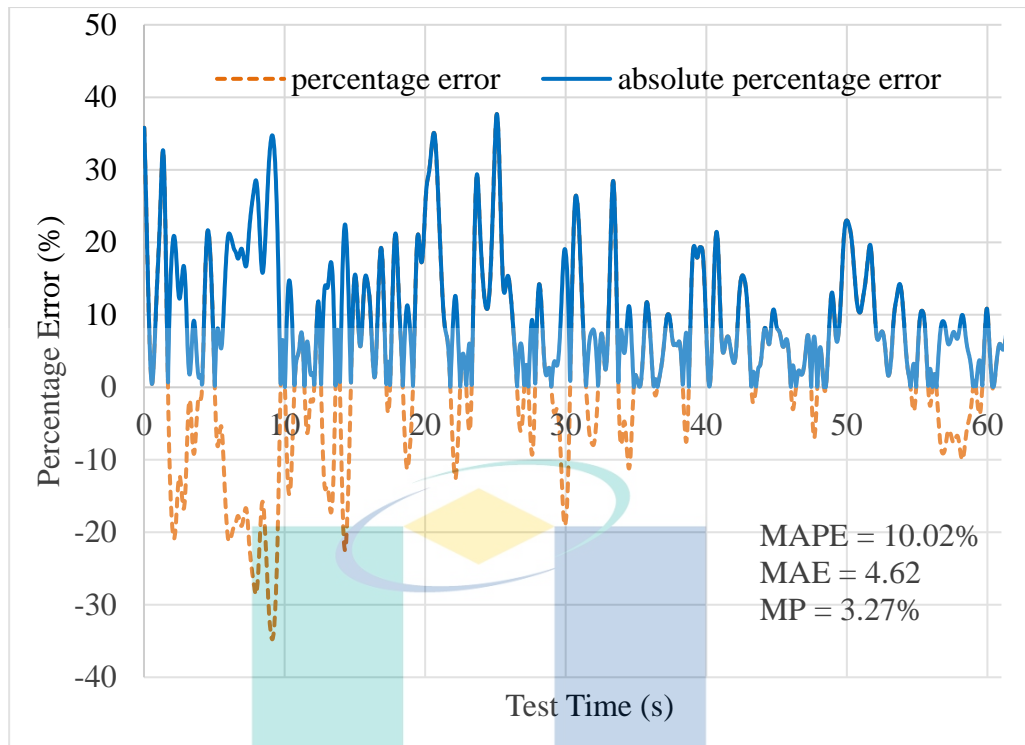
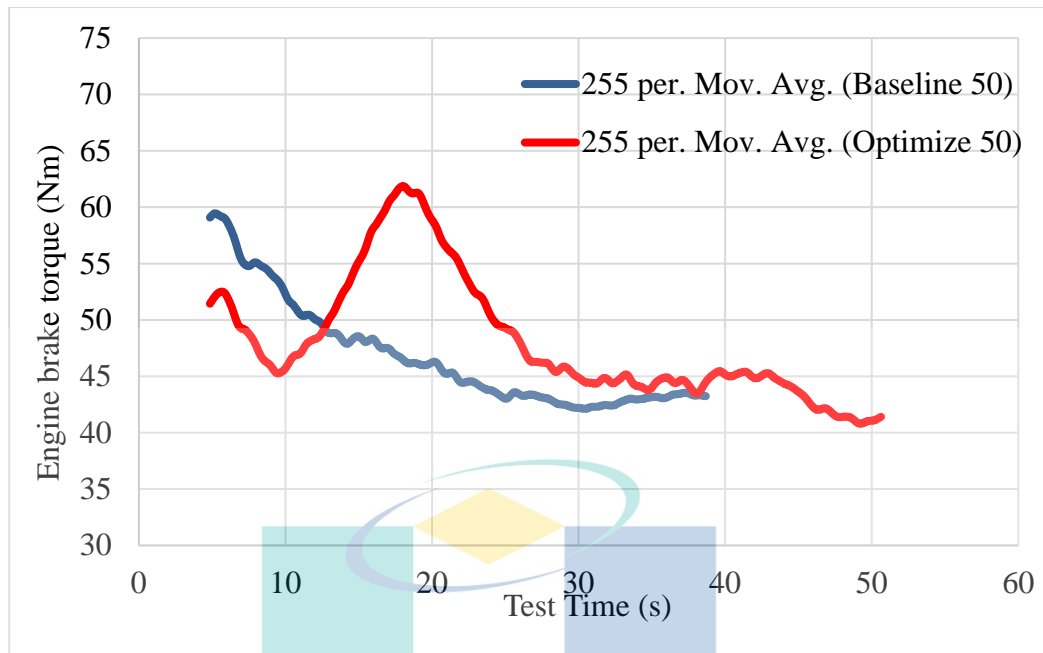


Figure 6.23 Error plot for the comparison of the optimised engine brake torque and the baseline case for 45 bar injection setup

Based on Figure 6.24, the comparison of the measured optimal and baseline engine brake torque of 50 bar injection pressure produced the same trend as 45 bar case. It can be seen through the overall plot, the optimised engine brake torque for 50 bar is higher than the baseline torque. However, in a specific time range between 0-12 sec of the earliest test time (based on the moving averaged trend lines), the engine torque of the baseline case is significantly higher than the optimised case. The trend of the optimal data for the case of 45 bar and 50 bar showing the same trend where engine brake torque is lower at about 0-15 secs after the test started before rising again and achieved the maximum torque point. And after the maximum torque point, the torque gradually decreased as the engine speed increased. The engine power increased with engine speed, but the torque seems lower since most of the energy supplied to the engine is converted to kinetic energy.



MAPE	MAE	MPE
13.95%	6.67Nm	5.76%

Figure 6.24 Comparison of the optimised engine brake torque with the baseline case for 50 bar injection setup

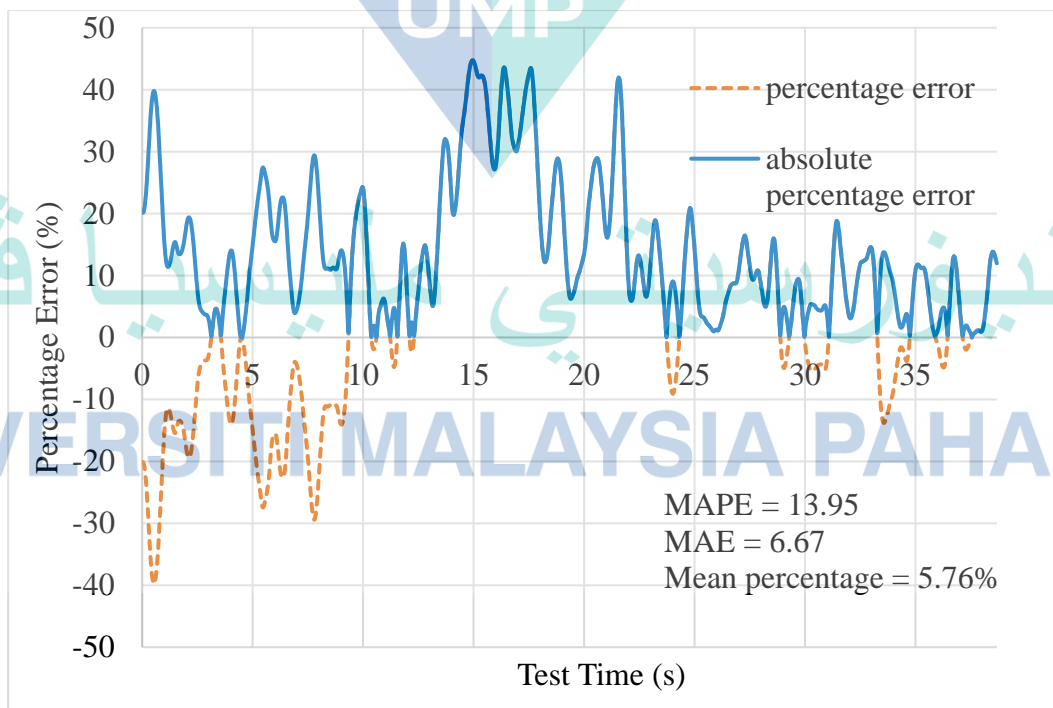


Figure 6.25 Plot of Mean Percentage (MP) and Mean Absolute Percentage Error (MAPE) for the comparison of the optimised engine brake torque and the baseline case for 50 bar injection setup

Based on the 50 bar case's plotted error in Figure 6.25, the MAPE, MAE and MPE of the 50 bar case are 13.95%, 6.67Nm and 5.76%, respectively. The comparison of the plotted graph and the error analysis confirmed that the optimisation procedure has increased the engine brake torque response, measured from the vehicle testing. In terms of maximum brake torque value, for 45 bar injection pressure case, the maximum brake torque recorded for the baseline case is about 65 bar, whereas, for optimised cases, the maximum brake torque is about 63 bar. For the 50 bar injection pressure case, the maximum brake torque for the baseline case is about 71 bar, whereas, for optimised cases, the maximum brake torque is about 68 bar. Thus, we can conclude that the optimisation process didn't increase the maximum torque at any specific point. Instead, the optimisation has increased the overall torque, averaged throughout the test window. The maximum achievable torque for the HPDI-CNG engine is halved the maximum torque for the port injection gasoline of the same engine, which is about 148 Nm.

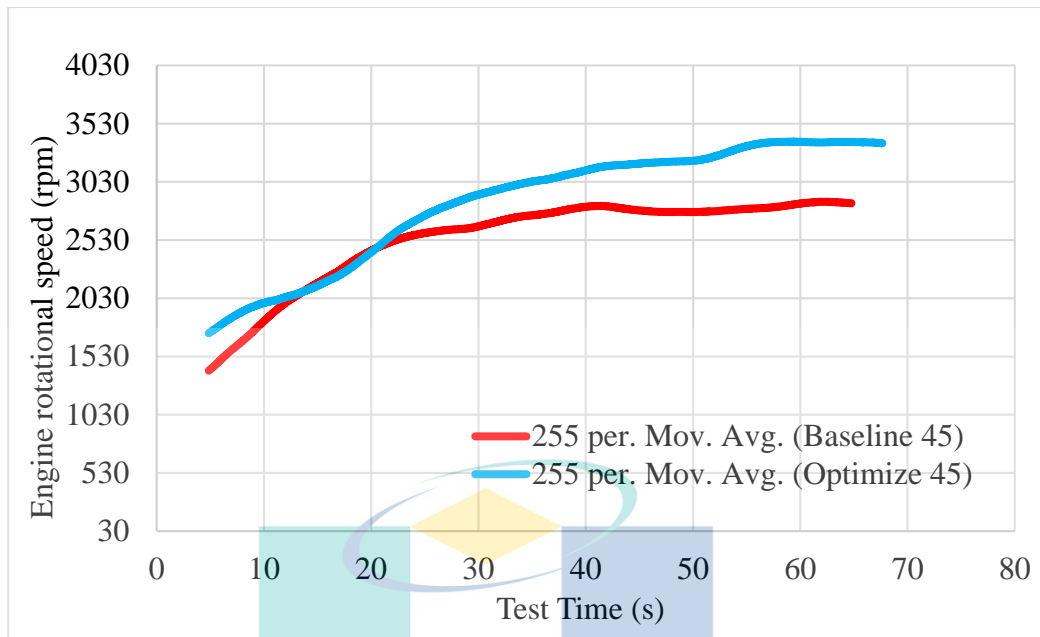
Based on the results discussed in Section 5.4, the air supply is slightly increased as the engine speed increased. At low engine speed, the air supply is sufficient to support the engine needs for combustion, consequently generating sufficient torque to move the HPDI-CNG vehicle on the chassis dynamometer. However, as the engine speed is gradually increased, the air supply became insufficient to further support the combustion, even more fuel is added. Hence the engine cannot generate higher torque and higher engine speed to accelerate the vehicle further. The torque dropped while the power increased after the peak torque point as the effect of increased speed dominated the power. In a naturally aspirated engine, the air intake pressure must be greater than the cylinder pressure to enable sufficient induction of air. Since the high injection pressure of CNG is commenced partially during exhaust and intake stroke, it affects the averaged cylinder pressure to become higher than the air intake pressure, thus lowering volumetric efficiency and consequently engine torque. The importance of air intake pressure was demonstrated by the study of (Abdullah, Shahrudin, Mamat, & Zulkifli, 2014). At the same time, the study on the effect of injection timing on volumetric efficiency has been detailed by (Mohammed et al., 2011a).

Figure 6.26 and Figure 6.27 present engine rotational speed comparison of optimised and baseline cases for 45 bar and 50 bar injection pressure. The comparisons clearly show that the resultant engine rotational speed increased with optimal maps for

both cases. The increase of about 500 rpm for 45 bar and 50 bar achieved when the engine accelerated towards a steady-state condition. The ability of the engine to produce higher engine rotational speed, proof that the engine managed to produce higher engine brake torque. It is because the engine acceleration and engine rotational speed are the outcomes of the engine torque. Moreover, theoretically, the resultant engine brake torque is proportional to the resultant engine rotational speed (Heywood, 1988). Thus, at the early time of the test, the optimised engine rotational speed was lower than baseline engine speed in both cases before rising again since they followed the trend of the corresponding engine brake torque. The MAPE, MAE, and MPE for the 45 bar case are 12.68%, 316 rpm and 11.93%. For 50 bar case, The MAPE, MAE, and MPE are 12.76%, 335.35rpm and 5.51%. The MAPE for 50 bar case is 0.08 larger than the 45 bar case is because it considers the absolute difference between optimised and the baseline data even though it produced a larger speed drop than the 45 bar case. The mean percentage for 50 bar case is lower than the 45 bar case because it considers the negative error when the optimised engine rotational speed is lower than the baseline engine rotational speed. As the engine rotational speed is considered as one of the engine output, the increment of the parameters is desirable. Specifically, in these two cases, the further increment of the engine speed until the end of test time, even after the peak torque point, is no longer driven by the engine's torque. Instead, the engine speed is driven by the inertia torque produced by the dynamometer and moving parts of the vehicle.

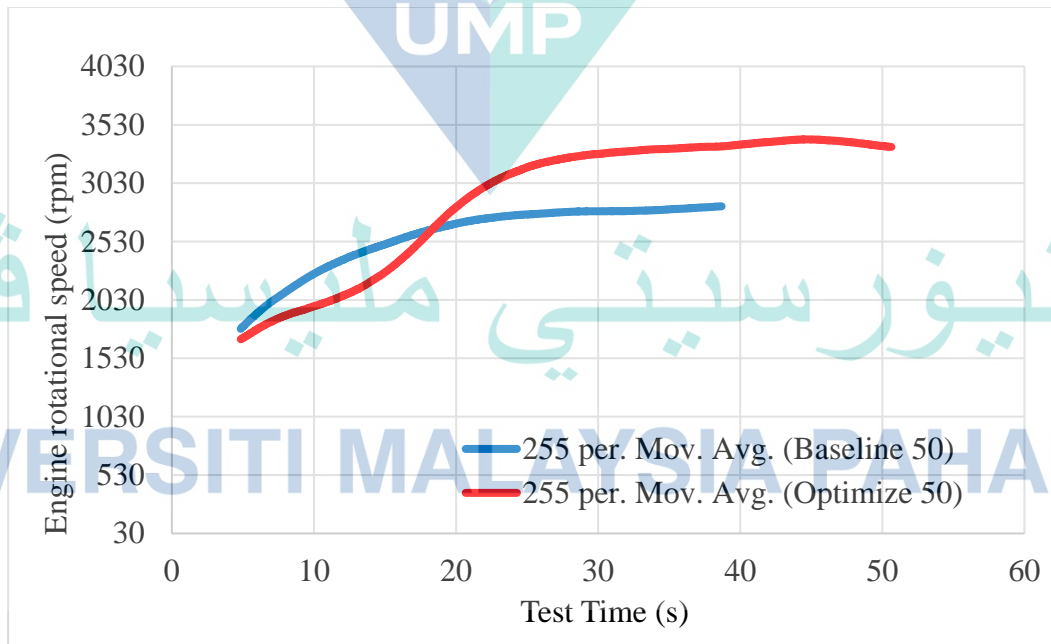
اونيورسيتي مليسيا قهغ

UNIVERSITI MALAYSIA PAHANG



MAPE	MAE	MPE
12.68%	316 rpm	11.93%

Figure 6.26 Comparison of the engine rotational speed with the baseline case for 45 bar injection setup



MAPE	MAE	MPE
12.76%	335.35rpm	5.51%

Figure 6.27 Comparison of the engine rotational speed with the baseline case for 50 bar injection setup

Figure 6.28 and Figure 6.29 present the comparison of engine brake power of the optimised and baseline case for the 45 bar and 55 bar injection pressure case, respectively. The brake power is a product of engine brake torque and engine rotational speed (Pulkrabek, 2003). In both cases, the brake power for optimised cases outperformed the baseline cases for most of the test time. The error between optimised and baseline quantities for both injection pressure is significantly higher compared to the engine brake torque comparison. This is because the engine rotational speed dominated the engine brake power. The engine rotational speed is progressively increased hence affecting the engine brake power. On the other hand, the 50 bar injection pressure produced a greater improvement of brake power as the MAE for 50 bar case is 0.75kW higher than the 45 bar case. Even though the brake power is dominated by the engine speed most of the time, the effects of brake torque are still visible, especially the resulted fluctuation of the brake power also and they are dropped for both cases at the early test period. These have corresponded with the dropped of engine brake torque. The overall MAPE, MAE and MPE for 45 bar cases are 18.92%, 2.15kW and 16.04%, respectively. In comparison, the overall MAPE, MAE and MPE for 50 bar cases are 12.52%, 2.90kW and 23.46%. Thus, the brake power is proportional and positively correlated to the engine speed and engine brake torque.

UMP

اونيورسيتي مليسيا قهغ

UNIVERSITI MALAYSIA PAHANG

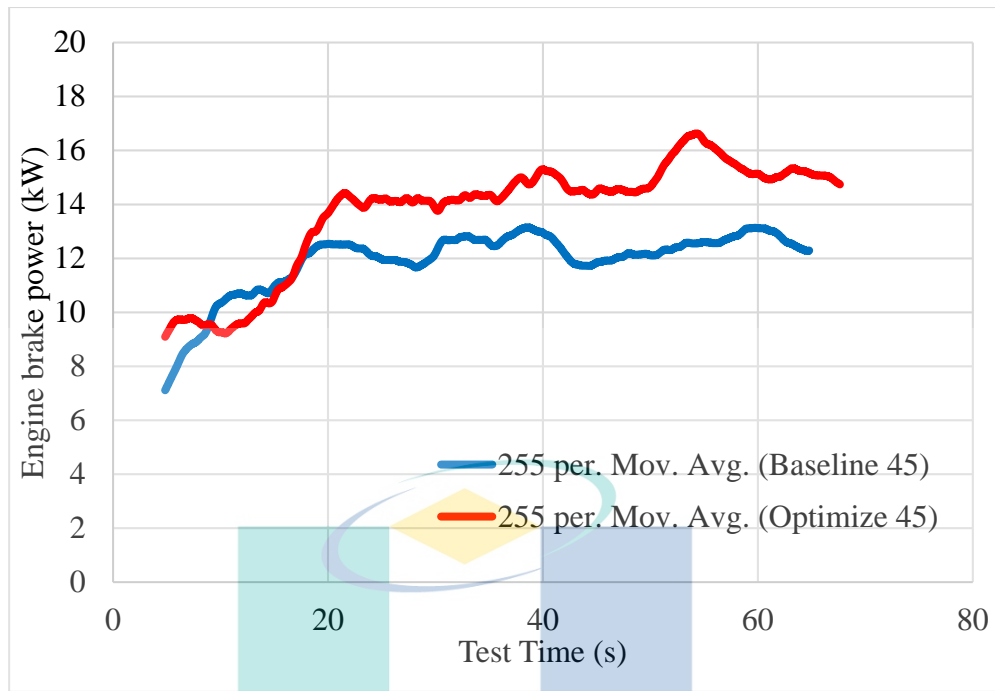


Figure 6.28 Comparison of the engine brake power with the baseline case for 45 bar injection setup

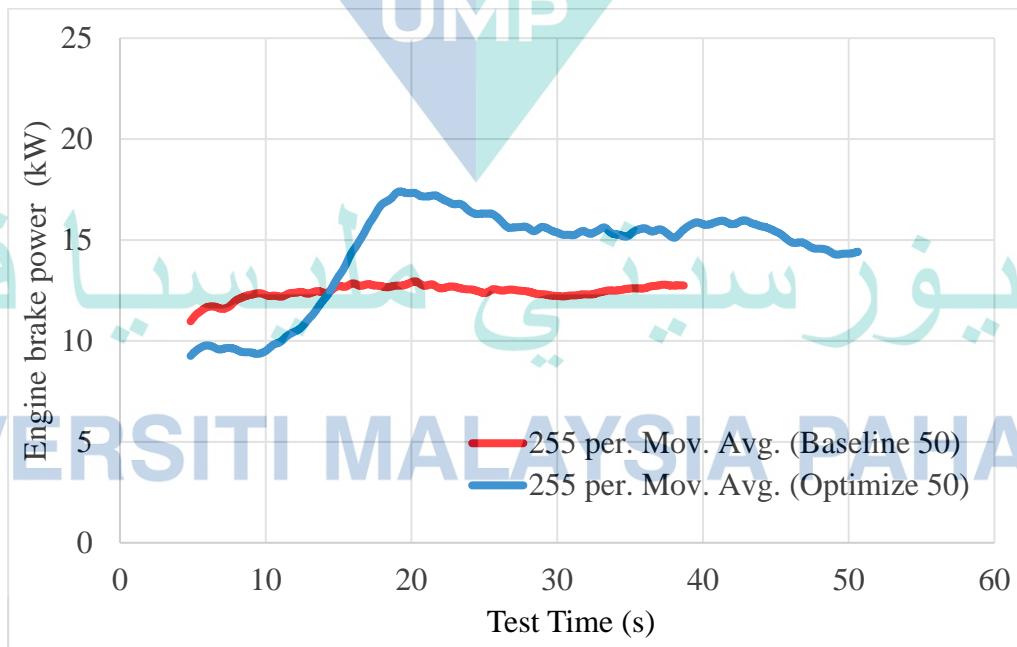
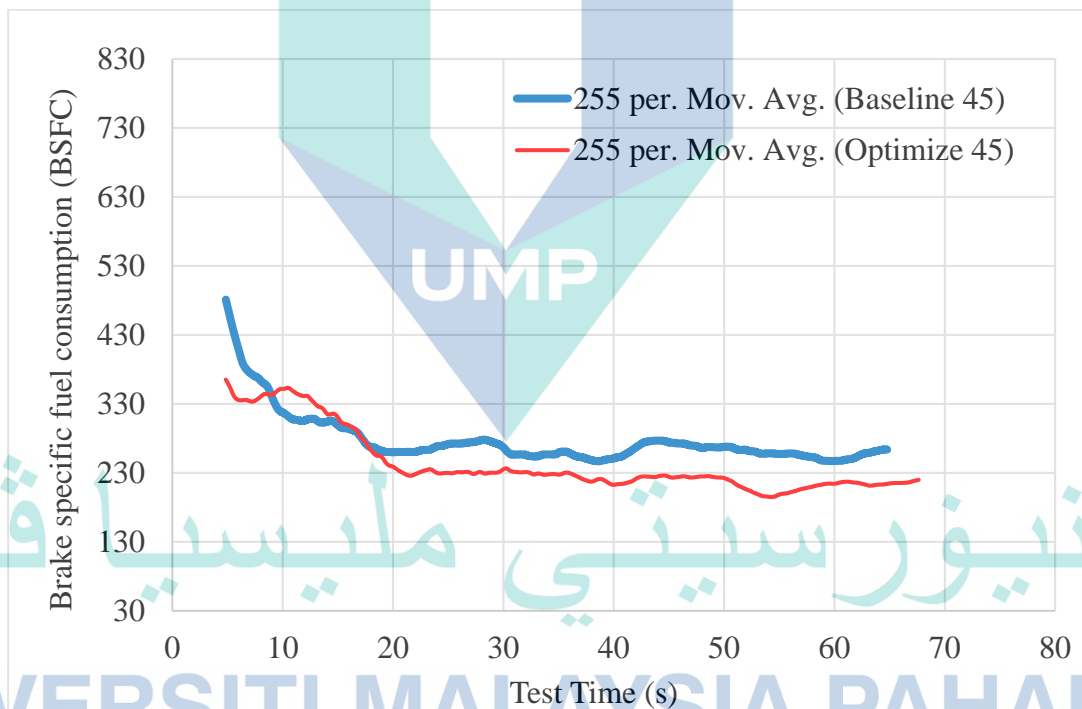


Figure 6.29 Comparison of the engine brake power with the baseline case for 50 bar injection setup

Figure 6.30 and Figure 6.31 present the comparison of BSFC for optimised and baseline cases for 45 bar and 50 bar injection pressure, respectively. The brake specific fuel consumption (BSFC) is a ratio of the fuel mass flow rate to the engine brake power. It indicates how much fuel is used to produce an amount unit of power. The smaller the value of BSFC is preferred as the engine is considered to be more efficient. This normalise parameter is of utmost importance for the comparison of fuel consumption of different engines capacity. Based on the plotted results, the BSFC of the optimised cases shown an improvement compared to the baseline case. These are noticeable after about 15 secs after the test started. The transient BSFC reading continuously lower than the baseline case until the end of the test window. When the optimised engine brake torque is lower than the baseline torque, the resultant BSFC is higher than the baseline BSFC in both cases.



MAPE	MAE	MPE
15.59%	46.32g/kWh	12.10%

Figure 6.30 Comparison of the engine brake specific fuel consumption (BSFC) with the baseline case for 45 bar injection setup

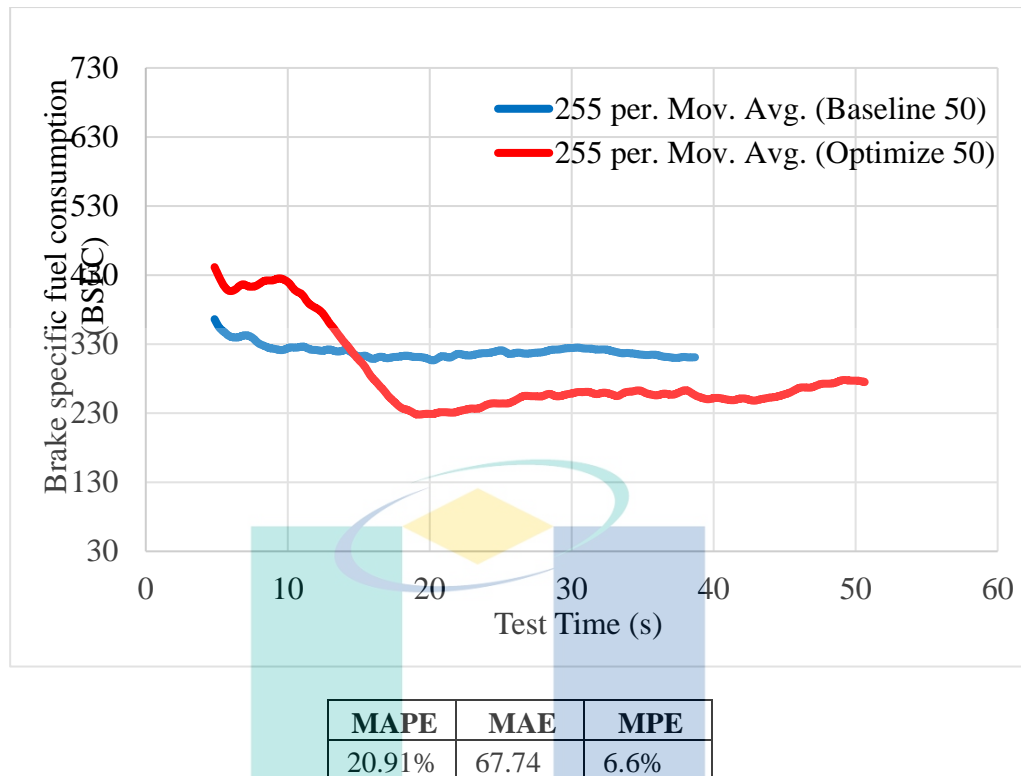
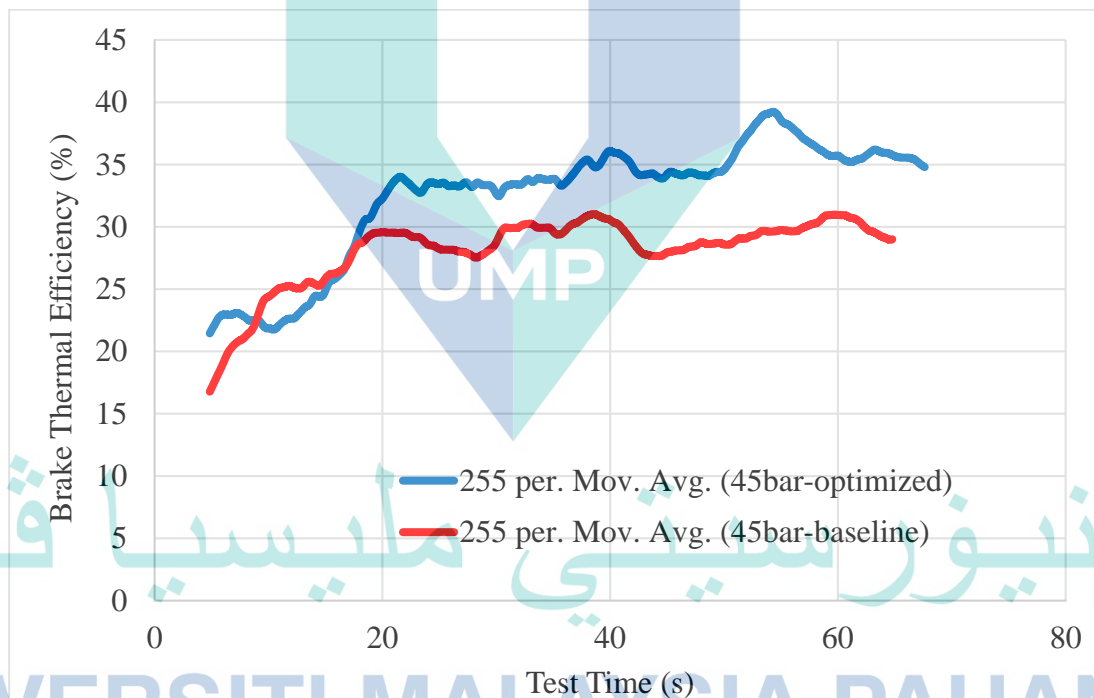


Figure 6.31 Comparison of the engine brake specific fuel consumption with the baseline case for 50 bar injection setup

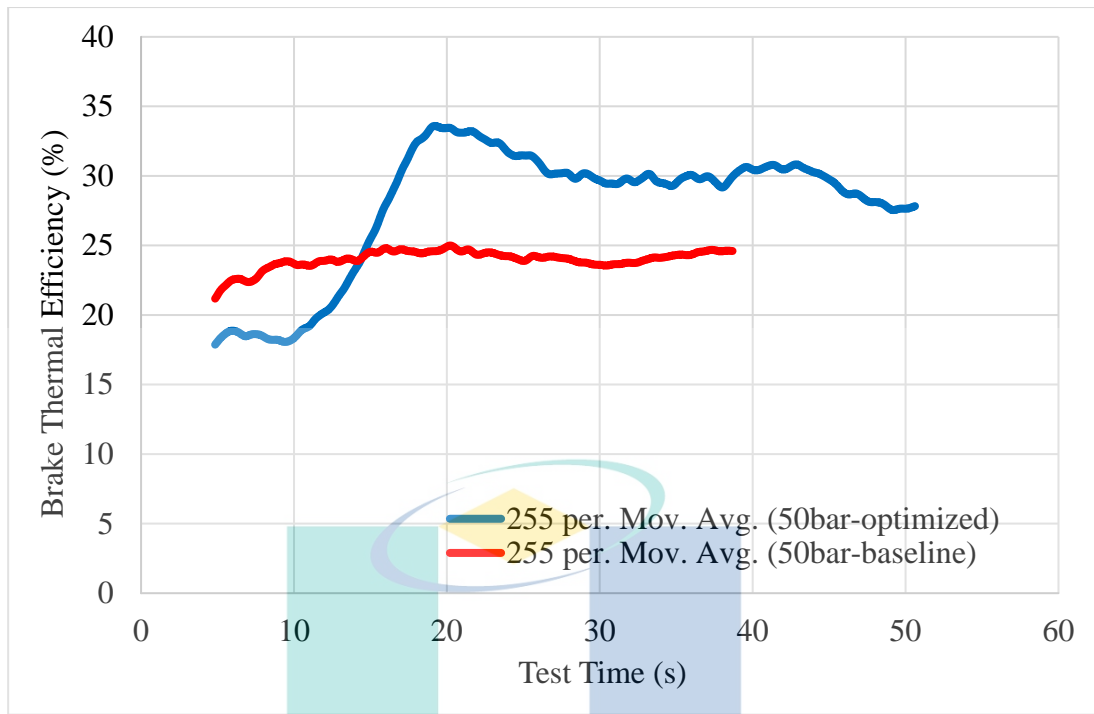
The optimal maps have proven to increase the engine brake torque, engine speed, and engine brake power throughout the optimisation stage. Moreover, the optimisation based calibration improved the fuel consumption based on the results of BSFC. These are the major advantages of applying the minimisation of BSFC as the objective function. Since BSFC are derived based on the power to fuel consumption ratio, the GA solver had analysed the possible option to minimise the BSFC by increasing the power or reducing the vehicle's fuel consumption. The corresponding MAPE, MAE and MPE for 45 bar injection pressure is 15.59%, 46.32g/kWh and 12.10%. Whereas for 50 bar injection pressure, the MAPE, MAE and MP are 20.91%, 67.74kW and 6.6%, respectively. Based on MAE, the 50 bar injection pressure case produce a better fuel consumption reduction as the MAE for the 50 bar case is 21.42 g/kWh lower than the BSFC for the 45 bar injection pressure. Typical BSFC plot over a wide range of typical engine speed (up to 7000 rpm) produced an inverse quadratic curve. It is a reciprocal of brake torque curve for a normal aspirated SI engine. And the minimum BSFC point is usually coincident with the maximum brake torque point (Heywood, 1988). However, in the study, since the maximum engine speed is limited to 3500 rpm, the inverse quadratic curve of BSFC is incomplete.

The brake thermal efficiency (BTE) measures how efficient the power generation is for a unit of fuel mass supplied to an engine. It is one of the most important non-dimensional parameters to characterise engine efficiency. Figure 6.32 and Figure 6.33 present the comparison of BTE of the optimised and baseline engine for 45 bar and 50 bar injection pressure. The optimised BTE shows a lower than baseline BTE at the early test time corresponding to the lower engine brake torque in both cases. The MAPE, MAE and MPE for 45 bar injection pressure are 18.92%, 5.08% and 16.04%. The MAPE, MAE and MPE for 50 bar cases are 23.46%, 5.6%, and 12.52%. The optimisation calibration at 50 bar injection pressure produced a more significant improvement from the baseline as the MAE for 50 bar case is 0.52% higher than the MAE for 45 bar case. The maximum BTE of 45 bar cases at about 38% is greater than the maximum BTE recorded by Kalam and Masjuki (2011) at WOT conditions.



MAPE	MAE	MPE
18.92%	5.08%	16.04%

Figure 6.32 Comparison of the optimized engine brake thermal efficiency (BTE) with the baseline case for 45 bar injection setup



MAPE	MAE	MPE
23.46%	5.6%	12.52%

Figure 6.33 Comparison of the optimized engine brake thermal efficiency (BTE) with the baseline case for 50 bar injection setup

Based on the presented results from Section 6.3.1 until 6.3.3, the model-based calibration is considered to achieve the fourth objective successfully. The calibration of the ECU map parameters is made possible by using an optimum ANN model that provides the simplest structure and minimum error for training and validation data set. In general, the data-driven model, especially the ANN, is confirmed to be a powerful tool for internal combustion engine modelling. It has superiority over other methods by successfully predicting and validating an ill-performed HPDI-CNG engine operated under an abnormal combustion process. A new milestone that is hardly possible to achieve by using an analytical modelling approach.

The calibration's primary assumption was that the engine's base maps had been tuned to their best performance using the traditional calibration method in the first phase of the HPDI-CNG vehicle project. Thus, the current optimization-based calibration cannot be explored too far beyond the existing limits. The search for the optimum setup of each variable is then performed within the existing engine operating envelope. For example, the constraint for the range of the free variables at 1500 rpm was decided to be selected based on the current setup at 1500 ± 100 rpm only. It is found that this selection

method has become the enabler for a successful calibration process where the new optimized variables could be embedded in the real ECU maps and produced a smooth driving condition.

All four cases (45 bar, 50 bar, 55 bar, 60 bar) were successfully verified by simulation and real testing approach. Based on the simulation verification, the trend of the optimized engine performances, particularly the engine brake torque, has been identified earlier in the virtual environment. The results showed that the optimized engine brake torque is lower than the baseline torque at the early of the test runtime since it is the trend of the conventional torque curve where the brake torque gradually developed before reaching its peak value. This condition provides a smooth driving experience for the driver by eliminating the engine jerking situations such as those produced by the baseline torque. In addition, all the speed-sweep tests in the study were performed at a single test gear which has the closest value to unity. The best accuracy for the optimized torque response through simulation verification in terms of MAPE, MAE, RMSE and MP is 18.86%, 6.486Nm, 8.611Nm and 13.53%, respectively. All these errors are selected from the case of 50 bar injection pressure. For the optimisation cases, the larger the error is desirable.

The use of the MBC toolbox has truly assisted the calibration of ECU maps for the HPDI-CNG vehicle prototype. The calibration process became highly organised, and the outcome of the calibration can easily be analysed, extracted and implemented in the real hardware. The availability of various engine response modelling techniques, calibration methods, and optimisation solvers accommodated a wide-range and robust application for engine response modelling and calibration. In the current study, the ANN and RBF modelling techniques were exploited in the data-driven modelling stages. NBI optimization is used for the ANN topology optimisation, and GA is used for the calibration optimization of ECU maps. Even though the RNN technique was suggested as the preferred method for the dynamic and time series modelling based on the literature, the use of general or MLP-ANN has proven to be sufficient for this optimization study provided that large input data pairs are used. Moreover, the MLP-ANN is the only available variant of ANN in the MBC toolbox. Another main issue that hindered the use of RNN in the MBC environment is the mobility problem between the Neural Net toolbox model and the CAGE platform.

Based on the real hardware verification, the constrained optimization-based calibration of ECU maps delivered a significant improvement on the engine's performance output such as brake torque, brake power, engine rotational speed, BSFC and BTE, even though the optimized operating range of the HPDI-CNG engine is still lower than the typical performance of port-injected gasoline engine or a common CNGDI engine. The situation is a hardware-limited problem where we expected that if the HPDI-CNG performance needs to be on par with a port-injection gasoline engine, the physical configuration of the direct injector system must be modified to meet the GDI standard. Nevertheless, the outcome of the current study has become concrete proof that the modern optimisation technique such as GA is a viable means to improve the efficiency of the modern engine performance even by a few percentages. The best improvement recorded from the real hardware verification for the brake torque, brake power, engine rotational speed, BSFC, and BTE is 5.76% (MPE), 23.46% (MPE), 11.93% (MPE), 12.10% (MPE) and 16.04% (MPE), respectively.

Based on the overall optimisation based calibration outcome, the optimised values of the injection duration, ignition timing and injection timing were found to produce significant improvement on the engine performance parameter. The results support the third hypothesis of the study, emphasising that if these three parameters can be optimised, then the overall engine performance shall be improved. The results of the calibration also supported and agreed with the fourth hypothesis of the study. The fourth hypothesis predicted that the sole use of the speed-sweep test procedure is a reliable method of vehicle testing to reduce the experimental cost and effort in ECU maps calibration of modern vehicles in the framework of the model-based calibration. Therefore, the elimination of the DoE procedure (which is more appropriate for stationary testing is justified. However, the availability of DoE for transient data collection would give much help in the future.

The optimization work performed by Wong et al. (2012) on modelling and optimization of engine power and performance using numerical and nominal data is one of the most comparable works with the current study. The study utilised the least-squares support vector machine (LS-SVM) for the engine power modelling, and Quasi-Newton (QN) method, genetic algorithm (GA) and particle swarm optimisation (PSO) method for the power optimisation. Besides, a whole range of engine speed was optimised, and they

also utilised vehicle testing on a chassis dynamometer. The optimisation study focused on the maximisation of engine torque coupled with the knock limiting function. They used Honda Type-R K20A i-VTEC, 1998 cm³ engine.

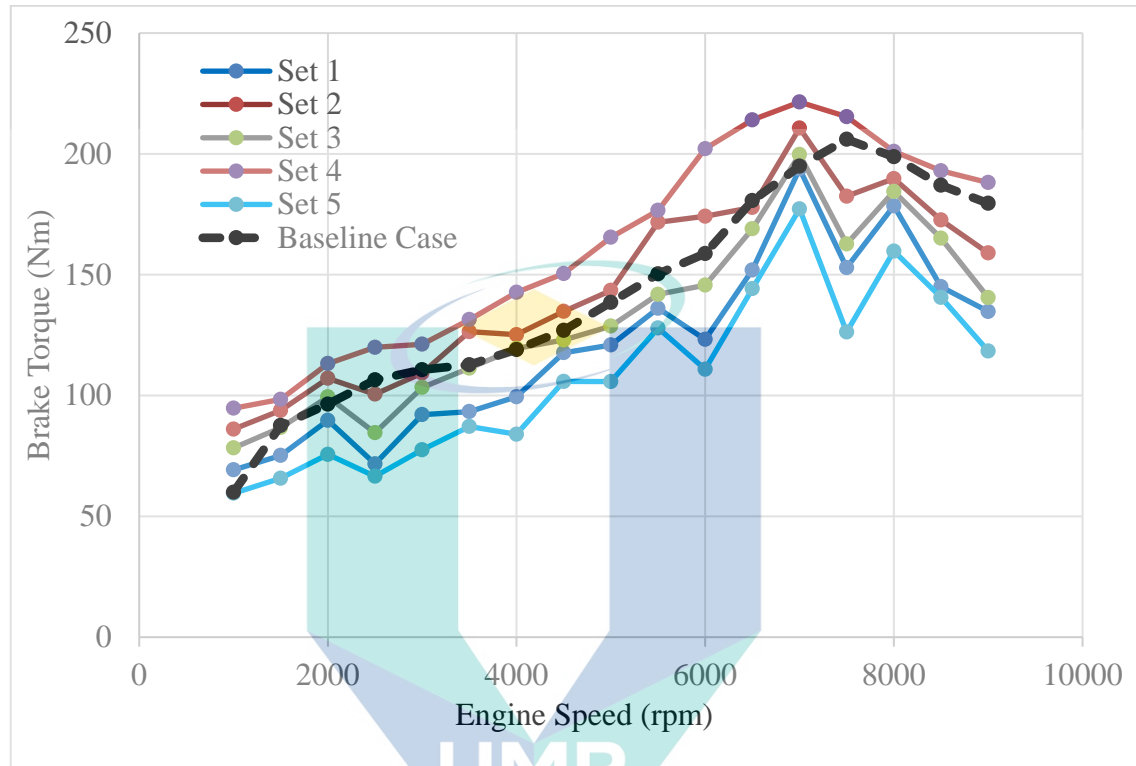


Figure 6.34 The plot of torque based on the optimised numerical and nominal data

Source: Wong et al.(2012)

The optimized variables in Wong et al. study were injection duration, ignition advance timing, valve overlap timing, high-speed valve timing and lift, engine speed, ignition system (nominal factor) and air intake systems (nominal factor). The current study decided not to include any limiting factor such as knock because the existing test subject is inherently underperformed, and there was no concern about the overloading incident. Each of the numerical variables was provided with a numerical constraint (which is expected to match the standard range in automotive engine application). And the objective function consisted of three terms, the torque model, the knock limiting model, and the fuel function model.

Implementation of such a typical range in the current study has led to a non-working engine condition, resulting in no data being measured. This is because the combustion characteristics in the existing HPDI-CNG platform are different since the modification of the fuel injection system. This difference is the wake-up call that drives

the effort to find a unique solution for the current study. It is always beneficial to review the assumption of the optimization work. Figure 6.35 presents the plot of torque as a function of variables optimized by GA in five different conditions with different weightage for each component in the objective function.

Based on Figure 6.35, the proposed solution of GA is not necessarily better than the baseline performance even though the same search space is used. It is a natural behaviour of a population-based, non-gradient optimization algorithm. Based on the solution, only the solution of set 2 and set 4 are comparable to the baseline torque. Comparison of the solution for set 4 (which gave the greatest improvement) provided MAE of 17.5 Nm, RMSE of 21.27 Nm, MAPE of 11.83%. Compared to the current study, the torque improvement gives MAPE, MAE and MPE of 10.02%, 4.62 Nm, and 3.27%. Even though the improvement is lower than the results of Wong et al., it is acceptable by considering other solutions proposed by GA in their optimisation.

In terms of fuel consumption, Zhao et al.(2012) had performed modelling and optimisation of an Atkinson cycle engine. The Atkinson cycle engine is developed based on a 1.8L double VVT Otto-cycle gasoline engine. The data generation for the ANN model has been generated by using the validated GT-Power model. The GT-Power model is used to calculate the engine torque, power and brake specific fuel consumption (BSFC). Moreover, it can also consider the effects of dilutions, mixture temperature, Variable valve timing (VVT) operations, geometrical compression ratio (GCR) and AFR. The ANN model is developed based on the input of engine speed (N), spark angle (SA), intake valve close (IVC) timing, exhaust valve open (EVO) timing, geometrical compression ratio (GCR), and air to fuel ratio.

In comparison to the current model in the study, the number of inputs of Zhao et al. model is lesser. It is because the engine performance data generated by the GT-Power model is an ideal process data. Even the number of inputs can be reduced to three by removing the intake valve close (IVC) timing, exhaust valve open (EVO) timing, geometrical compression ratio, (GCR) if not considering the use of Atkinson cycle. The objective function for the GA optimisation is based on BSFC. However, other models of torque, knock limiting factor, and exhaust gas temperature (also developed by ANN) is also used as the optimisation constrain. The spark advance (SA), AFR, intake valve close (IVC) timing, exhaust valve open (EVO) timing, geometrical compression ratio (GCR)

is defined as the optimized variables. In comparison, the optimization range is between 1000 rpm to 5200 rpm at WOT conditions. The average errors between ANN predictions and experimental results for torque and BSFC in the speed range below 4400 rpm are 1.3% and 2%, respectively, with the largest errors of 2.2% and 2.53%. Whereas, in the speed range below 4400 rpm, the average fuel economy improvement for the Atkinson cycle engine is 10.16%, with the largest up to 13% at 2400 rpm. This study has been selected because its optimization performed in a wider range of engine speeds. It operates in WOT condition, and the engine capacity is slightly larger than the current engine capacity. The current improvement for BSFC in terms of mean percentage error (MPE) is about 12.10% which is considered close to the results obtained by Zhao et al. Thus, the current results are considered acceptable for a 1.6-litre spark ignition HPDI-CNG engine.

6.4 Summary of Results

Section 6.2 presented the optimized ANN structure that represents the engine torque response. MLP-ANN with two hidden layers consisting of 36 and 26 have successfully predicted engine torque response and produced RMSE, R2, and validation RMSE values equal to 1.501, 0.985 and 3.773. verification of optimal setting showed the best percentage improvement recorded from the actual hardware verification for the brake torque, brake power, engine rotational speed, BSFC, and BTE is equal to 5.76% (MPE), 23.46% (MPE), 11.93% (MPE), 12.10% (MPE) and 16.04% (MPE), respectively. The next chapter presents the study's conclusion, highlighting significant findings and the attainment of each objective. The chapter also offers recommendations for future research concerning the current researched topic.

CHAPTER 7

CONCLUSION AND RECOMMENDATION OF THE STUDY

7.1 Introduction

This chapter concludes the main findings of the present study, especially the attainment of each objective. The chapter also highlights the contribution of the present study to the body of knowledge. Several recommendations are made for further exploration with regard to the current work.

7.2 Conclusion of the Study

Based on the injector testing and modelling, the injector seems to be sufficiently produced the required mass flow rate of fuel to the engine, primarily when operated at an injection pressure of 60 bar. At this injection pressure, the mass flow rate of the injector is about 1.24 g/s. The results matched the fuel requirement of the engine at 6000 rpm for stoichiometric combustion. However, in actual engine operation, the injector must deliver a higher fuel mass flow rate. The calculated fuel requirement only considers a stoichiometric mixture requirement, and thus, the measured injector flow rate is only capable of supplying the fuel for stoichiometric combustion only. The mass flow rate is linearly proportional to the injection pressure, as presented in Figure 4.1. The theoretical and measured relationship between the mass flow rate of CNG with injection pressure which is linearly proportional agreed with the first hypotheses of the study. For optimum performance of the engine, it is best to operate the injector with a variable injection pressure of gases to meet the fuel supply based on the engine speed requirement in an automated fashion. The injector possessed a fluctuations trend of mass flow rate. The effect of the short injection duration when opening and closing the injector nozzle is significant. When a longer injection duration increased, the fluctuation of mass flow rate is minimized. With the use of higher injection pressure of gases, the variation of mass flow rate out of the injector is also reduced. The needle armature is dampened by the high

pressure of gases that entered the injector axially. For case 2, the theoretical results suggested that the mass flow rate of CNG should be constant regardless of the injection duration. The stability of the mass flow rate is crucial as it affects the stability and consistency of the engine's air to fuel ratio, which on the other side will affect the engine output torque. Based on the results, it is expected that the engine can be operated steadily in a steady-state operation. However, the engine might face consistency and stability problems if operated in transient conditions. It is because, in transient operation, the injection duration is continuously adjusted to varying the fuel supply. Hence varying output torque is produced.

Based on the highest output performance of the models, at an injection pressure of 60 bar, the HPDI-CNG vehicle is predicted to produce 123.11 Nm of peak torque. Even though this torque is lower than the peak torque of a port-injection gasoline engine at 148 Nm, it is an anticipated outcome since the energy density (energy per unit volume) of the CNG is lower than gasoline fuel, plus it burns slower than gasoline. However, as stated before, the model simulated an ideal engine operation. The ideal terms refer to a complete combustion process where the mass of fuel supplied is fully utilised to convert chemical energy to mechanical work. Parameters such as ignition timing, injection timing, and injection duration are purely replicated from predefined values in the actual lookup table of the ECU. Other setups of the engine model were also based on the actual setup of the vehicle. Hence, we can expect that the current hardware setup is feasible to produce a baseline performance approaching the maximum engine brake torque of 123.11 Nm provided that the combustion process is performing as an ideal combustion process. The most influential parameter on the engine peak brake torque is the injection pressure. Higher injection pressure resulted in higher engine mean brake torque. This is because the higher injection pressure produced a higher CNG mass flow rate, which means higher chemical energy supplied for the energy conversion process. The second influential parameter is the ignition timing, where the maximum pressure predicted is 69.9 bar ~70 bar. The results are contrary to the characteristics of a gasoline engine where ignition timing is profoundly affected engine torque and speed. It is primarily due to the longer combustion period for CNG combustion, resulting in 'less sensitive' performance of engine output torque. The third influential parameter is the injection duration, where the maximum predicted engine brake torque is about 68.94 Nm. Both the injection pressure and injection duration are related to the controlling amount of fuel injected into the

cylinder, which affects the AFR of the cylinder mixture. The analytical engine modelling cannot predict the trend of the measured data accurately because the actual engine operation is associated with high cyclic variability and abnormal combustion. However, the predicted maximum brake torque is closed to the measured maximum brake torque value (manufacturer benchmarked), as demonstrated in the validation plot. The model has simulated ideal engine processes; hence it cannot predict the brake torque fluctuations.

In actual conditions, the HPDI-CNG engine output produced lower performances compared to the ideal simulated cases and standard GPI engine. The maximum engine speed, brake torque and brake power recorded as 3175 rpm, 69.06 Nm, and 19.10 kW, respectively. The maximum brake torque is less than half of 148 Nm, which is the maximum brake torque of the GPI version. The maximum engine speed of HPDI-CNG is also less than half of the maximum engine speed for the GPI version, which is about 7000 rpm. It can be concluded that the current configuration of CNG direct injection, which utilised the HPDI-CNG configuration, is not effective in increasing CNG engine performance. It even lowered the engine performance compared to the existing CNGDI engine. The engine's operating envelope defined by the minimum and maximum MAP is -32 KPa and -4 kPa, respectively. The most advanced and the most retarded injection timing are 500° CA BTDC and 473° CA BTDC,0 respectively. The shortest and the longest ignition duration are about 11 ms and 22 ms, respectively. The most advanced and most retarded ignition timing advances are about 23 degrees before the top dead centre and 12 degrees before the top dead centre. And finally, the air to fuel ratios fluctuate in the range of 15.7 and 10.4. These data explain the operating envelope of the HPDI-CNG engine during vehicle testing or particularly the upper and lower limit of the vehicle performance. In detail, there are at least two main factors that affected the HPDI-CNG engine performances. They are 1) the ability of the fuel injection system to deliver fuel at the correct amount and time and 2) the air-breathing capability of the engine to induce the maximum amount of air in each engine cycle. On the issue of fluctuated results, the averaged CNG mass flow rate fluctuated by using the existing driver setup. The air mass flow rate also fluctuated as well as the ignition timing of the engine. Both fluctuations affected the engine AFR. These fluctuations are mostly due to the fluctuation of the engine rotational speed. At the same time, the speed fluctuated due to the fluctuation of engine brake torque. It is suggested that this is a cyclic fluctuations effect

of engine parameters since the engine speed is feedback to the ECU. Additionally, the inefficiency of the fuel delivery due to the existing delay in fuel path (due to the physical geometry of the throat or the thin passage protrude into the cylinder) has resulted in lagged engine response hence lowered the maximum engine torque and engine rotational speed. It is a known fact, to maximise the engine torque or power, the maximum pressure of combustion shall be achieved at about 5-10° ATDC. It could be achieved by tuning the predefined ignition timing in the ECU to be close to the MBT. However, even if the MBT is obtained for each engine's operating point, it is questionable whether the engine power and torque can be maximized based on the current injection configuration. However, the effect of throat geometry on the delay amount is not quantified and beyond the scope of the study. The air-breathing capability of the engine is affected by the high CNG injection pressure, which is commenced partially from the exhaust and intake stroke, at opened valve condition. It creates excess pressure build-up in the cylinder. When the intake stroke starts at a high cylinder pressure, the cylinder capability to induced fresh air is downgraded. Hence, a lesser amount of fresh air is managed to be inducted into the cylinder. Worse scenario, the total air dropped was happening at all CNG injection pressure setups. It is the reason why the supplied CNG fuel cannot be fully utilised to produce high engine brake torque.

The model-based calibration (MBC) optimisation successfully achieved its objectives. The calibration of the ECU map parameters was made possible by using an optimum ANN model that provides the simplest structure and yet the smallest error for the training and validation data set. The best accuracy of the torque response produced by the optimal ANN model in terms of MAPE, MAE, RMSE and MP are 2.182, 0.8246, 1.111 and 0.12, respectively. The calibration's primary assumption was that the engine's base maps had been tuned to their best performance using the traditional calibration method in the first phase of the HPDI-CNG vehicle project. Thus, the current optimization-based calibration cannot be explored too far beyond the existing limits. The search for the optimum setup of each variable is then performed within the existing engine operating envelope. For example, the constraint for the range of the free variables at 1500 rpm was decided to be selected based on the current setup at 1500 ± 100 rpm only. The constraint selection method has become the enabler for a successful calibration process where the new optimized variables could be embedded in the real ECU maps and produced a smooth driving condition. All four cases (45 bar, 50 bar, 55 bar, 60 bar) were

successfully verified by the simulation testing approach. Based on the simulation verification, the trend of the optimized engine performances, particularly the engine brake torque, has been identified earlier in the virtual environment. The best accuracy for the optimized torque response produced by the optimal simulation verification process in terms of MAPE, MAE, RMSE and MP is 18.86, 6.486, 8.611 and 13.53, respectively. All these errors are selected from the case of 50 bar injection pressure. For the optimisation cases, the larger the error is desirable. Based on the real hardware verification, the constrained optimization-based calibration of ECU maps delivered a significant improvement on the engine's performance output such as brake torque, brake power, engine rotational speed, BSFC and BTE, even though the optimized operating range of the HPDI-CNG engine is still lower than the typical performance of port-injected gasoline engine or a common CNGDI engine. The situation is a hardware-limited problem where we expected that if the HPDI-CNG performance needs to be on par with a port-injection gasoline engine, the physical configuration of the direct injector system must be modified to follow the GDI standard. Nevertheless, the outcome of the current study has become concrete proof that the modern optimisation technique such as GA is a viable means to improve the efficiency of the contemporary engine performance even by a few percent. The best improvement recorded from the real hardware verification for the brake torque, brake power, engine rotational speed, BSFC, and BTE is 5.76% (MPE), 23.46% (MPE), 11.93% (MPE), 12.10% (MPE) and 16.04% (MPE), respectively.

7.3 Contribution of the Study

Based on the framework of study deliberated in Chapter 1 until Chapter 6, The following points are considered as the primary contributions of the present study:

1. The configuration of the direct injection system is a unique design to minimise the modification of the engine cylinder head, even though the design is found to be irregular and inefficient compared to a standard GDI system design.
2. A comprehensive vehicle model based on an analytical approach, which coupled Simulink and SimScape model is developed, used to replicate a dynamic condition during the speed-sweep test procedure. Such a comprehensive vehicle model based on an analytical approach is hardly found in the literature.

3. The study has produced baseline data sets consisting of experimental and simulation data for the HPDI-CNG vehicle. The data is a dynamic data set that represents a vehicle acceleration process during the speed-sweep test procedure.
4. The injector flow characteristics study has produced a new flow specification of the injector when operated with CNG at the tested fuel injection pressure. In addition, the study has revealed the dynamic effects of improper injection control on the mass flow rate.
5. The study demonstrated the performances of the vehicle when operated with the HPDI-CNG concept. The results support the conclusion that the direct injector configuration utilised by the concept is not fit to be employed in a direct injection CNG engine.
6. The optimization procedure proposed a method to select a proper range for the free variables based on the maximum and minimum variable value at specified engine speed. This method has proven to allow the implementation of the optimal setup in real engine hardware.
7. The study also proved that the speed-sweep test method is an applicable test method to reduce calibration load since the verification results demonstrate an increased engine performance. It is found to be appropriate in the combined use of ANN modelling and GA optimization procedure.
8. The success of data-driven modelling using ANN is significant proof of the MLP-ANN superiority over other modelling methods even developed upon ill-performed engine data. Besides, the study proved that standard MLP-ANN could be used to model a transient process provided that large data pairs are available.

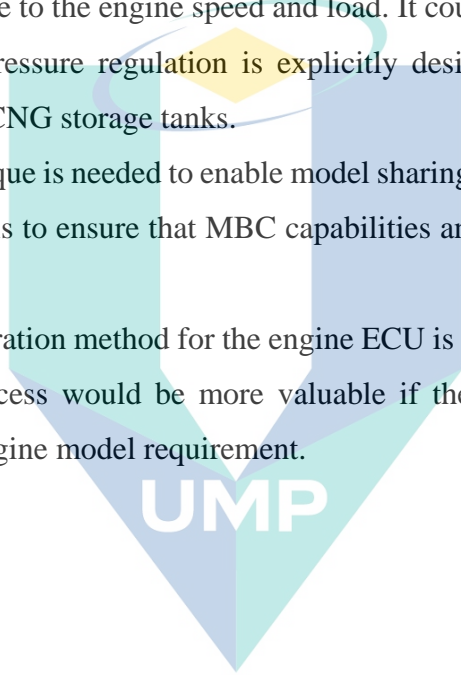
7.4 Recommendation for Future Works

Based on the outcome of the current study as well as the insight knowledge gained from the results and the literature, the following tasks are suggested to be explored in greater detail to improve the current topic of study further:

1. A multi-dimensional modelling study based on the computational fluid dynamic (CFD) approach on the estimation of delay due to the introduction of fuel passage is required to characterise the effect of the fuel path geometry.
2. It is worth reconsidering the suitability of the current direct injector configuration for the CNG direct-injection engine in the future. The present results indicated that

the design is not effective as a CNGDI engine's injector configuration. The injector itself may only suit a smaller engine cylinder capacity based on the measured mass flow rates.

3. A suitable signal driver at an appropriate voltage and current limits should be developed for the peak and hold injector to ensure optimized injector operation while minimising the injector losses due to hysteresis and increased operating temperature.
4. For optimal CNGDI system performance, the gas pressure should be automatically regulated relative to the engine speed and load. It could be realized if an additional controller for pressure regulation is explicitly designed to adjust the discharge pressure of the CNG storage tanks.
5. A unique technique is needed to enable model sharing between the ANN solver and MBC solver. It is to ensure that MBC capabilities and potential is maximised to a greater extend.
6. The future calibration method for the engine ECU is the online calibration process. This online process would be more valuable if the calibration technique could eliminate the engine model requirement.



اونيورسيتي ملايسيا قهغ

UNIVERSITI MALAYSIA PAHANG

REFERENCES

- A-Rashid, A.-A., & Firmansyah. (2009). The Effect of Fuel Rail Pressure on the Performance of a CNG-Direct Injection Engine. *SAE Technical Paper*, 1–7.
- Abd Alla, G. H. (2002). Computer simulation of a four stroke spark ignition engine. *Energy Conversion and Management*, 43(8), 1043–1061. [https://doi.org/10.1016/S0196-8904\(01\)00092-9](https://doi.org/10.1016/S0196-8904(01)00092-9)
- Abd Alla, G. H., Soliman, H. A., Badr, O. A., & Abd Rabbo, M. F. (2001). Combustion quasi-two zone predictive model for dual fuel engines. *Energy Conversion and Management*, 42(12), 1477–1498. [https://doi.org/10.1016/S0196-8904\(00\)00143-6](https://doi.org/10.1016/S0196-8904(00)00143-6)
- Abdullah, N. R., Shahrudin, N. S., Mamat, R., Mamat, A. M. I., & Zulkifli, A. (2014). Effects of air intake pressure on the engine performance, fuel economy and exhaust emissions of a small gasoline engine. *Journal of Mechanical Engineering and Sciences*, 6(June), 949–958. <https://doi.org/10.15282/jmes.6.2014.21.0091>
- Abdullah, S., Adril, E., Muchtar, A., & Ariffin, A. K. (2010). Friction Reduction in Compressed natural Gas Direct Injection Engine Using Piston Rings with Difusion Chromium Coating. *Journal of Applied Sciences*, 10(6), 462–470.
- Abdullah, S., Kurniawan, W. H., Ali, Y., & Mohamad, T. I. (n.d.). *Computational Study of Homogeneous and Stratified Combustion in a Compressed Natural Gas Direct Injection Engine*. 377–382.
- Abu-Nada, E., Al-Hinti, I., Al-Sarkhi, A., & Akash, B. (2006). Thermodynamic modeling of spark-ignition engine: Effect of temperature dependent specific heats. *International Communications in Heat and Mass Transfer*, 33(10), 1264–1272. <https://doi.org/10.1016/j.icheatmasstransfer.2006.06.014>
- Aesoy, V., & Pedersen, E. (2011). Modeling and Simulation for Design and Testing of Direct Injection Gaseous Fuel Systems for Medium-Speed Engines. *SAE International Journal of Fuels and Lubricants*, 4(2), 2011-01–2401. <https://doi.org/10.4271/2011-01-2401>
- Afrashteh, R. (2000). *Modeling, fault detection and diagnosis of an automotive engine using artificial neural networks*. Simon Fraser University.
- Alagumalai, A. (2014). Internal combustion engines: Progress and prospects. *Renewable and Sustainable Energy Reviews*, 38, 561–571. <https://doi.org/https://doi.org/10.1016/j.rser.2014.06.014>
- Aljamali, S., Abdullah, S., Wan Mahmood, W. M. F., & Ali, Y. (2016). Effect of fuel injection timings on performance and emissions of stratified combustion CNGDI engine. *Applied Thermal Engineering*, 109, 619–629. <https://doi.org/https://doi.org/10.1016/j.applthermaleng.2016.08.127>
- Ando, R., Koizumi, M., & Ishikawa, T. (2001). Development of a simulation method for dynamic characteristics of fuel injector. *IEEE Transactions on Magnetics*, 37(5), 3715–3718. <https://doi.org/10.1109/20.952697>

- Antunes, J M Gomes, Mikalsen, R., & Roskilly, A. P. (2009). *An experimental study of a direct injection compression ignition hydrogen*.
- Antunes, Jorge M G. (2010). *The Use Of Hydrogen As A Fuel For Compression Ignition Engines*. Newcastle University.
- Arsie, I., Pianese, C., & Rizzo, G. (2000). A Computer Code for S . I . Engine Control and Powertrain Simulation. *Electronic Engine Controls 2000: Modeling, Neural Networks, OBD, and Sensors, SAE 2000 World Congress, (724)*. <https://doi.org/10.4271/2000-01-0938>
- Arsie, I., Pianese, C., & Sorrentino, M. (2008). Development and Real-Time Implementation of Recurrent Neural Networks for AFR Prediction and Control. *SAE International Journal of Passenger Cars - Electronic and Electrical Systems, 1(1)*, 2008-01-0993. <https://doi.org/10.4271/2008-01-0993>
- Arsie, I., Pianese, C., & Sorrentino, M. (2009). Development of recurrent neural networks for virtual sensing of NOx emissions in internal combustion engines. *SAE International Journal of Fuels and Lubricants, 2(2)*, 2009-24-0110. <https://doi.org/10.4271/2009-24-0110>
- Aslam, M., Masjuki, H., Kalam, M., Abdesselam, H., Mahlia, T., & Amalina, M. (2006). An experimental investigation of CNG as an alternative fuel for a retrofitted gasoline vehicle. *Fuel, 85(5-6)*, 717-724. <https://doi.org/10.1016/j.fuel.2005.09.004>
- Atashkari, K., Nariman-Zadeh, N., Gölcü, M., Khalkhali, A., & Jamali, A. (2007). Modelling and multi-objective optimization of a variable valve-timing spark-ignition engine using polynomial neural networks and evolutionary algorithms. *Energy Conversion and Management, 48(3)*, 1029-1041. <https://doi.org/10.1016/j.enconman.2006.07.007>
- Atkinson, C, & Mott, G. (2005). Dynamic Model-Based Calibration Optimization : An Introduction and Application to Diesel Engines. *SAE Technical Paper Series 2005-01-0026, 2005(724)*. <https://doi.org/10.4271/2005-01-0026>
- Atkinson, Chris, Allain, M., & Houshun Zhang. (2008). Model-Based Transient Calibration Optimization for Next Generation Diesel Engines. *SAE International Technical Paper*.
- Atkinson, Chris, Allain, M., & Zhang, H. (2010). Using Model-Based Rapid Transient Calibration to Reduce Fuel Consumption and Emissions in Diesel Engines. *SAE Technical Paper Series, 1(April)*. <https://doi.org/10.4271/2008-01-1365>
- Atkinson, Christopher. (2014). Fuel Efficiency Optimization using Rapid Transient Engine Calibration. *SAE Technical Paper 2014-01-2359, (September 2014)*. <https://doi.org/10.4271/2014-01-2359>. Copyright
- Aziz, A. R. A., Firmansyah, & Shahzad, R. (2010). Combustion analysis of a cng direct injection spark ignition engine. *International Journal of Automotive and Mechanical Engineering, 2(1)*, 157-170. <https://doi.org/10.15282/ijame.2.2010.5.0013>

- Bakar, R. A., Sera, M. A., & Wong, H. M. (2002). Towards The Implementation Of CNG Engine : A Literature Review Approach To Problems And Solutions. *BSME-ASME International Conference on Thermal Engineering*, 402(January).
- Balat, M. (2005). World natural gas (NG) reserves, NG production and consumption trends and future appearance. *Energy Sources*, 27(10), 921–929. <https://doi.org/10.1080/00908310490449027>
- Baratta, M., Misul, D., Viglione, L., & Xu, J. (2019). Combustion chamber design for a high-performance natural gas engine: CFD modeling and experimental investigation. *Energy Conversion and Management*, 192(January), 221–231. <https://doi.org/10.1016/j.enconman.2019.04.030>
- Bartunek, B., & Hilger, U. (2000). Direct Induction Natural Gas (DING): A Diesel-Derived Combustion System for Low Emissions and High Fuel Economy. *SAE Technical Paper Series*, (724), 14. <https://doi.org/10.4271/2000-01-2827>
- Bayraktar, H., & Durgun, O. (2004). Development of an empirical correlation for combustion durations in spark ignition engines. *Energy Conversion and Management*, 45(9–10), 1419–1431. <https://doi.org/10.1016/j.enconman.2003.09.010>
- Beale, M. H., Hagan, M. T., & Demuth, H. B. (2001). Kalman Filtering and Neural Networks. In S. Haykin (Ed.), *MathWorks*. <https://doi.org/10.1002/0471221546>
- Beccari, S., Pipitone, E., Cammalleri, M., & Genchi, G. (2014). Model-based optimization of injection strategies for SI engine gas injectors. *Journal of Mechanical Science and Technology*, 28(8), 3311–3323. <https://doi.org/10.1007/s12206-014-0742-x>
- Berger, B. (2012). *Modeling and Optimization for Stationary Base Engine Calibration*. Technical University of Munich.
- Binder, A., Ecker, R., Glaser, A., & Müller, K. (2015). Gasoline direct injection. In Reif K. (eds) (Ed.), *Gasoline Engine Management* (Bosch Prof, pp. 110–121). https://doi.org/10.1007/978-3-658-03964-6_8
- Boretti, A. A., & Watson, H. C. (2009). Development of a Direct Injection high flexibility Cng/Lpg Spark Ignition engine. *SAE Technical Papers*, 4970. <https://doi.org/10.4271/2009-01-1969>
- Boretti, Alberto A., & Watson, H. C. (2009). The lean burn direct injection jet ignition gas engine. *International Journal of Hydrogen Energy*, 34(18), 7835–7841. <https://doi.org/10.1016/j.ijhydene.2009.07.022>
- Boretti, Alberto A., & Watson, H. C. (2009). The lean burn direct injection jet ignition gas engine. *International Journal of Hydrogen Energy*, 34(18), 7835–7841. <https://doi.org/10.1016/j.ijhydene.2009.07.022>

- Brahma, I., & Chi, J. N. (2012a). Development of a model-based transient calibration process for diesel engine electronic control module tables-Part 1: Data requirements, processing, and analysis. *International Journal of Engine Research*, 13(1), 77–96. <https://doi.org/10.1177/1468087411424376>
- Brahma, I., & Chi, J. N. (2012b). Development of a model-based transient calibration process for diesel engine electronic control module tables - Part 2: Modelling and optimization. *International Journal of Engine Research*, 13(2), 147–168. <https://doi.org/10.1177/1468087411424377>
- Caley, D., & Cathcart, G. (2006). Development of a natural gas spark ignited direct injection combustion system. *NGV2006, Cairo*, 15(1), 2012. Cairo, Egypt.
- Cammalleri, M., Pipitone, E., Beccari, S., & Genchi, G. (2013). A mathematical model for the prediction of the injected mass diagram of a S.I. engine gas injector. *Journal of Mechanical Science and Technology*, 27(11), 3253–3265. <https://doi.org/10.1007/s12206-013-0848-6>
- Çelik, M. B., & Ozdalyan, B. (2010). Gasoline Direct Injection. In B. O. E.-D. Siano (Ed.), *Fuel Injection* (p. Ch. 1). <https://doi.org/10.5772/9693>
- Chala, G. T., Aziz, A. R. A., & Hagos, F. Y. (2017). Combined Effect Of Boost Pressure And Injection Timing On The Performance And Combustion Of Cng In A Di Spark Ignition Engine. *International Journal of Automotive Technology*, 18(1), 85–96. <https://doi.org/10.1007/s12239-017-0009-5> Copyright © 2017 KSAE/ 094–09 pISSN 1229–9138/ eISSN 1976–383
- Chang, S. H., Yaacob, Z., & Mohsin, R. (2007). Effect of various manifold absolute pressures and air flowrates on throttle body injection mixer in compressed natural gas motorcycle . *Journal of Chemical and Natural Resources Engineering*, 1(May 2014), 40–49.
- Chebbi, O., & Chaouachi, J. (2015). Effective parameter tuning for genetic algorithm to solve a real world transportation problem. *2015 20th International Conference on Methods and Models in Automation and Robotics, MMAR 2015*, 370–375. <https://doi.org/10.1109/MMAR.2015.7283904>
- Chen, L., Wei, H., Zhang, R., Pan, J., Zhou, L., & Liu, C. (2019). Effects of late injection on lean combustion characteristics of methane in a high compression ratio optical engine. *Fuel*, 255(July), 115718. <https://doi.org/10.1016/j.fuel.2019.115718>
- Cheng, Q., Zhang, Z., & Xie, N. (2015). Power losses and dynamic response analysis of ultra-high speed solenoid injector within different driven strategies. *Applied Thermal Engineering*, 91, 611–621. <https://doi.org/10.1016/j.applthermaleng.2015.08.053>
- Chiang, Y.-M., Chang, L.-C., & Chang, F.-J. (2004). Comparison of static-feedforward and dynamic-feedback neural networks for rainfall–runoff modeling. *Journal of Hydrology*, 290(3–4), 297–311. <https://doi.org/10.1016/j.jhydrol.2003.12.033>

- Chiodi, M., Berner, H. J., & Bargende, M. (2006). Investigation on different injection strategies in a direct-injected turbocharged cng-engine. *SAE Technical Papers*. <https://doi.org/10.4271/2006-01-3000>
- Chitsaz, I., Saidi, M. H., Mozafari, A. A., & Hajjalimohammadi, A. (2013). Experimental and numerical investigation on the jet characteristics of spark ignition direct injection gaseous injector. *Applied Energy*, *105*, 8–16. <https://doi.org/10.1016/j.apenergy.2012.11.023>
- Cho, H. M., & He, B. Q. (2007). Spark ignition natural gas engines-A review. *Energy Conversion and Management*, *48*(2), 608–618. <https://doi.org/10.1016/j.enconman.2006.05.023>
- Choi, M., Lee, S., & Park, S. (2015). Numerical and experimental study of gaseous fuel injection for CNG direct injection. *Fuel*, *140*, 693–700. <https://doi.org/https://doi.org/10.1016/j.fuel.2014.10.018>
- Chow, A., & Wyszynski, M. L. (1999). Thermodynamic modelling of complete engine systems - a review. *Proceedings of the Institution of Mechanical Engineers Part D- Journal of Automobile Engineering*, *213*(D4), 403–415.
- Coppo, M., & Dongiovanni, C. (2007). Experimental Validation of a Common-Rail Injector Model in the Whole Operation Field. *Journal of Engineering for Gas Turbines and Power*, *129*(2), 596. <https://doi.org/10.1115/1.2432889>
- Coppo, M., Dongiovanni, C., & Negri, C. (2002). Numerical Analysis and Experimental Investigation of a Common Rail Type Diesel Injector. *Design, Application, Performance and Emissions of Modern Internal Combustion Engine Systems and Components*, (46628), 271–280. <https://doi.org/10.1115/ICEF2002-507>
- Corti, E., Cavina, N., Cerofolini, A., Forte, C., Mancini, G., Moro, D., ... Ravaglioli, V. (2014). Transient Spark Advance calibration approach. *Energy Procedia*, *45*, 967–976. <https://doi.org/10.1016/j.egypro.2014.01.102>
- Cox, G. B., DelVecchio, K. A., Hays, W. J., Hiltner, J. D., Nagaraj, R., & Emmer, C. (2000). *Development of a direct-injected natural gas engine system for heavy-duty vehicles: Final report phase 2*. <https://doi.org/10.2172/753776>
- Crossley, P. R., & Cook, J. A. (1991). A nonlinear engine model for drivetrain system development. *International Conference on Control 1991*, 921–925.
- Das, I., & Dennis, J. E. (1998). Normal-boundary intersection: A new method for generating the Pareto surface in nonlinear multicriteria optimization problems. *SIAM Journal on Optimization*, *8*(3), 631–657. <https://doi.org/10.1137/S1052623496307510>
- Das, L. (2000). A comparative evaluation of the performance characteristics of a spark ignition engine using hydrogen and compressed natural gas as alternative fuels. *International Journal of Hydrogen Energy*, *25*(8), 783–793. [https://doi.org/10.1016/S0360-3199\(99\)00103-2](https://doi.org/10.1016/S0360-3199(99)00103-2)

- Dempsey, A. B., & Reitz, R. D. (2011). Computational Optimization of Reactivity Controlled Compression Ignition in a Heavy-Duty Engine with Ultra Low Compression Ratio. *SAE International Journal of Engines*, 4(2), 2011-24-0015. <https://doi.org/10.4271/2011-24-0015>
- Desantes, J. M., Benajes, J. V., Molina, S. A., & Hernández, L. (2005). Multi-objective optimization of heavy-duty diesel engines under stationary conditions. *Proceedings of the Institution of Mechanical Engineers, Part D: Journal of Automobile Engineering*, 219(1), 77–87. <https://doi.org/10.1243/095440705X6488>
- Digesu, P., Ficarella, A., Laforgia, D., Bruni, G., & Ricco, M. (1994). Diesel Electro-injector: A Numerical Simulation Code. *SAE Transactions: Section 3: JOURNAL OF ENGINES*, 103, 120–133. <https://doi.org/10.4271/940193>
- Ding, Y., & Pan, Y. X. (2009). Optimal design for stiffness and damping of automobile friction clutch. *5th International Conference on Natural Computation, ICNC 2009*, 4, 369–373. <https://doi.org/10.1109/ICNC.2009.526>
- Douailler, B., Ravet, F., Delpech, V., Soleri, D., Reveille, B., & Kumar, R. (2011). Direct injection of CNG on high compression ratio spark ignition engine: Numerical and experimental investigation. *SAE 2011 World Congress and Exhibition, 2011-01-09*. <https://doi.org/10.4271/2011-01-0923>
- Duggal, V., Lyford-Pike, E., Wright, J., Dunn, M., Goudie, D., & Munshi, S. (2004). *Development of the HighPressure Direct-Injected, Ultra Low-NOx Natural Gas Engine*. Cole Boulevard, Golden, Colorado.
- Erfan, I., Chitsaz, I., Ziabasharhagh, M., Hajjalimohammadi, A., & Fleck, B. (2015). Injection characteristics of gaseous jet injected by a single-hole nozzle direct injector. *Fuel*, 160, 24–34. <https://doi.org/10.1016/j.fuel.2015.07.037>
- Etheridge, J., Mosbach, S., Kraft, M., Wu, H., & Collings, N. (2010). A fast detailed-chemistry modelling approach for simulating the SI-HCCI transition. *SAE Technical Papers*, 1. <https://doi.org/10.4271/2010-01-1241>
- Everett, R. V. (2011). *An Improved Model-Based Methodology for Calibration of an Alternative Fueled Engine*. The Ohio State University.
- Falcone, P., De Gennaro, M. C., Fiengony, G., Glielmo, L., Santini, S., & Langthaler, P. (2003). Torque generation model for Diesel Engine. *Proceedings of the IEEE Conference on Decision and Control*, 2(4), 1771–1776. <https://doi.org/10.1109/cdc.2003.1272869>
- Fang, Z., Ping, J., Hou, S., & Sun, J. (1998). In-Cylinder Injection Technology and Combustion Characteristics of NG Engine. *The Fourth International Symposium COMODIA 98*.
- Fiveland, S. B., & Assanis, D. N. (2000). A four-stroke homogeneous charge compression ignition engine simulation for combustion and performance studies. *SAE Technical Papers*, 1(724). <https://doi.org/10.4271/2000-01-0332>

- Flekiewicz, M. (2009). Ignition timing advance in the bi-fuel engine. *Transport Problems: An International Scientific Journal*, 4(2), 117–127. Retrieved from <http://www.doaj.org/doi?func=openurl&issn=18960596&date=2009&volume=4&issue=2&spage=117&genre=article>
- Fleming, Peter, & Purshouse, R. (2002). Genetic Algorithms In Control Systems Engineering. In *CONTROL SYSTEMS, ROBOTICS AND AUTOMATION* (Vol. 17). Encyclopedia of Life Support Systems (EOLSS).
- Fleming, Pj, & Purshouse, R. (2001). Genetic algorithms in control systems engineering. *Control and Systems Engineering, XVII*. Retrieved from <http://www.eolss.net/Sample-Chapters/C18/E6-43-26.pdf>
- Fleming, PJ, & Purshouse, R. (2002). Evolutionary algorithms in control systems engineering: a survey. In *Control Engineering Practice* (Vol. 10, pp. 1223–1241). [https://doi.org/10.1016/S0967-0661\(02\)00081-3](https://doi.org/10.1016/S0967-0661(02)00081-3)
- Fukuzawa, Y., Fukuzawa, Y., Shimoda, H., Shimoda, H., Kakuhama, Y., & Kakuhama, Y. (2001). Development of high efficiency Miller cycle gas engine. *Mitsubishi Heavy Industries, Ltd. Technical Review*, 38(3), 146–150. Retrieved from <http://www.mhi.co.jp/technology/review/pdf/e383/e383146.pdf>
- Garg, A. B., Diwan, P., & Saxena, M. (2012). *Artificial Neural Networks based Methodologies for Optimization of Engine Operations*. 3(5), 1–5.
- Ge, H.-W., Shi, Y., Reitz, R. D., Wickman, D. D., & Willems, W. (2009). Optimization of a HSDI Diesel Engine for Passenger Cars Using a Multi-Objective Genetic Algorithm and Multi-Dimensional Modeling. *SAE International Journal of Engines*, 2(1), 691–713. <https://doi.org/10.4271/2009-01-0715>
- Gogoi, T. K., & Baruah, D. C. (2010). A cycle simulation model for predicting the performance of a diesel engine fuelled by diesel and biodiesel blends. *Energy*, 35(3), 1317–1323. <https://doi.org/10.1016/j.energy.2009.11.014>
- Golzari, R. (2018). *Experimental study of the impact of port and direct fuel injection strategies on the efficiency, performance and emissions of a downsized GDI engine*. Brunel University London United Kingdom.
- Goto, S., Takahashi, S., Yamada, T., & Yamada, T. (2007). Development of high density gas engine 28AG. *Ishikawajima-Harima Giho/IHI Engineering Review*, 40(1), 216–219.
- Guo, S., Dooner, M., Wang, J., Xu, H., & Lu, G. (2017). Adaptive engine optimisation using NSGA-II and MODA based on a sub-structured artificial neural network. *ICAC 2017 - 2017 23rd IEEE International Conference on Automation and Computing: Addressing Global Challenges through Automation and Computing*, (September), 7–8. <https://doi.org/10.23919/IconAC.2017.8082008>
- Gutjahr, T., Kleinegraeber, H., Huber, T., & Kruse, T. (2015). Advanced Statistical System Identification in ECU-Development and Optimization. *SAE Technical Papers, 2015-Sept*. <https://doi.org/10.4271/2015-01-2796>

- Gutjahr, T., Kleinegraeber, H., Huber, T., & Kruse, T. (2017). Advanced Modeling And Optimization For Virtual Calibration Of Internal Combustion Engines. *Proceedings of the 2017 Ground Vehicle Systems Engineering and Technology Symposium (GVSETS)*. Michigan.
- Guzzella, L., & Onder, C. H. (2010). *Introduction to Modeling and Control of Internal Combustion Engine Systems*. <https://doi.org/10.1007/978-3-642-10775-7>
- Hafner, M., Jost, O., & Isermann, R. (2002). Mechatronic design approach for engine management systems. *Mechatronics*, 12(8), 1035–1046. [https://doi.org/10.1016/S0957-4158\(02\)00011-9](https://doi.org/10.1016/S0957-4158(02)00011-9)
- Hamad, A., Yu, D., Gomm, J., & Sangha, M. S. (2011). Radial basis function neural network in fault detection of automotive engines. *International Journal of Engineering, Science and Technology*, 2(10), 1–8. <https://doi.org/10.4314/ijest.v2i10.64007>
- Hardie, C., Tait, H., Craig, S., Chase, J. G., Smith, B. W., & Harris, G. (2002). Automated tuning of an engine management unit for an automotive engine. *Proceedings of the Institution of Mechanical Engineers, Part D: Journal of Automobile Engineering*, 216(10), 841–849. <https://doi.org/10.1177/095440700221600107>
- Hassan, M K, Aris, I., Mahmood, S., & Sidek, R. (2009). An Experimental Result of Exhaust Emission Concentration Relative to Various Injection Timing of CNG Fuelled Direct Injection Engine. *European Journal of Scientific Research*, 25(3), 405–416.
- Hassan, M K, Aris, I., Mahmood, S., & Sidek, R. (2010). Influence of Injection and Ignition of CNG Fuelled Direct Injection Engine at Constant Speed. *Australian Journal of Basic and Applied Sciences*, 4(10), 4870–4879.
- Hassan, Mohd Khair, Aris, I., N. Zainuddin, K., & A. Alina, N. (2009). Torque and Power of CNGDI Engine with Two Different Piston Crown Shapes. *Journal of Applied Sciences Research*, 5(8), 949–954.
- HP Injection Valve HDEV 5.2. (2014). Bosch Engineering GmbH, Abstatt, Germany.
- He, Y., & Rutland, C. J. (2004). Application of artificial neural networks in engine modelling. *International Journal of Engine Research*, 5(4), 281–296. <https://doi.org/10.1243/146808704323224204>
- Heywood, J. B. (1988). *Internal Combustion Engine Fundamentals*. McGraw-Hill.
- Ho, T., & Karri, V. (2011). Optimising multi-objective control methodology of a hydrogen powered car. *International Journal of Hydrogen Energy*, 36(10), 6269–6280. <https://doi.org/10.1016/j.ijhydene.2011.02.041>
- Hosseini, S., Abdollah, R., & Khani, A. (2008). A Developed Quasi-Dimensional Combustion Model in Spark-Ignition Engines. *Proceeding of the World Congress on Engineering*, II(1), 2–6.

- Hu, Q., Wu, S. F., Stottler, S., & Raghupathi, R. (2001). Modelling of dynamic responses of an automotive fuel rail system, Part I: Injector. *Journal of Sound and Vibration*, 245(5), 801–814. <https://doi.org/10.1006/jsvi.2000.3605>
- Huang, Z., Shiga, S., Ueda, T., Nakamura, H., Ishima, T., Obokata, T., ... Kono, M. (2003a). Basic characteristics of direct injection combustion fuelled with compressed natural gas and gasoline using a rapid compression machine. *Proceedings of the Institution of Mechanical Engineers, Part D: Journal of Automobile Engineering*, 217(11), 1031–1038. <https://doi.org/10.1243/095440703770383929>
- Huang, Z., Shiga, S., Ueda, T., Nakamura, H., Ishima, T., Obokata, T., ... Kono, M. (2003b). Correlation of ignitability with injection timing for direct injection combustion fuelled with compressed natural gas and gasoline. *Proceedings of the Institution of Mechanical Engineers, Part D: Journal of Automobile Engineering*, 217(6), 499–506. <https://doi.org/10.1243/095440703766518122>
- Ibrahim, A., & Bari, S. (2008). Optimization of a natural gas SI engine employing EGR strategy using a two-zone combustion model. *Fuel*, 87(10–11), 1824–1834. <https://doi.org/10.1016/j.fuel.2007.10.004>
- Ibrahim, A., & Bari, S. (2010). An experimental investigation on the use of EGR in a supercharged natural gas SI engine. *Fuel*, 89(7), 1721–1730. <https://doi.org/10.1016/j.fuel.2009.07.005>
- Isermann, R., & Sequenz, H. (2016). Model-based development of combustion-engine control and optimal calibration for driving cycles: general procedure and application. *IFAC-PapersOnLine*, 49(11), 633–640. <https://doi.org/10.1016/j.ifacol.2016.08.092>
- Iskandar, T. (2010). Compressed Natural Gas Direct Injection (Spark Plug Fuel Injector). In *Natural Gas* (p. Ch. 13). <https://doi.org/10.5772/9851>
- Jagadish, D., Kumar, P. R., & Madhu, M. K. (2011). Zero dimensional simulation of combustion process of a di diesel engine fuelled with biofuels. *International Journal of Mechanical and Mechatronics Engineering*, 5(8), 7. Retrieved from <http://waset.org/publications/1648/zero-dimensional-simulation-of-combustion-process-of-a-di-diesel-engine-fuelled-with-biofuels>
- Jahirul, M. I., Masjuki, H. H., Saidur, R., Kalam, M. A., Jayed, M. H., & Wazed, M. A. (2010). Comparative engine performance and emission analysis of CNG and gasoline in a retrofitted car engine. *Applied Thermal Engineering*, 30(14–15), 2219–2226. <https://doi.org/10.1016/j.applthermaleng.2010.05.037>
- Janakiraman, V. M. (2013). *Machine Learning for Identification and Optimal Control of Advanced Automotive Engines*. (The University of Michigan). Retrieved from <http://deepblue.lib.umich.edu/handle/2027.42/102392>
- Janakiraman, V. M., Nguyen, X., & Assanis, D. (2013). Nonlinear identification of a gasoline HCCI engine using neural networks coupled with principal component analysis. *Applied Soft Computing Journal*, 13(5), 2375–2389.

<https://doi.org/10.1016/j.asoc.2013.01.006>

- Jung, D., & Assanis, D. (2001). Multi-zone DI diesel spray combustion model for cycle simulation studies of engine performance and emissions. *SAE Technical Paper 2001-01-1246*, (724).
- Kalam, M. A., & Masjuki, H. H. (2011). An experimental investigation of high performance natural gas engine with direct injection. *Energy*, *36*(5), 3563–3571. <https://doi.org/10.1016/j.energy.2011.03.066>
- Kalam, M. A., Masjuki, H. H., Mahlia, T. M. I., Fuad, M. A., Halim, K., Ishak, A., ... Shahrir, A. (2009). Experimental test of a new compressed natural gas engine with direct injection. *SAE Technical Papers*, 4970. <https://doi.org/10.4271/2009-01-1967>
- Kamaruddin, T. N. A. T., & Mat Darus, I. Z. (2012). System Identification for Internal Combustion Engine Model. *2012 Sixth Asia Modelling Symposium*, 17–22. <https://doi.org/10.1109/AMS.2012.13>
- Kamel, M. M. (2005). Development of a Cummins ISL Natural Gas Engine at 0.2 g/bhp-hr. In *Cummins Westport Vancouver, British Columbia, Canada*.
- Kar, T., & Agarwal, A. K. (2015). Development of a single cylinder CNG direct injection engine and its performance , emissions and combustion characteristics. *Int. J. Oil, Gas and Coal Technology*, *10*(2). <https://doi.org/10.1504/IJOGCT.2015.070839>
- Karkamkar, A. (2013). Effect of Spark Timing on Combustion Process of SI Engines using MATLAB. *International Journal of Computer Applications*, *79*(October), 975–8887.
- Karlsson, J., & Fredriksson, J. (1999). Cylinder-by-Cylinder Engine Models Vs Mean Value Engine Models for Use in Powertrain Control Applications. *SAE Technical Paper*, (724). <https://doi.org/10.4271/1999-01-0906>
- Kesgin, U. (2003). Study on prediction of the effects of design and operating parameters on NOx emissions from a leanburn natural gas engine. *Energy Conversion and Management*, *44*(6), 907–921. [https://doi.org/10.1016/S0196-8904\(02\)00093-6](https://doi.org/10.1016/S0196-8904(02)00093-6)
- Kesgin, U. (2004). Genetic algorithm and artificial neural network for engine optimisation of efficiency and NOx emission. *Fuel*, *83*(7–8), 885–895. <https://doi.org/10.1016/j.fuel.2003.10.025>
- Keskinen, K., Kaario, O., Nuutinen, M., Vuorinen, V., Künsch, Z., Ola, L., & Larmi, M. (2016). Mixture formation in a direct injection gas engine : Numerical study on nozzle type , injection pressure and injection timing effects. *Energy*, *94*, 542–556. <https://doi.org/10.1016/j.energy.2015.09.121>
- Khairnar, G., Shrivastava, J., Pande, S., Londhe, R., Yaser Hussaini, A., Yogesh, & Ambekar. (2015). Development of a Single Cylinder Dedicated CNG Engine for Small 4 Wheeler Commercial Vehicles. *SAE Technical Paper*, 2–6. <https://doi.org/10.4271/2015-01-1681>. Copyright

- Khan, M. I., & Yasmin, T. (2014). Development of natural gas as a vehicular fuel in Pakistan: Issues and prospects. *Journal of Natural Gas Science and Engineering*, 17, 99–109. <https://doi.org/10.1016/j.jngse.2014.01.006>
- Khan, M. I., Yasmin, T., & Shakoor, A. (2015). Technical overview of compressed natural gas (CNG) as a transportation fuel. *Renewable and Sustainable Energy Reviews*, 51, 785–797. <https://doi.org/10.1016/j.rser.2015.06.053>
- Kodah, Z. ., Soliman, H. ., Abu Qudais, M., & Jahmany, Z. . (2000). Combustion in a spark-ignition engine. *Applied Energy*, 66(3), 237–250. [https://doi.org/10.1016/S0306-2619\(99\)00129-4](https://doi.org/10.1016/S0306-2619(99)00129-4)
- Korakianitis, T., Namasivayam, a. M., & Crookes, R. J. (2011). Natural-gas fueled spark-ignition (SI) and compression-ignition (CI) engine performance and emissions. *Progress in Energy and Combustion Science*, 37(1), 89–112. <https://doi.org/10.1016/j.pecs.2010.04.002>
- Kubesh, J. T., & Podnar, D. J. (1998). Ultra Low Emissions and High Efficiency from an On-Highway Natural Gas Engine. *SAE Technical Paper Series: State of Alternative Fuel Technologies*. <https://doi.org/10.4271/981394>
- Kumarappa, S., & Prabhukumar, G. P. (2008). Improving the Performance of Two Stroke Spark Ignition Engine by Direct Electronic CNG Injection. *Jordan Journal of Mechanical and Industrial Engineering Volume*, 2(4), 169–174.
- Lake, T. H., Stokes, J., Whitaker, P. A., & Crump, J. V. (1998). Comparison of Direct Injection Gasoline Combustion Systems. *SAE Technical Paper Series*, 1(412). <https://doi.org/10.4271/980154>
- Lee, T. K., Park, H., Hyun, J., Lee, C., & Song, H. H. (2019). Applicability of high-pressure direct-injected methane jet for a pure compression-ignition engine operation. *Fuel*, 251, 428–437. <https://doi.org/https://doi.org/10.1016/j.fuel.2019.04.067>
- Lei, Y., Liu, J., Qiu, T., Li, Y., Wang, Y., Wan, B., & Liu, X. (2019). Gas jet flow characteristic of high-pressure methane pulsed injection of single-hole cylindrical nozzle. *Fuel*, 257(August), 116081. <https://doi.org/10.1016/j.fuel.2019.116081>
- Liu, Y. F., Liu, B., Liu, L., Zeng, K., & Huang, Z. H. (2010). Combustion characteristics and particulate emission in a natural-gas direct-injection engine: Effects of the injection timing and the spark timing. *Proceedings of the Institution of Mechanical Engineers, Part D: Journal of Automobile Engineering*, 224(8), 1071–1080. <https://doi.org/10.1243/09544070JAUTO1532>
- Liu, Y., Yeom, J., & Chung, S. (2013). A study of spray development and combustion propagation processes of spark-ignited direct injection (SIDI) compressed natural gas (CNG). *Mathematical and Computer Modelling*, 57(1–2), 228–244. <https://doi.org/10.1016/j.mcm.2011.06.035>
- Ma, F, Ding, S., Wang, Y., Wang, Y., Wang, J., & Zhao, S. (2008). Study on combustion behaviors and cycle-by-cycle variations in a turbocharged lean burn natural gas S.I. engine with hydrogen enrichment. *International Journal of Hydrogen Energy*,

33(23), 7245–7255. <https://doi.org/10.1016/j.ijhydene.2008.09.016>

- Ma, Fanhua, Wang, Y., Liu, H., Li, Y., Wang, J., & Ding, S. (2008). Effects of hydrogen addition on cycle-by-cycle variations in a lean burn natural gas spark-ignition engine. *International Journal of Hydrogen Energy*, 33(2), 823–831. <https://doi.org/10.1016/j.ijhydene.2007.10.043>
- Ma, Fanhua, Wang, Y., Wang, M., Liu, H., Wang, J., Ding, S., & Zhao, S. (2008). Development and validation of a quasi-dimensional combustion model for SI engines fuelled by HCNG with variable hydrogen fractions. *International Journal of Hydrogen Energy*, 33(18), 4863–4875. <https://doi.org/10.1016/j.ijhydene.2008.06.068>
- Majczak, A., Barański, G., Sochaczewski, R., & Siadkowska, K. (2017). Cng Injector Research for Dual Fuel Engine. *Advances in Science and Technology Research Journal*, 11(1), 212–219. <https://doi.org/10.12913/22998624/68458>
- Malhotra, R., Singh, N., & Singh, Y. (2011). Genetic Algorithms: Concepts, Design for Optimization of Process Controllers. *Computer and Information Science*, 4(2), 39–54. <https://doi.org/10.5539/cis.v4n2p39>
- Mark H. Beale, Hagan, M. T., & Demuth, H. B. (2018). *Neural Network Toolbox User's Guide* (2018a ed.). Mathworks Inc.
- Martínez-Morales, J. D., Palacios-Hernández, E. R., & Velázquez-Carrillo, G. A. (2013). Modeling and multi-objective optimization of a gasoline engine using neural networks and evolutionary algorithms. *Journal of Zhejiang University SCIENCE A*, 14(9), 657–670. <https://doi.org/10.1631/jzus.A1300010>
- Mathworks. (2018). *Global Optimization Toolbox User Guide R2018b* (2018b ed.; The MathWorks Inc., Ed.). Natick, Massachusetts: The MathWorks Inc.
- MathWorks. (2018). *Model-Based Calibration Toolbox: CAGE User's Guide* (2018a ed.). Natick, Massachusetts: The MathWorks Inc.
- Mattarelli, E., Perini, F., & Rinaldini, C. A. (2009). Optimization of a Supercharged Single Cylinder Engine for a Formula SAE Racing Car. *SAE International Journal of Engines*, 2(1), 2009-01–0309. <https://doi.org/10.4271/2009-01-0309>
- Mazlan, S. K. (2017). *Study of Direct Injection and Pre-Chamber Application in Light Duty Gaseous Fuel Engines*. RMIT University.
- McTaggart-Cowan, G. P., Bushe, W. K., Hill, P. G., & Munshi, S. R. (2003). A supercharged heavy-duty diesel single-cylinder research engine for high-pressure direct injection of natural gas. *International Journal of Engine Research*, 4(4), 315–330. <https://doi.org/10.1243/146808703322743912>
- Metallidis, P., & Natsiavas, S. (2003). Linear and nonlinear dynamics of reciprocating engines. *International Journal of Non-Linear Mechanics*, 38(5), 723–738. [https://doi.org/10.1016/S0020-7462\(01\)00129-9](https://doi.org/10.1016/S0020-7462(01)00129-9)

- Miura, A., & Honjou, F. (2000). Further Development of Fuel Consumption For Heavy-duty CNG Engine. *Seoul 2000 FISITA World Automotive Congress*, 1–6.
- Mohamad, T., Harrison, M., Jermy, M., & Heoy Geok, H. (2010). The structure of the high-pressure gas jet from a spark plug fuel injector for direct fuel injection. In *Journal of Visualization* (Vol. 13). <https://doi.org/10.1007/s12650-009-0017-2>
- Mohamad, T I, & Geok, H. H. (2008). PLIF Flow Visualization of Methane Gas Jet from Spark Plug Fuel Injector in a Direct Injection Spark Ignition Engine. *Proceedings of the 1st WSEAS International Conference on VISUALIZATION, IMAGING and SIMULATION*, 35–40.
- Mohamad, Taib Iskandar. (2009). *Compressed natural gas direct injection (spark plug fuel injector)*. 289–306.
- Mohamad, Taib Iskandar, & Geok, H. H. (2009). *Visualization of Gas Jet in Water : A New Approach for Gaseous Fuel Injection Measurement. I*, 2–6.
- Mohammadi, A., Manzie, C., & Nešić, D. (2014). Online optimization of spark advance in alternative fueled engines using extremum seeking control. *Control Engineering Practice*, 29, 201–211. <https://doi.org/10.1016/j.conengprac.2014.02.008>
- Mohammed, S. E., Baharom, M. B., Aziz, A. R. A., & Firmansyah. (2011a). The effects of fuel-injection timing at medium injection pressure on the engine characteristics and emissions of a CNG-DI engine fueled by a small amount of hydrogen in CNG. *International Journal of Hydrogen Energy*, 36(18), 11997–12006. <https://doi.org/10.1016/j.ijhydene.2011.05.110>
- Mohammed, S. E., Baharom, M. B., Aziz, A. R. A., & Firmansyah. (2011b). The effects of fuel-injection timing at medium injection pressure on the engine characteristics and emissions of a CNG-DI engine fueled by a small amount of hydrogen in CNG. *International Journal of Hydrogen Energy*, 36(18), 11997–12006. <https://doi.org/https://doi.org/10.1016/j.ijhydene.2011.05.110>
- Mustang. (2005). *Mustang Dynamometer -Power Dyne PC Operators Manual*. Twinsburg, Ohio: Mustang Dynamometer.
- Narayanaswamy, K., & Rutland, C. J. (2004). Cycle Simulation Diesel HCCI Modeling Studies and Control. *SAE Technical Paper*, (724). <https://doi.org/10.4271/2004-01-2997>
- Neshat, E., & Saray, R. K. (2014). Effect of different heat transfer models on HCCI engine simulation. *Energy Conversion and Management*, 88, 1–14. <https://doi.org/10.1016/j.enconman.2014.07.075>
- Niedernolte, H., Klöpffer, F., Mitterer, A., & Schwarzer, F. (2006). Workflow for data evaluation during basic calibration of combustion engines. *Proceedings of the IEEE International Conference on Control Applications*, 2060–2065. <https://doi.org/10.1109/CACSD-CCA-ISIC.2006.4776957>
- Olsson, J.-O., Tunestål, P., Johansson, B., Fiveland, S., Agama, R., Willi, M., & Assanis, D. (2002). Compression Ratio Influence on Maximum Load of a Natural Gas Fueled

- HCCI Engine. *SAE Technical Paper*, 111(724), 442–458. <https://doi.org/10.4271/2002-01-0111>
- Park, C., Kim, C., Lee, S., Lee, S., & Lee, J. (2019). Comparative evaluation of performance and emissions of CNG engine for heavy-duty vehicles fueled with various caloric natural gases. *Energy*, 174, 1–9. <https://doi.org/https://doi.org/10.1016/j.energy.2019.02.120>
- Park, S. W. (2010). Optimization of combustion chamber geometry for stoichiometric diesel combustion using a micro genetic algorithm. *Fuel Processing Technology*, 91(11), 1742–1752. <https://doi.org/10.1016/j.fuproc.2010.07.015>
- Pezouvanis, A. (2010). *Engine Modelling for Virtual Mapping* (University of Bradford). Retrieved from <http://hdl.handle.net/10454/4419>
- Poulton, M. L. (1994). *Alternative Fuels for Road Vehicles*. WIT Press/Computational Mechanics.
- Pulkrabek, W. W. (2003). *Engineering Fundamentals of the Internal Combustion Engine*. Prentice Hall.
- Rahim, M. F. A., Jaafar, A. A., Taha, Z., & Mamat, R. (2020). Simulation study on the effect of fuel injection and air intake boundary setup on the brake torque response by using comprehensive vehicle model for natural gas vehicle (NGV). *IOP Conference Series: Materials Science and Engineering*, 863.
- Rahman, M. M., K. Mohamme, M., & A. Bakar, R. (2009). Effects of Air-Fuel Ratio and Engine Speed on Performance of Hydrogen Fueled Port Injection Engine. *Journal of Applied Sciences*, 9(6), 1128–1134. <https://doi.org/10.3923/jas.2009.1128.1134>
- Rakopoulos, C. D., Antonopoulos, K. A., & Rakopoulos, D. C. (2007). Development and application of multi-zone model for combustion and pollutants formation in direct injection diesel engine running with vegetable oil or its bio-diesel. *Energy Conversion and Management*, 48(7), 1881–1901. <https://doi.org/10.1016/j.enconman.2007.01.026>
- Rakopoulos, C. D., & Giakoumis, E. G. (2006). Review of Thermodynamic Diesel Engine Simulations under Transient Operating Conditions. *SAE Technical Paper*. <https://doi.org/10.4271/2006-01-0884>
- Rask, E., & Sellnau, M. (2004). Simulation-based engine calibration: Tools, techniques, and applications. *SAE Technical Papers*, 2004(724). <https://doi.org/10.4271/2004-01-1264>
- Ropke, K. (2014). Design of Experiments for Engine Calibration. *Design of Experiments in Engine Development*, 322–327.
- Rousseau, S., Lemoult, B., & Tazerout, M. (1999). Combustion characterization of natural gas in a lean burn spark-ignition engine. *Proceedings of the Institution of Mechanical Engineers, Part D: Journal of Automobile Engineering*, 213(5), 481–489. <https://doi.org/10.1243/0954407991527044>

- Rutherford, S. J., & Cole, D. J. (2010). Modelling nonlinear vehicle dynamics with neural networks. *International Journal of Vehicle Design*, 53(4), 260–287. <https://doi.org/10.1504/IJVD.2010.034101>
- S4P Service Manual. (2004). Perusahaan Otomobil Nasional Berhad, Shah Alam, Malaysia.
- SAE, I. (2011). *Engine Power Test Code - Spark Ignition and Compression Ignition - As Installed Net Power Rating*. Retrieved from <https://www.sae.org/standards/development/about-saej1349-certified-power/>
- Şahin, Z., & Durgun, O. (2008). Multi-zone combustion modeling for the prediction of diesel engine cycles and engine performance parameters. *Applied Thermal Engineering*, 28(17–18), 2245–2256. <https://doi.org/10.1016/j.applthermaleng.2008.01.002>
- Sakawaki, A., Kaji, H., Yamamoto, M., & Sakoda, S. (2009). Real-time Engine Control Parameters Optimization Method for Small Diesel Engine by Multi Objective Genetic Algorithm. *SAE International Journal of Engines*, 2(1), 2009-01–0241. <https://doi.org/10.4271/2009-01-0241>
- Sangha, M., Gomm, J., Yu, D., & Page, G. F. (2005). Fault Detection And Identification Of Automotive Engines Using Neural Networks. *IFAC Proceedings Volumes*, 38(1), 272–277. <https://doi.org/10.3182/20050703-6-CZ-1902.01933>
- Sankesh, D., Edsell, J., Mazlan, S., & Lappas, P. (2017). Comparative Study between Early and Late Injection in a Natural-gas Fuelled Spark-ignited Direct-injection Engine. *Energy Procedia*, 110, 275–280. <https://doi.org/https://doi.org/10.1016/j.egypro.2017.03.139>
- Schimpf, P. H. (2013). A Detailed Explanation of Solenoid Force. *International Journal on Recent Trends in Engineering and Technology*, 8(2). Retrieved from <http://searchdl.org/public/journals/2013/IJRTET/8/2/25.pdf>
- Seboldt, D. (2016). Injection strategies for low HC raw emissions in SI engines with CNG direct injection. *Automotive and Engine Technology*, 1(1), 81–91. <https://doi.org/10.1007/s41104-016-0002-4>
- Semin, & Abu Bakar, R. (2008). A Technical Review of Compressed Natural Gas as an Alternative Fuel for Internal Combustion Engines. *American J. of Engineering and Applied Sciences*, 1(4), 302–311. Retrieved from <http://thescipub.com/pdf/10.3844/ajeassp.2008.302.311>
- Senecal, P. K., Montgomery, D. T., & Reitz, R. D. (2000). A methodology for engine design using multi-dimensional modelling and genetic algorithms with validation through experiments. *International Journal of Engine Research*, 1(3), 229–248. <https://doi.org/10.1243/1468087001545155>
- Sequenz, H., & Isermann, R. (2011). Emission Model Structures for an Implementation on Engine Control Units. *IFAC Proceedings Volumes*, 44(1), 11851–11856. <https://doi.org/10.3182/20110828-6-IT-1002.03131>

- Sequenz, H., Mrosek, M., & Isermann, R. (2010). A Global-Local Emission-Model for NO. *ASME 2010 Dynamic Systems and Control Conference, Volume 1*, 719–726. <https://doi.org/10.1115/DSCC2010-4161>
- Serrano, J. R., Climent, H., Guardiola, C., & Piqueras, P. (2009). Methodology for characterisation and simulation of turbocharged diesel engines combustion during transient operation. Part 2: Phenomenological combustion simulation. *Applied Thermal Engineering*, 29(1), 150–158. <https://doi.org/10.1016/j.applthermaleng.2008.02.010>
- Sharafi, J., Moase, W. H., & Manzie, C. (2018). Multiplexed extremum seeking for calibration of spark timing in a CNG-fuelled engine. *Control Engineering Practice*, 72(October 2017), 42–52. <https://doi.org/10.1016/j.conengprac.2017.11.005>
- Sitthiracha, S. (2006). An analytical model of spark ignition engine for performance prediction. *The 20th Conference of Mechanical Engineering Network of Thailand*, (October), 1–60. Retrieved from <http://www.123seminaronly.com/Seminar-Reports/040/70087958-An-Analytical-Model-of-Spark-Ignition-Engine-for-Performance-Prediction.pdf>
- Song, J., Choi, M., Kim, D., & Park, S. (2017). Combustion Characteristics of Methane Direct Injection Engine Under Various Injection Timings and Injection Pressures. *Journal of Engineering for Gas Turbines and Power*, 139(8). <https://doi.org/10.1115/1.4035817>
- Song, J., Choi, M., & Park, S. (2017). Comparisons of the volumetric efficiency and combustion characteristics between CNG-DI and CNG-PFI engines. *Applied Thermal Engineering*, 121, 595–603. <https://doi.org/https://doi.org/10.1016/j.applthermaleng.2017.04.110>
- Szekely, G. A., & Alkidas, A. C. (2005). Combustion Characteristics of a Spray-Guided Direct-Injection Stratified-Charge Engine with a High-Squish Piston Reprinted From : SI Combustion and Direct Injection SI Engine Technology. *SAE Technical Paper Series*, 2005-01-19.
- Taha, Z., Rahim, M. A., & Mamat, R. (2017). Injection characteristics study of high-pressure direct injector for Compressed Natural Gas (CNG) using experimental and analytical method. *IOP Conference Series: Materials Science and Engineering*, 257(1), 012057. <https://doi.org/10.1088/1757-899X/257/1/012057>
- Tan, Y., & Saif, M. (2000). Neural-networks-based nonlinear dynamic modeling for automotive engines. *Neurocomputing*, 30(1–4), 129–142. [https://doi.org/10.1016/S0925-2312\(99\)00121-6](https://doi.org/10.1016/S0925-2312(99)00121-6)
- Tirkey, J. V., Gupta, H. N., & Shukla, S. K. (2010). Analytical study to minimize the engine exhaust emissions and safe knock limit of CNG powered four-stroke SI engine. *International Journal Of Energy And Environment*, 1(1), 31–52.
- Turkson, R.F., Yan, F., Ali, M. K. A., & Hu, J. (2016). Artificial neural network applications in the calibration of spark-ignition engines: An overview. *Engineering Science and Technology, an International Journal*, 19(3), 1346–1359.

<https://doi.org/10.1016/j.jestch.2016.03.003>

- Turkson, Richard Fiifi, Yan, F., Ahmed Ali, M. K., Liu, B., & Hu, J. (2016). Modeling and multi-objective optimization of engine performance and hydrocarbon emissions via the use of a computer aided engineering code and the NSGA-II genetic algorithm. *Sustainability (Switzerland)*, 8(1), 1–15. <https://doi.org/10.3390/su8010072>
- Turrio-Baldassarri, L., Battistelli, C. L., Conti, L., Crebelli, R., De Berardis, B., Iamiceli, A. L., ... Iannaccone, S. (2006). Evaluation of emission toxicity of urban bus engines: Compressed natural gas and comparison with liquid fuels. *Science of The Total Environment*, 355(1), 64–77. <https://doi.org/https://doi.org/10.1016/j.scitotenv.2005.02.037>
- Vong, C. man, & Wong, P. kin. (2010). Case-based adaptation for automotive engine electronic control unit calibration. *Expert Systems with Applications*, 37(4), 3184–3194. <https://doi.org/10.1016/j.eswa.2009.09.063>
- Wasiu, S. O., Sulaiman, S. A., & Aziz, A. R. A. (2011). An experimental study of different effects of EGR rates on the performance and exhaust emissions of the stratified charge piston direct injection compressed natural gas engine. *Journal of Applied Sciences*, 11(9), 1479–1490. <https://doi.org/10.3923/jas.2011.1479.1490>
- Wong, P. K., Tam, L. M., Li, K., & Vong, C. M. (2010). Engine idle-speed system modelling and control optimization using artificial intelligence. *Proceedings of the Institution of Mechanical Engineers, Part D: Journal of Automobile Engineering*, 224(1), 55–72. <https://doi.org/10.1243/09544070JAUTO1196>
- Wong, P. K., Tam, L. M., li, K., & Wong, H. C. (2008). Automotive engine idle speed control optimization using least squares support vector machine and genetic algorithm. *International Journal of Intelligent Computing and Cybernetics*, 1(4), 598–616. <https://doi.org/10.1108/17563780810919140>
- Wong, P., Tam, L., & Ke, L. (2012). Automotive engine power performance tuning under numerical and nominal data. *Control Engineering Practice*, 20(3), 300–314. <https://doi.org/10.1016/j.conengprac.2011.11.006>
- Wong, Pak Kin, Tam, L. M., & Ke, L. (2012). Automotive engine power performance tuning under numerical and nominal data. *Control Engineering Practice*, 20(3), 300–314. <https://doi.org/10.1016/j.conengprac.2011.11.006>
- Wu, B., Filipi, Z., Assanis, D. N., Kramer, D. M., Ohl, G. L., Prucka, M. J., & DiValentin, E. (2004). Using Artificial Neural Networks for Representing the Air Flow Rate through a 2.4 Liter VVT Engine. *SAE Technical Paper*, (724). <https://doi.org/10.4271/2004-01-3054>
- Wu, M. H., Lin, W., & Duan, S. Y. (2008). Investigation of a multi-objective optimization tool for engine calibration. *Proceedings of the Institution of Mechanical Engineers, Part D: Journal of Automobile Engineering*, 222(2), 235–249. <https://doi.org/10.1243/09544070JAUTO398>

- Wu, Mian Hong, Lin, W., & Duan, S. Y. (2006). Developing a neural network and real genetic algorithm combined tool for an engine test bed. *Proceedings of the Institution of Mechanical Engineers, Part D: Journal of Automobile Engineering*, 220(12), 1737–1753. <https://doi.org/10.1243/09544070JAUTO229>
- Yadollahi, B., & Boroomand, M. (2013). The effect of combustion chamber geometry on injection and mixture preparation in a CNG direct injection SI engine. *Fuel*, 107, 52–62. <https://doi.org/10.1016/j.fuel.2013.01.004>
- Yang, B., Wei, X., Xi, C., Liu, Y., Zeng, K., & Lai, M. C. (2014). Experimental study of the effects of natural gas injection timing on the combustion performance and emissions of a turbocharged common rail dual-fuel engine. *Energy Conversion and Management*, 87, 297–304. <https://doi.org/10.1016/j.enconman.2014.07.030>
- Yang, Z., Wang, L., & Li, S. (2008). Investigation into the optimization control technique of hydrogen-fueled engines based on genetic algorithms. *International Journal of Hydrogen Energy*, 33(22), 6780–6791. <https://doi.org/10.1016/j.ijhydene.2008.05.108>
- Yoon, P., Park, S., & Sunwoo, M. (2000). A Nonlinear Dynamic Model of SI Engines for Designing Controller. *FISITA World Automotive Congress*, 1–8.
- Yuan, B., & Gallagher, M. (2005). A hybrid approach to parameter tuning in genetic algorithms. *2005 IEEE Congress on Evolutionary Computation*, 2, 1096–1103 Vol. 2. <https://doi.org/10.1109/CEC.2005.1554813>
- Yusaf, T. F., Hoe, S., Fong, & Yusoff, M. (2005). Modeling of Transient Heat Flux in Spark Ignition Engine During Combustion and Comparisons with Experiment. *American Journal of Applied Sciences*, 2(10), 1438–1444. <https://doi.org/10.3844/ajassp.2005.1438.1444>
- Zeng, K., Huang, Z., Liu, B., Liu, L., Jiang, D., Ren, Y., & Wang, J. (2006). Combustion characteristics of a direct-injection natural gas engine under various fuel injection timings. *Applied Thermal Engineering*, 26(8–9), 806–813. <https://doi.org/10.1016/j.applthermaleng.2005.10.011>
- Zhai, Y. J., & Yu, D. L. (2009). Neural network model-based automotive engine air/fuel ratio control and robustness evaluation. *Engineering Applications of Artificial Intelligence*, 22(2), 171–180. <https://doi.org/10.1016/j.engappai.2008.08.001>
- Zhang, X., Palazzolo, A., Kweon, C.-B., Thomas, E., Tucker, R., & Kascak, A. (2014). Direct Fuel Injector Power Drive System Optimization. *SAE International Journal of Engines*, 7(3), 2014-01–1442. <https://doi.org/10.4271/2014-01-1442>
- Zhao, F., Lai, M., & Harrington, D. L. (1999). Automotive spark-ignited direct-injection gasoline engines. *Progress in Energy and Combustion Science*, 25, 437–562. Retrieved from file:///C:/Users/asus/AppData/Local/Mendeley Ltd./Mendeley Desktop/Downloaded/Zhao, Lai, Harrington - 1999 - Automotive spark-ignited direct-injection gasoline engines.pdf

- Zhao, J., & Xu, M. (2013). Fuel economy optimization of an Atkinson cycle engine using genetic algorithm. *Applied Energy*, 105, 335–348. <https://doi.org/10.1016/j.apenergy.2012.12.061>
- Zhao, J., Xu, M., Li, M., Wang, B., & Liu, S. (2012). Design and optimization of an Atkinson cycle engine with the Artificial Neural Network Method. *Applied Energy*, 92, 492–502. <https://doi.org/10.1016/j.apenergy.2011.11.060>
- Zheng, J. J., Wang, J. H., Wang, B., & Huang, Z. H. (2009a). Effect of the compression ratio on the performance and combustion of a natural-gas direct-injection engine. *Proceedings of the Institution of Mechanical Engineers, Part D: Journal of Automobile Engineering*, 223(1), 85–98. <https://doi.org/10.1243/09544070JAUTO976>
- Zheng, J. J., Wang, J. H., Wang, B., & Huang, Z. H. (2009b). Effect of the compression ratio on the performance and combustion of a natural-gas direct-injection engine. *Proceedings of the Institution of Mechanical Engineers, Part D: Journal of Automobile Engineering*, 223(1), 85–98. <https://doi.org/10.1243/09544070JAUTO976>
- Zweiri, Y. (2003). *Nonlinear Modelling and Estimation for Diesel Engines* (King's College London). <https://doi.org/10.13140/2.1.4839.3929>
- Zweiri, Y. H., Whidborne, J. F., Seneviratne, L. D., & Althoefer, K. (2010). A comparison of dynamic models of various complexity for diesel engines. *Mathematical and Computer Modelling of Dynamical Systems*, 8(3), 273–289. <https://doi.org/10.1076/mcmd.8.3.273.14100>
- Zweiri, Y H, Whidborne, J. F., & Seneviratne, L. D. (2001). Detailed analytical model of a single-cylinder Diesel engine in the crank-angle domain. *Proc. IMechE, Part D: J. Automobile Eng.*, 215(11), 1197–1216. <https://doi.org/10.1243/0954407011528734>
- Zweiri, Yahya H, Whidborne, J. F., & Seneviratne, L. D. (1999). *Complete Analytical Model of a Single-Cylinder Diesel Engine for Non-linear Control and Estimation*.

APPENDIX A
ADDITIONAL EQUATION OF VEHICLE MODEL

Coupling of crankshaft and driveline by a torsional spring-damper mechanism

The torsional spring-damper block represents a dynamic element that imposes a combination of internally generated torques between the two connected driveshaft axes, the rod and the case. The complete torque includes these components; 1) Linear damped spring, 2) Coulomb friction (including locking static friction), and 3) Hard stop compliance. It is mathematically given by:

$$T = T_{SD} + T_{HS} + T_C \quad \text{A.1}$$

Where

T_{SD} : Torque due to spring-damper action

T_{HS} : Torque due to hard-stop compliance

T_C : Torque due to Coulomb effect

The stiff-damping torque is a simple linear spring-damping model given by:

$$T_{SD} = -k\phi - \mu\omega \quad \text{A.2}$$

Where

k : torsional stiffness

ϕ : Relative angle between ring and hub

μ : Torsional damping

ω : Relative angular velocity

The hard stop torque, T_{HS} is applied if ϕ moves outside the angular gap between the upper and lower hard stop bounds

$$k_{HS}(\phi - \delta_+) - \mu_{HS}\omega; \quad \phi > \delta_+ \quad \text{A.3}$$

$$0 ; \quad \delta_- < \phi < \delta_+ \quad \text{A.4}$$

$$-k_{HS}(\phi - \delta_-) - \mu_{HS}\omega; \quad \phi < \delta_- \quad \text{A.5}$$

Where

δ_+ , δ_- : Upper and lower hard stop angular displacements

k_{HS} : Contact stiffness applied in hard stop regions

μ_{HS} : Contact damping applied in hard stop regions

The Coulomb friction torque, T_C is a constant, T_k if ω is nonzero (unlocked), and a constant T_S if ω is zero (locked).

$$T_S = |RT_K| \quad \text{A.6}$$

Where

T_k : kinetic friction

T_S : static friction

R : T_S / T_k

Locking Conditions

The Torsional Spring-Damper locks the connected driveshafts together if both:

$$|\omega| < \omega_{Toi} \quad \text{A.7}$$

Where

ω_{Toi} : Maximum relative speed for clutch locking

The torque across the torsional spring-damper is less than T_S . If the clutch locks, ω is reset to zero. If the torque across the torsional spring-damper exceeds T_S , the driveshafts unlock from one another, and ω becomes nonzero.

The additional equation for crankshaft dynamic modelling

The instantaneous angle of connecting rod and the angle of connecting rod at the top dead centre are given by:

$$\phi = \sin^{-1} \left(\frac{\delta}{r + L} \right) \quad \text{A.8}$$

$$\beta = \sin^{-1} \left(\frac{\delta + r \sin(\theta_1 - \phi)}{L} \right) \quad \text{A.9}$$

Crank Shaft Inertia Variation

The crankshaft inertia variation with crank angle, $J(\theta_1)$ is given by the following equation:

$$\begin{aligned} J(\theta_1) = & J_{crank} + M_{crank} (b_2 r)^2 + J_{con} \left[\left(\frac{r}{L} \right)^2 \frac{1}{\lambda(\theta_1)} \cos^2 \theta_1 \right] \quad \text{A.10} \\ & + M_{pis} r^2 \left[\sqrt{\frac{1 - \lambda(\theta_1)}{\lambda(\theta_1)}} \cos \theta_1 + \sin \theta_1 \right]^2 \\ & + M_{con} r^2 (1 - b_1)^2 \cos^2 \theta_1 \\ & + M_{con} r^2 \left[b_1 \sqrt{\frac{1 - \lambda(\theta_1)}{\lambda(\theta_1)}} \cos \theta_1 + \sin \theta_1 \right]^2 \end{aligned}$$

The rate of crankshaft inertia variation

The rate of crankshaft inertia variation with the crank angle, $\frac{\partial J(\theta_1)}{\partial \theta_1}$ is given by the following equation:

$$\begin{aligned}
\frac{\partial J(\theta_1)}{\partial \theta_1} = & 2J_{con} \left[\left(\frac{r}{L}\right)^3 \sqrt{\frac{1-\lambda(\theta_1)}{\lambda(\theta_1)^2}} \cos^3 \theta_1 - \left(\frac{r}{L}\right)^2 \frac{1}{\lambda(\theta_1)} \cos \theta_1 \sin \theta_1 \right] \\
& - 2M_{con}(1-b_1)^2 r^2 \cos \theta_1 \sin \theta_1 \\
& - M_{con} r^2 \left[b_1 \sqrt{\frac{1-\lambda(\theta_1)}{\lambda(\theta_1)}} \cos \theta_1 \right. \\
& \left. - \sin \theta_1 \right] \left\{ - \left[\frac{r b_1}{L \sqrt{\lambda(\theta_1)^3}} \right] \cos^2 \theta_1 - \cos \theta_1 \right. \\
& \left. + b_1 \sqrt{\frac{1-\lambda(\theta_1)}{\lambda(\theta_1)}} \sin \theta_1 \right\} \\
& - M_{pis} r^2 \left[\sqrt{\frac{1-\lambda(\theta_1)}{\lambda(\theta_1)}} \cos \theta_1 \right. \\
& \left. + \sin \theta_1 \right] \left\{ \left[\frac{r}{L \sqrt{\lambda(\theta_1)^3}} \right] \cos^2 \theta_1 - \cos \theta_1 \right. \\
& \left. + \sqrt{\frac{1-\lambda(\theta_1)}{\lambda(\theta_1)}} \sin \theta_1 \right\}
\end{aligned}$$

Instantaneous Friction Model and Its Component

The components of the instantaneous engine friction consist of the ring friction torque, skirt friction torque, bearing friction torque, valve train friction torque, auxiliaries and gear torque losses, and pumping friction torque.

Ring Friction Torque

$$T_{f1} = \eta r |G(\theta_1)| \left\{ \begin{array}{l} \sum_{ii=1}^N \left[\frac{E_{ii} g}{7.07 d_r (d_r / B_{ii} - 1)^3} \right] \pi d_r B_{ii} \\ + \sum_{ii=1}^N a_{ii} |p_i - p_{atm}| \pi d_r B_{ii} \\ + \frac{|p_i - p_{atm}| (\pi/4) d^2 - M_{pass} G_1(\theta_1) \dot{\theta}_1^2}{\eta + G_3(\theta_1)} \end{array} \right\} \quad \text{A.12}$$

The geometric function of the engine

$$G_3(\theta_1) = \frac{L \sqrt{1 - \{[\delta + r \sin(\theta_1 - \phi)]/L\}^2}}{\delta + r |\sin(\theta_1 - \phi)|} \quad \text{A.13}$$

The co-efficient of friction for hydrodynamic lubrication is given by

$$\eta = \begin{cases} c_1 - (c_1 - z) |\sin \theta_1| & \text{if } 1.5\pi \ll \theta_1 \leq 2.5\pi \\ z & \text{if otherwise} \end{cases} \quad \text{A.14}$$

Where

Z is the hydrodynamic friction co-efficient

$$z = \sqrt{\frac{\mu \dot{\theta}_1 r |G(\theta_1)|}{L_r}} \quad \text{A.15}$$

L_r is load per unit length which is given by

$$L_r = \sum_{ii=1}^N \left[\frac{E_{ii} g}{7.07 d_r (d_r / B_{ii} - 1)^3} + |p_{ind} - p_{atm}| \right] B_{ii} \quad \text{A.16}$$

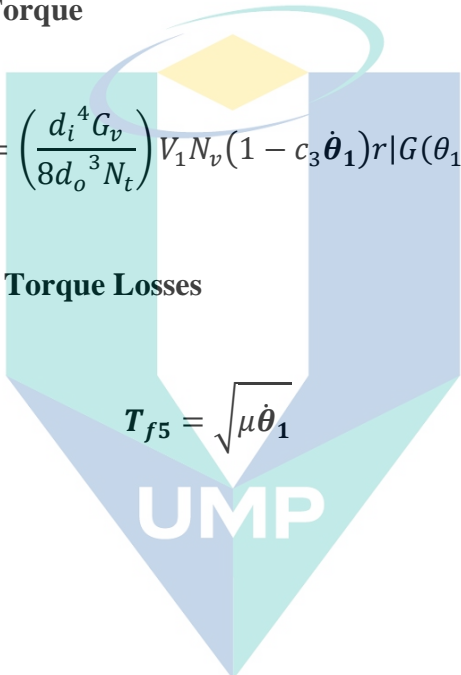
Skirt Friction Torque

$$T_{f2} = \left[\frac{\mu \dot{\theta}_1 r G(\theta_1)}{O_c} \right] dL_s r G(\theta_1) \quad \text{A.17}$$

Bearing Friction Torque

$$T_{f3} = \alpha A \frac{D_b}{2} (p_{ind} - p_{atm}) \frac{|\cos\theta|}{\sqrt{\dot{\theta}}} \quad \text{A.18}$$

Valvetrain Friction Torque


$$T_{f4} = \left(\frac{d_i^4 G_v}{8d_o^3 N_t} \right) V_1 N_v (1 - c_3 \dot{\theta}_1) r |G(\theta_1)| \quad \text{A.19}$$

Auxiliaries and Gear Torque Losses

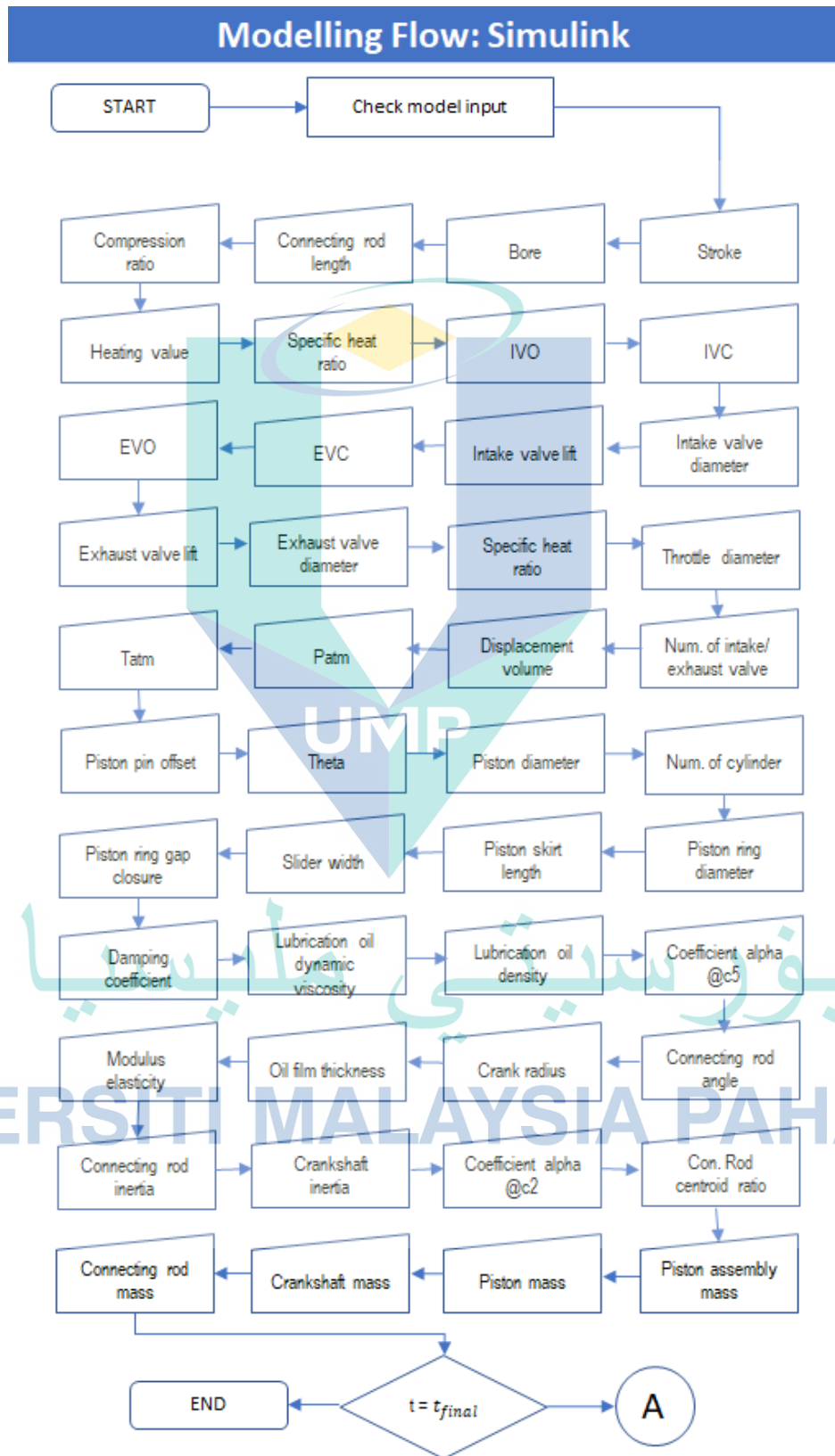
$$T_{f5} = \sqrt{\mu \dot{\theta}_1} \quad \text{A.20}$$

UMP

اونيورسيتي ملايسيا قهغ

UNIVERSITI MALAYSIA PAHANG

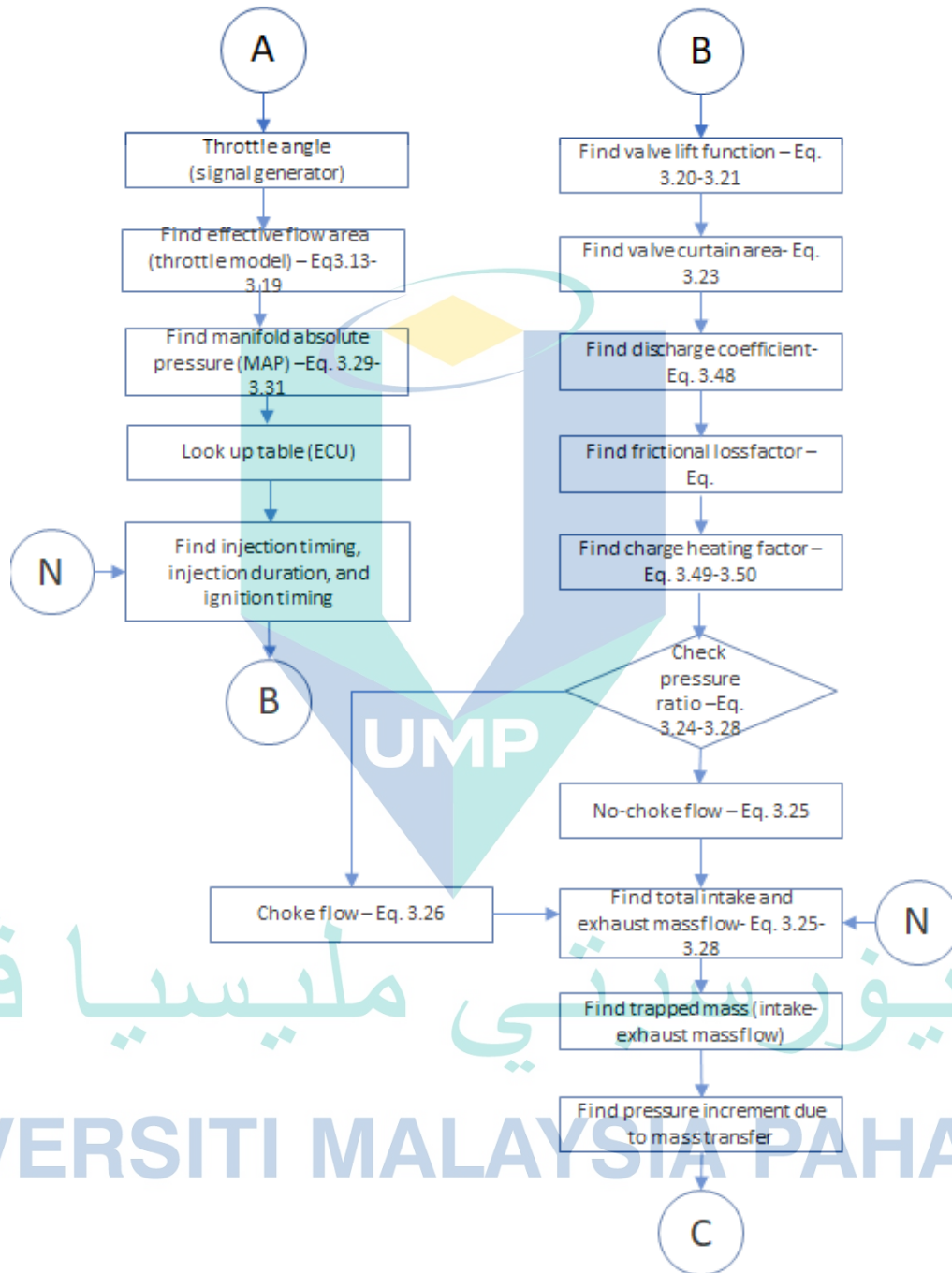
APPENDIX B
ANALYTICAL VEHICLE MODEL FLOW CHART



Modelling Flow: Simulink

1. Throttle angle input and throttle valve model

2. Engine cylinder model
a) Intake and exhaust valve flow



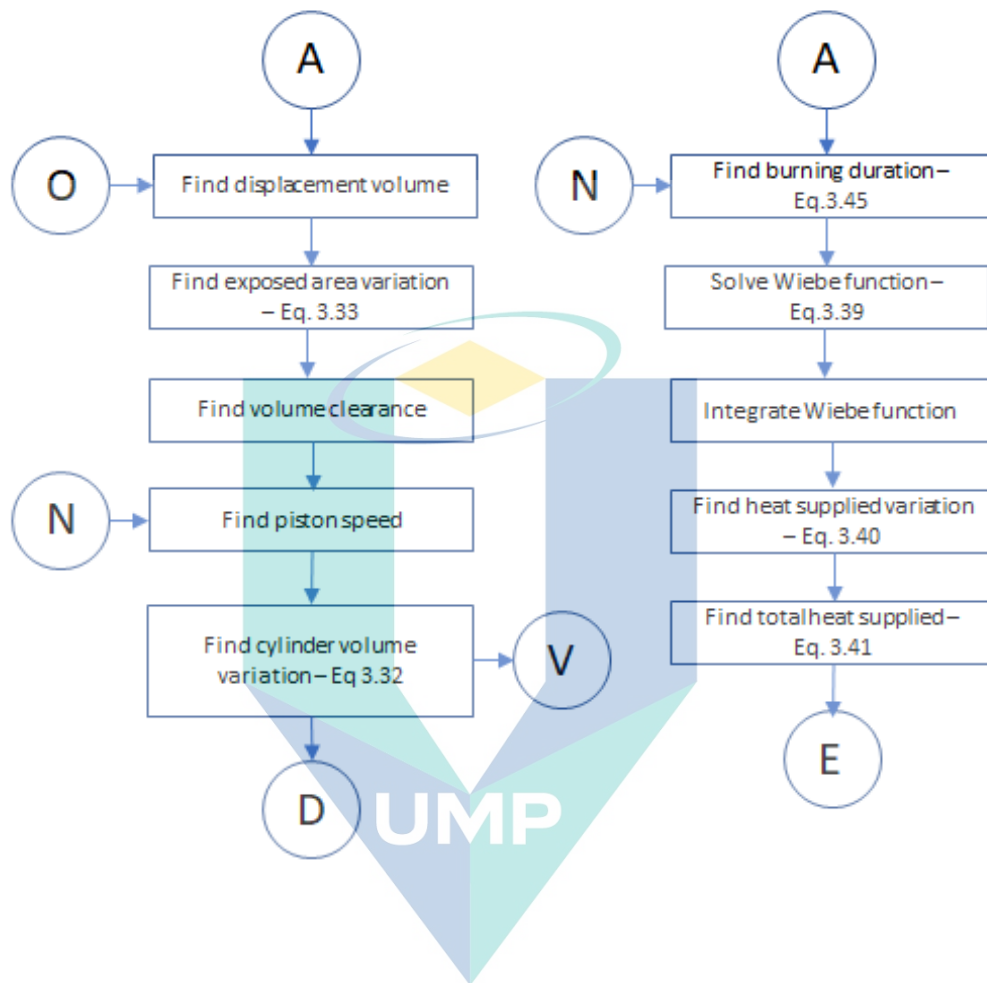
اونیورسیتی ملیسیا قهق

UNIVERSITI MALAYSIA PAHANG

Modelling Flow: Simulink

b) Crank-slider model

c) Heat release model



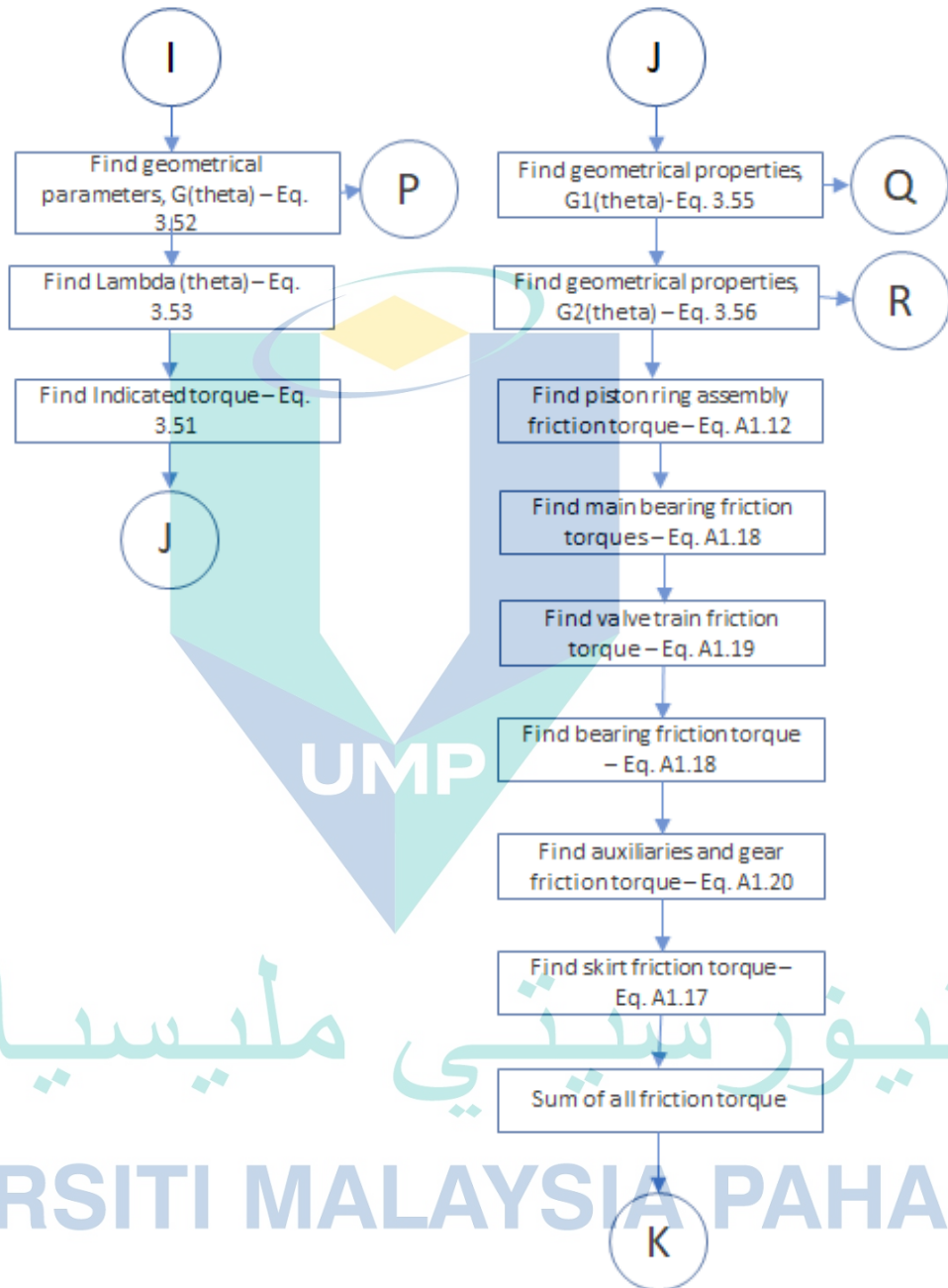
اونيورسيٲي ملايسيا قهغ

UNIVERSITI MALAYSIA PAHANG

Modelling Flow: Simulink

3. Indicated torque

4. Determination of frictional torque

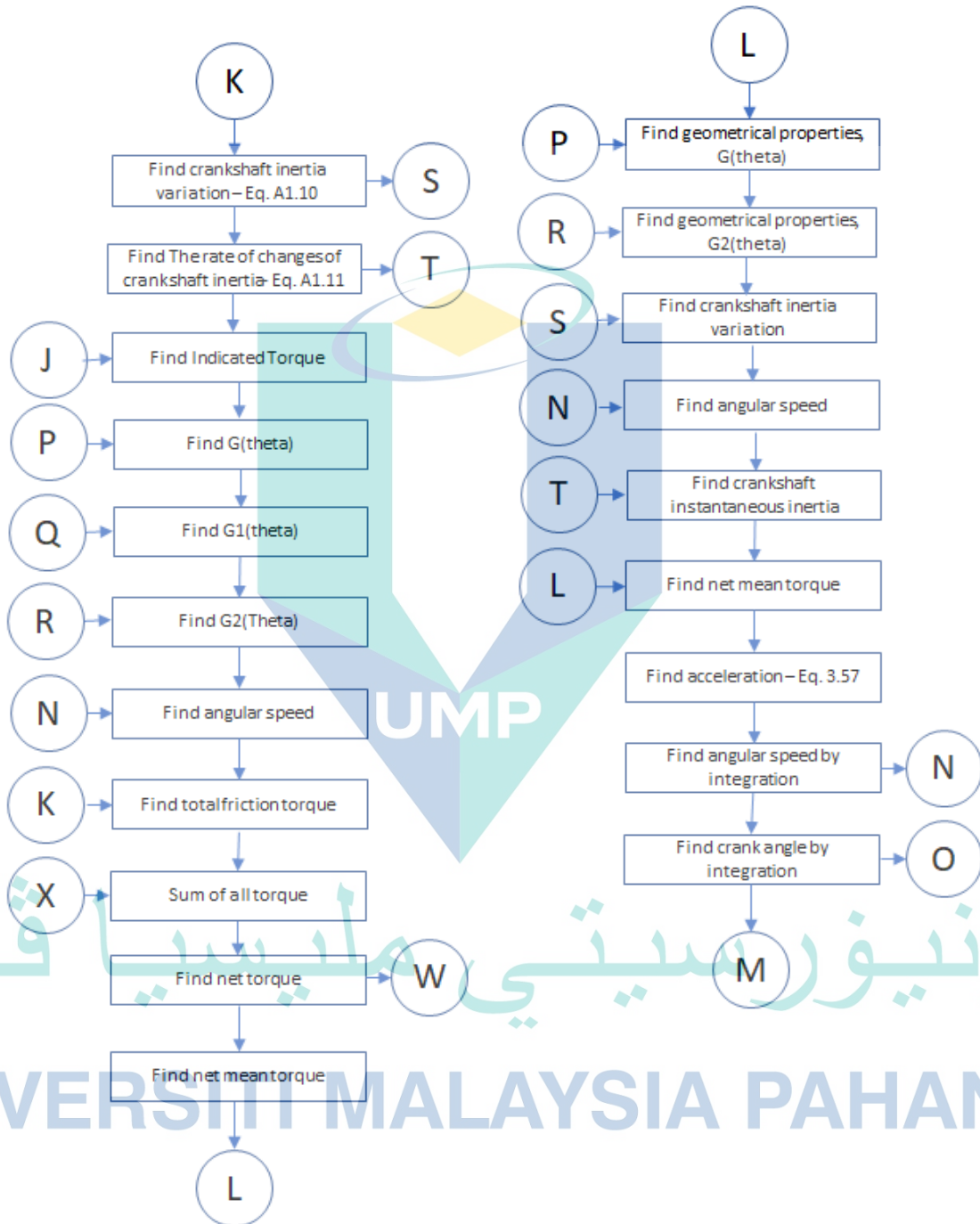


اونیورسیتی ملیسیا قهق
UNIVERSITI MALAYSIA PAHANG

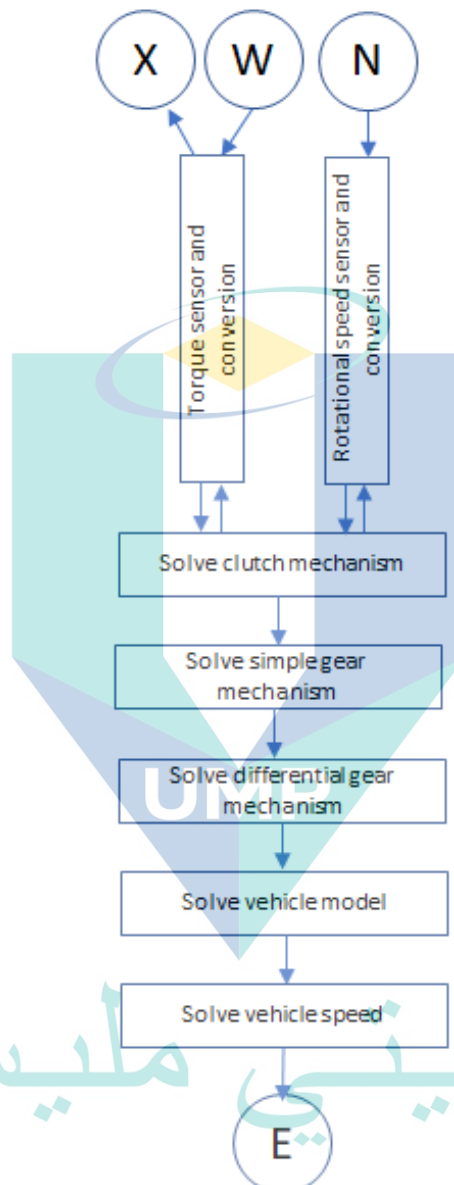
Modelling Flow: Simulink

5. Determination of Crankshaft Net Mean Torque

6. Determination of crankshaft angular acceleration, speed and crank angle.



Model Flow: SimScape



اونیورسیتی ملیسیا قهق

UNIVERSITI MALAYSIA PAHANG

APPENDIX C
INPUT FOR ANALYTICAL MODEL PER CYLINDER

Parameters	Value
Piston ring diameter (m)	0.08
Piston ring gap closure (m)	0.009
Co-efficient alpha, C5	0.01
Co-efficient alpha, C2	0.01
Number of intake/ exhaust valves	2/2
Diameter of intake/exhaust valves (m)	0.032
Displacement volume (m ³)	6.73*10 ⁻⁴
Number of cylinders	1
Oil density (kg/m ³)	0.8414
Coupler damping co-efficient	125
Oil dynamic viscosity (Pa.s)	0.19358
Piston skirt length (m)	0.043
Slider width (m)	0.003
Modulus of elasticity (N/m ²)	230*10 ⁹
Oil film thickness (m)	0.02
Crank radius (m)	0.044
Connecting rod length (m)	0.132
Cylinder bore diameter (m)	0.076
Piston pin offset (m)	0.00169
Atmospheric pressure (Pa)	101325
Piston diameter	0.073
Connecting rod angle at TDC (deg)	0.1745
Crankshaft inertia (kg.m ²)	0.0114
Connecting rod inertia, (kg.m ²)	0.001
Crankshaft mass (kg)	11.81
Connecting rod mass (kg)	0.395
Piston mass (kg)	0.264
Piston assembly mass (kg)	0.698

اونیورسیتی ملیسیا قهق

UNIVERSITI MALAYSIA PAHANG

APPENDIX D
EXCITATION FOR PARAMETRIC SIMULATION USING VEHICLE MODEL

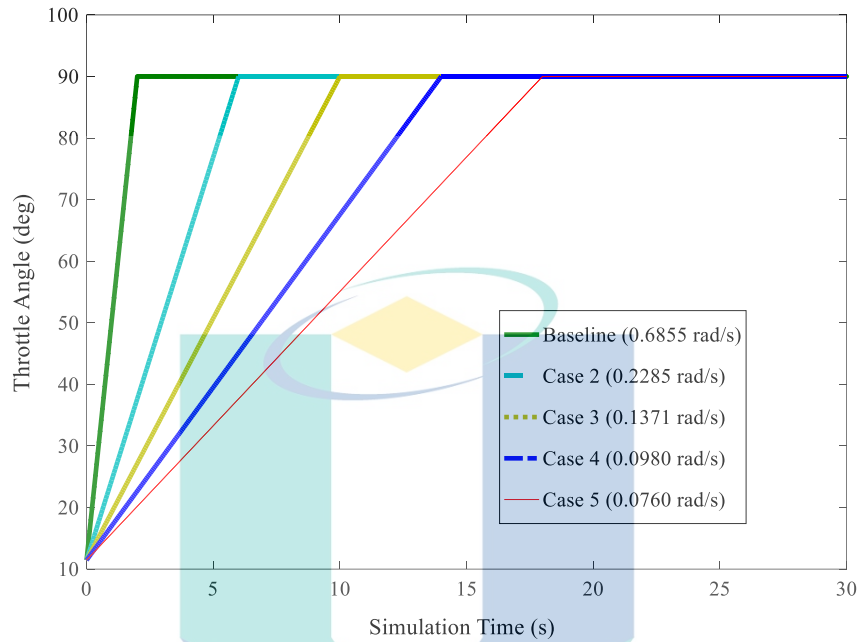


Figure D.1 The varied throttle opening rate imposed on the vehicle model

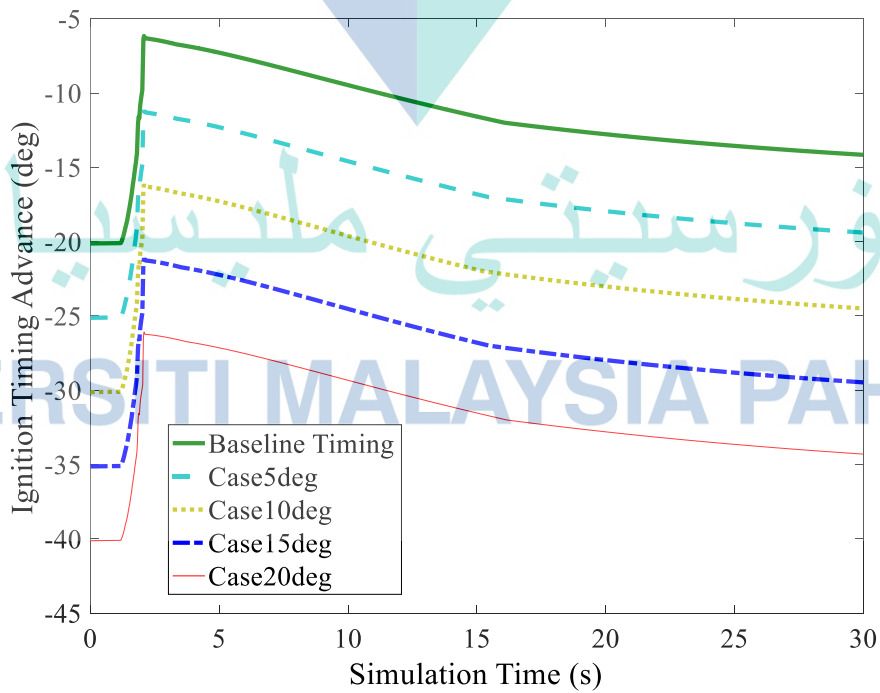


Figure D.2 The varied ignition timing which manipulated by using the output of the original ECU maps output

Table D.1 The variation of CNG mass flow rate through the injector at different CNG injection pressure

Injection Pressure (bar)	Mass flow rate (g/s)
20	0.4
30	0.55
40	0.7
50	1.1
60	1.2

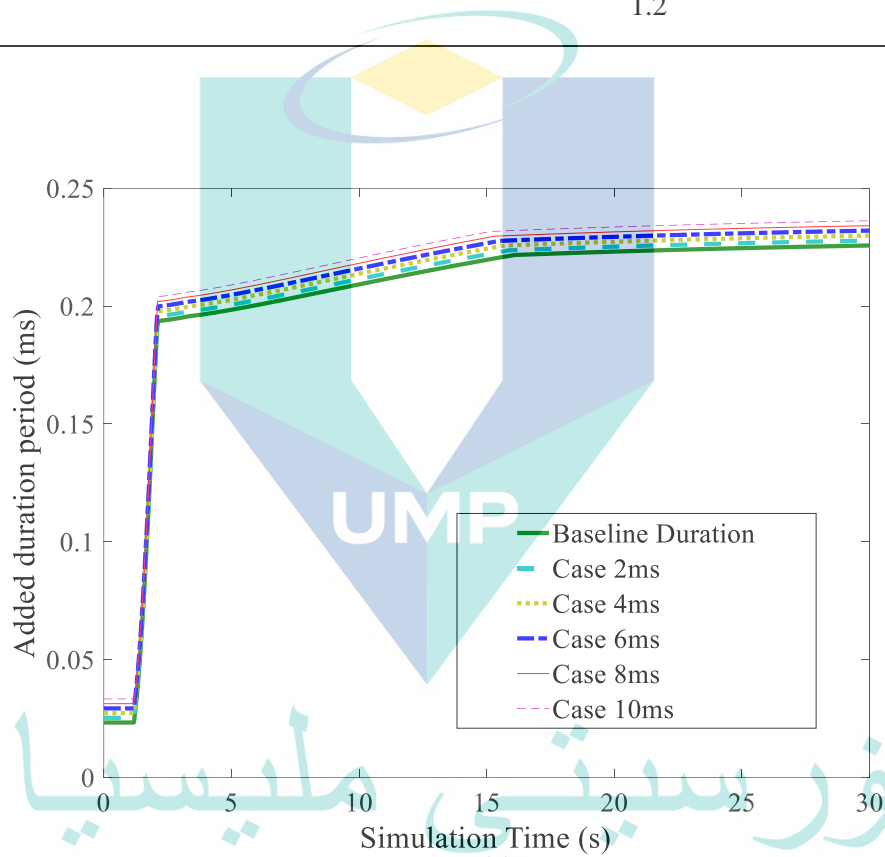
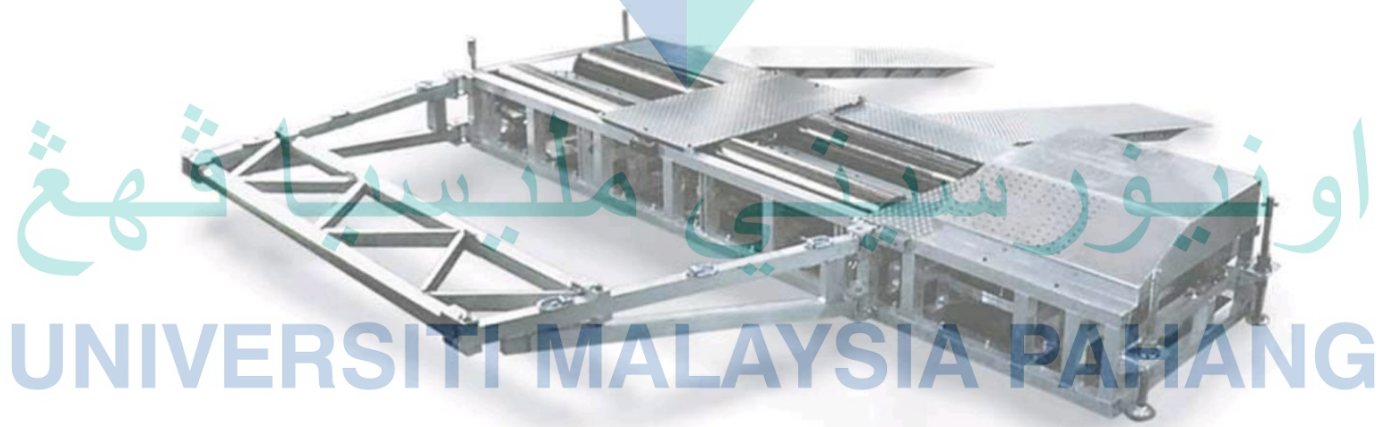


Figure D.3 Varied injection duration imposed on the vehicle model

APPENDIX E
DYNAMOMETER SPECIFICATION

Max Horsepower:	1,500 hp
Max Absorption:	900 hp
Loading Device:	Air-cooled eddy current power absorber (model MDK-250)
Inertia:	Approximately 2,000 lbs. base mechanical inertia
Max Speed:	175 mph
Controls:	Closed Loop Digital Controller with WindowsXP based PowerDyne Software. Includes Patented Virtual Road Simulation Technology.
Rolls/Wheelbase:	Precision machined and dynamically balanced, Knurled finish for superior tire traction, Belted for bi-directional capability 10.7" (272mm) diameter balanced rolls, 40" (1,016mm) face length, 28" (711mm) inner track width, 108" (2,743mm) outer track width, 19.6" (498mm) roll spacing
Roll Lock:	Industrial brake pad in contact with O.D. of roll
Roll Decelerator:	Allows vehicle deceleration without use of vehicle brakes. Eddy Current PAU used to decelerate rollers.
Air Requirements:	80 PSI, dry, regulated, oil free
Power Requirements:	115 VAC, single phase, 60 Hz, 15 Amps (computer) 230 VAC, single phase, 60 Hz, 40 Amps (dynamometer)
Axle Weight:	12,000 lbs (2,727 kg) maximum



APPENDIX F
HALTECH E8 SPECIFICATION

System Features	Detail specifications
Hardware compatibility	Piston Engines: 4, 5, 6 & 8 cylinders, Rotary Engines: 2 rotor, Max Operating RPM: 16000 RPM, Variable RPM range map points, Map resolution: 32 RPM ranges by 32 load points for all 3D maps
Trigger Signal Type Trigger Pattern	Hall Effect Sensor, Optical Sensor, Inductive Magnetic Reluctor Single Pulse per Cycle, Multi-tooth, Nissan Optical, Bosch Motronic, Subaru, Mitsubishi Std
Ignition Configuration	Single Distributor, Twin Distributor, Direct Fire Wasted Spark, Direct Fire Coil on plug, Ignition toggle support for rotary engines
Injector Firing Mode	Sequential, Multi-Point, Throttle Body (Batch), Staged
ECU Inputs	Crank Position Sensor, Cam Position Sensor, MAP Sensor (1,2 and 3 Bar), Throttle Position (potentiometer type), Coolant Temperature, Air Temperature, Barometric Pressure, Oxygen Sensor, Road Speed, Auxiliary Analog Input (x3), Auxiliary Digital Input (x1)
ECU Outputs	Injector Drivers: 4, Up to 4 injector Outputs, Fuel Pump Relay Control, PWM outputs (x4), Idle air control (IAC), Auxiliary digital out (x2)
Accessories	Boost/Fuel/Ignition Trim module, Idle Air Control Motor, Oxygen Sensor, Electronic boost control, solenoid Ignition Modules, Ignition Coils
Data Storage Features	Map Storage and Retrieval, Laptop Data Logging, On Board Data Logging

UMP

اونيورسيتي مليسيا قهغ

UNIVERSITI MALAYSIA PAHANG

APPENDIX G

INNOVATE AFR METER SPECIFICATION

The LM-2 combines an air/fuel ratio meter, a full-function 32-channel datalogger, and powerful software to deliver a complete tuning workshop. The meter digital signal processing technology provides data on exactly how rich or lean an engine is running at any load. The LM-2's self-calibrating circuitry also compensates for changes in temperature, altitude, and sensor condition.

Patented Direct Digital™ wideband sensor control, 100% digital wideband air/fuel ratio technology.

Wideband O2 Compatible with ALL fuel types

Single or Dual Channel A/F Version Available

OBD-II Scan tool- read/clear DTCs and log up to 16 channels of CAN OBD-II Data

Log directly to SD card

Playback log data on screen and/or with powerful LogWorks software

Large high-contrast graphics LCD

Built-in RPM converter (direct frequency or with optional inductive clamp)

4 fully-differential analog inputs

2 configurable linear analog outputs

Positive lock connectors for all connections

Innovate MTS serial IN and OUT

USB connection to your PC

The LM-2 also features two fully programmable linear analog outputs to connect to analog gauges, dyno computers, ECUs, piggyback controllers, and other devices with analog inputs.

With the provided LM Programmer software these analog outputs may also be defined by the user.

اونيورسيتي ملايسيا قهغ

UNIVERSITI MALAYSIA PAHANG

APPENDIX H

LIST OF PUBLICATIONS

- Rahim, M. F. A., Rahman, M. M., & Bakar, R. A. (2012). Cycle Engine Modelling Of Spark Ignition Engine Processes during Wide-Open Throttle (WOT) Engine Operation Running By Gasoline Fuel. *IOP Conference Series: Materials Science and Engineering*, 36, 12041. <https://doi.org/10.1088/1757-899x/36/1/012041>
- Taha, Z., Rahim, M. A., & Mamat, R. (2017). Injection characteristics study of high-pressure direct injector for Compressed Natural Gas (CNG) using experimental and analytical method. *IOP Conference Series: Materials Science and Engineering*, 257(1), 012057. <https://doi.org/10.1088/1757-899X/257/1/012057>
- Alias, M. H. R., Rahim, M. F. A., Rodzi, M. H. M. I., & Bakar, R. A. (2018). Effect of Injection Pressure, Injection Duration, and Injection Frequency on Direct Injector's Mass Flow Rate for Compressed Natural Gas Fuel. *MATEC Web of Conferences*, 225, 02008. <https://doi.org/10.1051/mateconf/201822502008>
- Rahim M.F.A., Jaafar A.A., Mamat R., Taha Z. (2020) Parametric Study of CNG-DI Engine Operational Parameters by Using Analytical Vehicle Model. In: Osman Zahid M., Abd. Aziz R., Yusoff A., Mat Yahya N., Abdul Aziz F., Yazid Abu M. (eds) *iMEC-APCOMS 2019*. *iMEC-APCOMS 2019*. Lecture Notes in Mechanical Engineering. Springer, Singapore
- MFA Rahim, AA Jaafar, Z Taha, and R Mamat (2019) Study on the Effect of Fuel Injection and Air Intake Boundary Setup on the Brake Torque Response by Using Comprehensive Vehicle Model for Natural Gas Vehicle (NGV) in Speed-Sweep Simulation, In: *UTP-UMP-UAF SYMPOSIUM ON ENERGY SYSTEMS 2019 (SES2019)*, 1-2 OCTOBER 2019 , Kuantan, Pahang, Malaysia. pp. 1-7.
- MFA Rahim, AA Jaafar, R Mamat, Z Taha MHR Alias (2019) Performance assessment of HDPI-CNG vehicle using speed-sweep test method, In: *5th International Conference On Mechanical Engineering Research (ICMER 2019)*, 30-31 July 2019 , Kuantan, Pahang, Malaysia. pp. 1-7.
- Mohamad Hafidzul Rahman, Alias and Mohd Fadzil, Abdul Rahim and R. A., Bakar (2019) Single Hole Direct Injector Simulation Validation and Parametric Sensitivity Study. In: *5th International Conference On Mechanical Engineering Research (ICMER 2019)*, 30-31 July 2019 , Kuantan, Pahang, Malaysia. pp. 1-7.